The Investigation of Transmission-Line Matrix and Finite-Difference Time-Domain Methods for the Forward Problem of Ground Probing Radar

By

Antonios Giannopoulos

Thesis submitted to the

Department of Electronics

and the committee on graduate studies of

THE UNIVERSITY *of York*

in partial fulfilment of the requirements

for the Degree of

Doctor of Philosophy

Supported by

"ALEXANDER S. ONASSIS"

Public Benefit Foundation

Grant No: O-013

March 1997

To my parents

Στους γονείς μου
Αλέξανδρο και Πιπίνα

«ἐν οἶδα ὅ,τι οὐδέν οἶδα»
Σωκράτης (469–399) π.Χ.

"I know nothing except the fact of my ignorance"
Socrates (469–399) BC

Abstract

The application of the transmission line matrix and the finite-difference time-domain methods for two and three dimensional numerical modelling of ground probing radar (GPR) is the subject of this thesis. Basic principles of GPR are discussed at the outset and the suitability of the chosen approach for its numerical simulation is demonstrated.

Efficient absorbing boundary conditions are introduced in the two dimensional formulation of the transmission line matrix in order to limit the computational domain. Their performance is evaluated and it is demonstrated that by using different forms of implementation they can perform similarly or better than the finite-difference time-domain method.

Two dimensional models are used to study the effects of the constitutive parameters of the subsurface to the GPR signals and the limits of horizontal and vertical resolution as well as responses from common geological targets.

A solution to the instabilities introduced by absorbing boundary conditions in the three dimensional transmission line matrix method using the symmetrical condensed node is reported as a modification of an existing formulation. The good performance of this absorbing boundary condition in free-space scattering problems is demonstrated using a scattering field transmission line matrix model.

Three dimensional models based on these numerical techniques are used to study the GPR responses from small localized targets and the advantages and disadvantages of different orientations of the transmitting and receiving antennas. The potential benefit of the use of magnetic field sensors in ground probing radar is demonstrated using the three dimensional finite-difference time-domain model.

Comparisons between the two formulations studied for the simulation of ground probing radar are reported.

Contents

List of Tables

List of Figures

Acknowledgments

Firstly, I would like to thank my supervisor Dr. Julian Tealby for his guidance, support and encouragement throughout this project. I thank the members of the remote sensing group over these years: Dr. John Dittmer, Tania Campbell and Allan Patterson who shared with me the excitements and disappointments of research. I would like to thank especially my good friend and colleague Panagiotis Tsourlos for his friendship, support and, most importantly, for the stimulating night-long discussions and life-saving cooking. To Dr. John Szymanski I express my gratitude for his encouragement and support over these years. I thank Dr. Baljinder Randhawa for the fruitful discussions on FDTD.

Thanks are due to the "ALEXANDER S. ONASSIS" Public Benefit Foundation for funding this project and to ERA TECHNOLOGY for allowing me to use their GPR system and data.

To my friends and colleagues in Greece I express my gratitude for their friendship and support. I am particularly grateful to Gregory Gerotziafas and Olga Iassonidou. I would also like to thank my friends at York: Theodore Papadopoulos and Tina Davis and wish them the best in their endeavors.

I thank my dear friend Geraldine Daly for her invaluable moral support and encouragement over the most difficult period of this project. I am also grateful to her for painstakingly proofreading this thesis.

Last but by no means least, I would like to express my gratitude to my family and especially to my parents. Without their emotional and financial support over these years this project would had never happened. The least I can do is to dedicate this work to them.

Declaration

This thesis is the work of the author except where indicated. Work presented in this thesis has been previously reported as follows:

Millard, S. G., Shaw, M. R., Giannopoulos A. and Soutsos M. N. *Modelling of sub-surface pulsed radar for non-destructive testing of structures*, Journal of Materials in Civil Engineering, (submitted)

Giannopoulos, A., Tealby, J.M. and Tsokas, G.N. *Numerical Modelling of ground penetrating radar*, Geophysical Prospecting, (submitted)

Giannopoulos, A., Tealby, J.M. and Szymanski, J.E. *Modelling and inversion techniques for radar applied to archaeological investigations*, IEE Colloquium on Radar and microwave techniques for non-destructive evaluation, Savoy Place, London, U.K., pp. 2/1 - 2/3, 1995

Giannopoulos, A. and Tealby, J.M. *Comparison of performance of absorbing boundary conditions in TLM and FDTD*, Electronics Letters, Vol. 31, pp. 1639 - 1640, 1995

Giannopoulos, A., *Modelling of GPR,* presented at: IRUA Meeting, York, 22 March 1994

Giannopoulos, A., Tealby, J. and Tsokas, G. *Numerical modelling of ground penetrating radar*, Extended Abstracts of the 56th EAEG meeting, Vienna, Austria, P048, 1994

Tealby, J. M., Oxley, J., Campbell, T., Giannopoulos, A. and Dittmer, J. *Analysis of Ground Probing Radar data, including polarization effects, when used in condition assessment of ancient monuments,* in Geophysical Exploration of Archaeological Sites, Series: Theory and Practice of Applied Geophysics, A. Vogel and G. Tsokas eds., vol. 7, Vieweg Verlag Publishing, pp. 235 - 247, 1993

Giannopoulos, A., Tealby, J.M. and Tsokas, G. N. *A 2D forward model of ground probing radar: The transmission line matrix method,* Proceedings of the 2nd Congress of the Greek Geophysical Union, Florina, Greece, Vol. II, pp. 172 - 183, 1993

Giannopoulos, A., Tealby, J and Tsokas, G. *Ground Probing Radar - a brief account of its merits and limitations based on case histories in N. Greece,* 2nd Symposium of the Greek Archaeometry Society, Thessaoloniki, Greece, 1993

Szymanski, J., Campbell, T., Dittmer, J., Giannopoulos, A. and Tsourlos, P. *Non-destructive site diagnosis at medieval abbey sites in the U.K.*, Medieval Europe, 6, pp. 201 - 206, 1992

Coppack, G., Emerick, G., Wilson, K., Dittmer, J., Szymanski, J., Tsourlos, P. and Giannopoulos, A. *Recent archaeological discoveries at the medieval site of Fountains Abbey,* Medieval Europe, 6, pp. 47 - 52, 1992

1

Introduction

1.1 Raison d' être

The use of electromagnetic signals, either naturally occurring or artificially generated, to probe the subsurface forms the basis of an important class of geophysical techniques. A number of different EM geophysical methods have been developed over the years by using different arrangements of the receiving and transmitting transducers operating in frequency or time domains. However, the basis of most of these EM methods is the use of low frequency electromagnetic signals. Therefore, in the analysis of the responses obtained by these methods, only phenomena associated with diffusion of electromagnetic energy into the earth are considered. The idea of employing higher frequencies where phenomena associated with the wave nature of the electromagnetic fields, although not a new one, had received little attention because these waves will not penetrate at sufficient depths to provide information about "classic" geophysical targets such as ore and oil deposits. Further, the analog equipment available at the early stages of development of such high frequency techniques made the manipulation of recorded data a very tedious if not an impossible task.

It is a well recognized fact that the use of such high frequency techniques, referred to as *ground probing radar* (GPR), is constantly increasing. Such an interest in GPR can be attributed to particular advantages of the method over other geophysical techniques,

especially for targets located at shallow depths. These advantages are mainly its non-destructive nature, its high resolving ability and the small amount of time required to acquire data. Further, advances in electronics have made possible the construction of small, field portable, equipment providing good quality digital data – a fact that has added to the appeal of the method to scientists and engineers involved with the exploration of the subsurface.

Advancing beyond the stage of detecting underground features using GPR into trying to extract specific information about the nature, type, size, location and other characteristics of GPR targets, however, one runs into difficulties. The extraction of such information from the GPR data is not often a simple process. This is mainly due to the complexity of the factors involved in the GPR's detection mechanism. Hence, data interpretation is strongly dependent on the experience and expertise of the GPR user.

Interpretation of GPR data can be assisted and improved with the aid of a model which will provide a close approximation to the response of GPR to subsurface targets and it will provide the means of studying the effects of the lossy environment, in which they are located, on the GPR signals. In addition, the construction of such a model is the first required step in designing an automated process which – usually by trial and error – will eventually provide an approximate image of the subsurface (data inversion).

The aim of this thesis is to investigate the construction of GPR models implemented in a digital computer using two numerical modelling techniques: the *transmission line matrix* (TLM) and the *finite-difference time-domain* (FDTD) methods. In doing so however, the complexity of the actual system to be modelled and its environment restricts the generality of the models to the use of simple idealized sources and subsurface media. On the other hand, such simplification will allow the "clinical" acquisition of isolated GPR target signatures which are of essence in interpreting and understanding GPR data.

1.2 Structure of the thesis

The diverse range of GPR applications makes it a cross-disciplinary tool used by scientists and engineers having different objectives and training. Hence, a thesis in an accessible form to researchers and practitioners of GPR with different backgrounds is required. Such a goal is very difficult to achieve, however; without analysing in detail concepts which form

the basis of geology, geophysics and engineering, and if this is to be attempted, the result will be a great amount of information – potentially obscuring the main aim of the work. The approach followed is to describe in detail the procedures involved in constructing GPR models and their use within the geophysical paradigm. Readers who are not familiar with the background of electromagnetic theory required can benefit from the use of the many excellent texts on electromagnetism cited in this work as the author did. Considering the above, the division of the material presented in this thesis in appropriate parts is as follows:

- **Chapter 2** reviews the basic principles of GPR as a radar system and as a geophysical method. A short account of its main areas of application is given and data acquisition strategies and processing procedures commonly employed are discussed.

- **Chapter 3** examines the factors influencing the GPR signals as they propagate into a lossy environment and discuss the difficulties associated with the formal analytical approach to predict the GPR response from subsurface targets. The pros and cons of different numerical modelling methodologies are then examined and the suitability of those investigated is established. The main assumptions made in applying them are stated and finally, a review of previous work on the subject is given.

- **Chapter 4** discusses the methodology of two dimensional GPR models. Particular emphasis is given to the application of absorbing boundary conditions to truncate the finite computational space. The shortcomings of the type of absorbing boundaries traditionally employed in TLM analysis lead to the investigation of the use of more advanced formulations available for other methods. These are successfully incorporated into the TLM algorithm. Results from a comparison of the performance of these absorbing boundary conditions in TLM and FDTD indicate a significant improvement in their performance when applied to TLM compared to their performance when they are applied to FDTD.

- **Chapter 5** presents the results of the application of the 2D methodology to the simulation of GPR responses from long (two dimensional) targets. In this Chapter, the influence of the medium parameters on the GPR signal are examined whether or not their values are dependent on the frequency of the electromagnetic fields. Further, issues of horizontal and vertical resolution are discussed and examples are given of the application of the models to such problems. GPR signatures of classic

geophysical targets are then presented and a comparison is presented between real GPR data obtained over a known target and the result of its simulation.

- **Chapter 6** discuss the extension of the methodology of two dimensional modelling to three dimensions. This is necessary since the inherent nature of the electromagnetic fields is three dimensional. Emphasis is given to the differences between 3D TLM methodologies and the corresponding 2D ones and, because the requirement in computer resources is substantially increased when TLM and FDTD are applied to 3D problems, an investigation into the application of better absorbing boundary conditions in the 3D TLM models – a more acute requirement than in the 2D case – reveals the problems encountered (manifested as instabilities in the numerical calculation). The instabilities observed when the symmetrical condensed node is used in TLM are not comparable to those in 2D TLM models and cannot be easily controlled using the same procedures.

  A remedy for this problem is provided in the form of a modified absorbing boundary condition, albeit with very good performance only for simulations involving free-space. The better performance of this modified absorbing boundary condition is then further demonstrated by considering free-space plane wave scattering from simple targets using a new scattered field formulation presented in **Appendix B**.

- **Chapter 7** presents the results of the application of 3D models to the GPR forward problem. The discussion is restricted to simple small localized targets and to an investigation of alternative arrangements of the GPR transmitting and receiving antennas. Further, the potential use of magnetic field sensors is investigated by examining synthetic GPR responses over small targets obtained by monitoring the magnetic field components – the numerical GPR signatures support the idea put forward of employing them in GPR surveying. This has, however, yet to be verified by experiment.

Comparison between the two numerical modelling methods are presented at every opportunity when it is felt that will be of benefit. Finally, **Chapter 8** presents a discussion of the findings of this thesis and discusses directions for future research.

2

Basic principles of Ground Probing Radar

2.1 Introduction

This Chapter provides some background information on GPR. An attempt has been made to describe GPR both as a radar system and as a geophysical technique. This approach has been taken in order for the Chapter to serve as a short introduction to GPR for readers with an engineering or radar systems background as well as for geophysicists and practitioners of GPR. Therefore, the basic concepts of radar are explained and GPR is presented as a particular type of radar system. Following a short discussion of GPR systems and the antennas which they commonly employ, GPR is examined in the context of exploration geophysics. The differences between GPR and low frequency electromagnetic methods are discussed, as well as its similarities with seismic methods. The various survey modes employed in GPR surveying and some common data processing techniques are explained. Finally, a review of some of the key applications of GPR is presented.

2.2 The concept of radar

Radar is an electromagnetic system for the detection and location of objects.[1] The fundamental principle of radar is the transmission and reception of electromagnetic waves which, in travelling from and back to the radar system, "acquire" information about objects located in their path at various distances from the radar system. According to Skolnic (1981):

> "Radar is used to extend the capability of one's senses for observing the environment, especially the sense of vision. The value of radar lies not in being a substitute for the eye, but in doing what the eye cannot do."

The radar's transmitting antenna radiates an electromagnetic wave — preferably in a given direction — which travels through air at the speed of light. When this wave encounters an isolated object, a portion of it will be reflected back towards the radar's receiving antenna.[2] The reception of this signal constitutes the detection of the object and, in principle, from the time elapsed between the transmission and reception of the electromagnetic wave from radar the distance to the object can be determined. Modern radar systems can not only detect the presence of an object, but also through sophisticated design and signal processing algorithms, can provide information about its angular position, size, velocity, direction and nature.

The history of radar goes back to the beginning of electromagnetism. The underlying mechanism of radar detection — the reflection of electromagnetic waves from metallic and dielectric objects — was verified experimentally by Heinrich Hertz in 1886 (Skolnic, 1981) and the first patent for a radar system as an obstacle detector was obtained by the German engineer Hülsmeyer in 1904. The main development of radar started in the mid-twenties and generally reached a peak in the thirties and during World War II when radar's abilities were realized by the military and were used for defensive and offensive purposes (Skolnic, 1981).

Even in today's much more peaceful world the military applications of radar remain the basic driving force for its development. Radar however, has a number of very important civilian applications. Some of them are: *Air traffic control and navigation, ship safety,*

[1] The word *radar* is a construction from "*ra*dio *d*etection *a*nd *r*anging".

[2] The transmitting and receiving antennas of a radar system could be the same physical object.

space exploration, remote sensing, law enforcement, etc.

2.3 The radar equation

Although the fundamental concept of radar is quite simple, the effective realization of it as a system is a complicated task involving the use of many different electrical and electronic devices. The performance of a radar system is described by the *radar equation*(Skolnic, 1981; Kingsley and Quegan, 1992). This equation serves as a mathematical description of radar's detection mechanism and it gives a first estimate of its performance and abilities.[3]

$$P_r = \frac{P_t G_r G_t \sigma^2 \lambda^2 L_s}{(4\pi)^3 R^4} \tag{2.1}$$

where, P_r is the power received by the radar (watt), P_t is the transmitted power (watt), G_r and G_t are the gain of the transmitting and receiving antennas respectively, σ is the radar cross-section (RCS) (square metre),[4] λ is the wavelength of the electromagnetic wave (metre), L_s is a factor representing the average losses of the system and R is the distance to the object (metre). The gain of an antenna is a measure of the increased power radiated in a given direction as compared with the power with which an isotropic antenna would have radiated (Skolnic, 1981). The RCS is a measure of the size of the object as seen by the radar. In a real system the power received (P_r) is not only that due to the reflecting object — noise is always present, originating inside or outside the radar system. The signal to noise ratio (SNR) is defined as the power received over the power of the noise present (Kingsley and Quegan, 1992).

$$SNR = \frac{P_r}{P_n} \tag{2.2}$$

Therefore, solving the radar equation for the range (R) of the radar and taking into account the SNR defined in (2.2)

$$R = \left[\frac{P_r G_t G_r \sigma^2 \lambda^2 L_s}{(4\pi)^3 \, (SNR) \, P_n} \right]^{1/4} \tag{2.3}$$

An estimate for the maximum range could be obtained from (2.3) for a given radar configuration. Closely related to the radar range and consequently to its performance are

[3] In fact the use of the *radar equation* to assess the performance of a radar system usually results in an overestimation of its quality (Skolnic, 1981).

[4] The symbol σ is used as well to denote conductivity. Confusion is unlikely to occur since RCS is not going to be used frequently in this work and therefore will not be discussed further.

issues involving the accuracy of the measurement of range and the radar's resolving ability. Resolution is defined as the minimum distance between objects in order that both can be detected as individual entities by the radar (Kingsley and Quegan, 1992). Clearly, if a radar transmits a pulse of duration τ, two objects could be detected separately if their separation is (Kingsley and Quegan, 1992)

$$\Delta R = \frac{c\tau}{2} \tag{2.4}$$

where c is the speed of light. The factor which most influences the accuracy of the range measurement is the frequency content of the transmitted signal. The higher the frequency content of the transmitted pulse, the greater the accuracy of the range measurement (Kingsley and Quegan, 1992). Bandwidth (B) is used as a measure of a radar system's ability to accurately determine range. It is defined as (Kingsley and Quegan, 1992)

$$B = \frac{1}{\tau} \tag{2.5}$$

where τ is the radar's pulse duration in seconds and B is measured in hertz. The larger the bandwidth of a radar system the greater its accuracy in determining range. The effective bandwidth of real radar systems is constrained by the bandwidth of their antennas and receiver, and could be significantly smaller than that calculated by (2.5).

Another important factor related to the measurement of range is how often a new pulse is transmitted by the radar. If a pulse is transmitted before the return of the reflections (echoes) from an object at a certain range, the location of the object is ambiguous because there is no unique time reference for the range calculation (Kingsley and Quegan, 1992). The pulse repetition frequency (PRF) is selected at the design stage, taking into account the desirable maximum unambiguous range.

There are many other factors which influence the performance of a radar system and which an engineer should consider in the design of a radar system. Most of them are relevant to specific types of radar systems.[5] Because this thesis is not concerned with this aspect of GPR there will be no further discussion here.

[5]For example, the use of the Doppler effect to determine the velocity of an object.

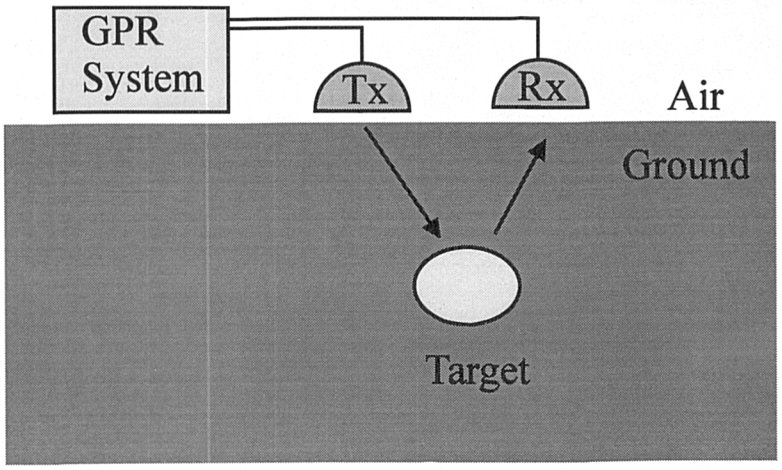

Figure 2.1: Schematic representation of the GPR detection mechanism.

2.4 General principles of ground probing radar

GPR is a particular type of radar system which is designed to locate discontinuities in the electrical properties of the subsurface, but its basic principle of operation is the same as that of a general purpose radar used for detecting objects above the ground. In Figure 2.1 the detection mechanism of a GPR is illustrated. The transmitting antenna couples an electromagnetic wave into the ground. This wave will propagate with a velocity determined by the electrical properties of the subsurface and a portion of it will be reflected back towards the receiving antenna when it encounters a discontinuity in these properties. This discontinuity can either be man made or naturally formed.

The *radar equation* can be used to describe the GPR's detection mechanism. Since the development of this equation was based on the assumption that radar waves propagate in air, which is a lossless medium, it should be modified accordingly to take into account the effects of the subsurface media in which the waves generated by a GPR will propagate. The factor which is primarily associated with the ability of a GPR to detect a discontinuity at a certain range (depth) is the attenuation which electromagnetic waves suffer as they propagate in a lossy medium. Therefore, the radar equation for the GPR case is (Smith, 1984)

$$P_r = \frac{P_t G_r G_t \sigma^2 \lambda^2 L_s e^{-\alpha 4R}}{(4\pi)^3 R^4} \tag{2.6}$$

where α is the attenuation constant in Nepers/m. The exponential term related with

attenuation plays an important role on the effective range of a GPR and, most importantly, introduces a dependence of the GPR performance on the detailed electrical properties of the subsurface.[6]

Iizuka (1984), summarizes the differences between GPR and general atmospheric[7] radars:

A. The range of interest in GPR is of the order of meters, whereas that for atmospheric radars is of kilometres.

B. Attenuation of the electromagnetic waves in the earth is a dominant factor in GPR, unlike atmospheric radars.

C. The inhomogeneous nature of the earth, which is important in GPR, is insignificant in most cases for atmospheric radars.

D. The target dimensions sought with GPR are of a different order of magnitude (smaller) than the ones which are usually detected with atmospheric radars.

E. Targets in all cases are stationary, unlike those sought by atmospheric radars which are usually moving.

2.5 GPR systems

Several types of GPR systems have been proposed and constructed with the modulation of the transmitted signal as their main design criterion. These systems fall into two main categories: **continuous wave** systems and **carrier-free** systems.

In continuous wave systems (CW) a pulse — usually a single tone — is transmitted continuously from the GPR antenna and the amplitude and phase of the reflected signal is recorded. Their bandwidth is small and consequently the depth (range) resolution is very poor. They have, however, been used in conjunction with holographic techniques to produce a site plan view of the subsurface for a given depth (Junkin and Anderson, 1988). The main advantages of continuous wave systems are that they do not require broadband

[6]The velocity of propagation of electromagnetic waves in earth is less than the speed of light ($c_m < c$) and should be taken into account in the definition of range resolution for the GPR case.

[7]The term *atmospheric* is used to denote that the medium of propagation for the radar waves is free space.

antennas and the peak power of the GPR transmitter can be kept small while the total transmitted power is high.

In carrier-free systems the signal is transmitted without being modulated into a carrier. These type of systems have an inherently large bandwidth and therefore their ranging abilities are superior to those of continuous wave systems. Harmuth (1981) defines a carrier-free radar as one with a relative bandwidth $n > 0.8$ where n is given by:

$$n = \frac{f_h - f_l}{f_h + f_l} \tag{2.7}$$

and f_h and f_l are the highest and lowest frequencies transmitted by the radar respectively. There are two different types of carrier-free systems: **mono-pulse** and those versions in which **pulse compression** techniques are used. In the mono-pulse systems a single pulse or impulse is sent from the transmitting antenna, but overly short pulses will limit the amount of radiated energy. Pulse compression techniques have been used in order to allow the use of long pulses to achieve a large radiated energy whilst at the same time obtaining the good ranging performance of a short pulse. Therefore, pulse compression can be described as a process of "synthesizing" a large bandwidth. The most common system using pulse compression is the **frequency modulated continuous wave (FM-CW)** GPR, (Olver et al., 1982) where the frequency of a carrier is modulated to increase the bandwidth of the system. A digital version of this type is the **step frequency** GPR (Iizuka and Freundorfer, 1983; Iizuka et al., 1984). Most of the commercially available GPR systems are of the mono-pulse carrier-free type and the general schematic of a carrier-free GPR system is illustrated in Figure 2.2 (Kingsley and Quegan, 1992).

2.5.1 GPR antennas

The GPR antennas are very important parts of the system. Their design is constrained by the following requirements:

A. Small physical size and weight to facilitate their use in surveying.

B. Faithful transmission of short pulses.

C. Short impulse response.

D. Good directivity (high gain in particular directions).

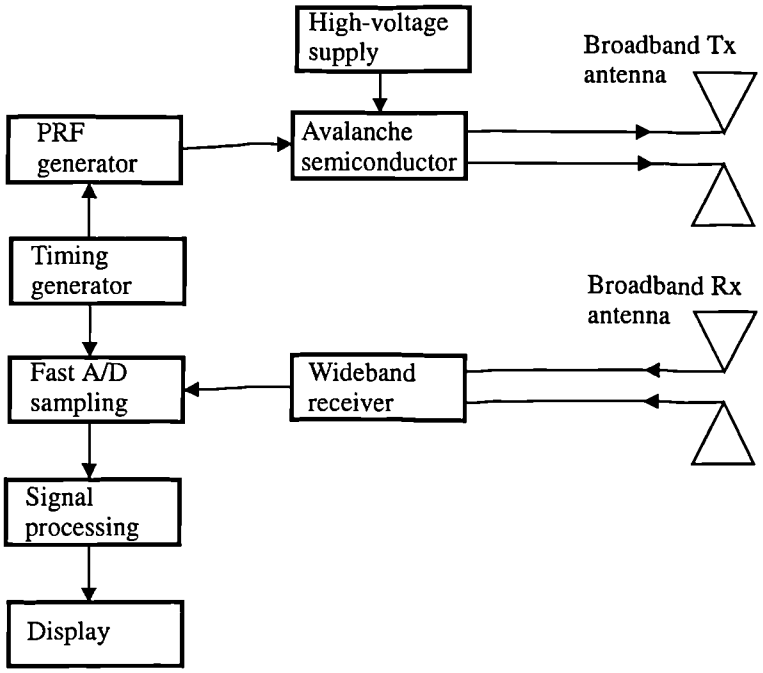

Figure 2.2: Schematic of a general carrier free GPR system (Kingsley and Quegan, 1992).

To facilitate the faithful transmission of short pulses broadband antennas are used in GPR systems (Daniels et al., 1988). Such antennas are: the **resistively loaded dipoles**, the two dimensional biconical antennas, known as **bow-ties**, and travelling wave antennas such as **TEM horns** (Balanis, 1982).

TEM horns have been used at a distance from the ground surface and in applications where high frequencies and small depth of penetration are required. Resistively loaded dipoles and bow-ties are used in more general applications of GPR. They are usually operated in close proximity to the ground in order to couple more efficiently the electromagnetic energy into the subsurface. Operating the GPR antenna close to the ground results in an alteration of the antenna characteristics (impedance) from the nominal values measured when the antenna is situated in free space. The electrical properties of the region of the subsurface influencing the GPR antenna can be estimated by measuring the antenna's input impedance (King et al., 1981). Therefore, the performance of a GPR antenna located in close proximity to the ground will depend on the detailed dielectric properties of the subsurface — unfortunately, the analytical calculation of the electromagnetic fields radiated from an antenna in close proximity to an interface is rather complicated and a general closed form solution is not yet available (see Chapter 3). However, the evaluation of the electromagnetic fields at distances far away from the antenna (far-field) has been accomplished where asymptotic techniques can be used. Such studies, which lead to the

calculation of the radiation patterns of a horizontal dipole located close to a half-space, have been reported by Engheta et al. (1982), who treated the problem when the dipole is located on the interface and Smith (1984) who reported formulas for the radiation patterns when the dipole is located at a height above the half-space. In Figure 2.3 the principle radiation patterns of an infinitesimal dipole located at various heights above a lossless half space calculated by the formulas given by Smith (1984) are presented. The most important conclusions from the work of Smith (1984), and recently the one of Arcone (1995) who studied the radiation patterns of GPR antennas using a numerical approach based on the work of Engheta et al. (1982), are summarized below:

- An antenna located close to a dielectric half-space radiates preferentially into the dielectric medium.
- The subsurface directivity of the antenna is increased as it is raised from the interface. However, increasing the height of the antenna results in an increase in the power of the back lobe (radiation in air) leading to an overall decrease in directivity. The optimum distance to achieve good directivity according to Smith (1984) is 0.1λ (where λ is the free space wavelength).
- The power in the side lobes decreases as the antenna is raised above the interface.
- The directivity of the antenna is low when is located on the interface, mainly due to the increased power of the side lobes.

In addition, since the receiving and transmitting antennas are located close to each other, mutual coupling effects occur. Different orientations of the receiving antenna with respect to the transmitting one produces varying levels of mutual coupling.

2.6 GPR as a geophysical method

Generally, techniques for obtaining information for subsurface features belong to the realm of exploration geophysics. Therefore, GPR could be viewed as another geophysical technique. Geophysical methods are classified in two main categories:

A. **Passive** : These methods measure the local disturbances of natural occurring fields due to the presence of subsurface features and they do not employ artificial sources

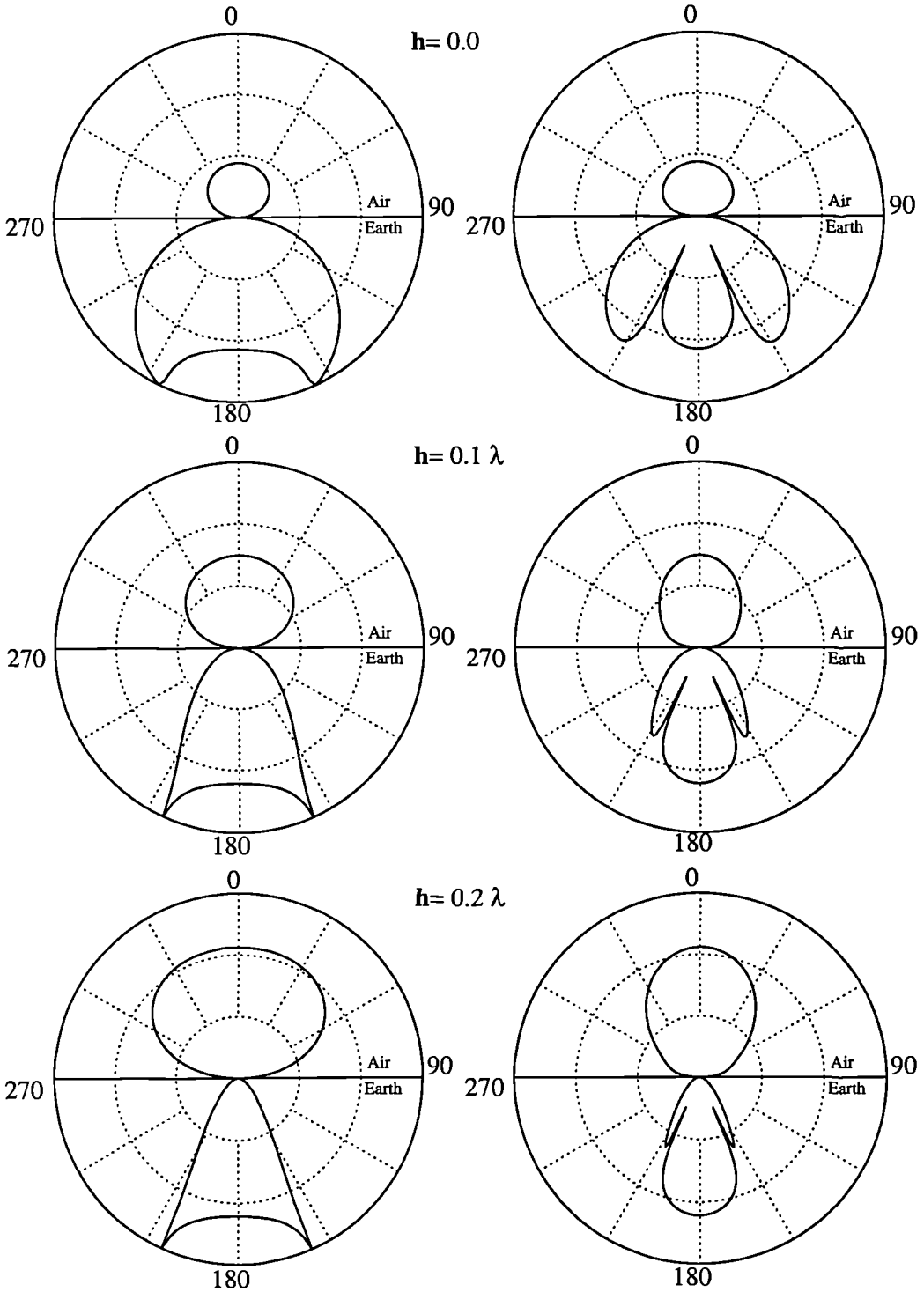

Figure 2.3: Steady-state radiation field strength patterns in both H (left) and E (right) planes of an infinitesimal horizontal dipole located at various heights (h) above a dielectric half-space ($\epsilon_r = 6$) (Linear scale).

of energy. In this category belong the magnetometery, gravitometery and magnetotelluric methods.

B. **Active** : These methods use artificially generated fields. In this category belong the GPR, low-frequency electromagnetic approaches, resistivity and seismic methods.

The electromagnetic nature of the GPR's waves classes it as an electromagnetic method, but the similarities between GPR and the other low frequency electromagnetic geophysical techniques are limited. This is a direct result of the differences in the mechanisms of energy propagation. In the case of GPR, electromagnetic energy propagates into the subsurface in the form of waves, whereas in the case of low frequency electromagnetic methods, the energy is diffused. Therefore, data acquisition, processing and interpretation are rather different in GPR and in low-frequency electromagnetic methods. On the other hand, for both GPR and seismic methods, wave propagation is the basis of their detection mechanisms. Although the nature of the waves used by the two methods are different — electromagnetic and acoustic respectively — their similar underlying model of energy propagation within the subsurface makes possible, to a certain extent, the use of similar procedures in both methods for acquisition, processing, presentation and interpretation of data.

The seismic method has been developed rapidly, mainly due to its significance in the location of oil reservoirs. Consequently, GPR has benefited significantly from the use of processing tools developed and used originally for the processing of seismic data.

2.7 GPR data acquisition schemes

This section describes the basic surveying modes used for GPR data acquisition. The terminology used is the same as that used in describing acquisition schemes for seismic methods.

Common offset mode

The basic procedure in acquiring data with a GPR involves the movement of the transmitting and receiving antennas — maintaining a constant separation distance between

them — over a straight line. The resulting data set is called a *scan* or a *section* and it is formed by the GPR time recordings — known as *traces* — at discrete points over the entire length of the line (Figure 2.4). Some systems facilitate continuous recording of GPR traces. With these systems a cart carrying the transmitting and receiving antennas could be dragged over the length of the scan line. If the velocity with which the cart is moving is known, the position of the individual GPR traces on the scan line can be calculated. In situations where this velocity is not known and, most importantly, not constant, distortions in the presentation of the GPR data set is unavoidable. Moreover, data processing algorithms which require the actual position of the GPR traces on the scan line (i.e. migration) can not be applied easily. The main advantage of continuous recording over the manual mode at discrete steps is the substantial increase of the speed of surveying. In some applications (i.e. road evaluation) where long scan lines are necessary, continuous recording is the only practical way to obtain data in reasonable time.

The above procedure could be repeated at regular intervals to form a grid of scan lines in order to obtain information about the spatial extent of the GPR targets over the area covered by the grid. In some cases, additional data are gathered with scan lines oriented orthogonal to the first ones. In most cases, the direction of the GPR scan is chosen in such a way that it will be orthogonal to the assumed strike direction of the targets of interest.

A particularly important factor in designing a GPR survey is the orientation of the transmitting and receiving antennas in respect to the scan line direction and to themselves. Figure 2.5 presents the various configurations possible. In practice the *parallel* and *cross* configurations (see Figure 2.5) are mainly used. As is apparent from Figure 2.5 there are three general types of different alignments of the transmitting and receiving antennas for the cross configuration. From these the type (c) is mainly used, especially in systems where the GPR antennas are placed in a specially designed cart which is pulled across the scan line. The parallel and cross configurations are used to delineate different types of targets. For example, the parallel configuration is more sensitive to planar targets, where as the cross configuration is more suitable for the detection of long thin targets and edges (Tealby et al., 1993). By using both configurations over the same scan line the information content about the survey site is substantially increased (Motoyuki, 1992; Motoyuki et al., 1995). An advantage of the cross configuration over the parallel one is the reduced level of coupling between the transmitting and receiving antennas.

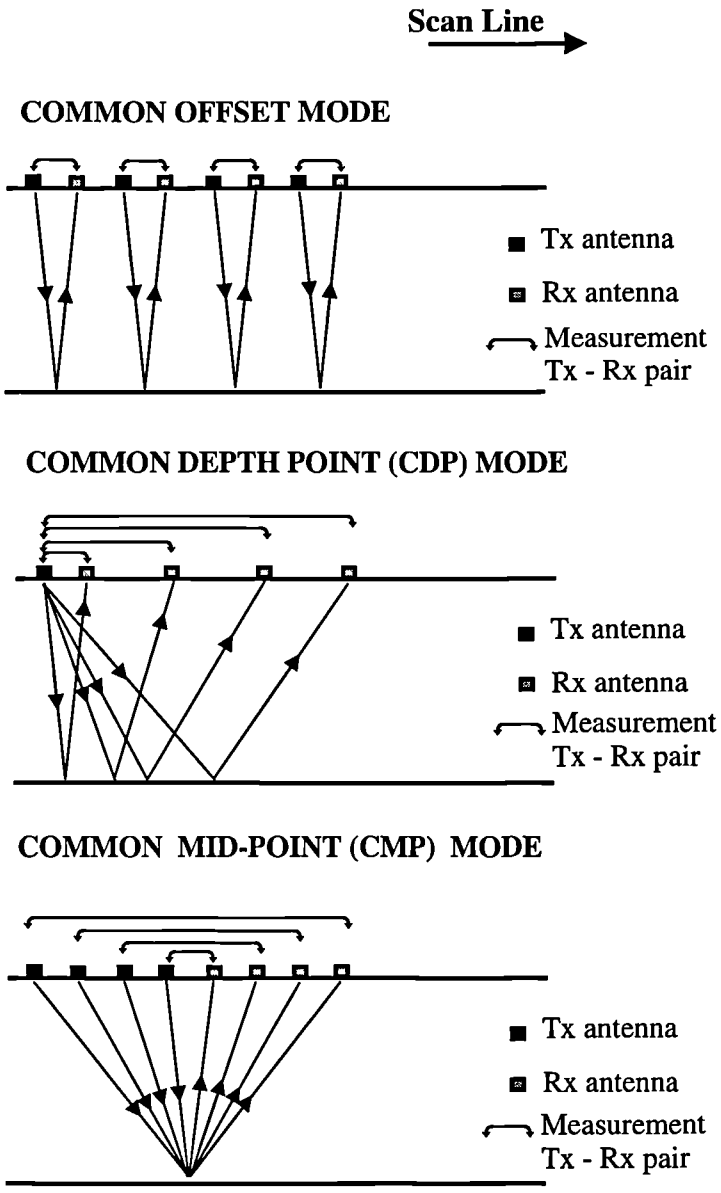

Figure 2.4: GPR survey modes

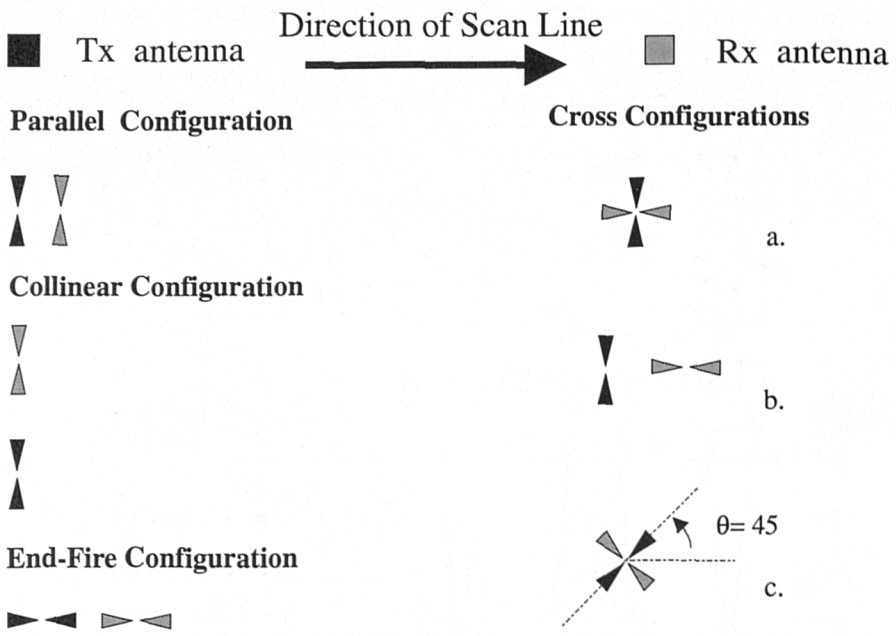

Figure 2.5: GPR Tx and Rx antenna configurations used in surveys.

Common depth point and common mid point survey modes

Another possible survey mode is to keep the transmitting or receiving antenna in a fixed location while the second antenna is moved along the scan line at regular intervals (Figure 2.4). This mode is called **wide angle reflection – refraction (WARR)** or **common depth point (CDP)**. However, if the reflector is not horizontal there is no common depth point — therefore the term **common source gather (CSG)** is used here.

Finally, both the transmitting and receiving antennas can be moved simultaneously away from a common centre point along the scan line (Figure 2.4). This mode is known as **common mid point (CMP)**.

The CDP and CMP modes are used mainly for the determination of the velocity of propagation. In determining the velocity using these modes one makes the assumption that reflections originate from a horizontal interface.

2.8 GPR data presentation

A GPR survey usually produces a large amount of data which should be presented in a form which facilitates their analysis and interpretation. The most common way of

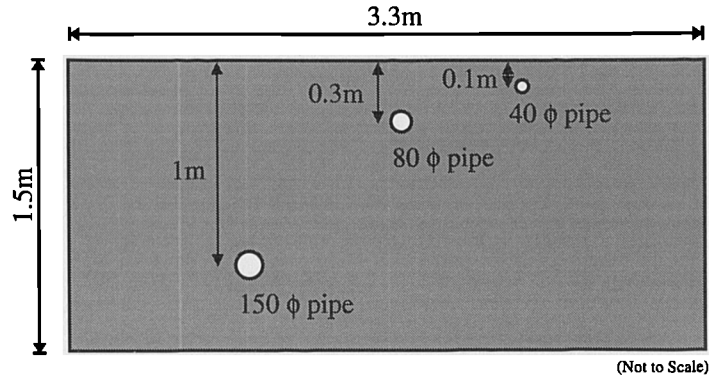

Figure 2.6: Schematic drawing of the ERA Technology test site, illustrating the locations of the three buried pipes.

presenting GPR data is as an image of which the vertical axis is the two-way travel time of the GPR signals and the horizontal axis denotes the position of the data along the scan line. Usually, different colors are used to represent the variations in amplitude strength of the received GPR signals. Alternatively, instead of colors, different shades of gray could be used resulting in a grey-scale image of the GPR data. A different type of presentation instead of color or grey-scale images is the standard seismic "wiggle trace" format. In this type of presentation the GPR traces are displayed as an ensemble of curves. In Figures 2.7 and 2.8 the GPR data measured over three buried pipes with an ERA Technology GPR system at the ERA's test site are presented in various formats; a schematic cross-sectional drawing of the test site is illustrated in Figure 2.6. The raw data is presented using a gray-scale and wiggle traces formats. The GPR scan is conducted using the cross configuration (case (c) of Figure 2.5) and the signal applied to the transmitting antenna is a 2 nanoseconds pulse. From the raw data the characteristic hyperbolic response obtained from buried pipes is apparent. However, the response of the pipe located at 1m depth is very faint and hardly recognizable. Signal processing techniques could be used to enhance the raw data and facilitate interpretation.

2.9 GPR data processing

The desired information about the location and nature of the subsurface targets is conveyed in the GPR's received signal (traces). Daniels et al. (1988) describe the nature of

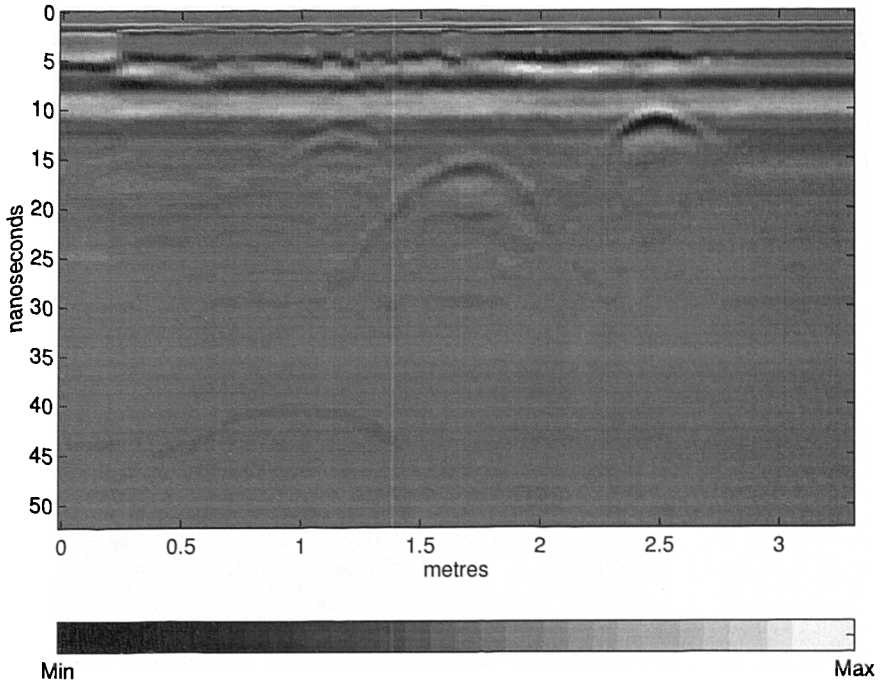

Figure 2.7: Raw GPR data measured over three buried pipes and displayed as a gray scale image.

the received signal by a GPR as a convolution of time functions

$$f_r(t) = f_s \star f_a \star f_b \star f_g \star f_u \star f_g \star f_a + n \tag{2.8}$$

where f_s is the signal applied to the transmitting antenna, f_a is the antenna response, f_b is a breakthrough function, f_g is the response of the ground, f_u is the response from the underground targets and n is noise.

The only term of the above equation which is known with certainty is the signal applied to the antenna (f_s). What is desirable is the determination of the response of the underground targets (f_u). This response is made up from two other time functions which are f_d and f_x and represent the distribution of targets in the ground and an individual target response respectively. The target distribution is the final aim when the nature of the targets sought is known, and their individual response is simple. Furthermore, when the problem is to identify the nature of a target (target recognition) its individual response is of interest.

Noise is always present in GPR data and is incoherent. Unwanted contributions to the received signal are characterized as *clutter*. Clutter is defined as coherent interference (Sheriff, 1991) present in GPR data. A particular kind of clutter, which is related to reflections due to the inhomogeneous nature of the subsurface, is referred to as *geological noise* (Davis et al. 1985). These reflections, which are real and originate from many small spurious targets, could mask returns from the desired targets.

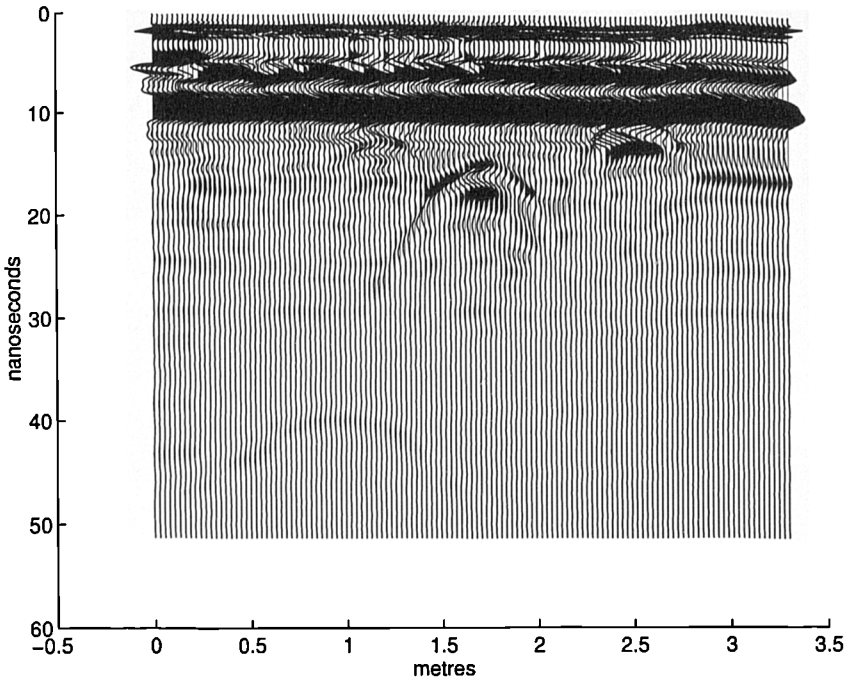

Figure 2.8: Raw GPR data measured over three buried pipes and displayed in "wiggle" traces format.

The GPR's traces gathered along a scan form a sectional image of the subsurface. Usually, interesting areas in that image, which in geophysical jargon are called anomalies, are quite apparent without any processing of the data. However, signal processing techniques are often employed in order to "clear" the data of unwanted information such as noise and clutter. Consequently, the responses from the desired target(s) are highlighted or even revealed from a noisy background. As mentioned above, the similarities between GPR and the seismic method have influenced GPR data processing approaches, and seismic packages are often used to process GPR data (Maijala, 1992; Liner and Liner, 1995; Young et al., 1995). From the plethora of signal processing techniques, those used most commonly are discussed below.

Averaging

This procedure takes place usually within the radar system itself — before storing the data — in order to increase the SNR. A number of nominally identical waveforms are averaged to produce the final one. The term *stacking* is also used to describe averaging and has originated from the seismic industry. It should be noted that averaging does not reduce geological noise (i.e. clutter)

Subtraction of the mean waveform

This technique aims to reduce clutter. It is assumed that the mean waveform of a large data set is a measure of the system's clutter (Daniels et al., 1988) which also presupposes that the desired target's responses spread over only a relatively few waveforms. If the ground were homogeneous, clutter removal would be a simple calibration procedure involving two measurements in two different locations; one over the target and one over a non-target area (Daniels et al., 1988).

Gain [8]

To compensate for the attenuation of the signal due to the lossy medium of propagation, an exponential weighting can be applied to the data. For optimum results the attenuation constant as well as the velocity of propagation should be known. Usually, only estimates of these values are available and the success of the gain procedure is mostly dependent on the operator's expertise.

A common problem in applying exponential weighting to the GPR data is that the noise level can be exaggerated, especially at large time values. Furthermore, it is sometimes advantageous to apply a reduction at short times, so as to suppress the direct coupling and surface reflections, and to gain the rest of the signal. This process facilitates data presentation, making a better use of the dynamic range of the display system. There are a variety of different gain processes available. Most commonly, the automatic gain control (AGC) is used (Yilmaz, 1987; Sheriff, 1991). This type of gain does not preserve information contained in the relative amplitude differences of the data.

The effect of applying the processes of *mean waveform removal* and *exponential gain* to the raw GPR data presented in Figure 2.7 is illustrated in Figure 2.9. Comparing the processed GPR section with the raw data image of Figure 2.7, the hyperbolic response from the deeper pipe is now clearly visible.

Thresholding

A time or amplitude threshold can be applied to the data so as to discard any sections that do not convey any useful information. Thresholding is mainly used for data pre-

[8] The process of applying gain to the GPR data should not be confused with the *gain* of its antenna

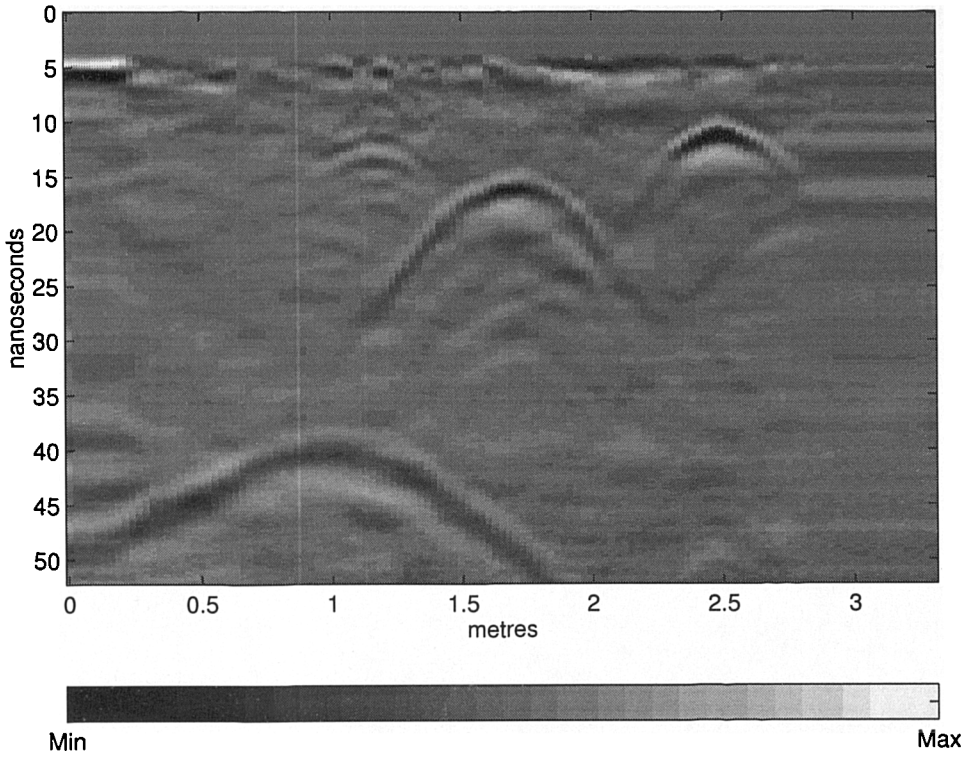

Figure 2.9: GPR data after subtraction of the mean waveform and application of exponential gain.

sentation, especially when one wants to suppress the strong surface reflections at short times.

Filtering

Frequency or time domain filters can be applied to GPR data to reject certain frequency bands from the received signal.

Deconvolution

Deconvolution is the "process designed to restore a waveshape to the form it had before it underwent a linear filtering action" (Sheriff, 1991). From equation (2.8) the recorded signal from a GPR can be represented as the convolution of various functions and therefore as the output of a cascade of different "filters". The purpose of deconvolution is to reverse the effects of some of these "filtering" processes. The result of deconvolution, is in most cases, a compression of the GPR wavelet and an increase in temporal resolution. According to Turner (1994) the application of deconvolution to GPR data has been unsuccessful mainly because assumptions implied from common deconvolution approaches developed to process seismic data (Yilmaz, 1987) and applied to GPR do not generally hold. Most importantly,

the non-stationarity of the GPR signal as it propagates through the subsurface is the main reason for the failure of deconvolution.

Resonance based characterization of GPR targets

The identification of certain types of GPR targets by determining their characteristic complex natural resonances is another process which has been applied to GPR data (Chan et al., 1979). The broadband nature of the GPR signal facilitates such an approach. Although promising results have been reported (Chan et al., 1979), such an approach has not yet become an integral part of the GPR processing routine and is still subject of research.

Migration

Profiling with GPR over a small localized target results in a set of responses which form a *hyperbola* (Davis and Annan, 1989). This hyperbolic response is caused by the "side-looking" of the GPR antennas at areas not directly under them. Therefore, signals from the same target arrive at different times for different positions of the GPR along the scan line. Isolated hyperbolic responses are characteristic of buried pipes, sewers and cables (Annan et al., 1984) and assist in their identification.

When the antenna is directly over a simple, small, isolated target, the time delay of the response is a minimum and the corresponding data point of the recording is the apex of the hyperbola. Therefore, the apex also signifies the physical location of the target in the horizontal direction (scan line). If the velocity of propagation of the electromagnetic waves in the subsurface is known, an estimate of the actual burial depth of the target can be made.

Migration is one technique for converting this hyperbolic response into a point, which is the apex of the hyperbola. Therefore, it is an 'imaging' transformation of the GPR's data set into an approximate sectional image of the subsurface. There are several migration techniques (Claerbout, 1992; Yilmaz, 1987), which are mainly developed for the processing of seismic data, that can be employed in the GPR's data processing routine (Fisher et al., 1992; Ho et al., 1994).

A simple migration algorithm has been developed during the earlier stages of this project.

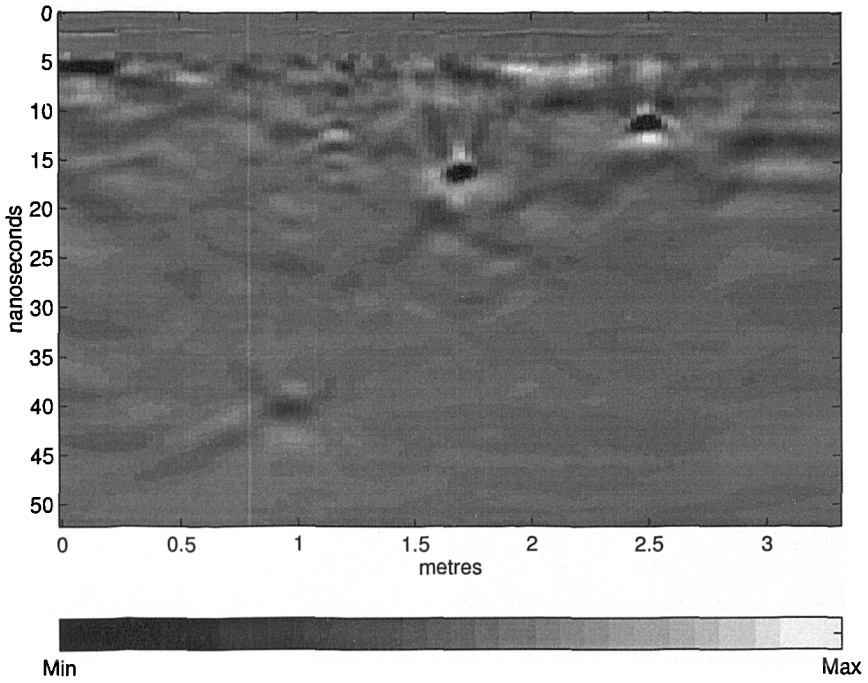

Figure 2.10: The migrated GPR section of the three buried pipes.

The method used is *maximum convexity migration* and is basically a computerized version of a geometrical migration (Robinson and Treitel 1980). The assumption of a constant velocity of propagation is necessary for the application of the method.

The algorithm treats every data point of the GPR's "image" as an apex of a hyperbola where its geometry is determined by the given velocity. A summation is performed of the values of the data points which intersect with the calculated hyperbola. All of the "energy" due to a real reflection point adds in phase and is preserved, whereas extraneous energy adds out of phase and is removed.

The algorithm performs well for simple cases while the assumption of a constant velocity of propagation is valid. However, the result is strongly dependent on the estimation of the velocity of propagation. Moreover, positioning problems of the recordings also affect the result, since the actual physical position of every waveform is needed. More sophisticated algorithms should be used (see Patterson et al., 1995) when distortions are introduced by uneven sampling along the scan line. In Figure 2.10 the migrated section from the GPR data of Figure 2.7 collected at the ERA Technology test site is illustrated and the position of the three pipes is clearly reproduced. The simple algorithm performed satisfactorily because no strong lateral or vertical variations of velocity are encountered.

2.10 GPR data analysis and interpretation

The aim of a GPR survey is to provide useful information about the possible underground targets. This information varies from mere detection of a region of different characteristics from the surroundings to the identification of the type, shape and depth of underground targets of interest. The analysis and interpretation of GPR data is carried out after the processing of the GPR data and its success or failure is strongly related to the expertise of the interpreter. In interpreting GPR data the following basic rules of thumb are important:

- Continuity of the recorded reflections from a target through the recorded GPR scan.
- Consistency of the recorded anomalies in successive GPR scans.
- Use of *a priori* information available from the application of other geophysical techniques or other sources of information.
- Knowledge of the limitations of the GPR system used.

2.11 Applications of GPR

The range of applications of GPR is quite diverse. This makes GPR a cross-disciplinary tool used by a variety of engineering and scientific disciplines. A more detailed account of the applications of GPR could be found in the review papers by Daniels et al. (1988), Peters and Young (1986), Peters et al. (1994). Some of the areas in which GPR has been applied include:

- **Non-destructive testing:** GPR has been used to determine the integrity of standing structures and the proper location of reinforcing elements embedded in them. (Parry and Davis, 1992; Bungey and Millard, 1995).
- **Location of buried utilities:** This is one of the most important applications of GPR, which is commonly employed for the location of water and gas pipes in urban areas (Annan et al., 1984; Michiguchi et al., 1988; Scott, 1989; Tsuchihashi et al., 1989) or in advance of horizontal drilling to determine the possible existence of hazards (Kathage, 1992).

- **Geological and environmental surveys**: GPR has been successfully employed for shallow depth geophysical problems such as the determination of stratigraphy (Stewart and Unterberger, 1976; Moffat and Puskar, 1976; Davis and Annan, 1989; Pilon and Grieve, 1991). Moreover, GPR has important applications in hydrogeology (Overmeeren, 1994) and general environmental problems (Brewster and Annan, 1994)

- **Archaeology**: The location and identification of archaeological ruins is an area where GPR has found a number of useful applications (Vaughan, 1986; Imai et al., 1987; Kong et al., 1992; Tealby et al., 1993, Tsokas et al., 1994; Giannopoulos et al., 1993). It is mainly employed to provide high resolution data on areas of interest determined by other geophysical reconnaissance surveys.

- **Location of buried ordinance and mines**: The ability of GPR to locate both metallic and non-metallic targets renders it as an important tool for the location of buried mines and ordinance (Bruschini et al., 1996; Chan et al., 1979).

2.12 Discussion

In this Chapter, GPR was presented both from a radar systems perspective and as a geophysical technique. The major differences between general atmospheric radar system and GPR are highlighted with an emphasis to the important role that the medium in which the GPR waves should propagate. Different GPR systems and the antennas which are commonly employed have been discussed. From a geophysical point of view, the differences between the low frequency electromagnetic geophysical techniques and GPR, as well as, the similarities of GPR with the seismic method have been explained. Finally, data acquisition and processing schemes and major areas of GPR applications were examined.

3

The GPR forward problem

3.1 Introduction

The aim of this Chapter is to serve as an introduction to the GPR forward problem. The fundamental electromagnetic relations which describe the propagation and interaction of electromagnetic waves with matter (at a macroscopic scale) and which form the governing equations of the GPR forward problem are stated at the outset. Using a simple analysis, the influence of the electrical properties of the materials probed by a GPR on the propagating electromagnetic pulses is then examined. The difficulties associated with the analytical solution of the GPR problem are then discussed and an overview of the numerical modelling strategies used to solve electromagnetic problems follows. This leads to the choice of a particular type of model for the simulation of GPR. A short review of the relevant literature on GPR modelling is presented and the fundamental assumptions used in this work in constructing GPR models are presented.

3.2 Fundamental electromagnetic relations

All electromagnetic phenomena, on a macroscopic scale, are described by the well known Maxwell's equations (Stratton, 1941; Balanis, 1989). These are first order partial differen-

tial equations which express the relations between the fundamental electromagnetic field quantities and their dependence on their sources.

$$\nabla \times \mathbf{E} = -\frac{\partial \mathbf{B}}{\partial t} \tag{3.1}$$

$$\nabla \times \mathbf{H} = \frac{\partial \mathbf{D}}{\partial t} + \mathbf{J}_c + \mathbf{J}_s \tag{3.2}$$

$$\nabla \cdot \mathbf{B} = 0 \tag{3.3}$$

$$\nabla \cdot \mathbf{D} = q_v \tag{3.4}$$

where t is time (seconds) and q_v is the volume electric charge density (coulombs/ cubic meter). In Maxwell's equations, the field vectors are assumed to be single-valued, bounded, continuous functions of position and time. Alternatively, Maxwell's equations can be cast in integral form by applying Stokes' and divergence theorems to the differential expressions:

$$\oint_C \mathbf{E} \cdot d\hat{\mathbf{l}} = -\frac{\partial}{\partial t} \iint_S \mathbf{B} \cdot d\hat{\mathbf{s}} \tag{3.5}$$

$$\oint_C \mathbf{H} \cdot d\hat{\mathbf{l}} = \frac{\partial}{\partial t} \iint_S \mathbf{D} \cdot d\hat{\mathbf{s}} + \iint_S \mathbf{J}_c \cdot d\hat{\mathbf{s}} + \iint_S \mathbf{J}_s \cdot d\hat{\mathbf{s}} \tag{3.6}$$

$$\oint_S \mathbf{B} \cdot d\hat{\mathbf{s}} = 0 \tag{3.7}$$

$$\oint_S \mathbf{D} \cdot d\hat{\mathbf{s}} = q_v \tag{3.8}$$

Using the integral form of Maxwell's equations, appropriate relations for the variations of the field vectors across boundaries of different media, where discontinuous distributions of charges and currents usually occur, are derived to determine the variations of the field vectors (Balanis, 1989). These *boundary conditions*, when the electrical parameters of the media either side of an interface are finite, dictate that:

- the components of the electric and magnetic field intensity vectors (**E**,**H**) tangential to the interface are continuous.
- the components of the electric and magnetic flux density vectors (**D**,**B**) normal to the interface are continuous.

Further, the macroscopic effects of charged particles contained in a given medium on the electromagnetic fields interacting with it are described by the *constitutive relations* which

are (Balanis, 1989):

$$\mathbf{D} = \bar{\bar{\epsilon}} * \mathbf{E} \tag{3.9}$$

$$\mathbf{B} = \bar{\bar{\mu}} * \mathbf{H} \tag{3.10}$$

$$\mathbf{J_c} = \bar{\bar{\sigma}} * \mathbf{E} \tag{3.11}$$

where $*$ denotes convolution and the tensors $\bar{\bar{\epsilon}}$, $\bar{\bar{\mu}}$ and $\bar{\bar{\sigma}}$ are the permittivity (farads/meter), permeability (henries/meter) and conductivity (siemens/meter) of the medium respectively, and are usually referred to as the *constitutive parameters*. They could, in general, be functions of position, direction, the strength of the applied field and time.

Since, in this work, all media are assumed to be *isotropic* and *linear,* the tensors of the constitutive parameters reduce to scalars. Further, in most cases it will be assumed that they are not functions of time and therefore the convolutions in equations 3.9–(3.11) reduce to multiplications. Finally, all media in this work are considered to be non-magnetic and therefore it is assumed that their permeability has a value approximately equal to that of the permeability of a vacuum

$$\mu \approx \mu_0 = 4\pi \times 10^{-7} \qquad \text{(Henries/meter)}$$

Moreover, the electric and magnetic field vectors can be decoupled from equations (3.1) and (3.2). This results in two second order differential equations involving only electric or magnetic field vectors. These equations are the vector wave equations for the electric and magnetic fields (Balanis,1989):

$$\nabla^2\mathbf{E} = \mu_0\epsilon\frac{\partial^2\mathbf{E}}{\partial t^2} + \mu_0\sigma\frac{\partial\mathbf{E}}{\partial t} + \mu_0\frac{\partial\mathbf{J_s}}{\partial t} + \frac{1}{\epsilon}\nabla q_v \tag{3.12}$$

$$\nabla^2\mathbf{H} = \mu_0\epsilon\frac{\partial^2\mathbf{H}}{\partial t^2} + \mu_0\sigma\frac{\partial\mathbf{H}}{\partial t} - \nabla\times\mathbf{J_s} \tag{3.13}$$

To solve any electromagnetic field problem with known initial and boundary conditions, one can use Maxwell's equations or the wave equations (electric or magnetic). There are other possible formulations which can serve as a starting point for the solution of an electromagnetic field problem (e.g. the use of vector potentials or Hertz vectors (Kong, 1986, Balanis, 1989, Wait, 1986). However, these are derived from Maxwell's equations and are generally introduced when their use will simplify the mathematical formulation of a given electromagnetic problem.

3.3 Complex permittivity and conductivity

In linear and isotropic media, the tensors of the constitutive parameters ϵ and σ reduce to scalar quantities. However, their values in most cases depend on the frequency of the electric field. For a time harmonic variation of the electromagnetic fields, Maxwell's equation 3.2 for source free media becomes

$$\nabla \times \mathcal{H} = \jmath\omega\tilde{\epsilon}\mathcal{E} + \tilde{\sigma}\mathcal{E} \tag{3.14}$$

where $\tilde{\epsilon} = \epsilon' - \jmath\epsilon''$ and $\tilde{\sigma} = \sigma' - \jmath\sigma''$ are the complex permittivity and conductivity of the medium respectively (with an implicit $e^{\jmath\omega t}$ dependence). The complex permittivity characterizes the macroscopic properties of distribution of dipoles in a dielectric material and the complex conductivity characterizes the macroscopic properties of moving free charges (King et al., 1981). It is evident from the above equation that permittivity and conductivity occur in the combination

$$\jmath\omega\tilde{\epsilon} + \tilde{\sigma} \tag{3.15}$$

from which the following three sets of effective constitutive parameters can be established:
A) The real effective permittivity and conductivity

$$\epsilon_e = \epsilon' - \frac{\sigma''}{\omega} \tag{3.16}$$

$$\sigma_e = \sigma' + \omega\epsilon'' \tag{3.17}$$

B) The complex effective permittivity $\tilde{\epsilon}_e$ with real and imaginary parts

$$\epsilon'_e = \epsilon_e \tag{3.18}$$

$$\epsilon''_e = \frac{\sigma_e}{\omega} \tag{3.19}$$

C) The complex effective conductivity $\tilde{\sigma}_e$ with real and imaginary parts

$$\sigma'_e = \sigma_e \tag{3.20}$$

$$\sigma''_e = -\omega\epsilon_e \tag{3.21}$$

The choice of a set of effective constitutive parameters is not absolute since

$$\sigma' - \jmath\sigma'' + \jmath\omega(\epsilon' - \jmath\epsilon'') = \sigma_e + \jmath\omega\epsilon_e = \jmath\omega(\epsilon'_e - \jmath\epsilon''_e) = \sigma'_e - \jmath\sigma''_e \tag{3.22}$$

In the GPR literature, the complex effective permittivity has mainly been used and sometimes erroneously described as the complex permittivity ($\tilde{\epsilon}$). Further, any measurements

of the dielectric properties of geological materials determine the effective constitutive parameters rather than the pure complex permittivity and conductivity because it is impossible to distinguish between σ' and $\omega\epsilon''$ or ϵ' and σ''/ω without a molecular or atomic interpretation (King et al., 1981). Moreover, it is convenient to use the relative permittivity which is a dimensionless ratio defined as

$$\tilde{\epsilon}_r = \frac{\tilde{\epsilon}}{\epsilon_0} \tag{3.23}$$

where ϵ_0 is the permittivity of vacuum.

3.4 Basic electromagnetic theory - Propagation of plane waves in lossy media

The detailed form of the propagation of electromagnetic waves in a lossy medium such as soils or rocks is an important factor in understanding GPR data. Although the actual GPR waves originating from the transmitting antenna are approximately spherical in nature, a simplification can be made in assuming that at a "sufficient" distance away from their sources the electromagnetic fields can be represented as plane waves. This idealized view allows the straightforward calculation of some important factors influencing the propagation of GPR signals and has been used for the approximate calculation of the GPR range from its radar equation and as the starting point of simple 1D models (Maser, 1992). This section describes some general concepts on the propagation of plane waves detailed - a treatment of the subject can be found in standard electromagnetic textbooks (Kraus, 1991; Johnk, 1975; Ramo et al., 1994; Balanis, 1989).

Using a Cartesian coordinate system, and assuming a time harmonic variation of the electromagnetic fields, a plane wave propagating in the z direction in a homogeneous, isotropic and linear medium with constitutive parameters ϵ_e and σ_e, and with its electric field vector oriented along the x axis, can be described by the one-dimensional wave equation (which can be obtained from (3.12) for time harmonic fields) as:

$$\frac{d^2\mathcal{E}_x}{dz^2} = -\omega^2\mu_0\epsilon_e\mathcal{E}_x + \jmath\omega\mu_0\sigma_e\mathcal{E}_x \tag{3.24}$$

Introducing the complex *propagation* constant $\tilde{\gamma}$ defined as

$$\tilde{\gamma} = \alpha + \jmath\beta = \jmath\omega\sqrt{\mu_0\tilde{\epsilon}_e} \tag{3.25}$$

where α and β are the *attenuation* and *phase* constants respectively, equation (3.24)

becomes

$$\frac{d^2\mathcal{E}_x}{dz^2} - \tilde{\gamma}^2\mathcal{E}_x = 0 \tag{3.26}$$

A solution of this equation is:

$$\mathcal{E}_x = \mathcal{E}_0^+ e^{-\tilde{\gamma}z} + \mathcal{E}_0^- e^{\tilde{\gamma}z} \tag{3.27}$$

which describes the propagation of waves propagating in the positive and negative z directions. Moreover, the phase and attenuation constants can be calculated from (3.25) (Johnk, 1975)

$$\alpha = \frac{\omega\sqrt{\mu_0\epsilon'_e}}{\sqrt{2}}\sqrt{\sqrt{1+(\frac{\epsilon''_e}{\epsilon'_e})^2}-1} \quad \text{(Np/meter)} \tag{3.28}$$

$$\beta = \frac{\omega\sqrt{\mu_0\epsilon'_e}}{\sqrt{2}}\sqrt{\sqrt{1+(\frac{\epsilon''_e}{\epsilon'_e})^2}+1} \quad \text{(rad/meter)} \tag{3.29}$$

Therefore, a wave propagating in the positive z direction is described by

$$\mathcal{E}_x^+(z) = \mathcal{E}_0^+ e^{-\alpha z} e^{j(\omega t - \beta z)} \tag{3.30}$$

and in the time domain

$$E_x(z,t) = E_0^+ e^{-\alpha z}\cos(\omega t - \beta z) \tag{3.31}$$

from the above equation a constant phase point of this wave propagates with a velocity

$$v_p = \frac{\omega}{\beta} \tag{3.32}$$

From equations (3.32) and (3.29) it is evident that the velocity of propagation of a plane wave, as well as the attenuation it suffers, are functions of the constitutive parameters and of the frequency of the electric field. This has important implications for the propagation of pulses. Since a pulse can be interpreted as a Fourier sum of time-harmonic components of different frequencies, when such a pulse propagates its shape will not be preserved if the variations in the phase velocities of its time-harmonic components are significant. This phenomenon is known as *dispersion* (Balanis, 1989). The relations (3.28) and (3.29) can be simplified by considering extremes of the ratio $(\epsilon''_e/\epsilon'_e)^2$. So that α and β can be

replaced by the approximate relations

$$\alpha \approx \begin{cases} \frac{\omega \epsilon_e''}{2}\sqrt{\frac{\mu_0}{\epsilon_e'}} & \text{if } (\frac{\epsilon_e''}{\epsilon_e'})^2 \ll 1 \\ \omega\sqrt{\frac{\mu_0 \epsilon_e''}{2}} & \text{if } (\frac{\epsilon_e''}{\epsilon_e'})^2 \gg 1 \end{cases} \tag{3.33}$$

$$\beta \approx \begin{cases} \omega\sqrt{\mu_0 \epsilon'_e} & \text{if } (\frac{\epsilon_e''}{\epsilon_e'})^2 \ll 1 \\ \omega\sqrt{\frac{\mu_0 \epsilon_e''}{2}} & \text{if } (\frac{\epsilon_e''}{\epsilon_e'})^2 \gg 1 \end{cases} \tag{3.34}$$

Further, examining Maxwell's equation (3.14) in terms of the value of the ratio ϵ_e''/ϵ_e', termed the *loss tangent* (Balanis, 1989), two regions can be distinguished where the nature of the electromagnetic fields differ significantly.

$$\nabla \times \mathcal{H} = \jmath\omega\epsilon_e'(1 - \jmath\frac{\epsilon_e''}{\epsilon_e'})\mathcal{E} \tag{3.35}$$

When the loss tangent is $\ll 1$ it is evident from the above that the displacement current $\jmath\omega\epsilon_e'\mathcal{E}$ dominates the conduction current $\omega\epsilon_e''\mathcal{E}$ and the **wave nature** of the fields prevails. However, when the loss tangent is $\gg 1$ the **diffusive nature** of the fields is predominant. Therefore, because the underlying concepts of GPR surveying are based on the wave nature of the electromagnetic fields, it is evident that the potential applications of GPR are generally restricted when the loss tangent is $\gg 1$. Under such circumstances it may be preferable to use a low frequency EM method which will be much more effective than GPR (Nabighian, 1987).

From Maxwell's equation (3.1), the magnetic field can be calculated easily and is

$$\mathcal{H}_y^+ = \frac{1}{\sqrt{\frac{\mu_0}{\tilde{\epsilon}_e}}}\mathcal{E}_x^+ \tag{3.36}$$

$$\mathcal{H}_y^- = -\frac{1}{\sqrt{\frac{\mu_0}{\tilde{\epsilon}_e}}}\mathcal{E}_x^- \tag{3.37}$$

for waves propagating in the positive (3.36) and the negative 3.37 directions respectively. Moreover, from the above relations the *intrinsic impedance* Z of the medium is defined as

$$Z = \sqrt{\frac{\mu_0}{\tilde{\epsilon}_e}} \quad \text{Ohms} \tag{3.38}$$

or more familiarly, using the real effective permittivity and conductivity,

$$Z = \sqrt{\frac{j\omega\mu_0}{\sigma_e + j\omega\epsilon_e}} \tag{3.39}$$

Suitable approximations can be made for Z depending on the value of the loss tangent. Therefore, for the case where the loss tangent $\ll 1$, Z could be approximated as a real number equivalent to a "resistance"

$$Z \approx \sqrt{\frac{\mu_0}{\epsilon_e}} \tag{3.40}$$

3.5 Constitutive parameters of soils and rocks

From the analysis of the previous section, it is clear that the constitutive parameters of the media probed by GPR play an important role in the nature of the electromagnetic fields propagating in them, and consequently on the GPR response. Unfortunately, there is no simple model to describe the variations of permittivity and conductivity for the great variety of soils and rocks that can be encountered in GPR surveying. This, to a great extent, is a result of the formation of soils and rocks as "mixtures" of a number of simpler substances which each have different influences on the electromagnetic fields. When media are composed of only one or a few substances (e.g. water), the determination of their constitutive parameters is considerably simplified and relations are available which describe their variations with temperature, pressure and frequency (King et al., 1981). However, soils and rocks rarely fall into this category. From the point of view of GPR surveying, the variation of constitutive parameters with the frequency of the applied electromagnetic field is the most important.

Several authors have reported experimental results and proposed empirical formulae for the variations of the constitutive parameters of soils and rocks (Hipp, 1974; Hoekstra and Delaney, 1974; Olhoeft, 1976; Katsube and Collet, 1976; Wobschall, 1977; Wang, 1980; King et al., 1981; Dobson et al., 1985; Hallikainen et al., 1985; Smith and Scott, 1989; Turner, 1994; Wensik, 1993). The above list is not exhaustive and there will be no attempt here to analyze the various measurement techniques reported in these papers or their detailed findings. Instead the priority of this section is to present some important observations and conclusions drawn from these works. These are:

- the constitutive parameters depend on pressure and temperature.

- the presence of water, in any form (bound or free) has a very strong effect on the measured constitutive parameters. This is a result of the high relative permittivity of water especially at low frequencies. Its effect at higher frequencies is associated with the polarization relaxation phenomena.
- non-linear effects have not been observed for the frequencies considered in these investigations. The overall frequency range encompasses the useful frequencies used in exploration geophysics (i.e. low frequency EM methods and GPR).
- the imaginary part of the complex conductivity can be ignored since its contribution is considered to be negligible.
- the effective permittivity increases with the amount of water present. For frequencies **below** 1 GHz this increase is observed with a pattern which suggests a dependence on soil type. For frequencies **above** 1 GHz, the increase in effective permittivity with water content is effectively independent of soil type.
- for the GPR frequency range (10^7-10^9 Hz), experimental evidence indicates that the effective permittivity of soils and rocks is independent of frequency (i.e. constant) and the effective conductivity increases almost linearly with it.

For the frequency range of most GPR systems, it is suggested that the Debye relaxation formula can be used to describe the complex permittivity of soils and rocks (Hipp, 1974)

$$\tilde{\epsilon} = \epsilon_\infty + \frac{\epsilon_s - \epsilon_\infty}{1 + \jmath\omega\tau} \tag{3.41}$$

where ϵ_∞ is the value of permittivity measured at very high (theoretically infinite) frequency, ϵ_s is the static (DC) permittivity and τ is the relaxation time. With the addition of a real static conductivity the real and imaginary parts of the effective complex permittivity are

$$\epsilon'_e = \epsilon_\infty + \frac{\epsilon_s - \epsilon_\infty}{1 + \omega^2\tau^2} \tag{3.42}$$

$$\epsilon''_e = \omega\tau\frac{\epsilon_s - \epsilon_\infty}{1 + \omega^2\tau^2} + \frac{\sigma_s}{\omega} \tag{3.43}$$

Usually, for the GPR frequency range $\omega^2\tau^2 \ll 1$ (Smith and Scott, 1989) and the approximations

$$\epsilon'_e \approx \epsilon_s \tag{3.44}$$

$$\epsilon''_e \approx \omega\tau(\epsilon_s - \epsilon_\infty) + \frac{\sigma_s}{\omega} \tag{3.45}$$

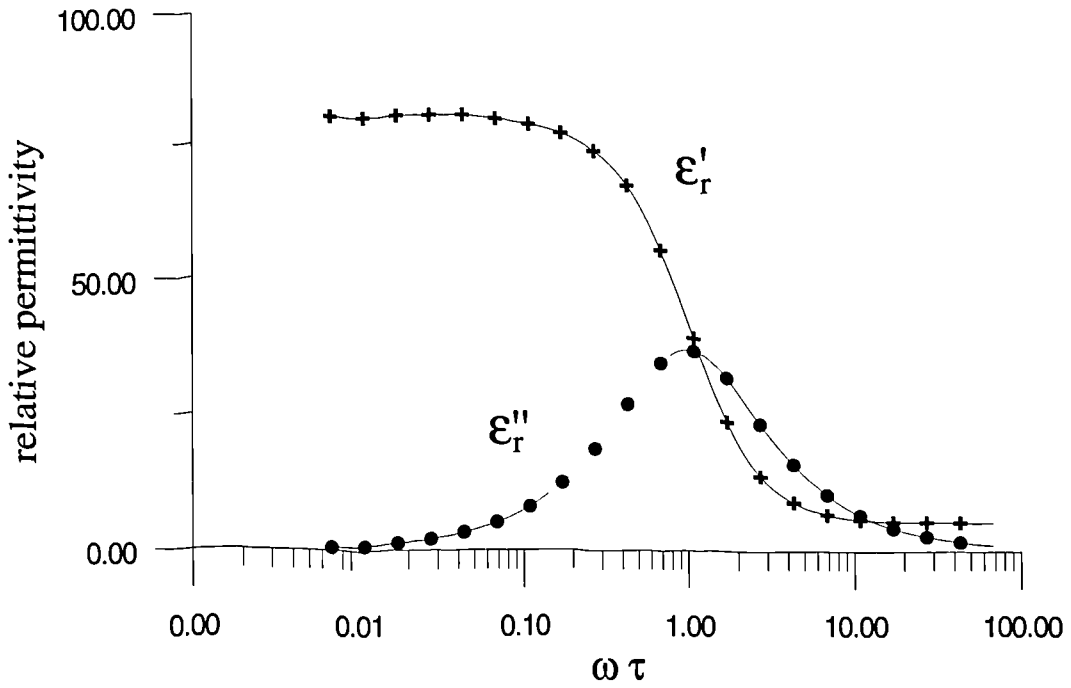

Figure 3.1: Plot of the real (ϵ_r') and imaginary (ϵ_r'') parts of the complex relative permittivity of water at a temperature of 15° C versus the parameter $\omega\tau$, calculated using the Debye formula with $\epsilon_{r\infty} = 5.5$, $\epsilon_{rs} = 82.3$ and $\tau = 10.9 \times 10^{-12}$ sec, (King et al., 1981)

can be made. The independence of the real part of the complex effective permittivity has an important implication on the GPR response. If the loss tangent is $\ll 1$: the velocity of propagation of the electromagnetic waves does not depend strongly on frequency and therefore an overall signal velocity could be assumed, which is in accordance with experimental evidence from GPR surveys (Davis and Annan, 1989). The linear dependence of the imaginary part of the complex effective permittivity with frequency results in a "low pass" filtering effect on the GPR pulses as they propagate in the subsurface. This tends to broaden the GPR pulse as it propagates in the subsurface (Vainikainen et al., 1992).

In Figure 3.1 the variations of the real and imaginary parts of the complex permittivity of water with the parameter $\omega\tau$ are plotted using the Debye formula. Examining Figure 3.1, it is evident that for values of $\omega\tau \ll 1$ the real part is almost constant and approximately equal to the low frequency permittivity of water whereas the imaginary part monotonically increases as the value of $\omega\tau$ approaches 1.

In general, to determine accurately the variation of the constitutive parameters of soils and rocks encountered in a GPR survey, measurements should be performed on samples either *in situ* or in a laboratory. However, this is not the usual procedure - typical values of the

Material	ϵ_{er}	σ_e (mS/m)
Air	1	0
Distilled Water	80	0.01
Fresh Water	80	0.5
Sea Water	80	30000
Dry Sand	3-5	0.01
Saturated Sand	20-30	0.1-1.0
Limestone	4-8	0.5-2
Shales	5-15	1-100
Silts	5-30	1-100
Clays	5-40	2-1000
Granite	4-6	0.01-1
Dry Salt	5-6	0.01-1
Ice	3-4	0.01

Table 3.1: Typical values of relative permittivity and conductivity for common geological materials at 100 MHz (Davis and Annan, 1989)

effective permittivity and conductivity are used and obtained from tables available in the literature. These tables are, in most cases, results of measurements at particular frequencies and do not give any information about the variations of the constitutive parameters with frequency. In Table 3.1 some typical values for the relative effective permittivity and conductivity of different geological media are presented (Davis and Annan, 1989)

3.6 Difficulties with the analytical solution of the GPR forward problem

The solution of the GPR forward problem, as of any electromagnetic field problem, is obtained by solving Maxwell's equations with the appropriate initial and boundary conditions. There are two approaches to accomplish such a task. One is to use analytical techniques and the other is to employ a numerical method. The major advantages of the analytical approach are the very useful insights which it provides into the physics of the problem and the speed with which numerical values can be obtained for the fields. The most significant drawbacks of the analytical methods are that they are usually very complex and difficult to formulate. Moreover, the solution obtained could be restricted to

a particular problem or suite of problems, and it may be necessary to reformulate if the parameters of the problem change significantly. However, the most important difficulty in obtaining an analytical solution to an electromagnetic problem is that the problem may not in fact have a closed form solution (i.e. the required result can not be obtained from a simple calculation of the final functional form of the solution). This is true for many practical electromagnetic problems which according to De Hoop (1991)

> "Except for the canonical problems in electromagnetics whose solution can be expressed in terms of analytic functions of a not too complicated nature and for analytic approximation techniques (usually of an asymptotic nature), both in the long and short wavelength regimes, that can be applied to a wider variety of cases, radiation and scattering problems in electromagnetics have to be addressed with the aid of numerical methods."

Unfortunately, the GPR forward problem belongs to the long list of practical electromagnetic problems for which a closed form solution does not exist even for simple GPR targets. This is a direct consequence of the fact that the GPR forward problem involves the infamous boundary value problem of a radiating dipole in the presence of a lossy half space (see Figure 3.2). The solution of this problem has been the subject of investigations by prominent mathematicians and physicists (Wait, 1961) from the early years of this century, when the first solution was published by Sommerfeld (1909), and is still the subject of research (King et al., 1992). The difficulty associated with the problem is that the electromagnetic fields are given by integral expressions which can not be evaluated in closed form and, further, the kernels of these integrals (known as *Sommerfeld integrals*) contain singularities which make even their numerical evaluation quite complicated. Closed form solutions exist only for few special cases and for a non conducting half space (Nikoskinen, 1990; Nikoskinen, 1993). Approximations to these integrals (usually of an asymptotic nature) and hence to the fields, have been obtained by various authors (Annan, 1973; Yokoyama, 1994; King and Sandler, 1994) ; key amongst these solutions are the ones reported by Baños (1966) where a detailed review and treatment of the problem can be found. Results and methodologies for the numerical evaluation of these integrals have been reported as well (Siegel and King, 1970; Bubenik, 1977; Rahmat-Samii et al., 1981; Johnson and Dudley, 1983; Dvorak, 1992; Annaert, 1993). The full GPR forward problem is even further complicated by the presence of targets within the half space which

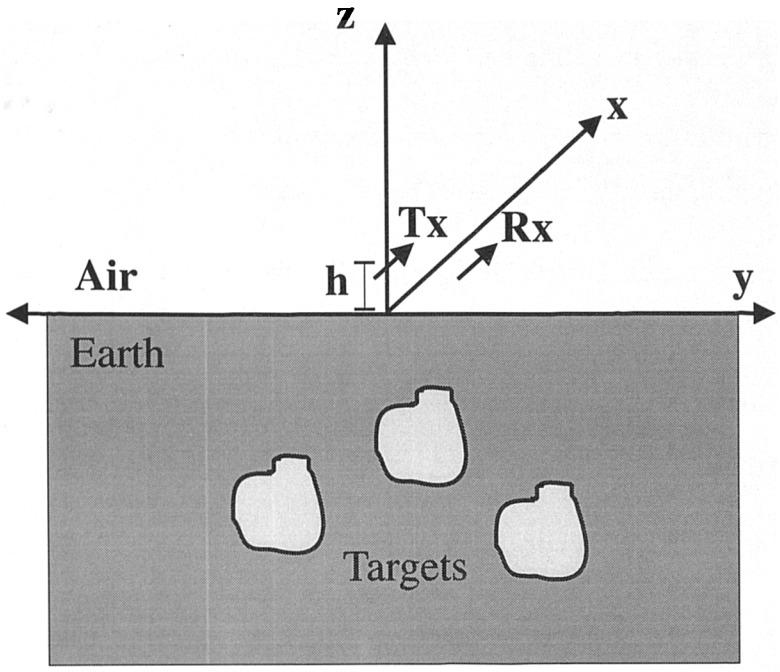

Figure 3.2: The GPR forward problem. Tx and Rx are the transmitting and receiving antennas respectively located at a height (h) above the Air-Earth interface.

in essence makes the problem very difficult to formulate analytically. Therefore, the use of numerical techniques is essentially the only viable way to obtain a solution to the GPR forward problem: although lacking in mathematical rigor this approach provides a useful approximate answer to the problem.

3.7 Numerical modelling for the solution of electromagnetic problems

The growing interest in numerical modelling techniques is directly related to the advent of the digital computer and the rapid advancements in the relevant technologies which resulted in a substantial and continuing increase in the available computational power. However, modelling as a procedure is distinct from pure computation. Although computation is an essential part of the general modelling process, numbers produced by a computer program do not convey any information by themselves, unless they are part of a rational procedure which describes a physical phenomenon.

The construction of a numerical model for the solution of a particular electromagnetic problem can be divided into five steps (Miller, 1988; Christopoulos, 1995)

- **Conceptualization:** Which is the process of describing the problem in terms of physical principles in a simple form.
- **Formulation:** The process of transformation of the physical principles into a more comprehensive, formal mathematical representation.
- **Numerical implementation:** The step in which a computer algorithm is constructed from the mathematical representation with the aid of numerical techniques.
- **Computation:** The outcome of the numerical implementation after execution as a computer program.
- **Validation:** The process of verification of the output for physical reasonableness having in mind the complexity of the problem.

The classification of numerical modelling techniques is mainly based on the second step; the formulation of the electromagnetic problem. The formal mathematical representation of the electromagnetic fields, which is used to build the modelling procedure, could be directly Maxwell's equations in differential or integral forms, or (equivalently) the vector wave equations, or any other formulations directly related to Maxwell's equations or the vector wave equations (e.g vector potentials, Hertz vectors, Greens functions). The choice of a differential or an integral formulation leads to numerical methods known as *differential equation methods* (DE) or *integral equation methods* (IE) respectively. Equally important in the formulation stage of the problem is the decision about the domain of the formulation. When time is explicitly present as a variable, the numerical methods are characterized as *time domain methods* (TD) whereas, if a time harmonic variation of the electromagnetic fields is assumed, the numerical methods are characterized as *frequency domain methods* (FD). In general, time domain methods are most suited for problems when the transient response is of interest, whilst frequency domain techniques are mainly used when the steady-state response is required. Examining the nature of the problem facilitates the decision of the appropriate domain for the formulation of the model.

The choice between a differential or integral formulation of the problem is made based on the merits and demerits of the two formulations when applied to the types of problems of interest. In general, integral equation methods, such as the *method of moments* (Harrington, 1993), are based on integral representations of the electromagnetic fields. Integral representations are usually obtained using appropriate Greens functions, although

formulations using vector potentials or Hertz vectors are possible (Morita et al., 1990). Differential equation methods are based on formulations which are directly obtainable from Maxwell's curl equations or the vector wave equations.

The main advantages of IE methods compared with DE are as follows:

- No special consideration is needed to satisfy the radiation condition;
- The dimensionality of the problem can be reduced by one (not for inhomogeneous problems, however).

The main disadvantages of IE methods compared with DE are as follows:

- Closed forms of specialized Greens functions which can expedite the solution of certain type of problems are not generally available;
- The overall implementation of the model is more complicated and requires a degree of analytical manipulation.

The main advantages of DE methods compared with IE are as follows:

- Simpler formulation and implementation of the numerical model;
- The treatment of inhomogeneities present in the problem is simple and straightforward;
- Models based on a DE formulation are applicable to a wide range of problems without requiring modification to the numerical algorithms.

The main disadvantages of DE methods compared with IE are as follows:

- A volume of space (assuming a general 3D problem) containing the object must be discretized, whereas in IE methods a 2D integration can be performed over the target's surface (this does not apply in the case of inhomogeneous objects);
- An approximate boundary condition has to be applied to truncate the model since the radiation condition is not enforced by the DE formulation.

The relative applicability of DE and IE methods, in respect of various modelling issues, is summarized in Table 3.2 as presented in a review paper by Miller (1988). Electromagnetic modelling is a field of ongoing research and, with the constant increase in the available computational power, solutions to complicated problems can now be obtained which were previously intractable. Moreover, this increase in computational power has led to a growth in the development and use of DE based models (as is evident from the number of papers about them published in recent years (Shlager and Schneider, 1995)) since the lack of computer resources was previously the main drawback of these type of models. This by no means suggests that IE methods are less important. For a number of types of electromagnetic problems IE based models are far more efficient than DE ones, and they have also benefited from the improvements in computer technology. The popularity of DE based models can be attributed mainly to the fact that they can be used when the problem geometry is rather complicated without the need for very sophisticated and complex algorithms.

Finally, other electromagnetic models can be used based on the presupposition that the wavelength of the electromagnetic fields interacting with the object of interest is small compared with the object's size. These models are based on ray tracing concepts and some initial studies on their application to the GPR forward problem have been reported.

3.8 The choice of model type for the GPR forward problem

To decide on the type of model suitable for the simulation of GPR, the nature of the problem has to be examined in the light of the advantages and disadvantages of potential formulations. Clearly, since most GPR systems employ signals of wide bandwidth and operate in the time domain, a time domain model will be more suitable than a frequency domain one. This will save in computational effort since the transient solution will be calculated directly instead of having to calculate the response of the same model for a number of frequencies and then use an inverse Fourier transformation to obtain the required time domain response. However, the description of frequency dependent parameters becomes more difficult and, as a first approximation, it is often necessary to consider them as frequency independent.

The choice of a differential equation based model instead of an integral equation approach

ISSUE	TD DE	TD IE	FD DE	FD IE
Medium				
Linear	√	√	√	√
Dispersive	~	×	√	√
Lossy	√	×	√	√
Anisotropic	√	~	√	√
Inhomogeneous	√	×	√	×
Nonlinear	√	×	×	×
Time-varying	√	×	×	×
Object				
Wire	~	√	~	√
Closed surface	√	√	√	√
Penetrable volume	√	√	√	√
Open surface	~	√	~	√
Boundary Conditions				
Interior problem	√	√	√	√
Exterior problem	~	√	~	√
Linear	√	√	√	√
Nonlinear	√	√	×	×
Time-varying	√	√	×	×
Half-space	~	×	~	√

Table 3.2: Relative applicability of IE and DE based FD or TD models when issues concerning the media, objects and boundary conditions in a problem are considered. √ : Highly suited or most applicable, ~: Moderately suited or neutral, ×: Unsuited or least applicable. (Miller, 1988)

is justified in general by the ability of a DE method to handle inhomogeneous problems more efficiently than the IE methods. Moreover, since a half space Greens function is not available in closed form, an IE approach will not result in a more computationally efficient model. Overall the simplicity of a DE model makes it more appealing when compared with the more complicated IE methodology.

3.8.1 Review of previous work on GPR Modelling

The application of modelling techniques to obtain synthetic GPR data has not been treated extensively in the literature. At the beginning of this project the relevant papers[1] published about GPR modelling[2] using numerical techniques were few and only considered 2D targets. Some other works appeared in the course of the project and are reported in chronological order:

Modelling of the subsurface interface radar (Moghadam et al., 1991)

This paper describes a 2.5D model of GPR based on the finite difference time domain method. The source of the problem is considered as 3D, where the spatial dimensions of it are assumed to be 2D; hence the name 2.5D. The results presented in the paper are limited to a few cases of rebars and rectangular voids displaying the characteristic hyperbolic response which should be obtained from such targets. A solution obtained by such a model will be more accurate than a pure 2D approach, but if the pure "pattern" of the GPR response is of interest a 2D model will produce similar results with less computational effort. The transformation of Maxwell's equation in the invariant direction results in the calculation of a transformed response. To obtain the final response a number of solutions (approx. 35, each for a different wavenumber) need to be calculated for each trace of a simulated GPR scan. Moreover, the constitutive parameters of the media in the model were considered to be frequency independent.

[1] Because of the diversity of the applications of GPR and its interdisciplinary nature the literature consulted was mainly from the research fields of electrical engineering and geophysics.

[2] 1D models based on plane wave propagation have been used in several studies and are not included here since their applicability is rather limited.

Numerical Simulation of subsurface radar for detecting buried pipes (Liu and Shen, 1991)

The authors of this communication presented an application of the 2D transmission line matrix method for the simulation of the GPR response from buried pipes. They have used a rather large computational domain which was necessary, not because of the dimensions of the targets (pipes), but due to the fact that efficient absorbing boundary conditions were not used to truncate the model space. This "brute-force" computation leaves room for development.

Detecting sub-surface features in concrete by impulse radar (Bungey and Millard, 1993)

The work presented in this paper is not mainly in the area of numerical modelling of GPR. However, the authors report the use of a ray tracing model as part of their investigation on the detection and identification of the presence of reinforcing bars and voids in concrete.

Ground penetrating radar simulation in engineering and geophysics (Goodman, 1994)

This paper describes the application of a ray tracing approach to GPR modelling of mainly archaeological targets. The inherent assumption of this approach is the high frequency approximation implied by the application of such methods. However, this is not valid if a GPR model is to be able to cope with general class of targets. Moreover, with a ray-tracing approach, not all the electromagnetic phenomena associated with the interaction of the electromagnetic fields with the targets are considered, and the real effect of the air-earth interface is ignored.

Comparison of ray and Fourier methods for modeling monostatic ground-penetrating radar (Zeng et al., 1995)

In this paper 2D models for GPR based on ray-tracing concepts and a frequency domain approach are presented. The ray tracing model has the same limitations as the model reported by Goodman (1994). The Fourier method, however, includes diffraction effects absent from a ray tracing model but assumes a constant velocity and attenuation within the model. The geometry of the targets is replaced by discrete point diffractors and their combined effect produces the final solution, which is obtained in the (f–k) (frequency–

wavenumber) domain and subsequently Fourier transformed to produce the final result. This method is based in essence on the same concept of an $(f - k)$ migration with constant velocity (Stolt, 1978; Yilmaz, 1987) but used in reverse (i.e. instead of collapsing hyperbolas to produce them).

3.8.2 Scale modelling of GPR

Another approach to GPR modelling is to perform controlled experiments with a scaled version of a GPR system. This approach, known as *scale modelling* (Frischknecht, 1987), involves the construction of a test area of relatively small dimensions, usually of the order of few cubic metres. This test area is most often a tank filled with a material of known dielectric properties, usually a water solution, in which some simple targets are immersed and their response measured with the scaled version of a GPR system (Smith and Scott, 1989). A scale model can be likened to a test site, but the environment is rather more controllable and it is easier to change the targets and their characteristics. The main drawback of such an approach is that it requires specially built GPR systems (scaled). Moreover, compared with a numerical approach it lacks versatility in the range of models that can be handled.

3.9 Assumptions for the modelling of GPR in two and three dimensions

In constructing a GPR model in two and three dimensions, some assumptions are necessary. These mainly result from the need to keep the amount of computational resources, required by the model, to a manageable level and to facilitate the study of the important features of the GPR response to a target, without cluttering the solution with details which can obscure the fundamental response. However, the approach followed should ideally be easily extendable and able to handle more "complicated" GPR modelling scenarios if required. The assumptions made for both 2D and 3D models are

- all media are considered to be non-magnetic, linear and isotropic.
- the GPR transmitting antenna is modeled as an ideal Hertzian dipole in the 3D models and as a line source in the 2D ones. In the 3D case, this is a result of reducing the computational resources required to a manageable level, whereas the

2D case is a consequence of the assumption of the invariance of the problem in one direction.

- the constitutive parameters are, in most cases, assumed not to vary with frequency. This assumption simplifies the time domain model. However, a formulation able to handle a Debye relaxation model for the complex permittivity will be presented.

Therefore, for the 2D case the governing equations reduce to the ones describing the propagation of TM mode electromagnetic waves (relative to the invariance direction of the model).

3.10 Discussion

In this Chapter the fundamental electromagnetic relations which are the governing equations of the GPR forward problem have been presented. An analysis of the effects of the electrical properties of the materials probed by a GPR reveals that for its frequency range the electromagnetic waves propagate with a velocity determined by the real part of the complex permittivity, which can be assumed to be independent of frequency. Therefore, significant pulse distortion is not expected (and is actually not observed) in GPR data, although the linear dependence of the attenuation constant with frequency has as an effect the broadening of the GPR pulse as it propagates in the subsurface medium (Vainikainen et al., 1992). Examining the difficulties with the analytical evaluation of the half space problem, the numerical solution of the GPR problem remains the only viable choice of method. Further, the choice of a DE based approach is justified as a result of the simplicity and generality of such a formulation, considering the difficulties that will be encountered with an IE based model. Finally, a TD model is the obvious choice considering the transient nature of the responses which will be obtained. An overview of the work reported in the literature indicates that there is scope for development, especially for the 3D case and in the application of the transmission line matrix algorithm. Finally, the main assumptions involved in constructing a manageable GPR model in respect of computer resources, GPR model are stated.

4

Two dimensional numerical modelling of GPR — PART I: Methodology

4.1 Introduction

The aim of this Chapter is to present the methodology of 2D GPR modelling using the TLM and FDTD methods. The rudiments of the two methods are examined and the basic principles which lead to the construction of the numerical algorithms are explained. The errors and limitations of the methods are discussed, with emphasis on their equivalent dispersion relations. A short review of absorbing boundary conditions is presented and those used in this work, in particular, are examined.

By introducing more effective absorbing boundary conditions within the TLM algorithm, a major improvement in the performance of TLM models is obtained. The incorporation of these absorbing boundary conditions in TLM is examined and their performance compared with that when they are applied in FDTD, as well as with the performance of the commonly used TLM absorbing condition of the "matched termination". Specific guidelines to stabilize higher orders of the absorbing boundary conditions are given, and

pitfalls in their application in GPR models are examined. Finally, general issues regarding the numerical implementation of the 2D GPR models are discussed and the validation of the algorithms by means of simple closed-form solutions is presented.

4.2 The governing equations

As was discussed in Chapter 3, the solution to the GPR forward problem is obtained as a solution to Maxwell's equations subject to the specific geometry (boundaries) and initial conditions of the problem. This results in a three-dimensional problem of which the approximate solution using a numerical model is rather computationally intensive. A simpler approach is required which gives a good estimate for GPR signatures without the computational requirements of a 3D model. Assuming that there is no variation in the problem's geometry and of the electromagnetic fields in one direction, the GPR problem reduces to a 2D one. The reduction of the dimensionality of the problem by one allows the use of a reduced set of Maxwell's equations which significantly simplify the formulation and implementation of the model. Assuming that the invariance direction lies along the (y) axis of a Cartesian coordinate system, Maxwell's equations reduce to the well known (Balanis, 1989) TM_y set:

$$\mu_0 \frac{\partial H_x}{\partial t} = \frac{\partial E_y}{\partial z} \tag{4.1}$$

$$\mu_0 \frac{\partial H_z}{\partial t} = -\frac{\partial E_y}{\partial x} \tag{4.2}$$

$$\epsilon \frac{\partial E_y}{\partial t} + \sigma E_y = \frac{\partial H_x}{\partial z} - \frac{\partial H_z}{\partial x} \tag{4.3}$$

As is apparent from the above equations only the E_y, H_x and H_z components of the electromagnetic fields have to be considered. Further, the constitutive parameters ϵ and σ are considered to be scalars and independent of frequency. A formulation incorporating a Debye relaxation model for these constitutive parameters is examined in the next Chapter. This assumption is made because of the difficulty of introducing frequency-dependent parameters within models formulated in the time domain (Hoefer, 1985) because the resulting time convolutions substantially increase the complexity of the model. The values of these constitutive parameters are considered to be the effective real permittivity and conductivity, as discussed in the previous Chapter, and are readily available from tables used commonly in GPR data analysis. Further, from equations (4.1), (4.2), (4.3), the

electric and magnetic fields can be uncoupled, resulting in a scalar 2D wave equation for the electric field

$$\mu_0\epsilon\frac{\partial^2 E_y}{\partial t^2} + \mu_0\sigma\frac{\partial E_y}{\partial t} = \frac{\partial^2 E_y}{\partial z^2} + \frac{\partial^2 E_y}{\partial x^2} \tag{4.4}$$

4.3 General concepts of the TLM method

As originally introduced, by Johns and Beurle (1971), TLM was presented as a computer implementation of an electrical network model used for the solution of an electromagnetic field problem. This electrical network is constructed as a mesh of orthogonal two-wire transmission lines. These transmission lines are interconnected at regular intervals, forming the TLM nodes. The characteristics of the TLM nodes depend on:

A. the way the transmission lines which form them are connected;

B. the properties of the media they model.

The propagation of voltage and current pulses in the TLM network simulate the propagation of electric and magnetic fields in the actual electromagnetic problem. Moreover, the constitutive parameters of the media present in the electromagnetic problem are simulated by transmission line parameters.

To implement a TLM network on a digital computer, both the spatial and time domains are discretized. The elementary space step Δl is defined as the distance between two adjacent TLM nodes and the time step Δt, with which the TLM solution is advanced, equals the time which a pulse takes to travel from one TLM node to an adjacent one. In Figure 4.1 a portion of a 2D TLM network formed by shunt connected transmission lines is illustrated. Wave propagation in the TLM model proceeds at discrete time steps in an iterative fashion. The iteration, which has a duration of one time step, is composed of two distinct processes:

- **Scattering**: which is the process of obtaining the reflected pulses moving away from the node due to the incident pulses on it;
- **Connecting**: which is the process of propagating the reflected pulses from a node to its adjacent nodes.

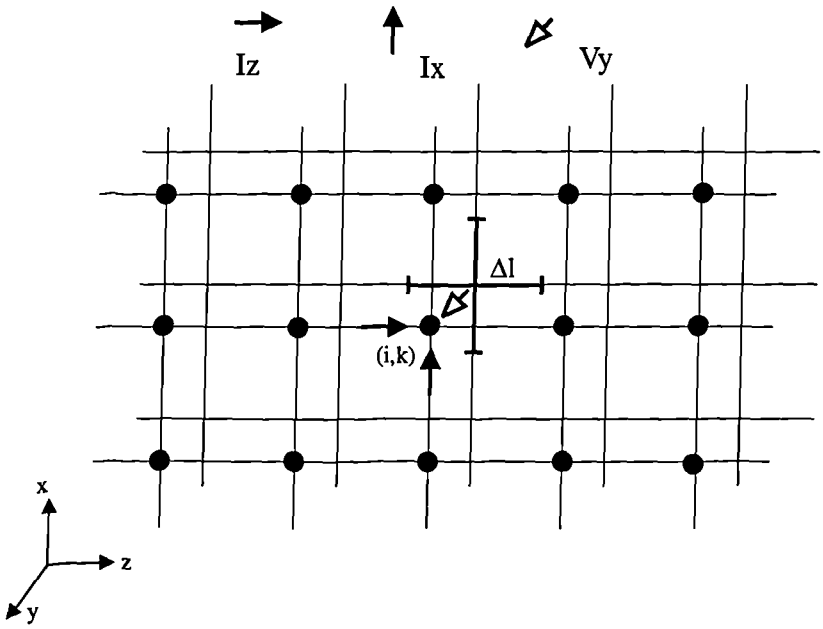

Figure 4.1: A portion of a 2D TLM network of shunted two-wire transmission lines.

The scattering process is considered to be instantaneous, while the connection process has a duration of one time step. In mathematical notation, these processes are:

(4.5) $$ {}^{r}\underline{V}^{n} = \underline{S}\ {}^{i}\underline{V}^{n} $$

(4.6) $$ {}^{i}\underline{V}^{n+1} = \underline{C}\ {}^{r}\underline{V}^{n} $$

where $\underline{S}$ and $\underline{C}$ are the scattering and connection matrices of the TLM node, ${}^{i}\underline{V}^{n}$ and ${}^{r}\underline{V}^{n}$ are column vectors of the amplitude of the incident and reflected pulses respectively, and ${}^{i}\underline{V}^{n+1}$ is a column vector of the amplitude of the incident pulses on the adjacent nodes at the next time step due to the reflection at the node. The integer n denotes any time instant multiple of Δt. In Figure 4.2, this process is depicted for the first two iterations in a 2D TLM network. The initial excitation of the network is a voltage pulse of unit amplitude incident on one of the branches of a TLM node (Al-Mukhtar, 1980). These scattering and connection processes directly relate TLM to the Huygens' model of wave propagation. According to Huygens (Balanis, 1989) :

> "Each point on a primary wavefront can be considered to be a new source of a secondary spherical wave and that a secondary wavefront can be constructed as the envelope of these spherical waves."

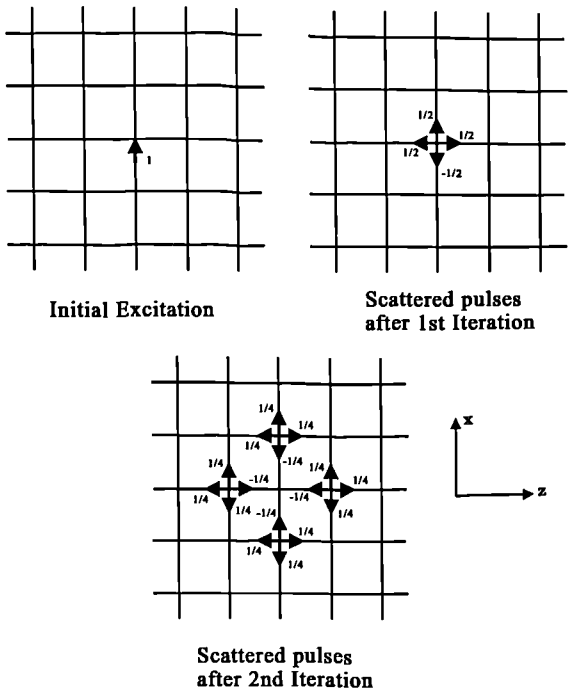

Figure 4.2: Two consecutive scattering events in a 2D TLM network. The initial excitation is a voltage pulse of unit amplitude.

The relation between TLM and Huygens' model was demonstrated, shortly after the introduction of the TLM method, by Johns (1974b). The use of an electrical network analogy and the relation of TLM to Huygens' model of wave propagation are the two main reasons of TLM being generally described in the relevant literature as a physical model (Hoefer, 1991).

For the simulation of two dimensional electromagnetic problems — where Maxwell's equations reduce to two uncoupled sets — there are two possible TLM network configurations. These TLM networks result from the different interconnection mechanisms of their transmission lines which leads to different 2D TLM nodes:

- The **series** TLM node, used to simulate TE modes.
- The **shunt** TLM node, used to simulate TM modes.

The TLM network used in this work, in view of the structure of the governing equations for the 2D GPR case, is that comprised of shunt nodes.

To preserve synchronism in the numerical implementation of the scattering and connecting processes pulses in the TLM network propagate with constant velocity. This is achieved

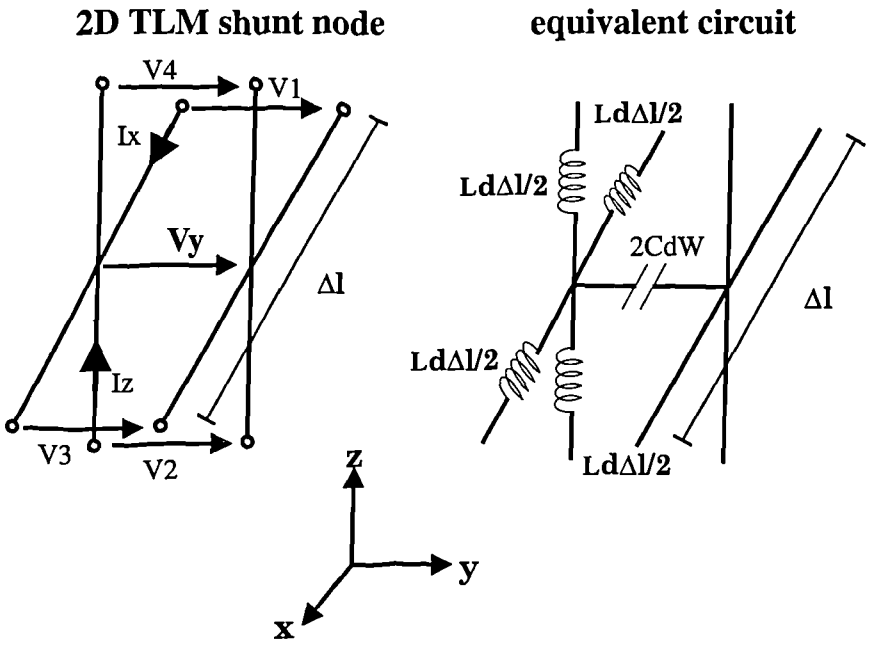

Figure 4.3: A 2D TLM shunt node as a junction of transmission lines and its equivalent circuit representation.

by considering the transmission lines which form the TLM network as loss-free and having a constant impedance. This results in a TLM network modelling a homogeneous and loss free medium which is called the "background medium". Regions of different constitutive parameters are modelled by introducing additional elements to the appropriate nodes in the form of transmission line stubs.

4.4 The 2D TLM shunt node

A 2D TLM shunt node is a junction of two shunted transmission lines which are part of a TLM network in the (x-z) plane (Figure 4.3). Regarding the length Δl of the lines between adjacent nodes as infinitesimal, the node can be represented as an equivalent circuit (see Figure 4.3) where the capacitance (C_d) and inductance (L_d) are distributed quantities of the lines. The equations governing the behaviour of voltages and currents at the node are (Ramo et al. 1984):

$$\Delta l \frac{\partial V_y}{\partial z} = -(L_d \Delta l) \frac{\partial I_z}{\partial t} \tag{4.7}$$

$$\Delta l \frac{\partial V_y}{\partial x} = -(L_d \Delta l) \frac{\partial I_x}{\partial t} \tag{4.8}$$

$$\Delta l \frac{\partial I_x}{\partial x} + \Delta l \frac{\partial I_z}{\partial z} = -2(C_d \Delta l) \frac{\partial V_y}{\partial t} \tag{4.9}$$

Uncoupling the voltage and currents from (4.8)–(4.9) results in a 2D wave equation for the voltage V_y in the TLM network.

$$\frac{\partial^2 V_y}{\partial x^2} + \frac{\partial^2 V_y}{\partial z^2} = L_d(2C_d)\frac{\partial^2 V_y}{\partial t^2} \tag{4.10}$$

Equations (4.8), (4.7) and (4.9) are isomorphic with (4.1), (4.2) and (4.3) when the term involving the conductivity σ is ignored in (4.3) (loss-free medium). Therefore, the following equivalences could be established:

$$E_y \equiv -\frac{V_y}{W} \qquad H_z \equiv \frac{I_x}{\Delta l} \qquad H_x \equiv -\frac{I_z}{\Delta l} \tag{4.11}$$

$$L_d \equiv \mu_b \frac{W}{\Delta l} \qquad C_d \equiv \frac{\epsilon_b}{2}\frac{\Delta l}{W} \tag{4.12}$$

Where the subscript b denotes a parameter of the homogeneous background medium which the TLM network models, and W is the separation between the wires of the transmission lines in the y direction. The value of W could be arbitrarily adjusted, but as is evident from (4.12), the value $W = \Delta l$ is the most suitable and simplifies the equivalences of distributed inductance with permeability and distributed capacitance with permittivity. The choice of the properties of the background medium depend on the TLM model. The best choice is to set the constitutive parameters of the background medium to be the minimum values expected for the various media presumed present. This is the best choice because with the addition of stubs at the appropriate nodes any other media can be modelled. Since free-space is always present in a GPR model, the constitutive parameters of the TLM background medium are hence chosen to be those of free-space. Therefore equation (4.12) becomes

$$L_d \equiv \mu_0 \qquad C_d \equiv \frac{\epsilon_0}{2} \tag{4.13}$$

with this choice of parameters, as is evident from equation 4.10, waves propagate in the 2D TLM network with a velocity

$$u_{tlm} = \frac{1}{\sqrt{2C_d L_d}} = \frac{1}{\sqrt{\epsilon_0 \mu_0}} = c \tag{4.14}$$

However, the velocity of propagation in the individual transmission lines and their impedance are:

$$u_l = \frac{1}{\sqrt{L_d C_d}} = \sqrt{2}c \tag{4.15}$$

$$Z_l = \sqrt{2}Z_0 \tag{4.16}$$

and the time step with which the TLM solution advances is

$$\Delta t = \frac{\Delta l}{\sqrt{2}c} \tag{4.17}$$

Another approach to constructing a TLM model is to adjust the parameters of the individual transmission lines to those of the background medium (Chen and Ney, 1994; Hoefer and So, 1991). However, with such an approach, it is apparent from (4.9) that the TLM network will model a medium which has twice the required value of permittivity. Following this approach, appropriate scaling of the output field quantities is necessary (Chen and Ney, 1994). It is believed that the first approach is easier from a conceptual point of view.

4.4.1 The 2D stub loaded TLM shunt node

As was demonstrated in the previous section, the 2D TLM network can model a homogeneous and loss-free medium with appropriate adjustment of the parameters of the individual transmission lines. However, to include regions with different constitutive parameters the properties of the nodes corresponding to these regions have to be altered accordingly. Changing the parameters of the lines which form the nodes will result in loss of synchronization in the numerical calculation since pulses will propagate between nodes with different velocities and will arrive at the nodes at different times (Akhtarzad and Johns, 1975b).

The approach which is taken to overcome this problem (Johns, 1974; Akhtarzad and Johns, 1975b) is to initialize the TLM network to model free-space as a "background medium" and to equip the nodes which should model regions of different constitutive parameters with two additional elements. These elements will supply the extra capacitance and conductance where required to model regions with different properties (permittivity and conductivity). Therefore, the node is loaded with one "permittivity" and one "loss" stub (Figure 4.4). The "permittivity" stub is a transmission line shunted at the node which has an open circuit termination, and transit time $\Delta t/2$. The capacitance C_s of the "permittivity" stub is related to the stub's admittance (Al-Mukhtar, 1980) by the following:

$$C_s = \frac{\Delta t}{2} Y_s \tag{4.18}$$

The "loss" stub is an infinitely long matched terminated line which is shunted at the node and absorbs energy from it, simulating a shunt conductance. The admittance Y_{loss} of this

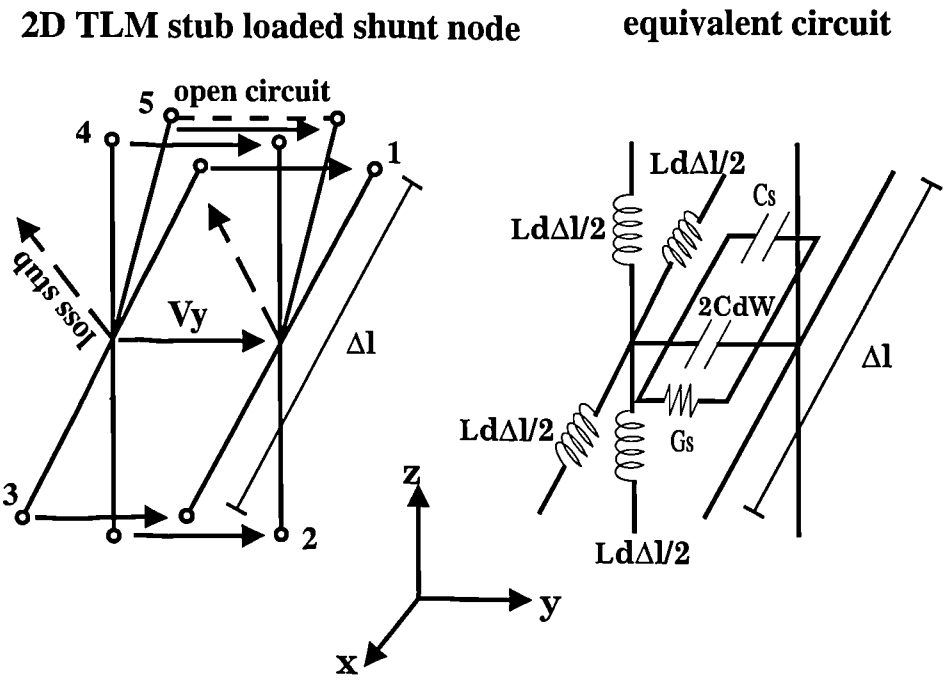

Figure 4.4: 2D TLM stub loaded shunt node and its equivalent circuit.

stub is equal to the conductance G_s which simulates.

$$G_s = Y_{loss} \tag{4.19}$$

In Figure 4.4, the equivalent circuit of the stub loaded node is presented. Analyzing that circuit reveals that equation (4.9) is modified as

$$\Delta l\frac{\partial I_x}{\partial x} + \Delta l\frac{\partial I_z}{\partial z} = -2(C_d\Delta l)\frac{\partial V_y}{\partial t} - C_s\frac{\partial V_y}{\partial t} - G_sV_y \tag{4.20}$$

Moreover, with the presence of these stubs equation (4.10) becomes

$$\frac{\partial^2 V_y}{\partial x^2} + \frac{\partial^2 V_y}{\partial z^2} = L_d(2C_d + \frac{C_s}{\Delta l})\frac{\partial^2 V_y}{\partial t^2} + L_d\frac{G_s}{\Delta l}\frac{\partial V_y}{\partial t} \tag{4.21}$$

which is a two dimensional wave equation for the voltage V_y in the TLM network. Equations (4.20) and (4.21) are isomorphic with equations (4.3) and (4.4), and the equivalences in equation (4.13) are modified as

$$L_d \equiv \mu_0 \qquad 2C_d + \frac{C_s}{\Delta l} \equiv \epsilon \qquad \frac{G_s}{\Delta l} \equiv \sigma \tag{4.22}$$

in order for the TLM model to describe a general inhomogeneous and lossy medium.

4.4.2 The Scattering Matrix

The scattering matrix for the 2D TLM stub loaded shunt node can be calculated using transmission line theory. Designating the branches of the node as 1,2,3,4 and 5 (Figure

4.4) we could calculate the reflected pulses from the node at a time step n from the known incident pulses and the scattering matrix as follows:

$$(4.23) \qquad \begin{bmatrix} {}^{r}V_1 \\ {}^{r}V_2 \\ {}^{r}V_3 \\ {}^{r}V_4 \\ {}^{r}V_5 \end{bmatrix} = \begin{bmatrix} \rho & \tau & \tau & \tau & \tau_s \\ \tau & \rho & \tau & \tau & \tau_s \\ \tau & \tau & \rho & \tau & \tau_s \\ \tau & \tau & \tau & \rho & \tau_s \\ \tau & \tau & \tau & \tau & \rho_s \end{bmatrix} \begin{bmatrix} {}^{i}V_1 \\ {}^{i}V_2 \\ {}^{i}V_3 \\ {}^{i}V_4 \\ {}^{i}V_5 \end{bmatrix}$$

where τ, ρ, are the transmission and reflection coefficients for the four main branches (1–4) and τ_s, ρ_s are the reflection and transmission coefficients for the "permittivity" stub. Note that there are reflections and transmission coefficients defined for the "loss" stub since there is no need to explicitly calculate the voltage pulse associated with it. The stub's effect is to extract energy from the node and no pulse returns from it to the node. Moreover, if the node does not have any stubs (background medium), τ_s and ρ_s are both zero and V_5 does not affect the calculations.

To calculate the reflection and transmission coefficients of the scattering matrix, it will be more convenient to normalize the admittances of the "permittivity" and "loss" stubs to the individual transmission line's admittance ($1/Z_l$). Therefore, from (4.13), (4.18), (4.19) and (4.22) results :

$$(4.24) \qquad \hat{Y}_l = 1$$

$$(4.25) \qquad \hat{Y}_s = 4(\epsilon_r - 1)$$

$$(4.26) \qquad \hat{G}_s = \sigma \Delta l Z_l$$

Consider a voltage pulse incident on the node from one of its main branches (1–4). For that pulse the rest of the transmission line branches and the stubs are seen to be connected in parallel. Therefore, the reflection coefficient in terms of the admittances is:

$$(4.27) \qquad \rho = \frac{1 - (3 + \hat{Y}_s + \hat{G}_s)}{4 + \hat{Y}_s + \hat{G}_s}$$

denoting $\hat{Y}$ as

$$(4.28) \qquad \hat{Y} = 4 + \hat{Y}_s + \hat{G}_s$$

then

$$(4.29) \qquad \rho = \frac{2 - \hat{Y}}{\hat{Y}}$$

from the relation $\tau = 1 + \rho$ (Kraus, 1991) the transmission coefficient can be calculated

$$\tau = \frac{2}{\hat{Y}} \tag{4.30}$$

Similarly, the reflection and transmission coefficients for the permittivity stub are:

$$\rho_s = \frac{2\hat{Y}_s - \hat{Y}}{\hat{Y}} \tag{4.31}$$

$$\tau_s = \frac{2\hat{Y}_s}{\hat{Y}} \tag{4.32}$$

The effect of the "loss" stub has been taken into account in the derivation of the reflection and transmission coefficients.

4.4.3 Output of field quantities and excitation of the 2D TLM model

In a TLM model, the amplitudes of the voltage pulses incident or reflected from the nodes are available at any time step. To obtain the field quantities of interest, these voltages pulses should be related to the total node voltage V_y and the currents I_x and I_z. This is achieved by representing the TLM node as a Thevenin equivalent circuit (Christopoulos, 1995). This Thevenin equivalent circuit is constructed by replacing the transmission line segment of the node by an appropriate voltage source connected in series with an impedance. This equivalent circuit is valid for the duration of a time step, while no other pulses are arriving at the node. The Thevenin equivalent circuit for the stub loaded shunt node is illustrated in Figure 4.5. From an analysis of that circuit using the parallel generator theorem (Benson and Harrison, 1975)

$$V_y = \frac{\sum_{k=1}^{5} {}^{i}V_k Y_k}{\sum_{k=1}^{5} Y_k} \tag{4.33}$$

gives for the stub loaded TLM node

$$V_y = \frac{2\,{}^{i}V_1 + 2\,{}^{i}V_2 + 2\,{}^{i}V_3 + 2\,{}^{i}V_4 + 2\,{}^{i}V_5 \hat{Y}_s}{\hat{Y}} \tag{4.34}$$

Moreover, from the circuits in Figure 4.5 the currents I_x and I_z are obtained

$$I_x = \frac{{}^{i}V_1 - {}^{i}V_3}{Z_l} \qquad I_z = \frac{{}^{i}V_2 - {}^{i}V_4}{Z_l}$$

Excitation of the TLM model is provided at the source node which simulates the GPR transmitting antenna. The direct simulation of the line source in a 2D TLM model is not

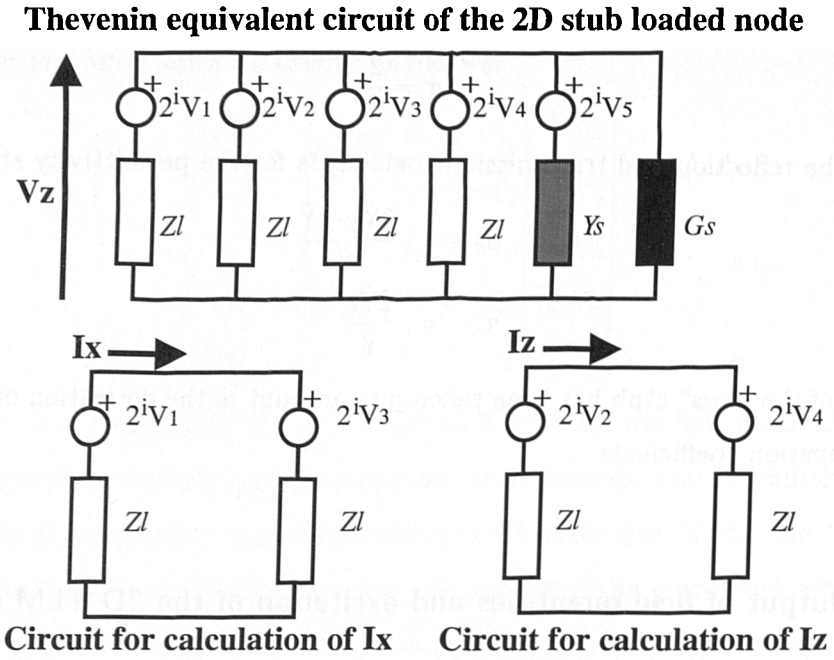

Figure 4.5: Thevenin equivalent circuits of the stub loaded shunt node for the calculation of node voltage and currents.

possible (Bader et al., 1994). The excitation takes the form of introducing in the TLM network voltage pulses of appropriate amplitude to simulate the presence of a current line source. This is achieved by perturbing the total voltage of the node simulating the source by

$$V_{inc} = \frac{IZ_l}{\hat{Y}} \tag{4.35}$$

where I is the function describing the current of the line source. As will be shown in the latter part of this Chapter, by a comparison with an analytical solution and the FDTD method, this excitation produces the correct fields of a current line source in the TLM model.

4.5 The connection process

After the calculation of the reflected voltage pulses from a 2D TLM shunt node, the connection process takes place. This involves the propagation of these reflected pulses away from the node where they originated. These pulses propagate a distance Δl in the network's transmission lines and they reach the surrounding nodes after an amount of time equal to a single time step Δt. They then become the incident pulses on these surrounding

nodes and the calculation proceeds with a new scattering process.

The scattering process is, in fact, an exchange of reflected pulses between the appropriate branches of neighboring nodes. It can however be expressed mathematically as:

$$\begin{bmatrix} {}^{i}V_1(i,k) \\ {}^{i}V_2(i,k) \\ {}^{i}V_3(i,k) \\ {}^{i}V_4(i,k) \end{bmatrix}^{n+1} = \begin{bmatrix} 0 & 0 & 1 & 0 \\ 0 & 0 & 0 & 1 \\ 1 & 0 & 0 & 0 \\ 0 & 1 & 0 & 0 \end{bmatrix} \begin{bmatrix} {}^{r}V_1(i+1,k) \\ {}^{r}V_2(i,k+1) \\ {}^{r}V_3(i-1,k) \\ {}^{r}V_4(i,k-1) \end{bmatrix}^{n} \tag{4.36}$$

where (i,k) are the coordinates of a TLM node in the network.

4.6 Overview of the FDTD method

The FDTD approach is a numerical method which provides a solution to Maxwell's equations, expressed in differential form, in the time domain. The method, originated by Kane Yee (1966), is based on the discretization of the partial derivatives in Maxwell's equations using central differencing. The resulting difference equations are used in an time marching iterative procedure to obtain the required solution.

Since the appearance of Yee's original paper, the FDTD method has been widely used in the solution of a diverse range of electromagnetic field problems such as, radar cross section estimations (Taflove and Umashankar, 1989), EMP coupling to dielectric structures (Holland et al., 1980), antenna modelling (Maloney, 1992; Jensen and Rahmat-Samii, 1995), electromagnetic field penetration (Taflove, 1980), and propagation in plasma and biological applications (Luebbers et al. 1991; Sullivan, 1992). Fang (1989), attributes the popularity of the FDTD method mainly for the following reasons:

- The solution is obtained with a sequential procedure and is very well suited for computer implementation.
- The method is very general and simple in nature. The computer programme which results from its implementation is very robust and could handle complex problems with a very small amount of preprocessing.
- The formulation is entirely in the time domain and therefore is particularly suited to transient problems. A frequency domain approach would require the solution

procedure to be repeated for a large number of frequencies in order to be able to perform a Fourier transformation.

Although one can easily establish that the above points apply equally well to TLM, the TLM method has not received the attention that FDTD has. This could be due to the fact that most scientists are more familiar with the concepts involved in FDTD modelling than with the ones involved in constructing a TLM model, but that by no means suggests that one method is better or more accurate than the other. However, in developing TLM models, familiarity with transmission line theory is of the essence, and this is a subject closely related only to electrical engineering, whereas the finite difference techniques are employed commonly for a range of scientific problems in a wide range of disciplines. Moreover, some computational advantages of the FDTD method play a decisive role when its application in a small computational environment is essential, as will be discussed later in this Chapter.

4.7 Central difference approximation of the partial derivatives

The use of finite differencing for the solution of partial differential equations is well established (Potter, 1973; Rosenberg, 1969; Smith, 1978). The replacement of a partial derivative by a difference equation follows from the definition of the derivative.

$$\frac{d\Psi}{dh} = \lim_{\Delta h \to 0} \frac{\Psi(h_1) - \Psi(h_2)}{\Delta h} \tag{4.37}$$

where $\Delta h = h_1 - h_2$. However, in finite differencing, Δh is finite rather than infinitesimal.

There are a number of different schemes for implementing a finite difference solution to a partial differential equation. It is beyond the scope of this work to describe all of them, and only the difference scheme employed by the FDTD method is presented.

The difference equations of the FDTD method are obtained by the use of central differences to approximate the spatial and time partial derivatives of the magnetic and electric field components in Maxwell's curl equations. Let $\Psi(x, y, z, t)$ be a field component, using the

Taylor series expansion for $\Psi(x+\Delta x, y, z, t)$ and $\Psi(x-\Delta x, y, z, t)$ results:

(4.38)
$$\Psi(x+\Delta x, y, z, t) = \Psi(x, y, z, t) + \Delta x \frac{\partial \Psi(x, y, z, t)}{\partial x} + \frac{(\Delta x)^2}{2!} \frac{\partial^2 \Psi(x, y, z, t)}{\partial x^2} + \frac{(\Delta x)^3}{3!} \frac{\partial^3 \Psi(x, y, z, t)}{\partial x^3} + O[(\Delta x)^4]$$

(4.39)
$$\Psi(x-\Delta x, y, z, t) = \Psi(x, y, z, t) - \Delta x \frac{\partial \Psi(x, y, z, t)}{\partial x} + \frac{(\Delta x)^2}{2!} \frac{\partial^2 \Psi(x, y, z, t)}{\partial x^2} - \frac{(\Delta x)^3}{3!} \frac{\partial^3 \Psi(x, y, z, t)}{\partial x^3} + O[(\Delta x)^4]$$

Subtracting (4.39) from (4.38)

(4.40)
$$\Psi(x+\Delta x, y, z, t) - \Psi(x-\Delta x, y, z, t) = 2\Delta x \frac{\partial \Psi(x, y, z, t)}{\partial x} + \frac{(\Delta x)^3}{3} \frac{\partial^3 \Psi(x, y, z, t)}{\partial x^3} + O[(\Delta x)^5]$$

Dividing by Δx, truncating the series after the first order partial derivative and rearranging terms results in:

(4.41)
$$\frac{\partial \Psi(x, y, z, t)}{\partial x} = \frac{\Psi(x+\Delta x, y, z, t) - \Psi(x-\Delta x, y, z, t)}{2\Delta x} + O[(\Delta x)^2]$$

which is the central difference approximation to the partial derivative. The term $O[(\Delta x)^n]$ denotes the order of approximation of the difference equation to the actual derivative.[1] In a similar manner the other temporal or time partial derivatives could be approximated.

4.8 Formulation of the FDTD equations - 2D Yee cell

To apply the FDTD method, the spatial and time domains are discretized. The space step Δl and the time step Δt are the finite values which are used in the finite difference approximation of the partial derivatives in the governing equations of the problem. Therefore, the spatial and time domains are replaced by their discrete equivalents as:

(4.42)
$$(x, z; t) = (i\Delta x, k\Delta z; n\Delta t)$$

At each of the points (i, k) of the discretized spatial domain a 2D Yee cell is introduced. This 2D Yee cell is the building block of the 2D FDTD representation of the spatial domain. Here, the electric and magnetic field components of the governing Maxwell's

[1] If $f(x)$ is an approximation of $F(x)$ it is of order n, with respect to some quantity Δx, if n is the largest possible real number such that $|F - f| = O[(\Delta x)^n]$ as $\Delta x \to 0$ (Ames, 1977).

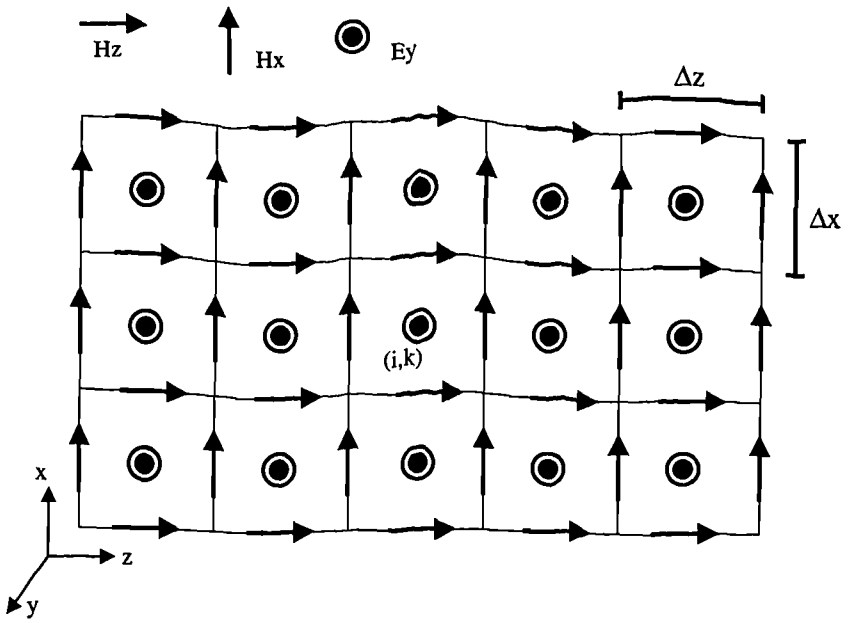

Figure 4.6: A portion of a 2D FDTD lattice showing the placement of the electric and magnetic field components.

equations are located in a manner suitable for the application of a finite difference approximation to their derivatives. Examining Figure 4.6, which represents a portion of the FDTD representation of the spatial domain of the problem, it is evident that the electric and magnetic field components are not located at the same point, but are offset a half spatial step from each other. This arrangement is necessary for the application of the central difference approximation to the spatial derivatives. The modelling of regions with different constitutive parameters is achieved by introducing appropriate values of permittivity and conductivity at the locations of the electric field components which interact with these regions. Since, in this work, all media in the GPR models are considered to be non-magnetic, the value of the permeability of vacuum is assigned to all magnetic field locations. Similarly to TLM, the FDTD algorithm proceeds in an iterative fashion: in its iteration the values of electric and magnetic field components at each Yee cell are updated using the FDTD equations. To compute these values a central difference approximation is used to provide the time derivatives. Similarly to the staggered arrangement of the field components in the FDTD lattice, the evaluation of their time derivatives is computed in different instants located half a time step apart. Therefore, whereas the electric field component is available at integer multiples of a time step, the magnetic ones are obtained at an instant offset by a half time step.

To formulate the FDTD equations equation (4.41) is applied to (4.1), (4.2) and (4.3). Therefore, (4.1) and (4.2) become

$$\frac{H_x\big|^{n+1/2}_{(i,k-1/2)} - H_x\big|^{n-1/2}_{(i,k-1/2)}}{\Delta t} = \frac{1}{\mu_0}\left(\frac{E_y\big|^{n}_{(i,k)} - E_y\big|^{n}_{(i,k-1)}}{\Delta x}\right) \tag{4.43}$$

$$\frac{H_z\big|^{n+1/2}_{(i-1/2,k)} - H_z\big|^{n-1/2}_{(i-1/2,k)}}{\Delta t} = -\frac{1}{\mu_0}\left(\frac{E_y\big|^{n}_{(i,k)} - E_y\big|^{n}_{(i-1,k)}}{\Delta z}\right) \tag{4.44}$$

which after rearranging result in two of the 2D FDTD update equations:

$$H_x\big|^{n+1/2}_{(i,k-1/2)} = H_x\big|^{n-1/2}_{(i,k-1/2)} + \frac{\Delta t}{\mu_0}\left(\frac{E_y\big|^{n}_{(i,k)} - E_y\big|^{n}_{(i,k-1)}}{\Delta x}\right) \tag{4.45}$$

$$H_z\big|^{n+1/2}_{(i-1/2,k)} = H_z\big|^{n-1/2}_{(i-1/2,k)} - \frac{\Delta t}{\mu_0}\left(\frac{E_y\big|^{n}_{(i,k)} - E_y\big|^{n}_{(i-1,k)}}{\Delta z}\right) \tag{4.46}$$

Applying, (4.41) to (4.3)

$$\frac{E_y\big|^{n}_{(i,k)} - E_y\big|^{n-1}_{(i,k)}}{\Delta t} = \frac{1}{\epsilon(i,k)}\left(\frac{H_x\big|^{n-1/2}_{(i,k+1/2)} - H_x\big|^{n-1/2}_{(i,k-1/2)}}{\Delta z} - \frac{H_z\big|^{n-1/2}_{(i+1/2,k)} - H_z\big|^{n-1/2}_{(i-1/2,k)}}{\Delta x} - \sigma(i,k)E_y\big|^{n-1/2}_{(i,k)}\right) \tag{4.47}$$

which after rearranging and by using a semi-implicit (Taflove, 1995) approximation for the $\sigma(i,k)E_y\big|^{n-1/2}_{(i,k)}$ term as

$$\sigma(i,k)E_y\big|^{n-1/2}_{(i,k)} = \sigma(i,k)\frac{E_y\big|^{n}_{(i,k)} - E_y\big|^{n-1}_{(i,k)}}{2} \tag{4.48}$$

becomes the FDTD update equation for the electric field

$$E_y\big|^{n}_{(i,k)} = \left(\frac{2\epsilon(i,k) - \sigma(i,k)\Delta t}{2\epsilon(i,k) + \sigma(i,k)\Delta t}\right)E_y\big|^{n-1}_{(i,k)} + \left(\frac{2\Delta t}{2\epsilon(i,k) + \sigma(i,k)\Delta t}\right)\left(\frac{H_x\big|^{n-1/2}_{(i,k+1/2)} - H_x\big|^{n-1/2}_{(i,k-1/2)}}{\Delta z} - \frac{H_z\big|^{n-1/2}_{(i+1/2,k)} - H_z\big|^{n-1/2}_{(i-1/2)}}{\Delta x}\right) \tag{4.49}$$

By iterating equations (4.49), (4.45) and (4.46) the 2D FDTD solution is obtained.

4.8.1 Excitation of the 2D FDTD model

The excitation of the 2D FDTD model is achieved by introducing a source term in the electric field update equation at the location of the source. This results from including

the source current density term J_y in the governing equation (4.3) and then following the procedures described in the previous section.

It can be easily shown that the electric field FDTD update equation for a 2D Yee cell in free-space containing the source becomes:

$$E_y\big|^{n}_{(i_s,k_s)} = E_y\big|^{n-1}_{(i_s,k_s)} + \left(\frac{\Delta t}{\epsilon_0}\right)\left(\frac{H_x\big|^{n-1/2}_{(i_s,k_s+1/2)} - H_x\big|^{n-1/2}_{(i_s,k_s-1/2)}}{\Delta z} - \frac{H_z\big|^{n-1/2}_{(i_s+1/2,k_s)} - H_z\big|^{n-1/2}_{(i_s-1/2,k_s)}}{\Delta x}\right) - \left(\frac{\Delta t}{\epsilon_0}\right)\frac{I}{\Delta x \Delta z} \tag{4.50}$$

where, I is the current on the line source.

4.8.2 Stability of the 2D FDTD method

One of the important differences between FDTD and TLM is that in an FDTD model there is a stability condition which relates both to the time step and the spatial steps. There is an upper bound for the value which the time step can take and any value greater than this will lead to an instability of the numerical solution. The FDTD stability condition (known as the CFL[2] stability criterion) is obtained by a von Neumann (Chew, 1990, Taflove and Brodwin, 1975) analysis of the FDTD method. The analysis is based on the requirement for the FDTD differentiation scheme to be stable for a Fourier mode propagating in the FDTD lattice. For the 2D FDTD algorithm, the stability condition requires that (Taflove, 1995)

$$\Delta t \leq \frac{1}{u_m\sqrt{\frac{1}{\Delta x^2}+\frac{1}{\Delta z^2}}} \tag{4.51}$$

where u_m is the velocity of propagation in the medium being modelled by the FDTD lattice. Since the stability criterion is derived for a homogeneous and loss-free medium, u_m is the phase velocity of electromagnetic waves in that medium. In practical situations where the model contains regions with different properties and consequently different phase velocities, u_m is considered to be the velocity of the "fastest" medium. Since free-space is always present in GPR modelling in determining the time step, u_m has the value of the velocity of light. For the case of $\Delta x = \Delta z = \Delta l$ the stability criterion becomes

$$\Delta t \leq \frac{\Delta l}{\sqrt{2}c} \tag{4.52}$$

[2]From the initials of Courand, Freidrichs and Lewy.

4.9 Errors in TLM and FDTD modelling

Both the TLM and FDTD techniques result from a series of approximations which have to be made in order to obtain a numerical solution to an otherwise unsolvable or very difficult problem. In both methods, although based on different modelling philosophies, similar errors are introduced in the calculations. The major source of these errors is discretization. This of course is an unavoidable consequence of the numerical nature of the methods which have to be implemented within a digital computer, having a finite number of memory cells and processor clock speed.

Truncation Error

This type of error is associated with the frequency domain response obtained via a discrete Fourier transformation from the time domain response which TLM and FDTD provides. Truncating the response in time affects the resolution in the frequency domain which could lead to errors in calculating frequency domain parameters. A remedy for this error is to run the TLM and FDTD models for a sufficient amount of iterations in order for the calculated response to ring down. Alternatively, techniques like the Prony algorithm for time extrapolation of the response can be used (Kunz and Luebbers,1993).

Coarseness Error

This is a modelling error directly related to the discretization of space in the numerical model and the description of the problem's geometry in it. This error can be significant if an inadequate amount of TLM nodes or Yee cells are used to describe the target in the model and therefore, in essence, not simulating the "right" target. To minimize this error, targets present in the model should be resolved by a sufficient amount of TLM nodes or Yee cells. This could have an impact on the computational resources required when a uniform grid is used and fine features are an essential part of the target's geometry. For the GPR case, the representation of small features is not necessary. Fine geometrical details (of a size much smaller than the wavelength of the centre frequency of the GPR antenna) of the targets sought in actual GPR surveys are not usually resolved.

Staircasing Error

The staircasing error is a consequence of the use of a Cartesian coordinate system to describe a TLM network or FDTD lattice and therefore the geometry of the TLM nodes and Yee cells. Targets whose geometry does not conform to this coordinate system will be modelled with a staircase approximation to their real boundary. For example, a cylindrical target will be modelled as a collection of rectangular nodes or cells in both TLM and FDTD models. The induced currents circulating a staircased surface are the source of this error. The path of these currents is not smooth, as it should be. However, for the 2D TM_y case of interest here it has been shown (Cangellaris and Wright, 1991) that staircase errors are not particularly significant since, from the governing equations, it is apparent that such currents are not induced on targets.[3]

However, for the general 3D case and the 2D TE_y one, this error has received much attention especially for the FDTD method. The approaches described in the literature are usually too complicated to implement and moreover require the use of "mesh generation" software packages which are not readily available. The essence of these approaches is to conform locally the FDTD lattice (Jurgens et al., 1992) to model the geometry of a target or to use an unstructured mesh (Madsen and Ziolkowski, 1988; Fusco, 1990).

Velocity Error

The most significant of the errors introduced in the numerical calculations in TLM and FDTD is the velocity error, which introduces an artificial dispersion of the electromagnetic pulses propagating in the models. Whereas, in a loss-free medium, all frequency modes of a pulse propagate with the same phase velocity, that is not the case for propagation of the same pulse in the TLM and FDTD models of such medium. The numerical phase velocity of propagation in the model deviates from the one in the actual medium by an amount which depends on the size of the wavelength of the electromagnetic wave compared to the spatial step Δl , and on the direction of propagation in the model. Controlling the velocity error imposes restrictions on the modelling procedure. In the following section this artificial numerical dispersion in 2D TLM and 2D FDTD is examined.

[3]The electric field vector has only one component in the strike (invariance) direction of the targets.

4.10 Numerical Dispersion in 2D TLM and 2D FDTD and equivalence of their propagation characteristics

The fact that wave propagation in a TLM network suffers from numerical dispersion was first examined in the paper introducing the TLM method by Johns and Beurle (1971). Although a complete analysis of wave propagation in a 2D shunt TLM network is not presented in that paper, using a procedure called "propagation analysis" (which was based on transmission line theory) two key observations were made. Firstly, that the numerical phase velocity of waves propagating in a TLM network is a function both of direction and of the ratio of wavelength to the spatial step. Secondly, it is demonstrated that the worst case of numerical dispersion is for propagation in the axial direction of the network whereas there is no dispersion for waves of any wavelength propagating along the diagonal of it.

The dispersion relations for both FDTD and TLM are obtained by considering the propagation of a Fourier mode in the models. This Fourier mode is

(4·53) $$\Psi_{i,k} = \Psi_0 e^{j\omega n\Delta t - \gamma_x \Delta x - \gamma_z \Delta z}$$

where Ψ is a field component and γ_x and γ_z are the components of the complex propagation vector.

A complete analysis and derivation of the dispersion relation for the 2D shunt TLM network has been obtained since using either a direct approach via the scattering matrix (Nielsen and Hoefer, 1993) or by transmission line theory (Simons and Bridges, 1991). Either derivation of the dispersion relation leads to the same result. The dispersion relation of the 2D shunt TLM network is (Simons and Bridges, 1991):

(4·54)
$$\sinh^2(\frac{\gamma_x \Delta l}{2}) + \sinh^2(\frac{\gamma_z \Delta l}{2}) = j\frac{\hat{G}_s}{4}\sin(\beta_l \Delta l) - 2(1 + \frac{\hat{Y}_s}{4})\sin^2(\frac{\beta_l \Delta l}{2})$$

where $\beta_l = \omega\Delta t$ is the phase constant of the individual transmission lines.

The dispersion analysis of the 2D FDTD method due to the more mathematical nature of the method is more straightforward to derive and has been reported by a number of authors (Chew, 1990; Taflove, 1995). When $\Delta x = \Delta z = \Delta l$ this relation is

(4·55)
$$\sinh^2(\frac{\gamma_x \Delta L}{2}) + \sinh^2(\frac{\gamma_z \Delta L}{2}) = j\frac{\sigma\mu_0 \Delta L^2}{4\Delta T}\sin(\omega\Delta T) - \epsilon\mu_0 \frac{\Delta L^2}{\Delta T^2}\sin^2(\frac{\omega\Delta T}{2})$$

where the use of capital L and T has been introduced to distinguish between the spatial step and time step in TLM and FDTD.

Simons and Bridges (1991) have shown that equations (4.54) and (4.55) are equivalent when $\Delta t = \Delta T$ and $\Delta l = \Delta L$ because then

$$\frac{\sigma\mu_0\Delta L^2}{4\Delta T} = \frac{\hat{G}_s}{4} \tag{4.56}$$

$$\epsilon\mu_0\frac{\Delta L^2}{\Delta T^2} = 2(1 + \frac{\hat{Y}_s}{4}) \tag{4.57}$$

This means that the 2D shunt node TLM network and the 2D FDTD model have equivalent propagation characteristics when the FDTD simulation is performed with a time step set by the limit of its stability criterion. Therefore, when $\Delta T = \Delta t$ and $\Delta L = \Delta l$ the two methods should provide identical results since wave propagation in the models is governed by the same relation and the same discretization is used. In actual GPR models, however, the responses obtained by 2D TLM and 2D FDTD are not exactly the same due to the differences in the excitation of the models and in the different performance of absorbing boundary conditions when applied to the two methods.

The amount of numerical dispersion which a wave suffers propagating in 2D TLM or 2D FDTD can be obtained for a given discretization from the dispersion relations. Consider a 2D FDTD model simulating free-space and with the time step ΔT set by the limit of the stability criterion.[4] Because there are no losses in the model $\gamma_x = j\beta_x$ and $\gamma_z = j\beta_z$ and equation (4.55) reduces to

$$\sin^2(\frac{\beta_x\Delta L}{2}) + \sin^2(\frac{\beta_z\Delta L}{2}) = \frac{\Delta L^2}{c^2\Delta T^2}\sin^2(\frac{\omega\Delta T}{2}) \tag{4.58}$$

Moreover, β_x, β_z are given by

$$\beta_x = \beta\cos(\theta) \tag{4.59}$$

$$\beta_z = \beta\sin(\theta) \tag{4.60}$$

where θ is the angle between the direction of propagation and the x axis. Equation (4.58) can be solved to obtain the value of β in the model using an iterative root finding method such as *Newton-Raphson* (Press et al. ,1992; Taflove, 1995)

$$\beta_{i+1} = \beta_i - \frac{\sin^2(\frac{\Delta L\cos(\theta)}{2}\beta_i) + \sin^2(\frac{\Delta L\sin(\theta)}{2}\beta_i) - \frac{\Delta L^2}{c^2\Delta T^2}\sin^2(\frac{\omega\Delta T}{2})}{\frac{\Delta L\cos(\theta)}{2}\sin(\Delta L\cos(\theta)\beta_i) + \frac{\Delta L\sin(\theta)}{2}\sin(\Delta L\sin(\theta)\beta_i)} \tag{4.61}$$

[4]Equivalently a 2D TLM model with the same discretization.

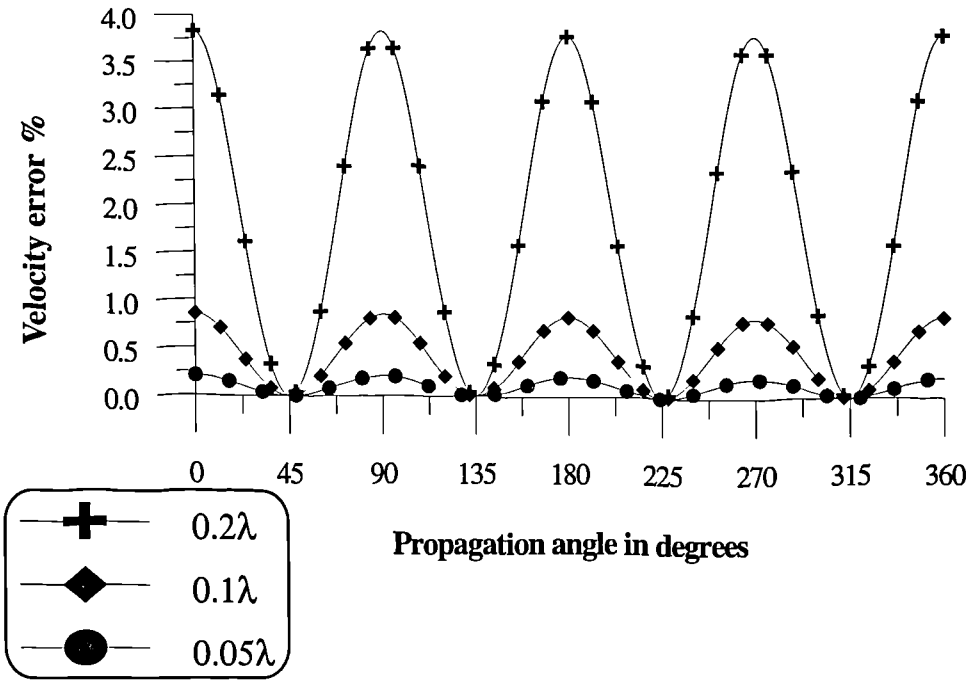

Figure 4.7: Percentage velocity error vs angle of propagation for different ratios of $\Delta l/\lambda$.

Moreover, it is convenient to normalize the spatial step ΔL to the free space wavelength. From the computed value of β, the ratio of the numerical phase velocity to the real free-space velocity could be estimated by

$$\frac{u_n}{c} = \frac{2\pi}{\beta} \tag{4.62}$$

and the percentage of velocity error from

$$(1 - \frac{u_n}{c}) * 100 \tag{4.63}$$

In Figure 4.7 the percentage of velocity error vs the angle of propagation for waves propagating in a 2D FDTD model — or equivalently a 2D TLM network — simulating free-space, is presented for different ratios of $\frac{\Delta l}{\lambda}$. It can be seen that the error depends on the direction of propagation, becoming worse for the case of $\theta = 0$ or $\theta = \frac{\pi}{2}$ as it was reported by Johns and Beurle (1971) for the TLM case. For a discretization where the highest frequency of interest has a wavelength of $10\Delta l$ the error is less than 1% for the worst case of axial propagation. This level of velocity error has been considered to be acceptable in the numerical calculations for the GPR models. Therefore, in all numerical calculations the pulse used to simulate the current of the line source in the models did not contain significant power for frequencies with wavelengths shorter than $10\Delta l$. This has important consequences in a 2D TLM or 2D FDTD GPR model since the shortest wavelength in the models is determined as the one in the medium having the highest value of permittivity.

This wavelength is related to the free-space wavelength by

$$\lambda_m = \frac{\lambda_0}{\sqrt{\epsilon_r}} \tag{4.64}$$

where λ_m is the wavelength in a medium of relative permittivity ϵ_r.

4.11 Overview of Absorbing Boundary Conditions (ABC) and their application in FDTD and TLM

One of the most important issues in GPR modelling using TLM and FDTD is the truncation of the computational domain (i.e. the TLM network and the FDTD lattice). This is a result of the "open nature" of the GPR forward problem. The natural boundary condition which should be satisfied is: [5]

$$\mathbf{E}(|\mathbf{r}| \rightarrow \infty) = 0 \tag{4.65}$$

which the physical interpretation that the electromagnetic fields should decay while propagating away from their sources. Obviously, this condition can not be accommodated in either TLM or FDTD since it requires an infinite computational domain. One approach to approximate this boundary condition is to implement it at the edges of a very large computational domain. This clearly results in a waste of computational resources, since most of the model will represent a space devoid of targets. Another approach will be to use a graded mesh with larger elements used further from the area of interest (Liu and Shen, 1991) to simulate a large "physical" space. Although this approach has been used to model time-independent geophysical problems (Oristaglio and Hohmann, 1984), it has not been pursued in this work mainly for two reasons. First, it increases unnecessarily the complexity of the model construction and secondly (and most importantly) it lowers the frequency range of the validity of the model since numerical dispersion will affect the propagation in regions where large spatial steps are used. The use of a graded mesh has to be considered when small features should be represented in the model and the largest dimension of a cell in the model is in accordance with the requirements posed for controlling the numerical dispersion error.

The approach followed in this work and commonly employed for the study of general open boundary electromagnetic problems is the application of artificial boundary conditions

[5] This is known as the Sommerfeld radiation condition (Chew, 1990)

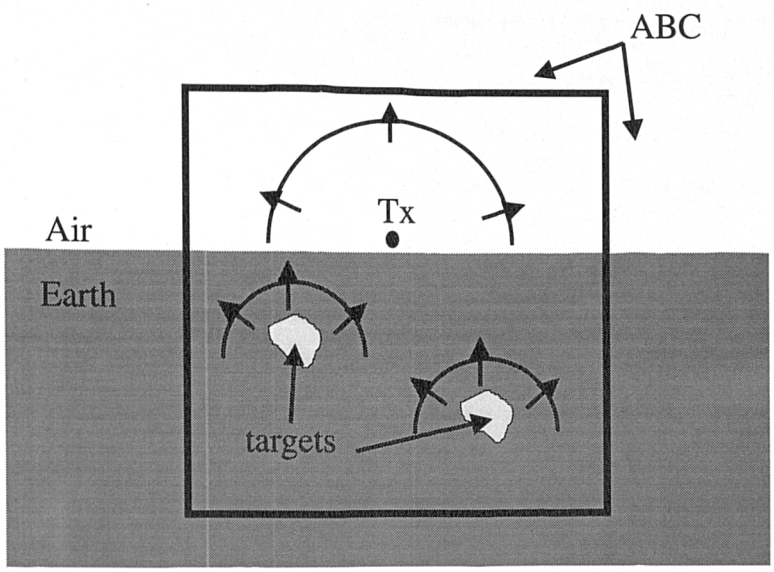

Figure 4.8: Use of ABCs to truncate a finite computational domain used to solve the GPR open boundary problem.

which are imposed on the truncation boundaries. These artificial boundary conditions are used to close (Figure 4.8) the computational domain and to absorb waves impinging on them, therefore simulating an unbounded space. In essence, an ABC is used to *predict* field values which are required but can not be calculated directly by the FDTD and TLM algorithms. In general, ABCs can be characterized either as *local* or *global* depending on the nature of their formulation. Local ABCs are applied individually on distinct points of the truncation boundary whereas global ones operate on the entire periphery of the computational domain. The output of local ABCs depend on information available inside the computational domain and around the point where the ABC is applied. The output of global ABCs is obtained from information available usually at one spatial step inside the periphery of the computational domain and the values predicted depend on all the points of the periphery of the model. Most of the ABCs developed and used in several DE based models are local ones. A global ABC has been reported for the FDTD method based on the surface equivalence theorem (Olivier, 1992), but its computational requirements are excessive when compared with the application of a local ABC. Further, formulations of global ABCs assume that the outwardly radiating fields are produced by targets or sources located within a homogeneous medium (usually free-space). This however, is not the case for GPR models.

The theoretical formulation of ABCs is not, in general, restricted to a particular numerical method. However, they have been developed mainly to be used with finite difference models due to their popularity for the solution of wave propagation problems. Because of the generality of the formulation of ABCs, the incorporation of the ABCs (as proposed by Higdon (1986) and Liao et al. (1984) and used in FDTD) into the TLM algorithm was considered here for the modelling of GPR by TLM. Finally, because the development of ABCs is a field of on-going research there will be no attempt to describe in detail recent advances in ABC technology. Moreover, only the basic principles of the ABCs used in this work are reviewed while their application and performance in TLM is examined in particular.

Application of ABCs in FDTD

Several formulations of ABCs have been introduced for the FDTD method, aiming to minimize the reflection of outgoing waves at the truncation boundaries of the FDTD lattice. Formulations exist for FDTD algorithms in spherical and cylindrical coordinate systems (Bayliss and Turkel, 1980), but most of them have been developed for the standard formulation of the FDTD algorithm in Cartesian coordinates. Although there are many different formulations, the starting point for most of them is the one-way wave equation (Enguist and Majda, 1977) and the differences between the various formulations arise mainly from the different approximations used in the discretization process of this equation for its implementation in the FDTD algorithm.

In FDTD an ABC is most commonly applied at the electric field components where a truncation boundary is located. As is illustrated in Figure 4.9 the ABC is applied in order to supply the required values for the electric field components which, due to the central difference approximation, can not be calculated directly from the FDTD algorithm.

Application of ABCs in TLM

In comparison to the FDTD method, the application of ABCs in TLM has not received the same attention. Traditionally, in TLM the absorbing boundary condition used for simulations of open boundary problems is to terminate the transmission lines forming the TLM network with a load having the characteristic impedance of the medium being modeled. This ABC is known as a **matched termination** ABC (Figure 4.10). However, as will be shown later, its performance is far from optimal, especially when the boundaries

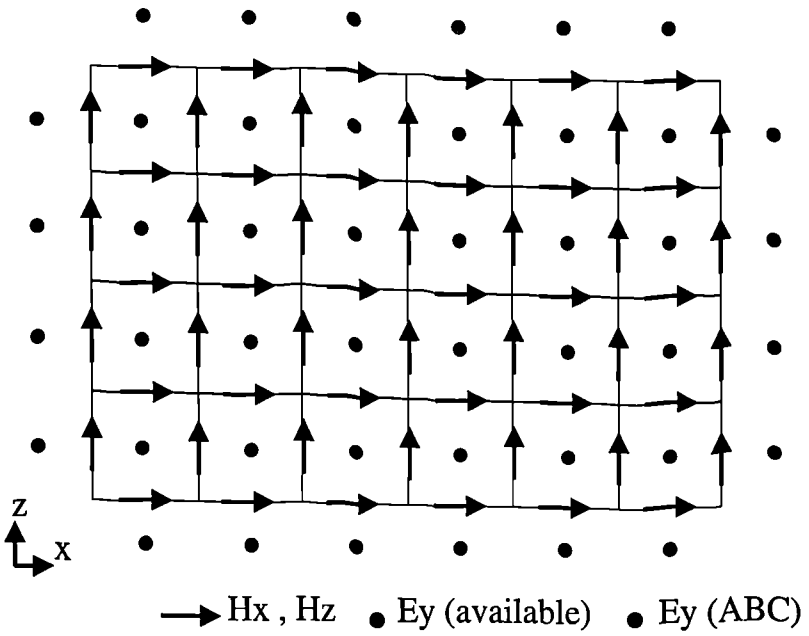

Figure 4.9: Application of an ABC to the 2D FDTD method. The ABC is used to predict the values of the electric field at the grey colored cells in order for the FDTD calculation to continue.

are located relatively close to the radiating targets and sources in the model. The poor performance of the matched termination ABC is a result of its formulation, which allow only waves incident normally on the boundary to be adequately absorbed. This, however, is rarely the case in actual simulations. An attempt to improve the performance of this ABC resulted in the **variable impedance ABC** introduced by Simmons and Bridges (1990). This ABC was based on an algorithm used to predict the angle of incidence of waves on the truncation boundary. This information was then used to make an appropriate adjustment to the terminating impedance of the transmission lines. Although an improvement in performance has been achieved with this technique it is not significant enough to render it suitable as a general solution for the TLM ABC problem.

As a number of ABCs have already been developed for the FDTD method, their introduction to TLM have been investigated for the modelling of GPR. Similar work has been carried out independently by Chen et al. (1993) for the Higdon's ABC. Although the theoretical concepts from which the various ABCs (e.g. the one-way wave equation) have been developed do not change, the incorporation of these ABCs in the TLM method is rather different from their standard use in FDTD. The formulation of the TLM method allows the ABC to be incorporated in different ways (see Figure 4.10) (Giannopoulos and

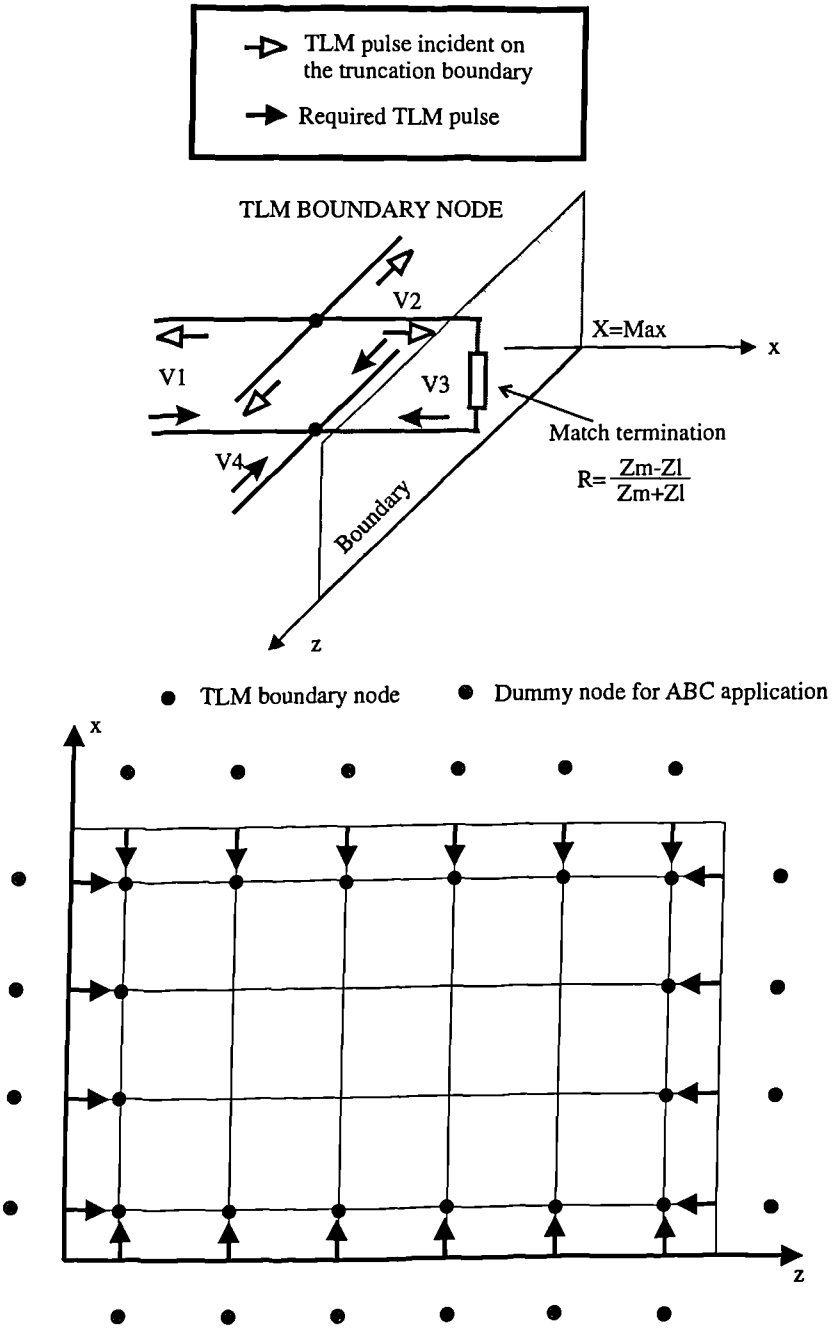

Figure 4.10: Application of ABCs to 2D TLM. The grey nodes are used in the (DN) ABC and the black nodes are used for the (NV) ABC. Finally, the required voltage pulses incident on a boundary can be obtained directly with the (PV) ABC.

Tealby, 1995):

A. At the center of the TLM nodes located just inside of the truncation boundaries. This formulation is in principle equivalent to the application of an ABC in the electric field component as in FDTD. From the predicted value of the total voltage (V_y) of the boundary node for the next time step, the voltage pulse, which should be incident on the node from the line which is directed towards the node from the truncation boundary, is estimated and passed to the TLM algorithm. This approach will be referred to henceforth as the "node voltage" (NV) ABC. For example, at the $x = X_{max}(I,k)$ truncation boundary the voltage pulse required by the TLM algorithm is ${}^{i}V_3^{n+1}(I,k)$ and can be calculated by :

(4.66)
$$ {}^{i}V_3^{n+1}(I,k) = 2V_y^{n+1}(I,k) - {}^{i}V_1^{n+1}(I,k) - {}^{i}V_2^{n+1}(I,k) - {}^{i}V_4^{n+1}(I,k) $$

where the value of $V_y^{n+1}(I,k)$ is predicted by an ABC. Other truncation boundaries can be treated in a similar way. Although this approach corresponds in principle to the application of an ABC in FDTD (use of the electric field component), it introduces an ambiguity in the calculation of the required TLM pulses at the corner nodes of the network where there are two unknowns (in (4.66)). However, numerical experiments showed that the performance of the ABCs with this approach is very similar to their performance in FDTD (Giannopoulos and Tealby, 1995).

B. An approach equivalent to FDTD can be formulated for the application of an ABC to TLM using a new concept. As is illustrated in Figure 4.10, a dummy node is introduced outside the TLM network and an ABC is used to predict the total node voltage on this node at the current time step. Consider the application of the ABC to the $x = X_{max}$ boundary. The reflected pulse ${}^{r}V_{1D}^{n}(I+1,k)$ from this dummy node will be the incident pulse on the TLM boundary node at the next time step. Therefore, the required pulse is:

(4.67)
$$ {}^{i}V_3^{n+1}(I,k) = {}^{r}V_{1D}^{n}(I+1,k) $$

If the value of the reflected pulse can be calculated, the required pulse is obtained. In any 2D TLM node the sum of the incident and reflected pulses on every branch is equal to the total node voltage

(4.68)
$$ V_y = {}^{i}V_j + {}^{r}V_j \qquad j = 1,2\ldots5 $$

this can be verified using the scattering matrix. Therefore, the pulse scattered from the dummy TLM node — and hence the required incident pulse to the boundary node — can be obtained if the incident pulse to the dummy node is known. This pulse is available since it is just the scattered pulse from the boundary node (directed towards the boundary) at the previous time step.

$$ {}^{i}V_{1D}^{n}(I+1,k) = {}^{r}V_{3}^{n-1}(I,k) \tag{4.69} $$

Therefore, an application of an ABC directly equivalent to FDTD (as is illustrated in Figure 4.9) is possible. Further, there is no problem at the corner TLM nodes. However, this ABC requires the storage of the scattered pulse from the TLM boundary node for the previous time step. This is not a significant drawback, considering that it resolves the ambiguity at the corner nodes and involves only the addition of one storage location for the boundary point. This application of an ABC to TLM will be referred to henceforth the "dummy node" (DN) approach.

C. Following the general description of boundaries in TLM, which is to place them midway between TLM nodes (Chen et al., 1993), the ABC could be applied directly on the individual voltage pulses on the transmission lines of the TLM network. This approach — called the "port voltage" (PV) ABC — is more consistent with the description of boundaries in TLM and, most importantly, the ABC is applied to both the magnetic and electric fields simultaneously, since the individual voltage pulses are associated directly with them (Giannopoulos and Tealby, 1995 ; Eswarappa and Hoefer, 1994).

From a comparison of the performance of the Higdon and Liao et al. ABCs when applied to TLM with the traditional "matched termination" ABC, their superior performance is demonstrated in particular when higher orders of the boundary conditions are used. Moreover, as will be presented later, these ABCs have been found to perform better when applied to TLM (using the PV approach) than with their typical application in FDTD.

4.12 One-way wave equation ABC — Higdon operator

The one-way wave equation is a partial differential equation which permits wave propagation only in certain directions. This equation results from factoring the wave equation

(Fang, 1989). The 2D scalar wave equation is:

$$\frac{\partial^2 U}{\partial x^2} + \frac{\partial^2 U}{\partial z^2} - \frac{1}{u^2}\frac{\partial^2 U}{\partial t^2} = 0 \tag{4.70}$$

where u is the wave velocity.[6] Equation (4.70) could be compactly written as

$$LU = 0 \tag{4.71}$$

where L is a differential operator defined as

$$L = D_x^2 + D_z^2 - \frac{1}{u^2}D_t^2 \tag{4.72}$$

and the following equivalences are used:

$$D_x^2 \equiv \frac{\partial^2}{\partial x^2} \quad D_z^2 \equiv \frac{\partial^2}{\partial z^2} \quad D_t^2 \equiv \frac{\partial^2}{\partial t^2} \tag{4.73}$$

further, equation (4.71) could be factored as

$$LU = L^+L^-U = 0 \tag{4.74}$$

where the operators L^+ and L^- are

$$L^- = D_x - \frac{D_t}{u}\sqrt{1-S^2} \qquad L^+ = D_x + \frac{D_t}{u}\sqrt{1-S^2} \tag{4.75}$$

and S is given by

$$S = \frac{D_z u}{D_t} \tag{4.76}$$

Application of $L^-U = 0$ to the boundary at $x = 0$ and of $L^+U = 0$ to the boundary at $x = X_{max}$ will absorb a plane wave propagating towards these boundaries at any angle. However, the presence of the radical in equation (4.75) renders L^+ and L^- as *pseudo-differential* operators (Taflove, 1995). Therefore, the application of these operators can not be directly implemented in any numerical scheme. A range of approximations for the radical in equation (4.75) results in several ABCs (Enguist and Majda, 1977; Mur 1981; Moore et al., 1988). These approximations result in schemes which can be used to predict the value of the electric field at the truncation boundary from its current and past values available in the computational domain. For example, the popular Mur ABC results from the following approximations to the radical.

$$\sqrt{1-S^2} \approx 1 \qquad \text{First order Mur ABC} \tag{4.77}$$

$$\sqrt{1-S^2} \approx 1 - \frac{1}{2}S^2 \qquad \text{Second order Mur ABC} \tag{4.78}$$

[6] U is the scalar field. For example in 2D FDTD $U = E_y$

The presence of the D_z operator in S makes the implementation of ABCs based on such approximations to the radical cumbersome, since spatial derivatives parallel to the direction of the boundary should be discretized. These derivatives can not be easily calculated at the corners of the computational domain, and lower order approximations are usually used at these locations (Mur, 1981).

The Higdon Operator

Based on the one-way wave equation Higdon (1986; 1987) and Keys (1985) have developed, independently, an ABC which is defined by the operator

$$\prod_{j=1}^{N}\left[\frac{\partial}{\partial x}+\frac{\cos(\theta_j)}{u}\frac{\partial}{\partial t}\right]U=0 \tag{4.79}$$

where θ_j is the angle of incidence to the $x = X_{max}$ boundary.[7] Higdon showed that this operator will completely absorb any waves incident on the boundary with angles θ_j. The relation between the Higdon's operator and ABCs developed from direct approximations to the radical in equation 4.75 is simple to establish since:

$$1-S^2=1-\frac{D_z^2v^2}{D_t^2}=1-\sin^2(\theta)=\cos^2(\theta) \tag{4.80}$$

From the above, it is easy to show that the first order Mur ABC corresponds to the first order Higdon ABC when the angle $\theta = \pi/2$ is used in the Higdon operator. Moreover Higdon (1987) showed that:

> "[The operator in (4.79) provides] a general representation of absorbing boundary conditions, in the following sense. If an absorbing boundary condition is based on a symmetric rational approximation to the portion of the dispersion relation corresponding to outgoing waves, then it is either:
>
> A. equivalent to (4.79), for suitable θ_j satisfying $|\theta_j| < \frac{\pi}{2}$; or
>
> B. unstable; or
>
> C. not optimal, in the sense that the reflection coefficients in the boundary condition can be modified so as to reduce the magnitude of the reflection coefficient for all Fourier modes corresponding to non-tangential incidence.
>
> "

[7] Similar operators could be defined for all truncation boundaries.

The important difference between the Higdon's operator and the ABCs based on a direct approximation to the radical in (4.75) is that using the Higdon's ABC operator provides the choice of optimizing its performance for certain angles of incidence — if required — whereas when using the other ABCs this optimization is inherent in the approximation of the radical in (4.75), and there is no option for specific angular optimization from the end user of the model. Further, one important characteristic of the Higdon's ABC is that it does not require the discretization of spatial derivatives parallel to the boundary and therefore its implementation is more straightforward. Because of the use of such a one-dimensional stencil there is no need for special treatment at the corners of the computational domain which are handled with the same accuracy as any other point on the truncation boundary. The general discretization scheme for the Higdon's ABC is (Higdon, 1986):

(4.81)
$$\prod_{j=1}^{N}[(\frac{\mathbf{I}-\mathbf{Z}^{-1}}{\Delta l})((1-b)\mathbf{I}+b\mathbf{K}^{-1})+\frac{\cos(\theta_j)}{u}(\frac{\mathbf{I}-\mathbf{K}^{-1}}{\Delta t})((1-a)\mathbf{I}+a\mathbf{Z}^{-1})]U=0$$

where **I**, **K**, **Z** are defined as:

(4.82)
$$\mathbf{I}U^n_{i,k}=U^n_{i,k} \qquad \mathbf{K}U^n_{i,k}=U^{n+1}_{i,k} \qquad \mathbf{Z}U^n_{i,k}=U^n_{i+1,k}$$

and the coefficients a, b are weighted space- and time- averages of the space and time derivatives. Higdon examined some specific approximations to (4.81) which are:

A. *Forward Euler*: $a=0$ and $b=1$

B. *Backward Euler*: $a=0$ and $b=0$

C. *Box scheme*: $a=0.5$ and $b=0.5$

From the above, the most popular (and the one used here) is the *box scheme* discretization. The first order ($N=1$) Higdon ABC as applied to the $x=X_{max}$ boundary of the 2D FDTD lattice is:

(4.83)
$$E_y\big|^n_{(I,k)}=E_y\big|^{n-1}_{(I-1,k)}+h(E_y\big|^n_{(I-1,k)}-E_y\,{}^{n-1}_{(I,k)})\big|$$

where

(4.84)
$$h=\frac{u\Delta t-\cos(\theta)\Delta l}{u\Delta t+\cos(\theta)\Delta l}$$

4.13 The Liao et al. ABC

Liao et al. (1984) introduced an alternative ABC which they called the "multi-transmitting formula" for the truncation of finite difference models used for the simulation of near-field seismograms. However, the application of the ABC is not restricted only to this type of problem and has been previously used for simulation of electromagnetic problems (Omick et al., 1993). The value of a field component at the truncation boundary is given for the next time step by the Liao et al. ABC according to:

$$U(x,t+\Delta t)=\sum_{m=1}^{N}(-1)^{m+1}C_m^N U(x-mc_A\Delta t,t-(m-1)\Delta t) \tag{4.85}$$

where C_m^N is the binomial coefficient

$$C_m^N=\frac{N!}{(N-m)!m!} \tag{4.86}$$

and c_A is called the "unified artificial transmitting velocity". The Liao et al. ABC is in essence a space-time extrapolation along the line

$$x-c_At=\text{constant} \tag{4.87}$$

As has been pointed out by Wagner and Chew (1995) and Taflove (1995) Liao et al.(1984) used a Newton backward difference interpolation to extrapolate for the required field value using information already available in the computational domain. Using the multi-transmitting formula (4.85) for $N = 2$ the value of the electric field predicted at the $x = X_{max}$ (I,k) boundary in FDTD is:

$$E_y\big|^n_{(I,k)}=2E_y\big|^{n-1}_{(I-c_A\Delta t,k)}-E_y\big|^{n-2}_{(I-2c_A\Delta t,k)} \tag{4.88}$$

The value of c_A could be conveniently adjusted to:

$$c_A=\frac{u}{\cos(\theta)} \tag{4.89}$$

optimizing the ABC for a specific angle of incidence. Inspecting equation (4.85), it is evident that the field values required by the ABC do not necessarily correspond to locations in which field values are available from the numerical algorithm.[8] Consequently, Liao et al. (1984) introduced a quadratic interpolation to obtain the required field values from

[8]For example in a FDTD model when the time step is related to the spatial step by the Courant stability criterion, electric field values are located $\sqrt{2}c\Delta t$ apart which may be different than the required $c_A\Delta t$

the available information stored in the numerical grid. With this modification the ABC becomes (Liao et al., 1984, Chew, 1990):

$$U(x, t+\Delta t) = \sum_{m=1}^{N} (-1)^{m+1} C_m^N \underline{T}^m \underline{\Phi}_m \tag{4.90}$$

where $\underline{T}^m$ is a row matrix of $(2m+1)$ elements,

$$\underline{T}^m = \begin{bmatrix} T_{m,1} & T_{m,2} & \dots & T_{m,2m+1} \end{bmatrix} \tag{4.91}$$

and it can be calculated by the following recursion relations:

(4.92)

$$\underline{T}^m = \underline{T}^1 \begin{bmatrix} T_{m-1,1} & T_{m-1,2} & \dots & \dots & T_{m-1,2m-1} & 0 & 0 \\ 0 & T_{m-1,1} & T_{m-1,2} & \dots & \dots & T_{m-1,2m-1} & 0 \\ 0 & 0 & T_{m-1,1} & T_{m-1,2} & \dots & \dots & T_{m-1,2m-1} \end{bmatrix}$$

for $m \geq 2$ and the three elements of $\underline{T}^1$ are:

$$T_{1,1} = \frac{(2-s)(1-s)}{2} \tag{4.93}$$

$$T_{1,2} = s(2-s) \tag{4.94}$$

$$T_{1,3} = \frac{s(s-1)}{2} \tag{4.95}$$

where $s = c_A \Delta t / \Delta l$, $\underline{\Phi}_m$ is a column matrix with elements:

$$\underline{\Phi}_m = \begin{bmatrix} \Phi_{1,m} \\ \Phi_{2,m} \\ \vdots \\ \Phi_{2m+1,m} \end{bmatrix} \tag{4.96}$$

in which

$$\Phi_{i,m} = U(t_m, x_i)$$

where

$$x_i = x_a - (i-1)\Delta l$$

$$t_m = t - (m-1)\Delta t$$

and x_a is the coordinate of the required field value. Similarly to the Higdon ABC, the Liao et al. ABC uses a one dimensional stencil and its implementation is straightforward. An interesting difference of the formulation of the Liao et al. ABC from the Higdon ABC is that it uses only field values calculated at past time steps, whereas the Higdon ABC

uses field values calculated at the current time step (when the required value should be predicted) located inside the computational domain. From the above formulation of the Liao et al. ABC, it is not clear how it could be optimized for different angles of incidence, as the Higdon ABC can be. Wagner and Chew (1995) proved that the Liao et al. ABC is consistent with the one-way wave equation and introduced a new more compact notation. Using the shift operators $\mathbf{K}$ and $\mathbf{Z}$ defined in (4.82) and the identity operator $\mathbf{I}$ they showed that the Liao et al. ABC can be written as (Wagner and Chew, 1995):

$$\prod_{j=1}^{N}[\mathbf{I} - \mathbf{A}\mathbf{K}^{-1}]U = 0 \tag{4.97}$$

and $\mathbf{A}$ is a backward spatial shift of $c_A\Delta t$ obtained via the quadratic interpolation:

$$\mathbf{A} = T_{11} + T_{12}\mathbf{Z}^{-1} + T_{13}\mathbf{Z}^{-2} \tag{4.98}$$

Using (4.97) the optimization of the ABC is straightforward.

4.14 Generation of higher orders of Higdon and Liao ABCs

Steich and Luebbers (1994) have introduced a simple and effective way to calculate higher orders of the Higdon and Liao ABCs using a matrix representation. This facilitates the computation of any order ABC from their first order coefficients. Both the Higdon and Liao ABCs provide an approximation for the required field value at the boundary using field values from the interior of the computational domain located along a line normal to the boundary (one-dimensional stencil). Moreover, they require field values not only of the current time step but of previous time steps as well. This information can be organized neatly in a matrix form. Consider the $x = X_{max}$ boundary of a 2D FDTD or TLM computational domain. Denote the required value which should be predicted by the ABC as $U^n_{(I,k)}$. Then in matrix form the required information by the ABC could be written as:

$$\underline{\mathbf{F}} = \begin{bmatrix} U^n_{(I,k)} & U^n_{(I-1,k)} & U^n_{(I-2,k)} & \cdots \\ U^{n-1}_{(I,k)} & U^{n-1}_{(I-1,k)} & U^{n-1}_{(I-2,k)} & \cdots \\ U^{n-2}_{(I,k)} & U^{n-2}_{(I-1,k)} & U^{n-2}_{(I-2,k)} & \cdots \\ \cdots & \cdots & \cdots & \cdots \end{bmatrix} \tag{4.99}$$

In the above matrix each row stores information about a particular time step and each column stores information about a particular location along the one dimensional space

stencil of the ABC. Similarly, the coefficients of an ABC can be represented as a matrix ($\underline{\mathbf{A}}$). For example, the Higdon and Liao first order ABCs are simply:

$$\underline{\mathbf{A}}_{H1} = \begin{bmatrix} -1 & h \\ -h & 1 \end{bmatrix} \qquad \text{Higdon first order ABC} \tag{4.100}$$

$$\underline{\mathbf{A}}_{L1} = \begin{bmatrix} -1 & 0 & 0 \\ T_{11} & T_{12} & T_{13} \end{bmatrix} \qquad \text{Liao first order ABC} \tag{4.101}$$

The required value is obtained by solving the following equation for the unknown field value:

$$\sum_{p=0}^{P}\sum_{q=0}^{Q} \underline{F}(p,q)\underline{A}(p,q) = 0 \tag{4.102}$$

Moreover, a general coefficient matrix for a higher order ABC can expressed as

$$\underline{\mathbf{A}} = \begin{bmatrix} a_{0,0} & a_{0,1} & \dots & \dots & a_{0,Q} \\ a_{1,0} & a_{1,1} & \dots & \dots & a_{1,Q} \\ \dots & \dots & a_{p,q} & \dots & \dots \\ \dots & \dots & \dots & \dots & \dots \\ a_{P,0} & a_{P,1} & \dots & \dots & a_{P,Q} \end{bmatrix} \tag{4.103}$$

and its elements are calculated using the formula (Steich and Luebbers, 1994):

(4.104)

$$\underline{A}(p,q) = -\sum_{p_1=0}^{P_1}\sum_{q_1=0}^{Q_1}\sum_{q_2=0}^{P_2}\sum_{q_2=0}^{Q_2} \delta_{(p_1+p_2)p}\delta_{(q_1+q_2)q}\underline{A}_1(p_1,q_1)\underline{A}_2(p_2,q_2)$$

where $\underline{\mathbf{A}}_1$ and $\underline{\mathbf{A}}_2$ are the coefficient matrices of the ABCs generating the higher order one ($\underline{\mathbf{A}}$). The range of p and q are $[0, P_1 + P_2]$ and $[0, Q_1 + Q_2]$ respectively, and δ is defined as

$$\delta_{vw} = \begin{cases} 0 & \text{if } v \neq w \\ 1 & \text{if } v = w \end{cases}$$

As an example, to construct a coefficient matrix for the second order Higdon ABC both $\underline{\mathbf{A}}_1$ and $\underline{\mathbf{A}}_2$ in 4.104 are matrices of the first order Higdon ABC. Using equation (4.104) the matrix for the second order Higdon has the form:

$$\underline{\mathbf{A}}_{H2} \begin{bmatrix} -1 & h_1 + h_2 & -h_1 h_2 \\ -h_1 - h_2 & 2 + 2h_1 h_2 & -h_1 - h_2 \\ -h_1 h_2 & h_2 + h_1 & -1 \end{bmatrix}$$

The above result can be verified easily by performing the calculations in (4.81). Similarly, higher orders of the Liao's ABC can be generated. The above procedure makes the implementation of higher orders of ABC easier in the FDTD and TLM algorithms. It should be noted that the traditional formulation of Liao's ABC (4.90) does not require such an algorithm for its efficient implementation. However, from an algorithmic point of view it is advantageous to use this general approach.

4.15 Theoretical reflection coefficients of the Higdon and Liao et al. ABC

The theoretical reflection coefficients of an ABC are used to obtain an estimate of their performance. Consider the $x = X_{max}$ (I, k) boundary and assume a plane wave incident on this boundary, from a homogeneous and loss-free medium, of the form

$$U_i = e^{j(\omega n\Delta t - \beta_x I\Delta l - \beta_z k\Delta l)} \tag{4.105}$$

a reflected wave will originate from the boundary

$$U_r = Re^{j(\omega n\Delta t + \beta_x I\Delta l - \beta_z k\Delta l)} \tag{4.106}$$

where R is the reflection coefficient. The total field at which a boundary operator **Q** (Higdon or Liao) is applied is

$$U = U_i + U_r \tag{4.107}$$

and

$$\mathbf{Q}U = \mathbf{Q}U_i + \mathbf{Q}U_r = 0 \tag{4.108}$$

Using (4.105) and (4.106) in (4.108) the reflection coefficient is obtained as:

$$R = -\frac{\mathbf{Q}e^{j(\omega n\Delta t - \beta_x I\Delta l - \beta_z k\Delta l)}}{\mathbf{Q}e^{j(\omega n\Delta t + \beta_x I\Delta l - \beta_z k\Delta l)}} \tag{4.109}$$

It is easy to show that R can be calculated for a specific ABC using the coefficient matrix described previously from the relation

$$R = -\frac{\sum_{p=0}^{P}\sum_{q=0}^{Q}\underline{A}(p,q)e^{j(\omega p\Delta t - \beta\cos(\theta)q\Delta l)}}{\sum_{p=0}^{P}\sum_{q=0}^{Q}\underline{A}(p,q)e^{j(\omega p\Delta t + \beta\cos(\theta)q\Delta l)}} \tag{4.110}$$

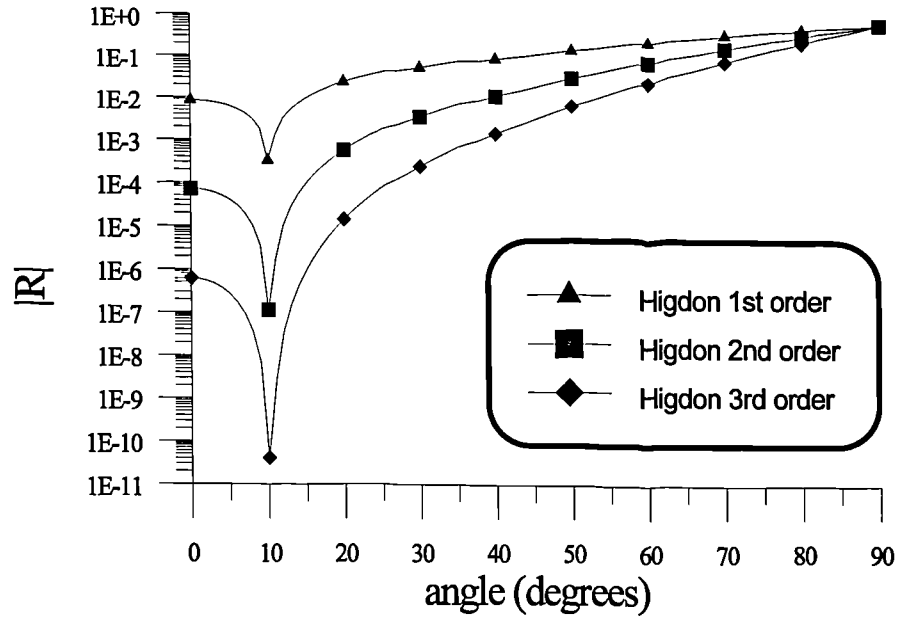

Figure 4.11: Magnitude of the theoretical reflection coefficient for the first, second and third orders of the Higdon ABC as a function of the incident angle. The wavelength of the electromagnetic waves is considered to be equal to $10\Delta l$.

In Figure 4.11, the magnitude of the reflection coefficients of the Higdon ABC for the first, second and third orders are presented as a function of the angle of incidence (θ). Similarly, the reflection coefficients for the three first orders of the Liao et al. ABC are illustrated in Figure 4.12.

For both ABCs, the optimization angles are $\theta_j = 0$. From these Figures it is evident that by increasing the order of the ABC its reflection coefficients are decreased, and hence better performance is expected. The effects of using different optimization angles θ_j on the reflection coefficients R are presented in Figure 4.13 for the second order ($N = 2$) of Higdon and Liao et al. ABCs, respectively.

From the decrease in magnitude of the reflection coefficients with increasing order of an ABC, it is natural to assume that their performance will be similarly improved. However, this is not strictly true in practical simulations. Applying the Liao and Higdon ABCs of the third order (or greater) to an FDTD model using single precision arithmetic does not result in stable solutions. Similar observations of instabilities introduced by higher order ABCs have been reported by Fang (1989) and Moghaddam and Chew (1991). Moreover, the effects of the different numerical velocities (numerical dispersion) for waves propagating at different angles in a FDTD or TLM model limit the reduction of the error reflected

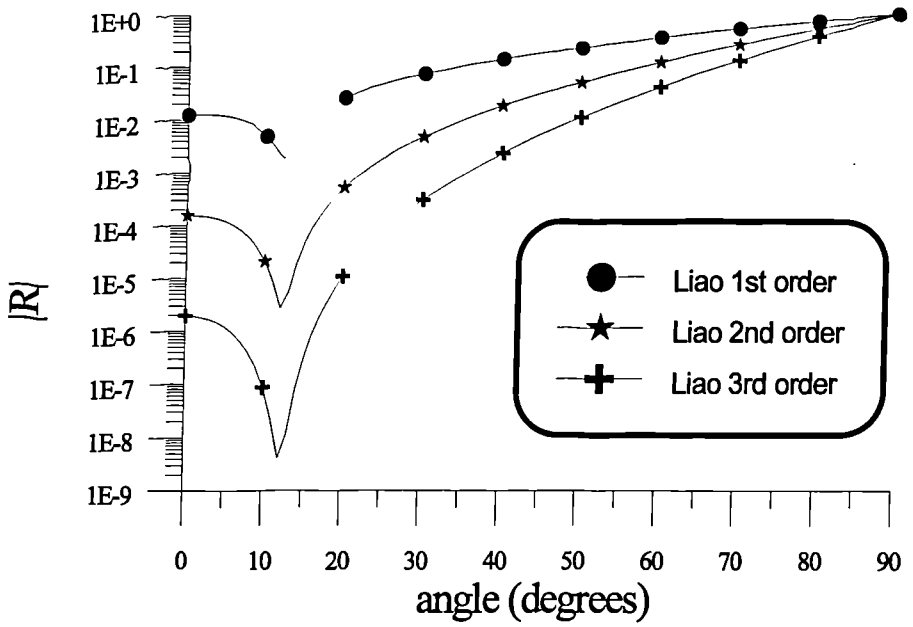

Figure 4.12: Magnitude of the theoretical reflection coefficient for the first, second and third orders of the Liao et al. ABC as a function of the incident angle. The wavelength of the electromagnetic waves is considered to be equal to $10\Delta l$.

waves to a certain level which can not be reduced by increasing the order of an ABC Taflove (1995).

4.16 Stability of the Higdon and Liao et al. ABC applied in FDTD and TLM

The cause of instabilities when the Higdon ABC is applied has been pointed out by Higdon (1986; 1987) and is related to the marginal stability of the ABC when the frequency of the incident wave to the truncation boundary approaches zero. Wagner and Chew (1995) reached a similar conclusion in an analysis of the Liao et al. ABC. At zero frequency the reflection coefficient of both Higdon and Liao ABCs have a marginally stable pole located on the unit circle $|R| = 1$ irrespective of the angle of incidence. The instabilities in the numerical implementation of these ABCs arise from the unavoidable use of finite precision arithmetic in the numerical algorithms. Therefore, numerical noise can render the schemes unstable. A verification of this conclusion is that stable solutions have been obtained, for example, with the third order Liao et al. ABC using double precision arithmetic in the numerical calculations (Fang, 1989). A remedy for the instabilities caused by numerical noise without increasing the numerical precision of the calculations[9] is to use stabilizing

[9]Changing the numerical precision of the calculation results in a substantial increase (doubles the amount of computer memory) of the required computer resources.

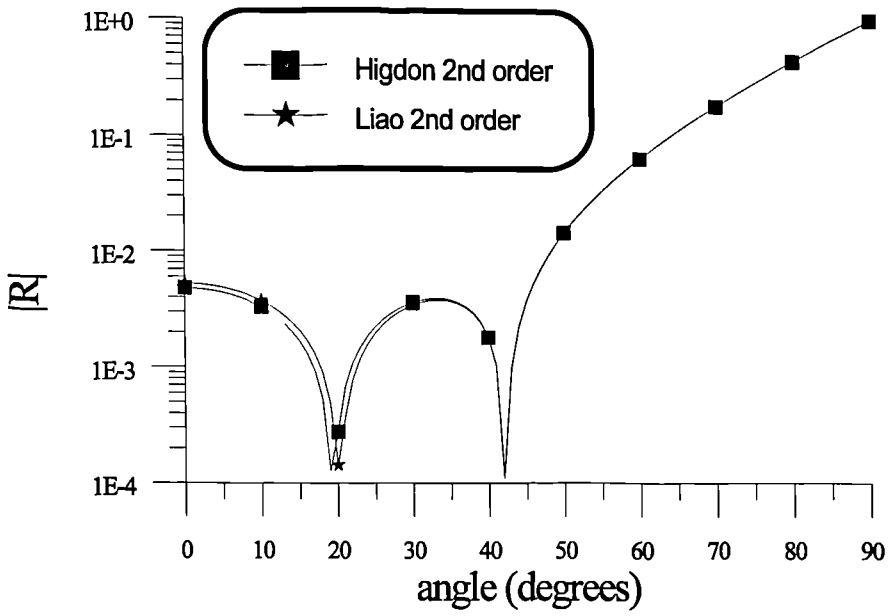

Figure 4.13: Magnitude of the theoretical reflection coefficients of the Higdon and Liao et al. ABC of the second order optimized for angles of incidence $\theta_1 = 17.0$ and $\theta_1 = 42.0$.

factors (i.e perturb the ABC coefficients), which introduces losses in the calculation of the fields predicted by the ABC and therefore keeps the solution stable. The introduction of these loss factors to the Higdon ABC was included in the original formulation of the ABC by Higdon. For the Liao ABC the introduction of loss factors has been reported by Moghaddam and Chew (1991) and more recently by Wagner and Chew (1995).

The main conclusion of these investigations as well as evidence from numerical experiments (Giannopoulos and Tealby, 1995) is that loss factors should be introduced in ABCs of the third and higher orders in FDTD to maintain stability. Usually, stabilizing higher orders than the third does not result in an appreciable increase in accuracy. Experimentally, it was found that the third order ABCs performed very well for GPR simulations when used in FDTD and the use of a higher order ABC is not required.

The stability of the Higdon and Liao ABC in TLM follows the same pattern as for the FDTD method when the NV and DN approaches are used. However, it has been found by numerical experiments (Giannopoulos and Tealby, 1995) that when the ABCs are applied to TLM using the PV approach their sensitivity to numerical noise increases. It has been observed that even the first order Higdon and Liao et al. ABC will lead to instabilities when the number of iterations is substantially high.[10] The same approach is followed

[10] An exact number could not be calculated because the amount of iterations which should be performed for the solution to start diverging depends on the size of the TLM network used. For the number of

in stabilizing the ABCs as for the FDTD case described above and from the analysis presented in the following sections, it is evident that the accuracy of the ABCs is not compromised by the introduction of the stabilizing factors.

For the Higdon ABC the stabilizing factors are included as loss terms in the general Higdon operator as (Higdon, 1985):

$$\prod_{j=1}^{N}[\frac{\partial}{\partial x}+\frac{\cos(\theta_j)}{u}\frac{\partial}{\partial t}+e_j]U=0 \tag{4.111}$$

where $e_j < 1$. For the Liao et al. ABC stabilization involves the perturbation of the parameters T_{11} , T_{12} and T_{13} and often only of T_{11} by a factor $-l$ ($|l| < 1$) (Wagner and Chew, 1995). Eswarrapa and Hoefer, (1994) suggested values for e_j in the range of $[0.01/\Delta l, 0.5/\Delta l]$. Steich and Luebbers (1994) suggested the subtraction of the value $l = 0.0075$ from T_{11} of the Liao ABC to maintain stability. This value has also been recommended by Moghaddam and Chew (1991). In general, the only way of obtaining an acceptable stabilized ABC is by trial and error.

The procedure used in this work to obtain stable Liao and Higdon ABCs in both TLM and FDTD is to test the ABC in a small computational domain (50 × 50) for a great number of iterations compared to the ones required usually by GPR models (around 5000). To stabilize the Liao ABC all the three basic coefficients (T_{11}, T_{12}, T_{13}) were perturbed by a percentage of their original value. The following values found to give optimal results for the Higdon and Liao ABCs.

- For application in FDTD and TLM with the NV and DN approaches only the third order Liao ABC had to be stabilized by perturbing (decrease) T_{11}, T_{12}, T_{13} by 1.5%, and the inclusion of a loss factor $e = 0.027/\Delta l$ was necessary to obtain a stable Higdon ABC.

- For applications in TLM with the PV approach the coefficients had to be perturbed by 0.17% for the second order Liao ABC and 3.38% for the third order one. The application of a third order Liao ABC did not result in an overall improvement in accuracy when compared to the second order ABC. Similarly for the Higdon ABC, the factors $e = 0.005$ for a second order ABC and $e = 0.075$ for a third order, had to be incorporated in the ABC.

iterations performed usually for GPR simulations no instabilities were observed for the first order Higdon and Liao ABCs.

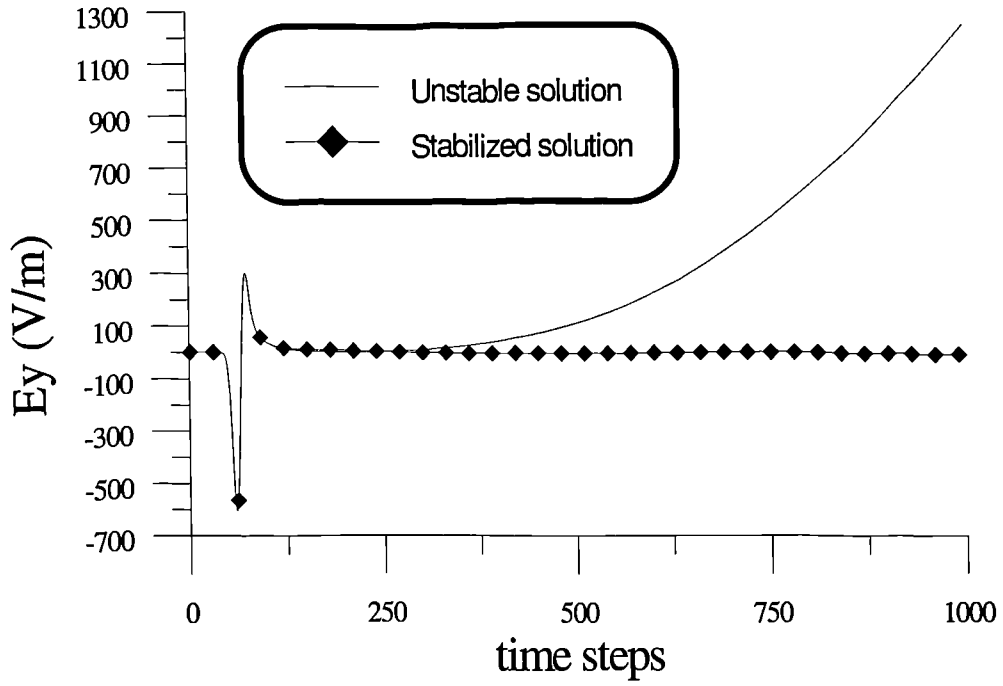

Figure 4.14: Effect of stabilizing factors introduced to the third order Liao et al. ABC when applied to TLM with the DN approach.

In Figure 4.14 the effect of introducing stabilizing factors to the Liao et al. ABC applied to TLM with the PV approach is compared with the unstable original application of the ABC. Further, the reflection coefficients of stabilized Higdon and Liao ABCs are presented in Figure 4.15. The effect of the stabilizing factors is to smooth-out the deep nulls observed in the reflection coefficient curves of the unstabilized ABCs. In the following discussion it is implied that the stabilized forms of the ABCs are used as described above.

4.17 Comparison of the performance of ABC when applied to FDTD and TLM

To assess the performance of an ABC applied to TLM and FDTD methods a numerical experiment using the same configuration for both methods was performed. The FDTD algorithm was operated at the maximum of its stability limit in order for the solution to be directly equivalent with the TLM solution. The numerical experiment consisted of a line source with a Gaussian current distribution located at the centre of a small domain of 50×50 nodes (D1) radiating in free-space. The output signal (E_y) was recorded at every node, except the source one, for 300 time steps. A reference solution was obtained using a 400×400 domain (D2). The two solutions will differ for those time steps for which

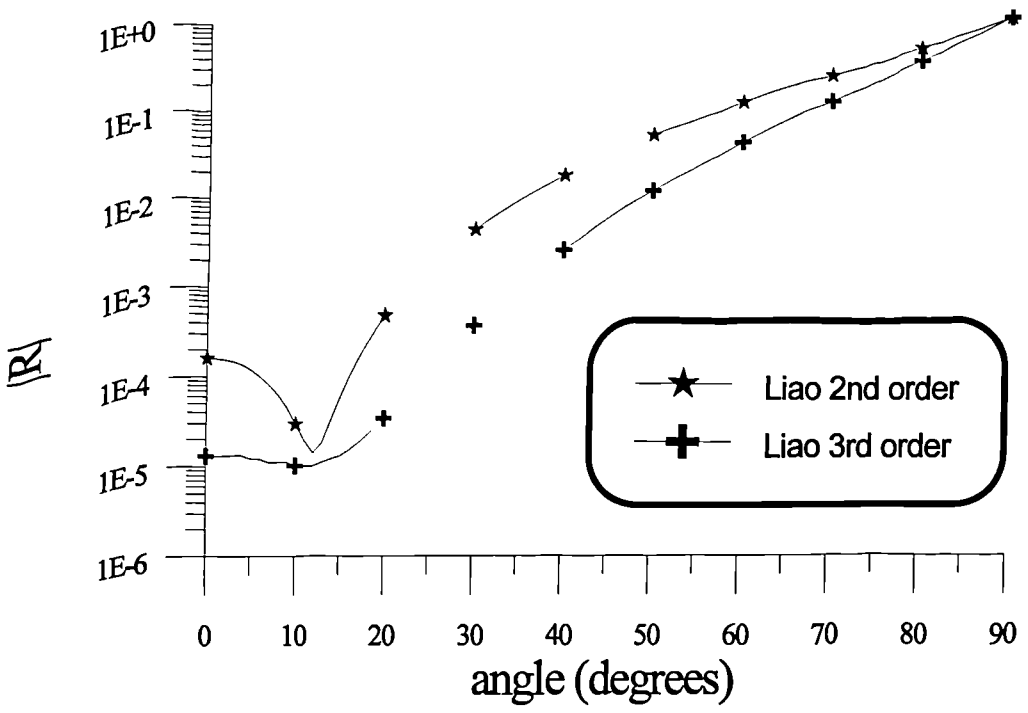

Figure 4.15: Theoretical reflection coefficients of the second and third order Liao ABC when stabilizing factors are used. The wavelength is considered to be $10\Delta l$.

the application of the ABC will have affected the solution in the smaller domain. The configuration is illustrated in Figure 4.16. Moreover, a global error measure is defined by (Giannopoulos and Tealby, 1995)

$$\text{error}(n) = \sqrt{\sum_{r=1}^{n}\sum_{x}\sum_{y}(E^{D1}_{yx,z} - E^{D2}_{yx,z})^2} \tag{4.112}$$

where n is the time step and x,z are the coordinates of a node relative to the source.

The same experimental setup has been used in the comparison presented by Giannopoulos and Tealby (1995). This investigation showed that an ABC applied to TLM with the (NV) approach performs similarly as when is applied in FDTD. However, a significant improvement in performance is obtained when the PV approach is employed in TLM. Even a first order ABC performs better than a second order one applied to FDTD. In Figure 4.17 and 4.18 the global errors for the Higdon and Liao ABCs when applied to TLM with the PV approach are compared with the global errors of the same ABCs when applied to FDTD. This substantial improvement in performance of an ABC when applied using the PV approach is a result of the formulation of the TLM method. The application of an ABC directly to the TLM voltage impulse of a boundary node is equivalent to its application to both the electric and magnetic fields simultaneously (Eswarrapa and Hoefer, 1994; Giannopoulos and Tealby, 1995). In FDTD the usual application of an ABC is only

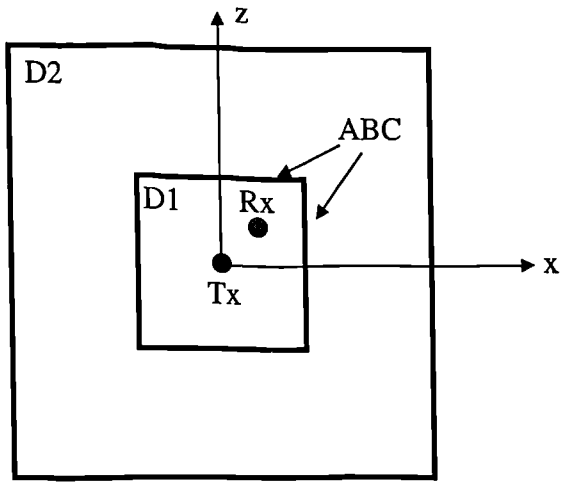

Figure 4.16: The configuration of the numerical experiment used to evaluate and compare the performance of ABCs in TLM and FDTD.

to the electric field.[11]

The performance of the ABCs when the DN approach is used in TLM is nearly identical to the corresponding performance of the ABCs in FDTD; supporting the argument that the use of a dummy node in TLM is an "equivalent formulation" to FDTD with the application of ABCs.

From the results of this comparison it is evident that TLM could provide more accurate results than FDTD, when the same discretization and ABCs are used in a model. However, recent advances in ABC technology make possible the application of a more efficient ABC in FDTD than the ones of Higdon and Liao. This ABC is the "perfectly matched layer" ABC introduced by Berenger (1994). This new ABC is currently the subject of validation and research.

[11] Applying the ABC to both the electric and magnetic field components results in a formulation called "superabsorbtion" (Mei and Fang, 1992). With this approach an improvement in performance similar to the TLM (PV) approach can be achieved. However, it was not pursued here since it involves the application of the boundary operator twice. Moreover, tests using this approach in FDTD show that it is preferable to use a third order boundary condition instead of "superabsorbtion" with an ABC of smaller order.

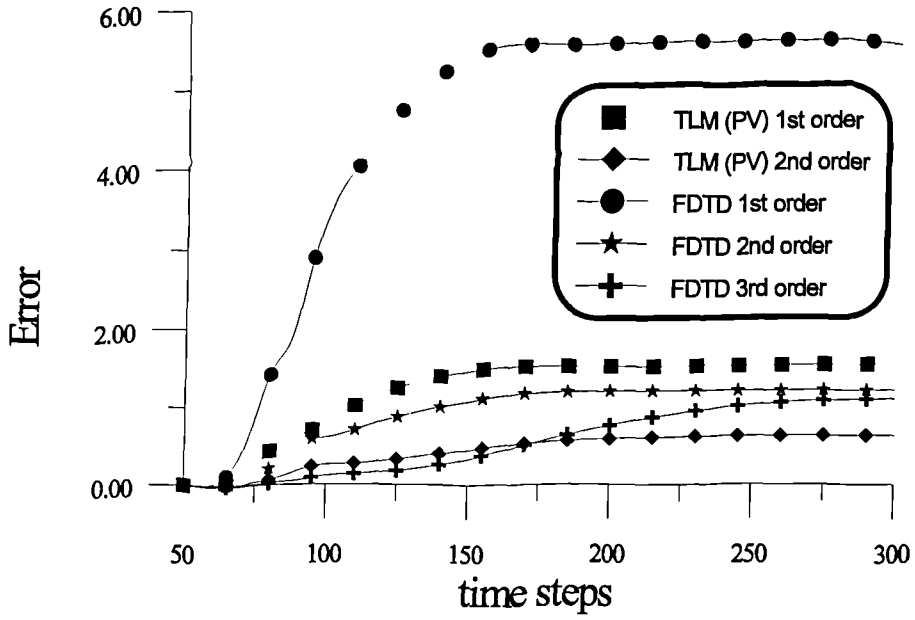

Figure 4.17: Comparison of the error measure of the Higdon ABC when applied to FDTD and TLM using the PV approach.

4.18 Comparison of the performance of Higdon and Liao ABC when applied to TLM with the "matched termination" ABC

The successful implementation of the Liao and Higdon ABC in 2D TLM results in a significant improvement in the responses obtained by a TLM model when compared with the same responses calculated using the "matched termination" ABC customarily employed in TLM models. The magnitude of this improvement is demonstrated by considering the difference between the benchmark solution obtained in the same manner, as was described in the previous section, and the solutions in the smaller domain (50×50) using the matched termination and the third order Liao ABC applied using the DN approach. In Figures 4.19 and 4.20, the waves reflected inside the TLM network are illustrated as surface plots over the small network at iteration $n = 85$ using the same scaling for both the "matched termination" case and the Liao et al. ABC (note the amplitude difference of these error waves). It is evident that using the ABCs proposed, here the simulation space is substantially clearer from artificial reflections generated by the truncation boundaries.

A comparison of the error measures of the Higdon and Liao ABCs revealed that they have a similar performance, with the Liao ABC performing slightly better, especially when a third order is used with the DN approach. The comparison of the error measures (4.112) between the first order Higdon ABC applied in TLM using the DN approach and the

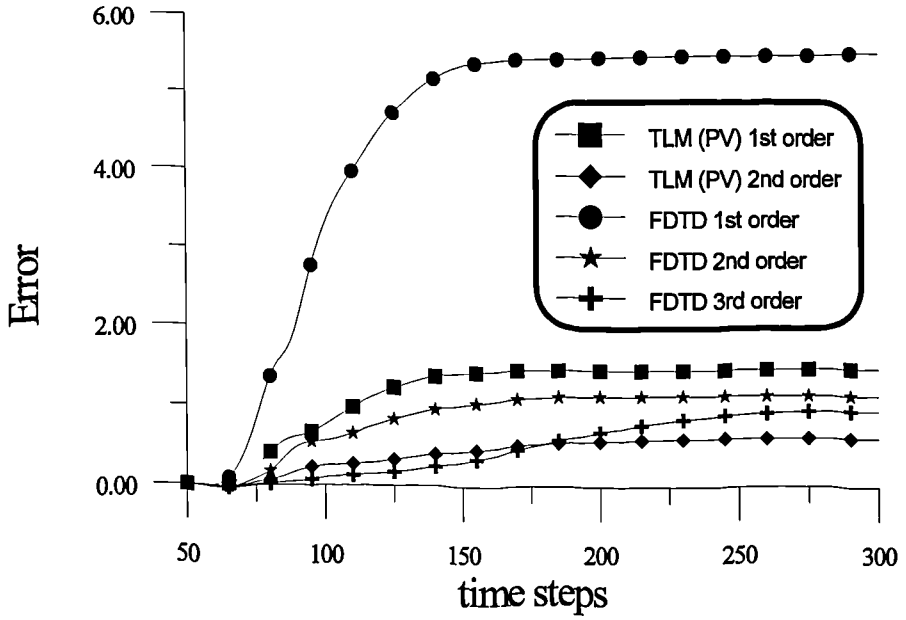

Figure 4.18: Comparison of the error measure of the Liao et al. ABC when applied to FDTD and TLM using the PV approach.

"matched termination", revealed that they produce identical responses (the numerical values of the error measures agree to the fourth decimal place). This suggests that there is possibly a relation between the "matched termination" ABC and the Higdon ABC, the former being equivalent to the first order of the latter.

The successful incorporation of the Higdon and Liao ABCs in TLM has important implications for a GPR model because the use of very large networks is avoided, rendering the method as an attractive alternative to FDTD.

4.19 Special considerations for the application of ABCs in 2D GPR models

The application of the Higdon and Liao et al. ABCs has been described assuming that the medium in which waves are propagated towards a truncation boundary is homogeneous and, in particular, free-space. However, in GPR simulations this is not the case and the ABCs should cope with waves impinging on them propagating in media with different constitutive parameters. For example, waves will propagate with different velocities in the portion of the model representing free-space and in the one representing the subsurface. Both Higdon and Liao et al. ABC should be used with an adjustment in the velocity u used in their derivation. From numerical tests it was found that $u = c/\sqrt{(\epsilon_r)}$ where ϵ_r is the relative permittivity of the medium adjacent to the ABC. Numerical tests have shown

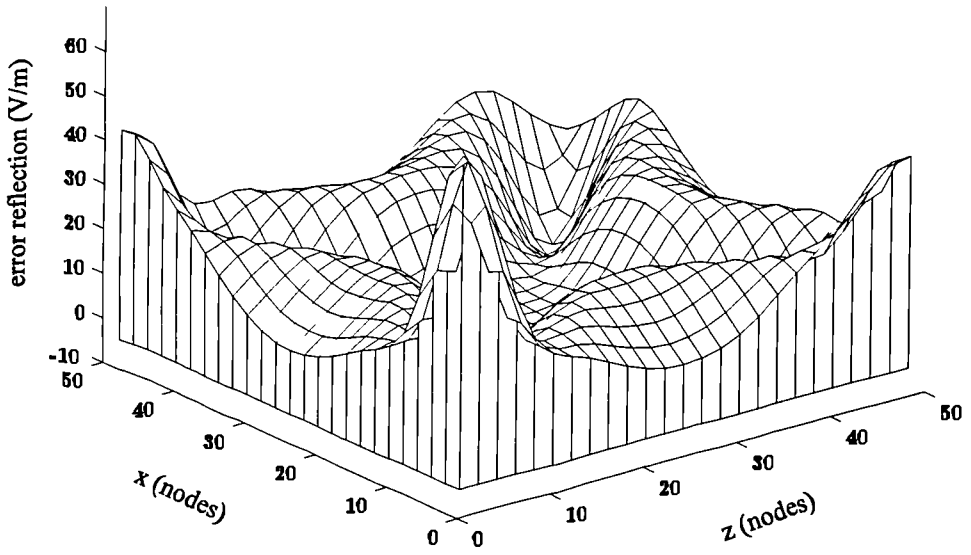

Figure 4.19: Snapshot of the error reflected waves at $n = 85$ of the small TLM network using the "matched termination" ABC.

that there is no need to modify the ABCs to account for any losses. This can be explained by considering that for small values of conductivity the mismatch will be negligible and that for large values the medium quickly attenuates any reflections.

This requirement to adjust the velocity of an ABC according to the medium adjacent to the truncation boundary is the main reason that simpler ABCs such as those examined by Morente et al. (1992), are not applicable for a GPR model. Moreover, Taflove (1995) suggested an adjustment of both c_A and of the Courant stability criterion in FDTD in such a way that the need for quadratic interpolation in Liao et al. ABC will be eliminated. This suggestion is not applicable for a GPR model and, if adopted, will result in substantial errors caused by the mismatched ABC. As an example, Figure 4.21 presents a comparison between responses obtained using the same Liao et al. ABC (second order), applied to truncate a model simulating a homogeneous medium of $\epsilon_r = 3$ and $\sigma = 0.01$ with and without the proper velocity adjustment, and with a benchmark solution obtained using a large computational domain which truncation boundaries did not affect the solution for the required simulated time window. The configuration used for this numerical experiment is the same as that depicted in Figure 4.16, with the only difference being the constitutive parameters of the simulated medium.

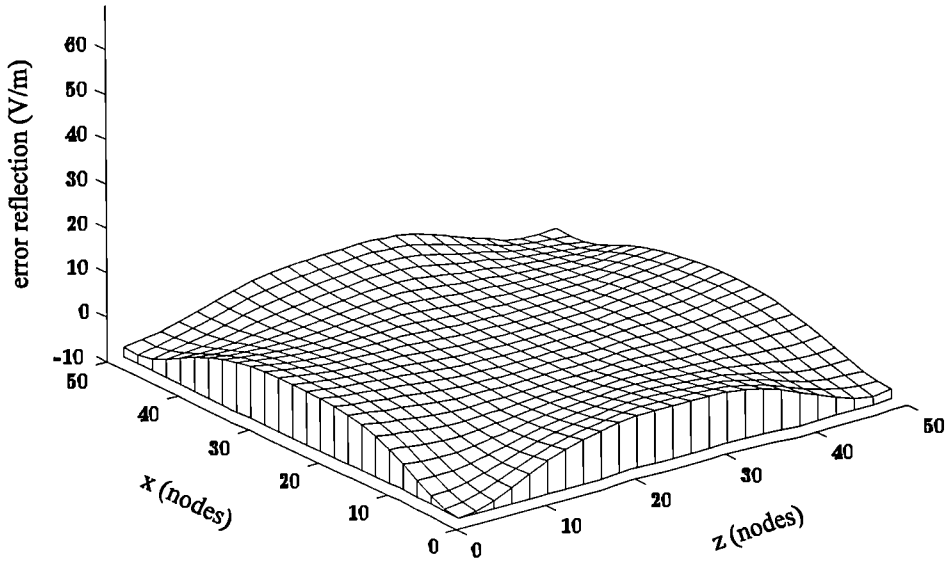

Figure 4.20: Snapshot of the error reflected waves at $n = 85$ of the small TLM network using the Liao et al. ABC of the third order and the DN approach.

4.20 Numerical implementation of 2D GPR models using TLM and FDTD

The implementation of the TLM and FDTD methodology described above into a computer program is considered in this section. The flow-charts for the TLM and FDTD GPR modelling programs are presented in Figures 4.22 and 4.23 respectively. Both algorithms are structured similarly and they have been constructed in a way that the same input file describing the geometry and parameters of a GPR model can be used for both the TLM and FDTD programs.

In evaluating the requirements in computer resources, the main concern considering a small computational environment (e.g Personal Computer) is the amount of physical memory that the programs require for the same GPR model. This is dominated by the storage requirements for the voltage pulses of the TLM nodes in the TLM network and the field quantities in the FDTD lattice. The following relations give an estimate of the amount of physical memory in bytes for a TLM and FDTD GPR model:

$$\text{bytes} = N_x \times N_z \times 5 \times \text{precision} \qquad \textbf{TLM} \tag{4.113}$$

$$\text{bytes} = N_x \times N_z \times 3 \times \text{precision} \qquad \textbf{FDTD} \tag{4.114}$$

where N_x and N_z are the number of TLM nodes or FDTD cells in the x and z directions

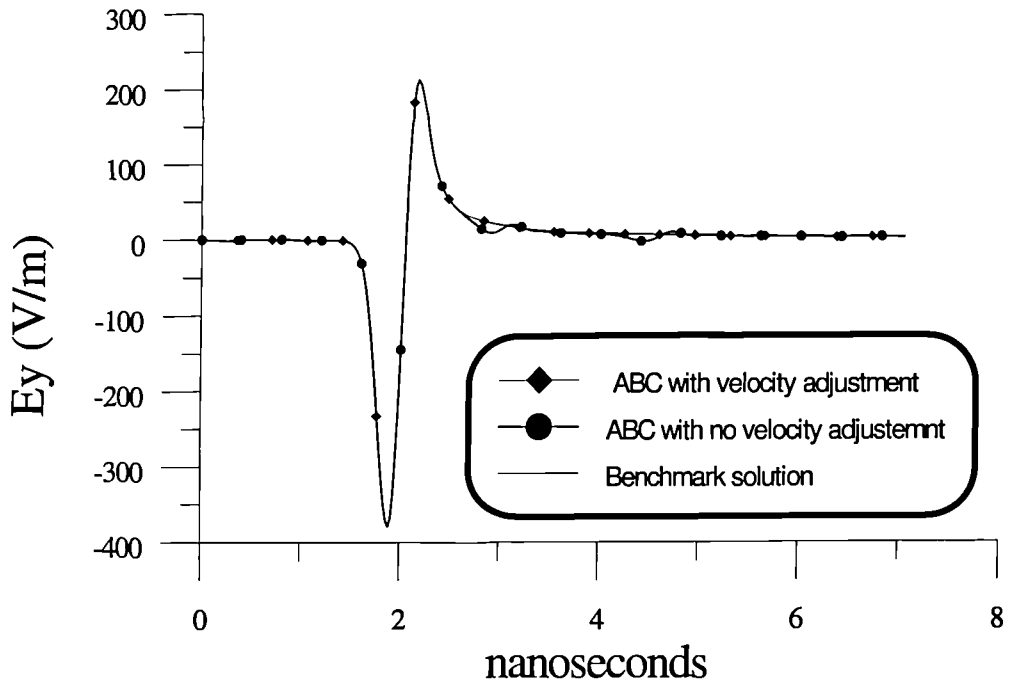

Figure 4.21: Effect of using the "wrong" velocity in the calculation of the ABC parameters. The simulated medium has parameters $\epsilon_r = 3$ and $\sigma = 0.01$ S/m. The response of a free-space Liao ABC is compared with the velocity adjusted ABC and a benchmark solution. The observation point is located at $(10\Delta l, 10\Delta l)$ with reference to the source.

respectively, and precision is the number of bytes required for the storage of a single real number. As is evident from (4.113) and (4.114), the FDTD model requires less computer memory than the TLM model.

4.21 Validation of the 2D TLM and FDTD algorithms for GPR modelling

The validation of the 2D TLM and FDTD algorithms is an important step of the modelling procedure. First, as will be examined in the next Chapter where results from the 2D GPR modelling are presented, the output of the numerical models is examined for physical reasonableness. Moreover, comparing the responses obtained with both models is another way of validating their correctness since they are based on different modelling concepts and their implementation leads to different algorithms. However, formally, the validation of the algorithms is performed by comparing the solution which they provide with available simple closed-form solutions.

The electromagnetic fields radiated by a line source located in free-space can be easily cal-

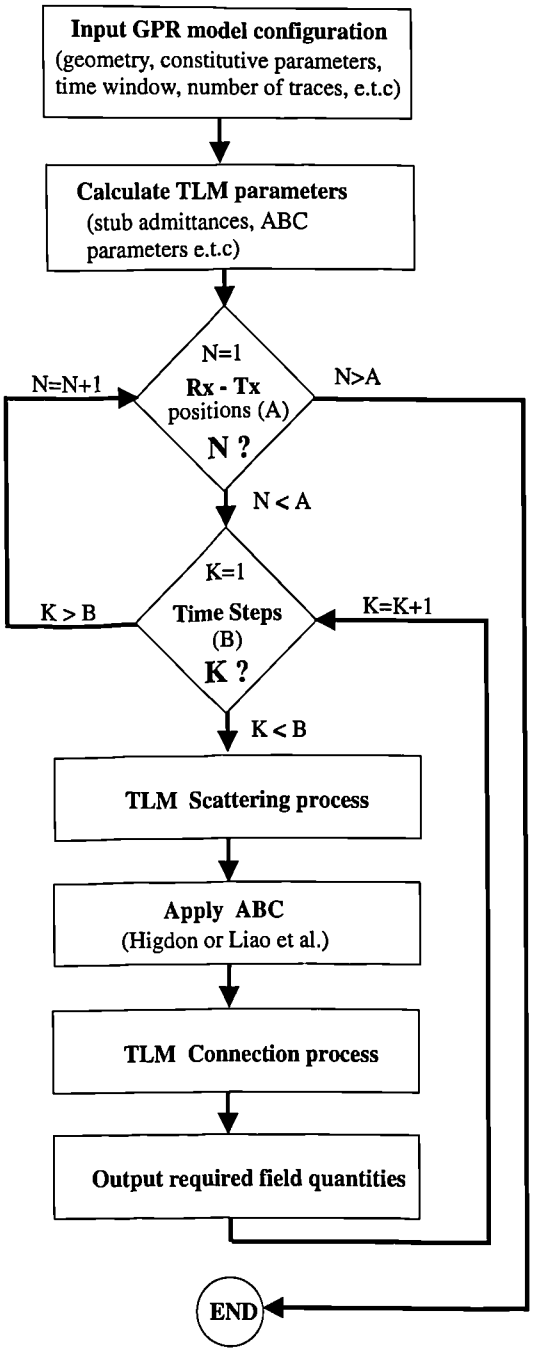

Figure 4.22: Flow-chart of the 2D TLM algorithm used for 2D GPR modelling.

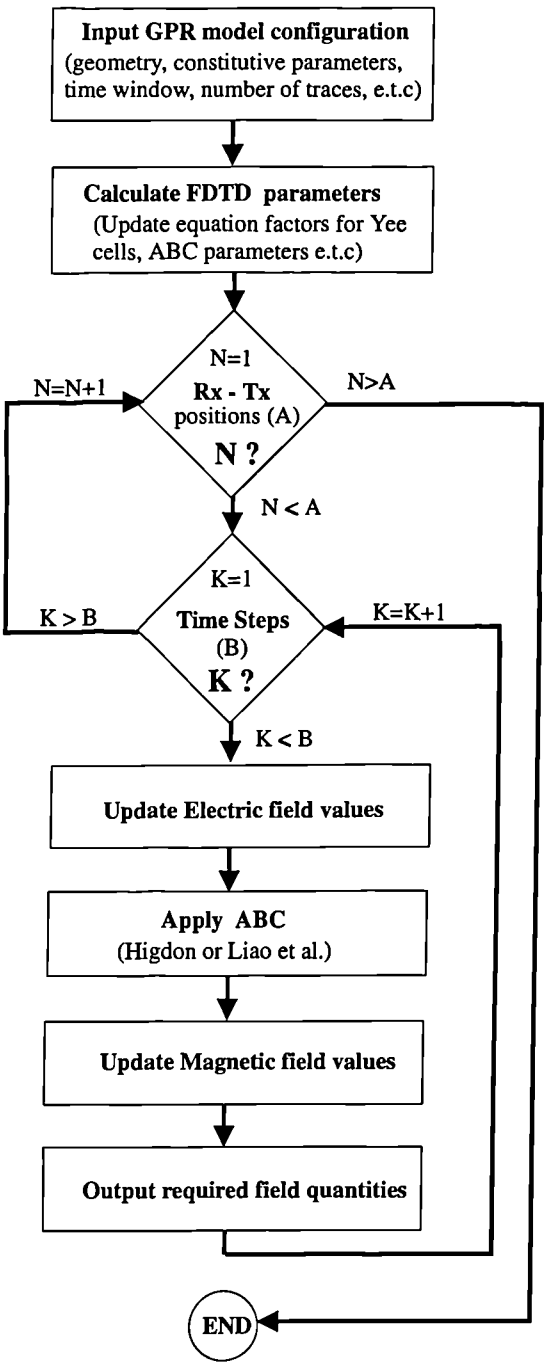

Figure 4.23: Flow-chart of the 2D FDTD algorithm used for 2D GPR modelling.

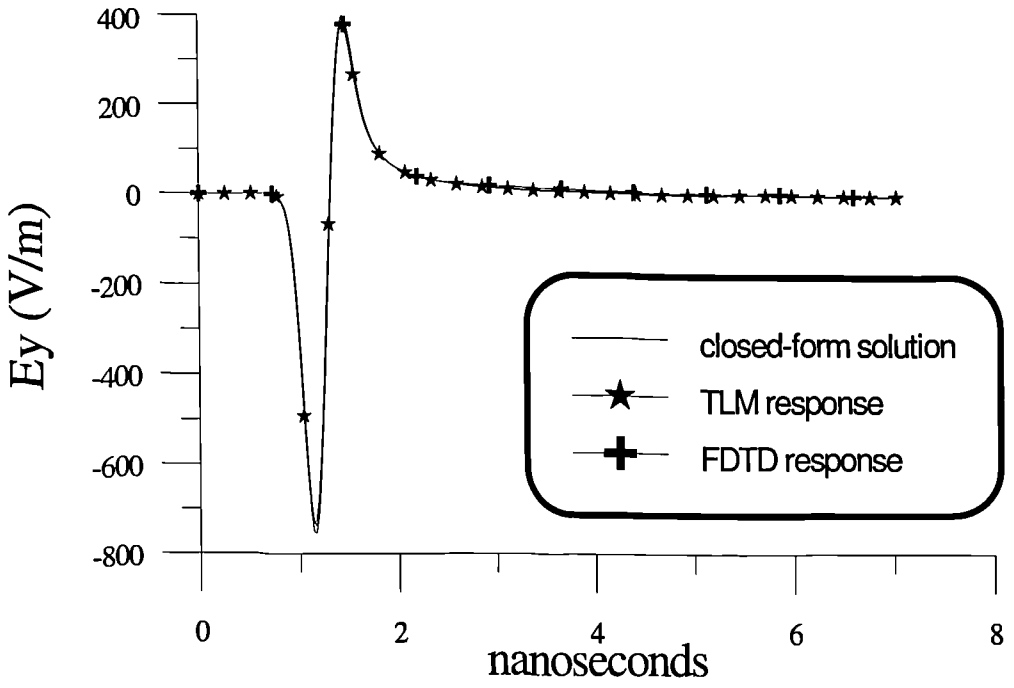

Figure 4.24: Comparison of the responses obtained by TLM and FDTD with a closed-form solution for a line source radiating in free-space.

culated using the corresponding scalar Greens function (Chew, 1990; Ward and Hohmann, 1987)

$$g(t,\rho) = \frac{1}{2\pi\sqrt{t^2 - s_0^2\rho^2}} H(t - s_0\rho) \tag{4.115}$$

where $s_0 = 1/c$ is the inverse of the velocity of light, ρ is the radial distance between the observation point and the source and $H(t - s_0\rho)$ is the Heaviside step function. Moreover, the Greens function for a line source radiating in a uniform lossy medium is (Chew, 1990; Sezginer and Chew, 1984)

$$g_l(t,\rho) = cH(ct-\rho)e^{-t/2\tau}\frac{\cosh(\sqrt{c^2t^2-\rho^2}/2c\tau)}{2\pi\sqrt{c^2t^2-\rho^2}} \tag{4.116}$$

where $\tau = \epsilon/\sigma$ and c is the velocity of light. In Figures 4.24 and 4.25 the responses obtained from 2D TLM and 2D FDTD are compared with the closed-form solutions is very good. The agreement between the numerical models and the analytical solutions. Although the TLM and FDTD models have the same propagation characteristics, the responses are not identical because of the different excitations of the two models. The current I(t) of the line source is assumed to have the form of a Gaussian pulse as:

$$I(t) = e^{(-\zeta(t-\xi\Delta t)^2)} \tag{4.117}$$

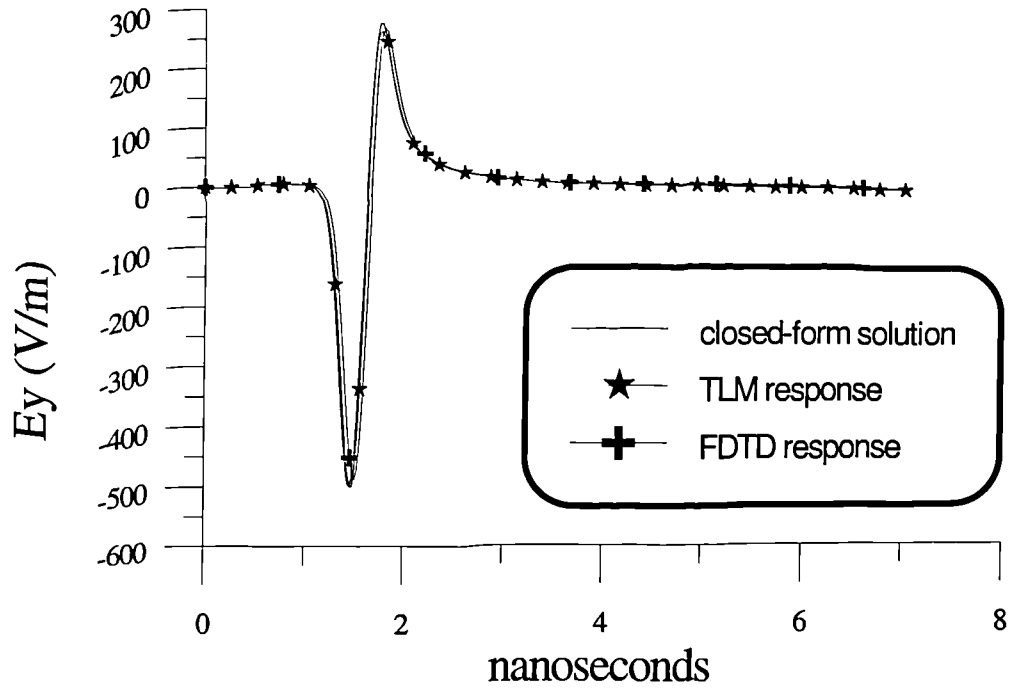

Figure 4.25: Comparison of TLM and FDTD responses with the closed-form solution of a line source radiating in a homogeneous medium with constitutive parameters $\epsilon_r = 3$ and $\sigma = 0.01$ S/m.

where $\zeta = (4/(\xi\Delta t)^2)$. Although any time function can be employed, a Gaussian pulse has been used because the energy which it contains above a certain frequency can be controlled easily by an appropriate choice of the parameter ξ and therefore the numerical dispersion error can be kept small.

Further, for responses in a uniform medium, the scattered electromagnetic field from a loss-free half-space due to a line source located above it has been obtained in closed-form by (Chew, 1990) using the Garniard-de Hoop method (de Hoop, 1960). In Figure 4.26, the response obtained from 2D TLM and 2D FDTD models for a line source located over a dielectric half-space are compared with the closed-form solution given in (Chew, 1990) and is evident that the agreement between these solutions is very good.

4.22 Discussion

In this Chapter, the methodology of 2D GPR modeling using the TLM and FDTD methods was presented. The basic concepts of the two methods were illustrated and the errors and limitations of the algorithms were examined. From the dispersion relation the similarities

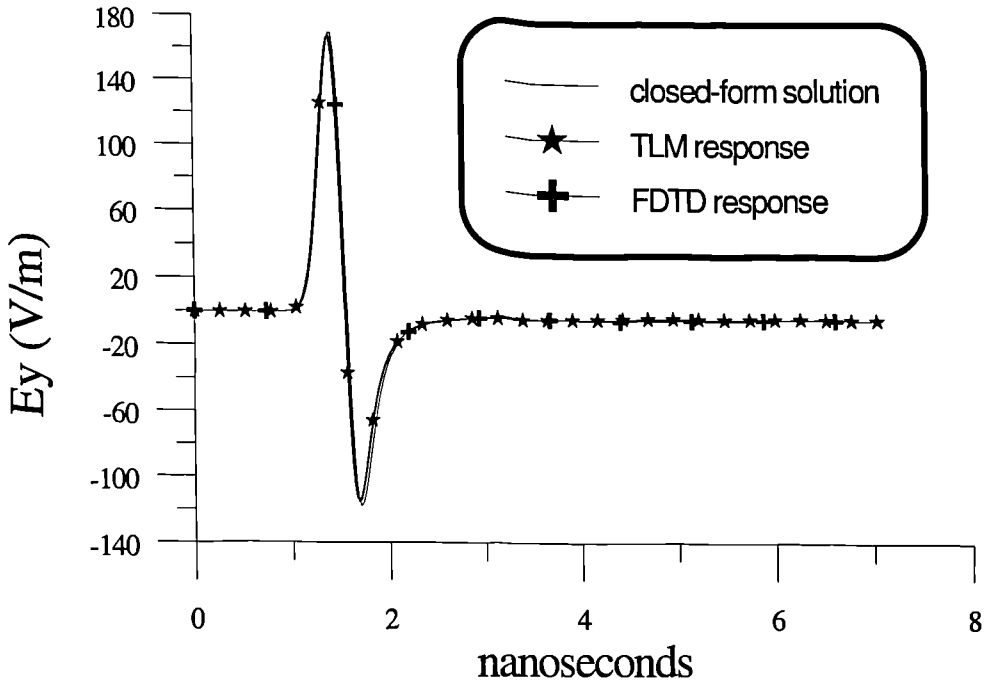

Figure 4.26: Comparison of the scattered electric field obtained by TLM and FDTD with the closed-form solution for the scattered electric field of a line source located over a loss-free half-space of $\epsilon_r = 3$. The source is located at $10\Delta l$ above the interface and the observation point is located at the same height and $10\Delta l$ away from the source.

of the two methods were discussed. The application of ABCs in FDTD was examined and their incorporation in TLM was introduced. A comparison of the performance of ABCs applied to TLM and FDTD was presented which revealed that in TLM the performance of ABCs is superior when compared with FDTD. Further, results from numerical experiments suggest that the "matched termination" ABC should be equivalent with the first order Higdon ABC when the latter is applied using the DN approach. By introducing better ABCs than the "matched termination" to the TLM method, its application to the GPR forward problem is possible without the need to introduce significant "white space" between the targets and the truncation boundaries. Issues of ABC stability and the procedures followed to overcome this problem were examined for both FDTD and TLM models. Finally, the numerical requirements of the two algorithms were presented and validation of the models using simple closed-form solutions was presented.

5

Two dimensional numerical modelling of GPR — PART II: Results

5.1 Introduction

The results from the application of the 2D TLM and FDTD methods to the modelling of GPR is the subject of this Chapter. Although the generality of the two methods does not put significant constraints on the composition or shape of the GPR targets that can be examined, there is an obvious need to limit the scope of this presentation. Therefore, an attempt has been made to restrict the models presented to simple cases of which the GPR responses are known either by measurements or by intuitive analysis. This serves to illustrate the modelling procedure as well as to examine some fundamental issues of GPR using numerical modelling. These include the attenuation and dispersion of GPR signals and the GPR resolution.

The influence of the constitutive parameters of the subsurface media has been the subject of several investigations (Arcone 1981, Turner, 1994). However, these works are mainly restricted by the assumptions of a one dimensional model and are concerned only with the

propagation of GPR signals in a given medium and not on the actual GPR response from a realistic GPR target which, however, can be easily obtained with the 2D TLM and FDTD models. Further, by incorporating a Debye relaxation model in the FDTD algorithm, the attenuation and dispersion of the GPR signal when the constitutive parameters of the subsurface media are frequency dependent are investigated.

In examining attenuation and dispersion, it is adequate to consider only a single trace obtained by one source and receiver pair, but the simulation of GPR signatures obtained as a set of synthetic GPR scans is more important in examining resolution and more complex models. Finally, a comparison between real GPR data measured over a culvert at the archaeological site of *Fountains Abbey* (England) are compared with the response obtained from a 2D model.

In the interest of minimizing repetition in the description of the models some common features of the modelling procedure are presented here. Following the usual notation in GPR work, the source and receiver are denoted as Tx and Rx respectively. For most of the results presented, the current of the line source is chosen to be the second derivative of a Gaussian pulse normalized to unit amplitude given by the following formula:

$$I(t) = \sqrt{\frac{e}{2\zeta}} \frac{d}{dt} [e^{-\zeta(t-t_0)^2}] \tag{5.1}$$

where $\zeta = 2\pi^2 f_s^2$, f_s is the peak frequency of the pulse's amplitude spectrum and $t_0 = 1/f_s$ is a time delay introduced in order for the pulse to start smoothly at zero time. This source function has been chosen because of its smoothness in both the time and frequency domains. In Figure 5.1, the source waveform is illustrated as well as its normalized amplitude spectrum for a peak frequency of $f_s = 600$ MHz. Although any other waveform can be used, it is essential to employ pulses which do not contain significant energy at wavelengths where numerical dispersion will significantly affect the solution obtained from the models. For simplicity, this type of excitation will subsequently be referred to as "ricker source" since it produces a propagating ricker wavelet commonly used in seismic modelling (Sherrif, 1991). As is evident from Figure 5.1, the pulse used to simulate the current of the line source smoothly rises from zero, attaining its first maximum at a later time. To facilitate the measurement of time intervals between events in GPR signatures it is easier to set as a time reference point the instant when the source pulse attains its positive maximum value instead of the actual "zero time" of the initiation of the source. Another simple process used to compensate for the finite distance between the source and receiver is a static time-shift, which can be introduced to the simulated data and is calculated as

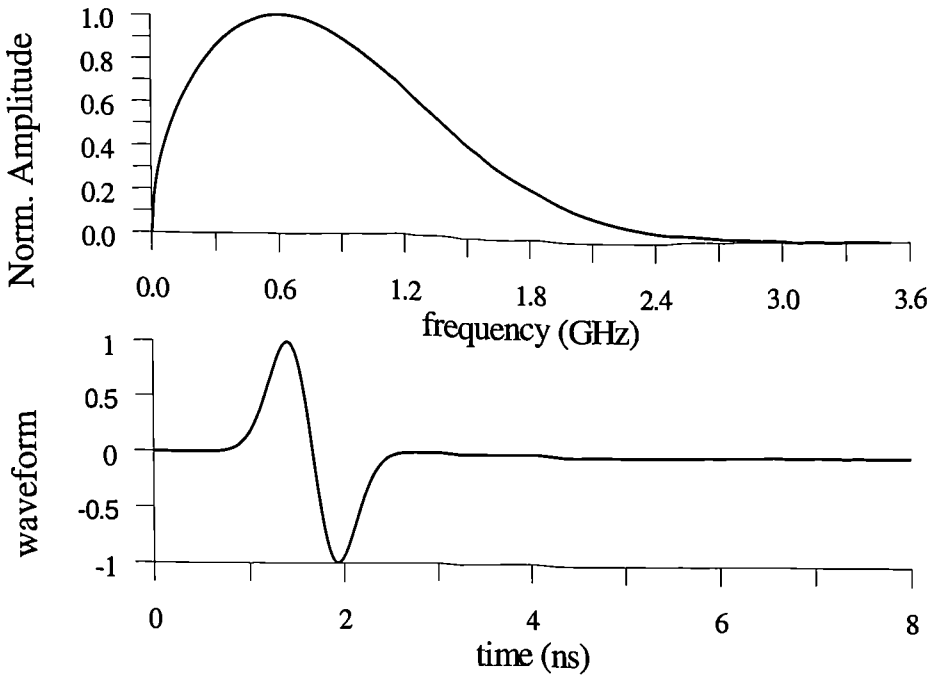

Figure 5.1: Normalized amplitude spectrum (Up) and time waveform (Bottom) of the "ricker source" when $f_s = 600$ MHz.

the time taken by the direct air wave to reach the receiver. This process henceforth is referred to as *time-zero adjustment.*

Since modelled GPR responses resemble real ones, the initial part of the response which is due to the direct waves from the source to the receiver has a significantly greater amplitude than the actual reflections recorded from the subsurface targets. Therefore, to facilitate the presentation of the simulated data without using "gain functions", as commonly employed in actual GPR data presentation, in some cases the direct waves are suppressed either by "thresholding" or by subtracting the response of the model without the target (half-space response). Thus presenting only the simulated response due to the target(s) (scattered field).

There will be no attempt to assign specific geological descriptions to the various media used in the models. Although there are few types of media encountered in GPR surveying where a set of constitutive parameters are commonly used to describe them (e.g. dry sand), the GPR models developed for this work are applicable to a wide range of different media and it will be rather restrictive to use specific media descriptions, since that could easily be accomplished if needed in any particular application. Finally, details of the technical characteristics of the models used to obtain the synthetic responses are presented in Table

5.1 at the end of the Chapter.

5.2 Line source over a half-space

The fields of a line source, which represents the Tx GPR antenna in the 2D models, located in close proximity to a half-space, are of interest in order to examine how the models simulate the propagation of GPR pulses in the subsurface. This can be achieved by examining the spatial distribution of the electric field in the model at a particular time instant using a monochromatic source. Therefore, for this case, the current of the line source has a continuous sinusoidal variation in time with a frequency of 600 MHz. The time instant when the observation is made is chosen at 10 cycles of the source's frequency in order for the initial transient field to exit the computational domain. Further, it is assumed that there are no losses ($\sigma = 0$) in the half-space.

The 2D TLM model (**A** in Table 5.1) used, comprised of 100 x 100 nodes simulating a physical space of $1m^2$, was divided in two halves. The upper half simulates free space and the lower half simulates the dielectric medium representing the half-space. The TLM network was truncated using a second order Liao et al. ABC as was discussed in the previous Chapter. The results are presented in the form of snapshot images taken over the entire TLM network to illustrate the spatial distribution of the fields in the model and are obtained by sampling the electric field at every node of the TLM network when the simulated time reaches 10 cycles of the source excitation function. Further, the electric field for each snapshot is normalized to unity.

In Figures 5.2 and 5.3 these snapshot images are presented. The snapshots in Figure 5.2 are obtained with the source located on the interface between air and the half-space. The values of the relative permittivity (ϵ_r) for the three snapshots are 3, 6 and 9. The snapshots in Figure 5.3 are obtained when the source is located at a height $d = 0.1\lambda_0$ above the interface for the same model configuration (values of the relative permittivity) as the ones in Figure 5.2. λ_0 is the free space wavelength of the 600 MHz sine wave (0.5 metres). Considering these snapshots, some useful conclusions about the propagation of GPR pulses in the 2D model can be reached:

A. There are two distinct regions of cylindrical wave propagation above and below the

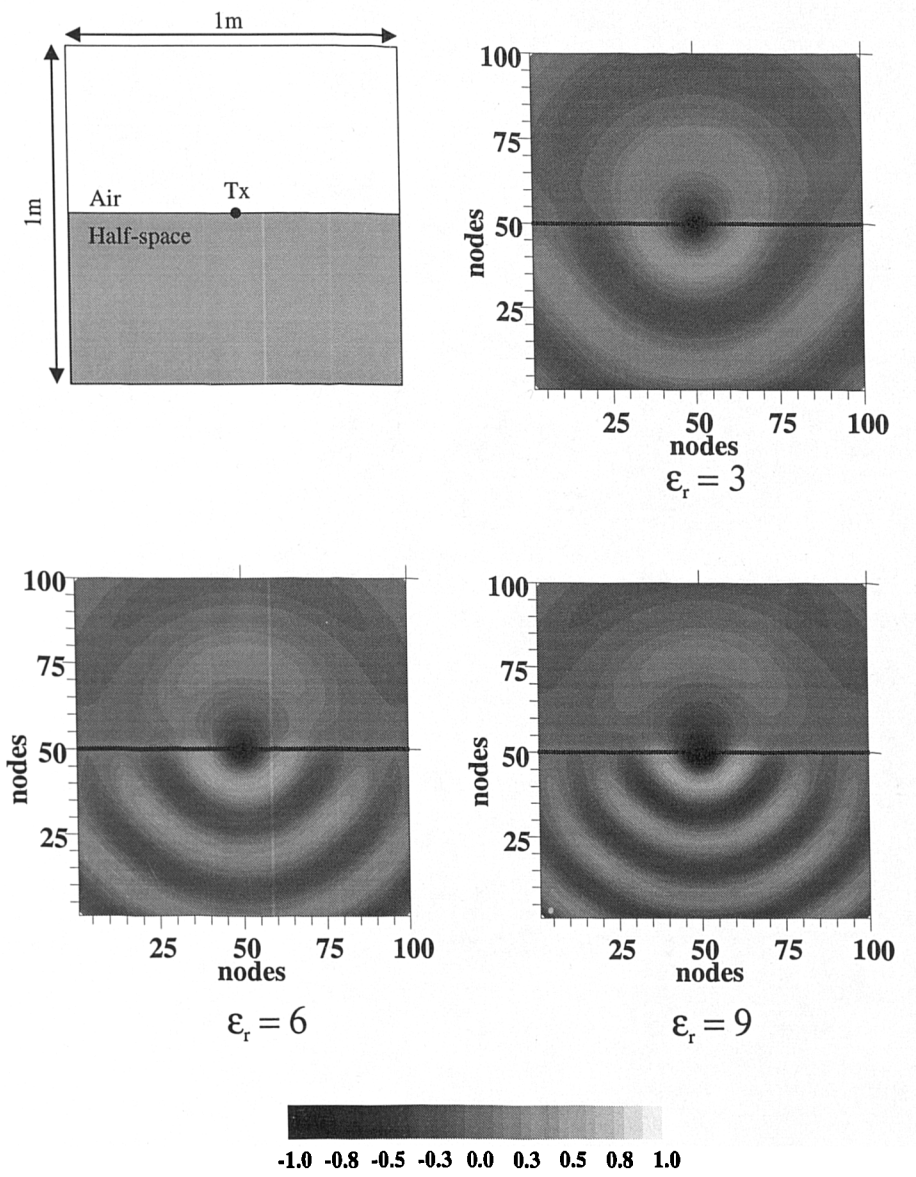

Figure 5.2: Snapshot images of the normalized electric field in a TLM half-space model for three different values of permittivity. The source is located on the interface and is a CW with frequency of 600 MHz. The snapshots are obtained after 10 cycles of the source's excitation.

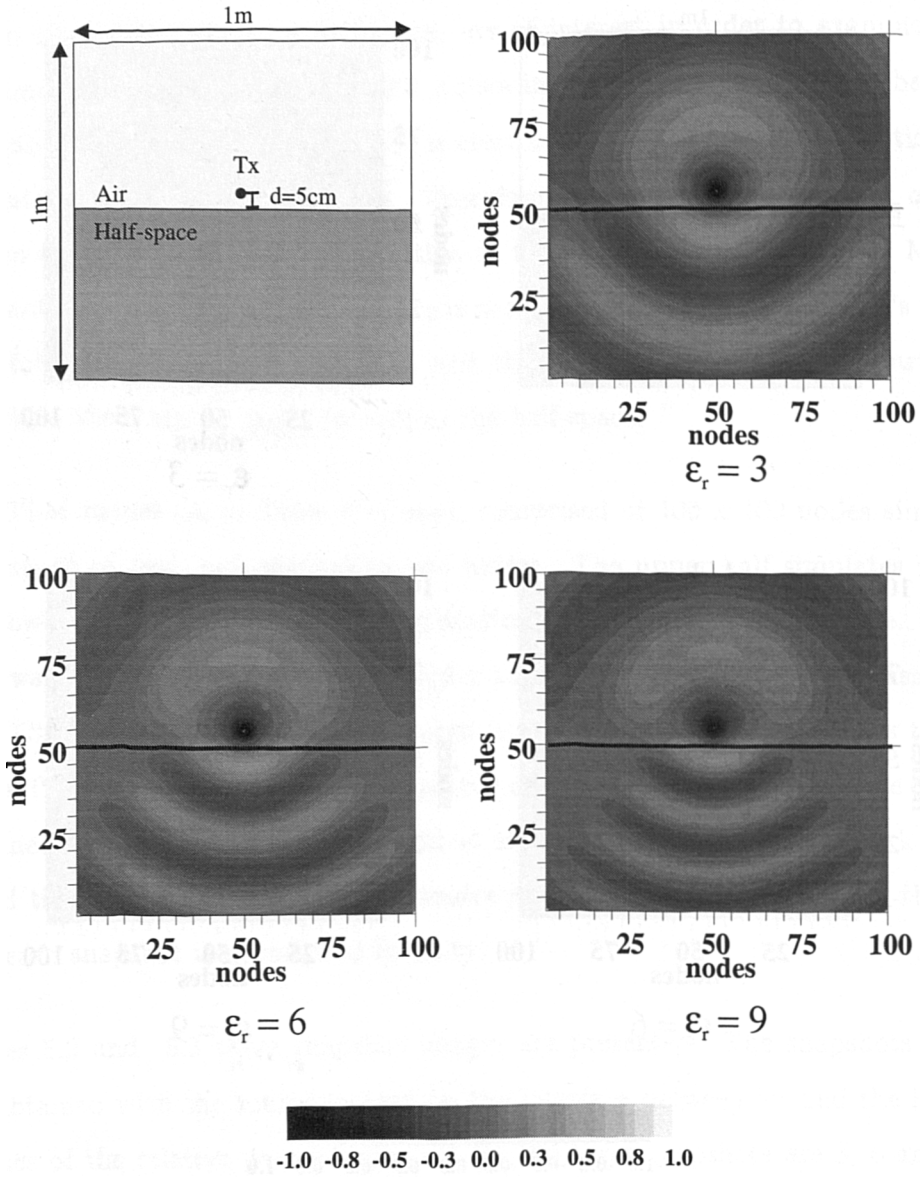

Figure 5.3: Snapshot images of the normalized electric field in a TLM half-space model for three different values of permittivity. The source is located at a height d = 5 centimetres above the interface and is a CW of 600 MHz. The snapshots are obtained after 10 cycles of the source's excitation.

interface. Propagation in the half-space results in shorter wavelengths as the value of relative permittivity is increased.

B. Since waves propagate in the dielectric half-space with a shorter wavelength than the ones in air, close to the interface the phases of the cylindrical waves do not match with each other. To compensate for this, lateral waves are generated in each region (Chew, 1990; Annan, 1973). The lateral wave in the dielectric half-space is known as the *head* or *flank* wave.

C. Raising the source above the interface has an effect on the spatial shrinking of the region of cylindrical propagating fields in the half-space. Further, the relative amplitude of the fields in the air, when compared with one of the fields in the half space, is increasing as the source is raised above the half-space. Therefore, situating the source at the interface results in a more efficient coupling of the GPR pulse into the subsurface. However, the spatial distribution of the field indicates that the directionality is reduced. Therefore, it is evident that the model is, at least qualitatively, in agreement with the observations of Smith (1984) regarding the directive properties of dipole antennas located over a dielectric half-space (see Chapter 3)

Finally, another important observation concerning the modelling procedure is that no artificial reflections are observed in the snapshots demonstrating the very good performance of the Liao et al. ABC introduced in the previous Chapter in 2D TLM.

5.3 2D GPR models of common-source gathers (CSG)

Under the assumption of a horizontally stratified earth, CSG[1] and common mid-point (CMP) sections are used in GPR surveying to obtain information about the variation of velocity with depth for the GPR signals. Theoretically, CSG and CMP sections are identical for a horizontally stratified model (Yilmaz, 1987). Therefore, in an idealized model the one which requires the least computational effort can be used. The obvious choice is the CSG since it involves only one source position, and therefore the complete gather can be obtained with a single computation. Although the assumption for a horizontally stratified earth is often not valid in real situations, useful results can still be obtained from CSG or CMP sections (Telford et al., 1990). The procedure for the estimation of the distribution of velocities of the GPR signals using a CSG or a CDP section is analogous

[1]the term *common source gather* (CSG) is used here instead of CDP or WARR

to the one used in seismics and will not be repeated here since it can be found in standard seismic texts (Telford et al., 1990).

Consider a 2D FDTD model (**B** in Table 5.1) illustrated in Figure 5.4 which comprises one horizontal layer and a semi-infinite one. The layer has a thickness of 0.5 metres, relative permittivity ($\epsilon_r = 4$) and conductivity ($\sigma = 0.01$) (S/m). The semi-infinite layer has constitutive parameters ϵ_r =9 and σ =0.01 (S/m). A CSG is obtained by situating the source at the left end of the model at a distance of 0.3m (30 cells) from the truncation boundary where a third order stabilized Liao et al. ABC is applied. The current of the line source is a 600 MHz ricker source and is located at a height $d = 0.1\lambda_0$ (5 centimetres) above the air-earth interface. The receivers (Rx) are located evenly on a line 4.2 metres long on the air-earth interface. The separation between the receivers is 0.1 metres and the first receiver is located 0.25 metres away from Tx.

The synthetic CSG section is obtained by sampling the electric field on the receivers. Its trace in the synthetic CSG is normalized to its maximum amplitude to aid the presentation. Observing the signals in the CSG, different types of waves can be distinguished. As they are marked on the CSG in Figure 5.4:

A) These signals correspond to the direct *air wave* travelling at the speed of light.

B) These signals are due to the direct *ground wave* travelling at a speed determined by the constitutive parameters of the first layer. It has a different polarity from the direct wave (180 degrees phase shift) which is consistent with observations in measured GPR CDP sections (Annan, 1985).

C) These signals are associated with the reflected waves from the interface between the two layers and form a semi-hyperbola.

D) These signals correspond to *air waves* propagating close to the air-earth interface and are the result of reflections close to the critical angle of waves incident from the subsurface, and have first been reflected from the interface between the two layers.

M) These signals are due to secondary (multiple) reflections between the air-earth interface and the semi-infinite layer.

The analysis of these responses can provide information about the velocity of propagation

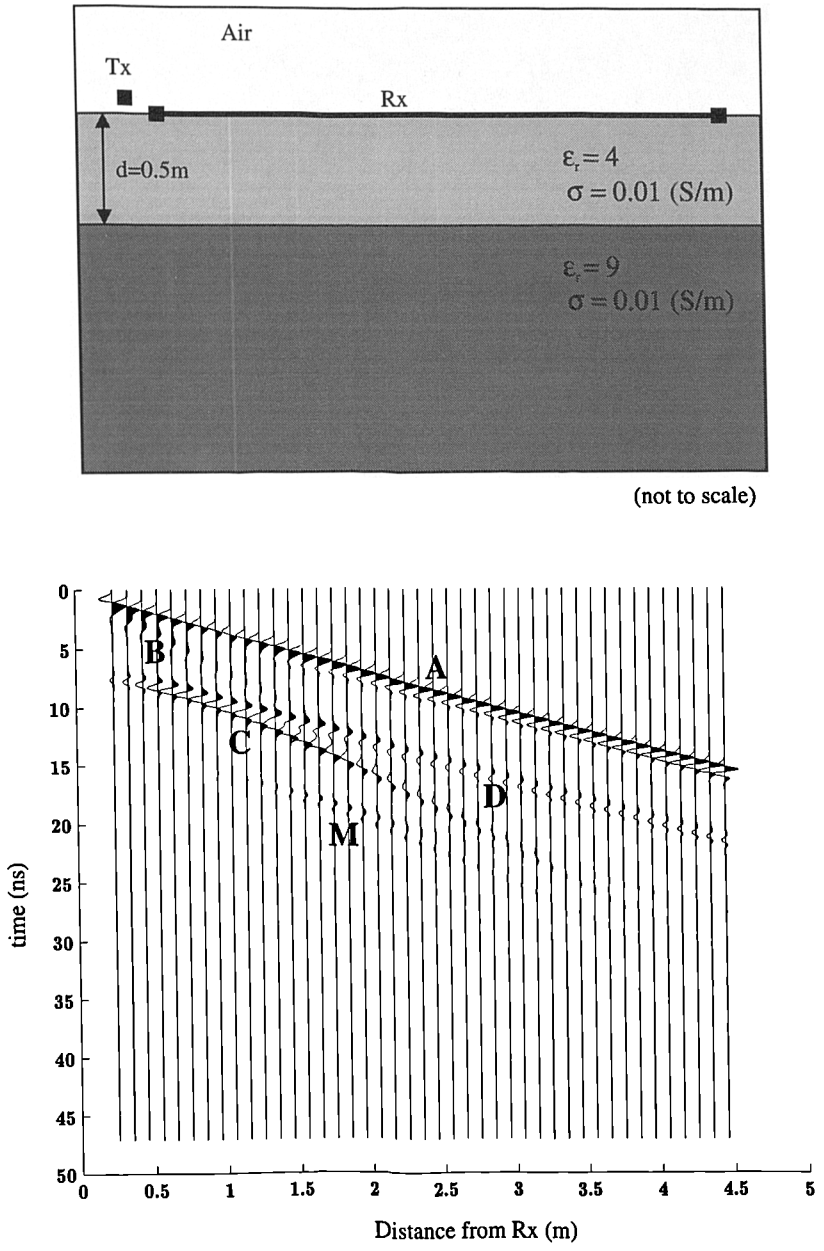

Figure 5.4: Synthetic GPR CSG consisting of 43 traces (bottom) and schematic of the 2D FDTD model used (top). The Tx is located at a height of 5 centimetres above the air-earth interface and the line of receivers has a length of 4.2 metres with the first one located 25 centimetres away from Tx. (Explanation of the labels on the CSG is given in the text)

in the subsurface using a (t^2–z^2) (time squared–offset squared) plot of the arrival time of these signals (Telford et al., 1990). Further, the velocity of the direct ground wave which gives an estimate of the velocity for the first layer can be obtained irrespective of the assumption of a horizontally layered model, provided that strong, lateral variations in the constitutive parameters of the top layer are not encountered.

In Figure 5.5, the CSG of a 2D FDTD model is shown using the same configuration as the one described above but with the constitutive parameters of the layers interchanged. The relative permittivity of the top layer is now $\epsilon_r = 9$ and of the semi-infinite layer is $\epsilon_r = 4$. In the CSG the events are marked as in the previous case. Reflections from the interface between the two layers are registered at a later time as expected. However, in this CSG there are events which are not observed in the previous model. These events marked as **E** correspond to the arrivals of waves which are incident from the first to the second layer with an angle close to the critical angle (between the two layers) propagate along their interface with the velocity of the second layer and arrive earlier at the surface than direct reflected waves.

5.4 Modelling attenuation and dispersion in GPR signals

Examining the propagation of GPR signals in a loss free dielectric environment provides an insight into the detection mechanism of GPR albeit for an ideal case. A realistic model should include the effects of attenuation and dispersion of the GPR signals as they propagate into the subsurface. In examining these phenomena, it is of interest to distinguish between the effects on GPR signals when the subsurface medium is described with frequency independent constitutive parameters and when these are a function of frequency. Although in practice, the constitutive parameters of media encountered in GPR surveying exhibit a dependence on frequency, this dependence may not be strong over the specific frequency range or "window" of interest in GPR. As was discussed in Chapter 3, for the GPR frequency range is it usually safe to assume that the real part of the complex permittivity is independent of frequency and that the imaginary part is, in many cases, a linear function of it. Further, it has been suggested that a Debye relaxation model can describe such variations of the complex permittivity. This type of variation of the constitutive parameters has been ascribed mainly to the presence of water (see Chapter 3).

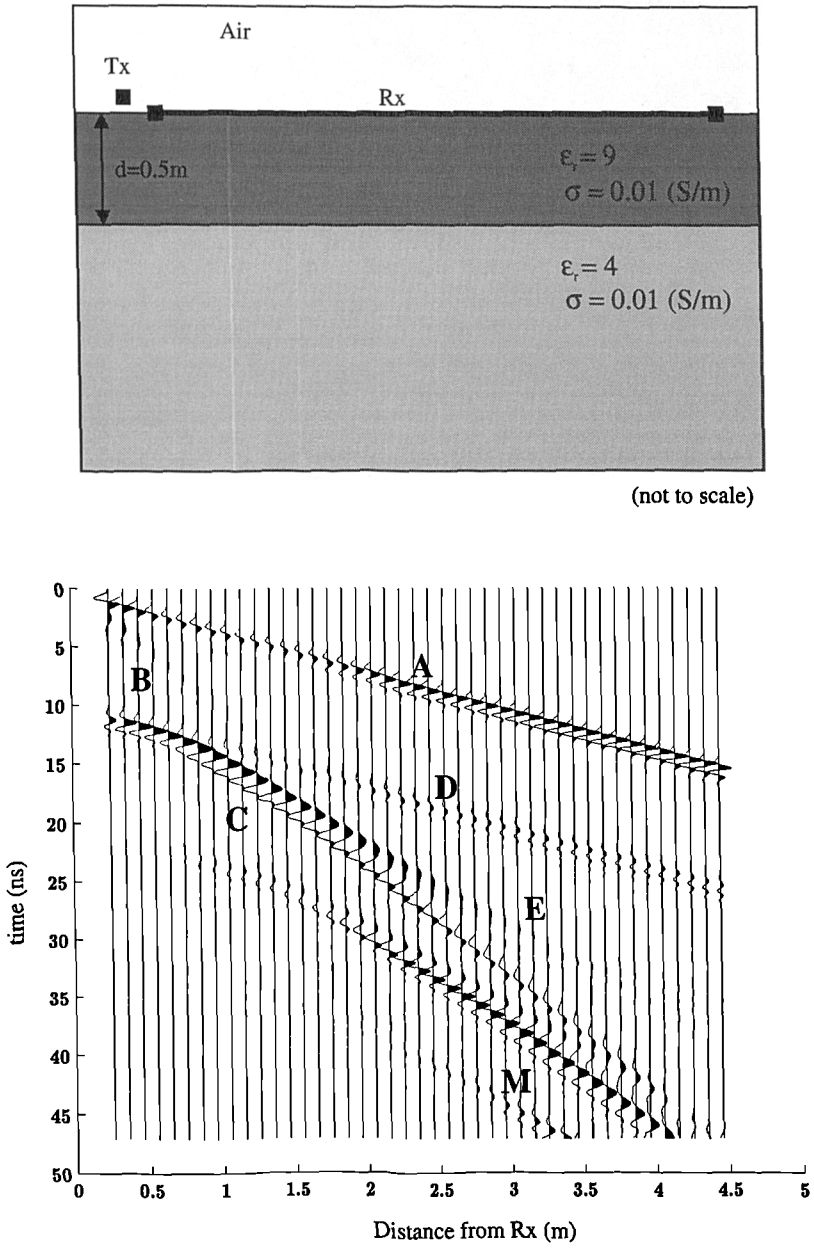

Figure 5.5: Synthetic GPR CSG consisting of 43 traces (bottom) and schematic of the 2D FDTD model used (top). The Tx is located at a height of 5 centimetresm above the air-earth interface and the line of receivers has a length of 4.2 metres with the first one located 25 centimetres away from Tx. (The explanation of the labels on the CSG is given in the text)

5.4.1 Frequency independent constitutive parameters

When the constitutive parameters are considered to be frequency independent, the effects of attenuation and dispersion can be examined by considering the loss tangent for the frequency independent constitutive parameters ϵ and σ

$$\tan\delta = \frac{\sigma}{\omega\epsilon}$$

the best scenario for GPR is when the loss tangent is $\ll 1$, as wave propagation prevails over diffusion and both the attenuation and velocity are essentially frequency independent. Further, the GPR signals will not suffer from dispersion. When the loss tangent is $\gg 1$ diffusion of the electromagnetic energy is the most pronounced phenomenon and GPR is not generally applicable. However, in the intermediate range when the loss tangent ≈ 1 it is not safe to assume that attenuation and velocity are frequency independent and, as well as attenuation, dispersion, will affect the GPR signals. An important parameter which represents the extent to which dispersion will affect the GPR signals is the frequency for which the loss tangent is equal to unity for a particular set of constitutive parameters. This transition frequency (Keller, 1987) is

$$f_t = \frac{\sigma}{2\pi\epsilon} \tag{5.2}$$

The variation of the attenuation constant, phase velocity and loss tangent with frequency in a medium with constant frequency independent relative permittivity ($\epsilon_r = 4$) for different values of conductivity (σ = 0.001,0.01,0.1 (S/m)) is illustrated in Figure 5.6. If in a model the amplitude spectrum of the source's excitation[2] contains significant energy around the transition frequency then, apart from signal attenuation, dispersion should be apparent in the received signal. The effects of attenuation and dispersion of the GPR signal for the set of constitutive parameters used in Figure 5.6 are presented in Figure 5.7 using a 2D TLM model (C in Table 5.1) of a perfectly conducting metal cylinder of radius r = 15 centimetres, buried at a depth of 0.5 metre. The simulated responses from the cylinder to a 600 MHz ricker source have been obtained with a separation between Rx and Tx of 0.25 centimetres, both located 5 centimetres above the interface and with the Tx–Rx pair centered above the target. The constitutive parameters of the subsurface medium where the cylinder is located are varied as in Figure 5.6 ($\epsilon_r = 4$, σ = 0.001, 0.01, 0.1 (S/m)). The first simulated response corresponds to the response from the cylinder when $\sigma = 0$ and serves as a reference for the ideal loss-free case. The following three simulated

[2]In an actual GPR system the system's bandwidth should be considered instead

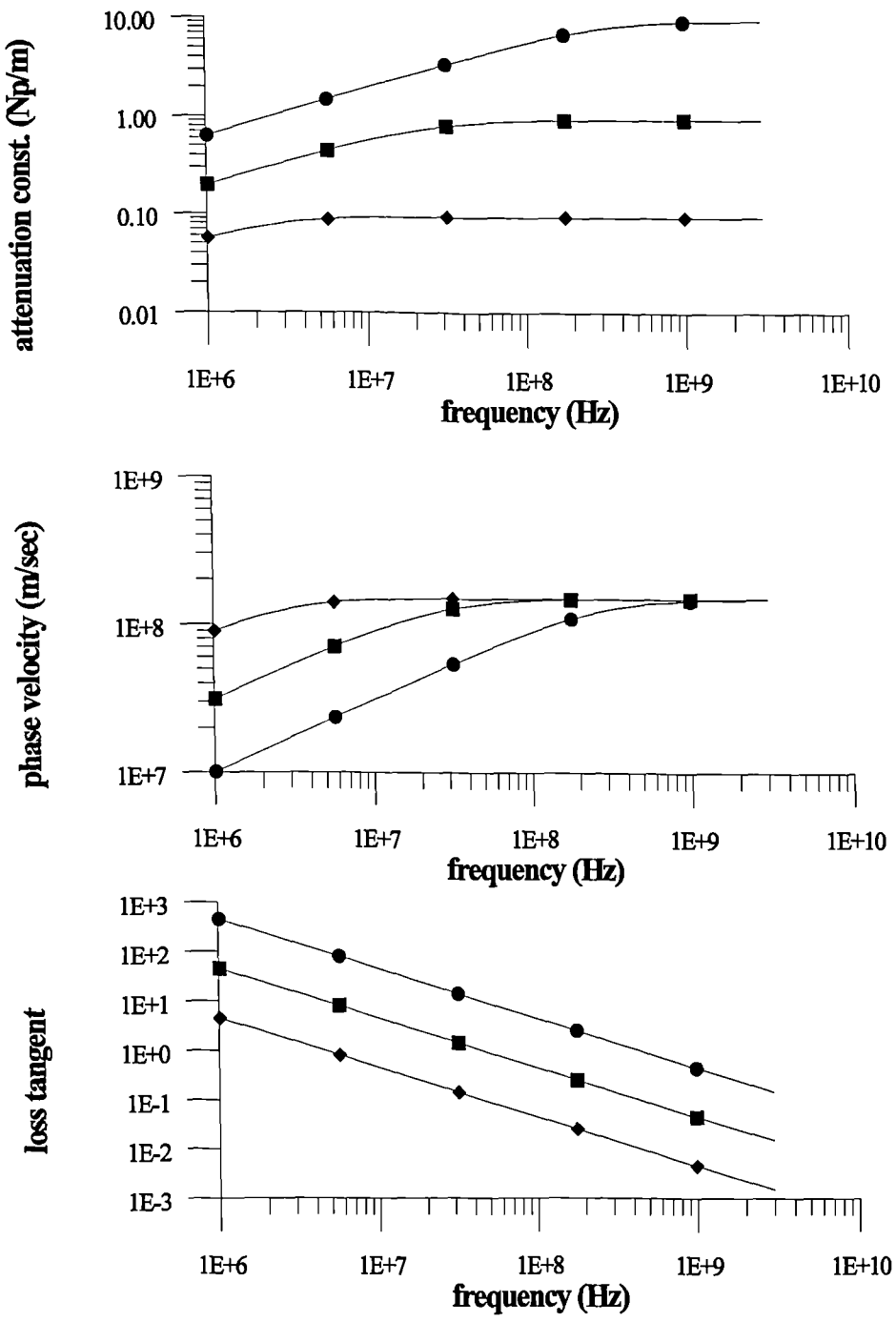

Figure 5.6: Variation of attenuation constant, phase velocity and loss tangent with frequency for a medium with frequency independent relative permittivity $\epsilon_r = 4$ and conductivity $\sigma = 0.001$ (S/m) (diamonds) , 0.01 (S/m) (squares) and 0.1 (S/m) (circles).

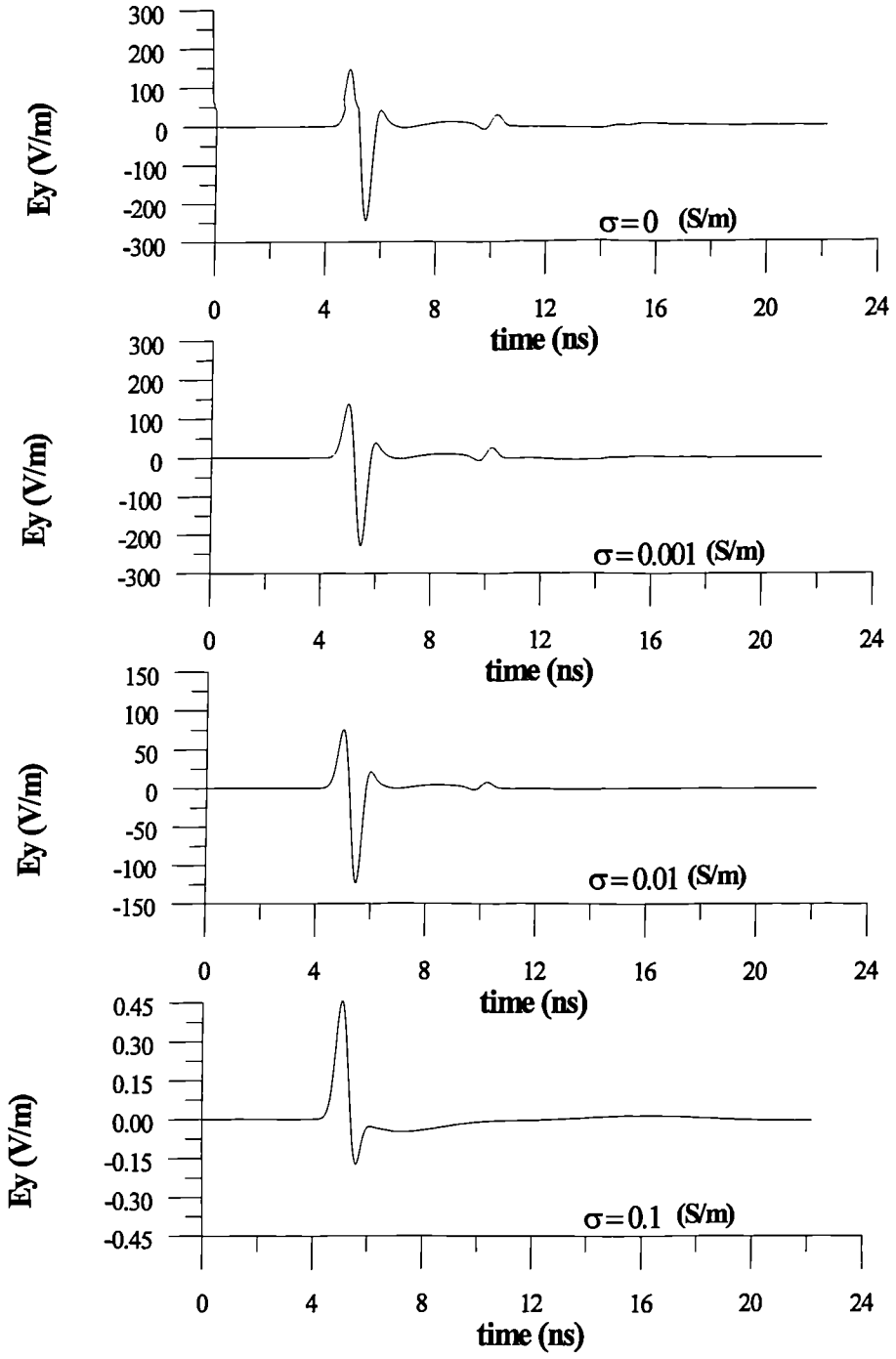

Figure 5.7: Simulated responses (reflected field only) from a perfectly conducting metal cylinder buried at a depth of 0.5 m. The relative permittivity of the host medium is set to $\epsilon_r = 4$ and the conductivity (σ) is varied. (Note the varying axis scales.)

responses are obtained for the three different values of conductivity (σ = 0.001,0.01,0.1 (S/m)). In examining the simulated responses for $\sigma = 0.001$ and 0.01 (S/m), a reduction in the amplitude in the received response is observed but the shape of the pulse has not been changed, which indicates that there are no effects associated with dispersion. The last response, obtained when $\sigma = 0.1$ (S/m), however, is significantly different from the rest since as well as the strong signal attenuation the shape of the pulse has been altered. This is the effect of dispersion due to the variations of attenuation and phase velocity with frequency. The transition frequency for this case is $f_t = 450$ MHz.

5.4.2 2D GPR model with frequency dependent constitutive parameters

As was examined in the previous section, dispersion effects can occur even if the constitutive parameters are assumed to be frequency independent, and will depend on the value of the transition frequency for a given set of medium parameters. From the discussion in Chapter 3, it is suggested that the frequency dependence of the constitutive parameters of media often encountered in GPR surveys can be described by a Debye relaxation model for permittivity which, repeated here for convenience, is:

$$\tilde{\epsilon}(\omega) = \epsilon_\infty + \frac{\epsilon_s - \epsilon_\infty}{1 + j\omega\tau} \tag{5·3}$$

where $\tilde{\epsilon}(\omega)$ is the complex permittivity; a function of frequency, τ is the relaxation time, ϵ_∞ is the value of permittivity when $\omega \to \infty$, and ϵ_s is the value of permittivity when $\omega \to 0$. In the following, the modifications required to incorporate a Debye relaxation model into the FDTD algorithm are discussed. The incorporation of such a model in 2D TLM has been recently described by Menezes and Hoefer (1994; 1996). However, since the FDTD formulation is more straightforward, this has been chosen in this work.

Equation, (5·3) could be written as:

$$\tilde{\epsilon}(\omega) = \epsilon_0\epsilon_{r\infty} + \epsilon_0\chi(\omega) \tag{5·4}$$

where $\chi(\omega)$ is the frequency domain electric susceptibility (Kunz and Luebbers, 1993). In the time domain the relation between the electric flux density and the electric field intensity becomes (Elliot, 1966):

$$\mathbf{D} = \epsilon_0\epsilon_{r\infty}\mathbf{E} + \epsilon_0 \int_0^t \mathbf{E}(t-\Lambda)\chi(\Lambda)d\Lambda \tag{5·5}$$

where $\chi(\Lambda)$ is the time domain electric susceptibility. The direct implementation of (5.5) in a time domain model is very difficult since it involves storing the time history of the electric field intensity at every FDTD cell which is part of the Debye medium. However, for a class of relaxation mechanisms there are efficient ways to overcome this problem (Luebbers et al., 1991; Bui et al., 1991;, Luebbers and Hunsberger, 1992). There are two different approaches of incorporating a Debye relaxation in the FDTD algorithm. The first, introduced by Luebbers et al. (1991) is the *recursive convolution* (RC) method and the second is the *auxiliary differential equation* (ADE) method (Kashiwa and Fukai, 1990; Gandhi et al., 1993).

The RC method is based on the functional form of the time domain electric susceptibility for a medium with a Debye relaxation. This is obtained as the Fourier transform of $\chi(\omega)$ and is (Kunz and Luebbers, 1993)

$$\chi(t) = \frac{\epsilon_{rs} - \epsilon_{r\infty}}{\tau} e^{-t/\tau} U(t) \tag{5.6}$$

where $U(t)$ is the Heaviside step function. Luebbers et al. (1991) noticed that the convolution required by (5.5) could be done recursively because of the exponential function in (5.6) which requires only the additional storage of one variable per FDTD cell for the Debye medium.

The ADE method is based on the frequency domain relation (Gandhi et al., 1993)

$$\mathcal{D} = \tilde{\epsilon}(\omega)\mathcal{E} \tag{5.7}$$

The basic principle of the ADE approach is to formulate an FDTD update equation for $\mathbf{D}$ from Maxwell's curl equation

$$\nabla \times \mathbf{H} = \frac{\partial \mathbf{D}}{\partial t} \tag{5.8}$$

and the required values of $\mathbf{E}$ can be obtained by using 5.7 and the definition of $\tilde{\epsilon}(\omega)$

$$\mathcal{D} = \epsilon_\infty + \frac{\epsilon_s - \epsilon_\infty}{1 + \jmath\omega\tau}\mathcal{E} \tag{5.9}$$

multiplying both sides of equation (5.9) by $(1+\jmath\omega\tau)$ and transforming in the time domain results in a differential equation relating $\mathbf{D}$ and $\mathbf{E}$

$$\mathbf{D} + \tau\frac{\partial \mathbf{D}}{\partial t} = \tau\epsilon_\infty\frac{\partial \mathbf{E}}{\partial t} + \epsilon_s\mathbf{E} \tag{5.10}$$

which can be conveniently discretized using central differences as described in the previous Chapter to obtain the required value of $\mathbf{E}$. The only additional storage requirement is

for the value of $\mathbf{D}$ in each FDTD cell part of the Debye medium. However, the above formulation does not take into account the presence of a conduction current term due to a static (DC) conductivity. Incorporation of such a term ($\sigma_s\mathbf{E}$) in (5.8) obviously results in an FDTD update equation with two unknowns, which is not desirable. One way to circumvent this difficulty is to incorporate the DC conductivity in the relation describing the complex permittivity in the frequency domain. This is straightforward for the Debye medium but the differential equation which results using the same procedure as described above is of a higher order (second), so that its discretization for implementation in the FDTD algorithm results in the requirement for storage of two values for $\mathbf{D}$ and $\mathbf{E}$ for each FDTD cell part of the Debye medium. This makes the original ADE approach less attractive than RC. However, with a simple modification (Young, 1995) this requirement for increased storage is alleviated without departing from the ADE basic concept.

Equation (5.7), using (5.4) and the definition of the polarization vector $\mathcal{P} = \epsilon_0\chi(\omega)\mathcal{E}$ (Elliot, 1966; Balanis, 1989), becomes

$$\mathcal{D} = \epsilon_\infty\mathcal{E} + \mathcal{P} \tag{5.11}$$

Maxwell's curl equation (5.8) including the conduction current term due to DC conductivity is:

$$\nabla \times \mathcal{H} = \jmath\omega\mathcal{D} + \sigma_s\mathcal{E} \tag{5.12}$$

Using (5.11) in (5.12) and transforming it to the time domain

$$\nabla \times \mathbf{H} = \epsilon_\infty\frac{\partial \mathbf{E}}{\partial t} + \frac{\partial \mathbf{P}}{\partial t} + \sigma_s\mathbf{E} \tag{5.13}$$

Further using the definition of $\mathcal{P}$ and $\chi(\omega)$ results in

$$\mathcal{P} = \frac{\epsilon_s - \epsilon_\infty}{1 + \jmath\omega\tau}\mathcal{E} \tag{5.14}$$

$$\mathcal{P} + \jmath\omega\tau\mathcal{P} = (\epsilon_s - \epsilon_\infty)\mathcal{E} \tag{5.15}$$

which can directly be transformed in the time domain resulting in:

$$\frac{\partial \mathbf{P}}{\partial t} = \frac{1}{\tau}[(\epsilon_s - \epsilon_\infty)\mathbf{E} - \mathbf{P}] \tag{5.16}$$

Using (5.16) in (5.13) results in:

$$\nabla \times \mathbf{H} = \epsilon_\infty\frac{\partial \mathbf{E}}{\partial t} + \frac{1}{\tau}[(\epsilon_s - \epsilon_\infty)\mathbf{E} - \mathbf{P}] + \sigma_s\mathbf{E} \tag{5.17}$$

The above equation can be discretized using the procedures described in the previous Chapter where the required value of $\mathbf{P}$ is obtained by a similar discretization of the

differential equation (5.16). The modified FDTD update equation for the electric field and the update equation for the polarization vector are:[3]

$$\mathbf{E}^n = c_1\mathbf{E}^{n-1} + c_2\Delta t[\nabla \times \mathbf{H}]^{n-1/2} + \frac{c_2\Delta t}{\tau}\mathbf{P}^{n-1/2} \tag{5.18}$$

$$\mathbf{P}^{n+1/2} = c_3\mathbf{P}^{n-1/2} + \frac{c_4\Delta_t}{\tau}(\epsilon_s - \epsilon_\infty)\mathbf{E}^n \tag{5.19}$$

where

$$c_1 = \frac{2\epsilon_\infty\tau - \Delta t(\epsilon_s - \epsilon_\infty) - \Delta t\tau\sigma_s}{2\epsilon_\infty\tau + \Delta t(\epsilon_s - \epsilon_\infty) + \Delta t\tau\sigma_s} \tag{5.20}$$

$$c_2 = \frac{2\tau}{2\epsilon_\infty\tau + \Delta t(\epsilon_s - \epsilon_\infty) + \Delta t\tau\sigma_s} \tag{5.21}$$

$$c_3 = \frac{2\tau - \Delta t}{2\tau + \Delta t} \tag{5.22}$$

$$c_4 = \frac{2\tau}{2\tau + \Delta t} \tag{5.23}$$

the magnetic field update equations remain unchanged. Figure 5.8 presents a comparison of the normal-incidence plane wave reflection coefficient calculated by a 1D FDTD model with the theoretical reflection coefficient for an electromagnetic wave incident from air on a water half-space. The theoretical reflection coefficient is given by the formula

$$R = \frac{\sqrt{\epsilon_0} - \sqrt{\tilde{\epsilon}(\omega)}}{\sqrt{\epsilon_0} + \sqrt{\tilde{\epsilon}(\omega)}} \tag{5.24}$$

since it is assumed that there is no variation in the magnetic permeability. The parameters of the Debye model for water are $\epsilon_{r\infty} = 1.8$, $\epsilon_{rs} = 81$ and $\tau = 9.4 \times 10^{-12}(sec)$. This test is the same as the one reported in Kunz and Luebbers (1993) for the RC approach. As is evident from Figure 5.8, the agreement between the analytical and the FDTD solutions is very good.

5.4.3 2D GPR response from a perfectly conducting metal cylinder buried in a medium with a Debye relaxation

One significant problem in using a Debye relaxation to describe the variation of permittivity in subsurface media encountered in GPR surveying is that this type of variation has been determined experimentally by fitting a Debye model to measured values of permittivity. But detailed material information is not always available in common practical

[3]Since the equations are the same for any electric field component a vector form of the update equations is given without showing the discretization of the spatial derivatives, which is the same as described in the previous Chapter

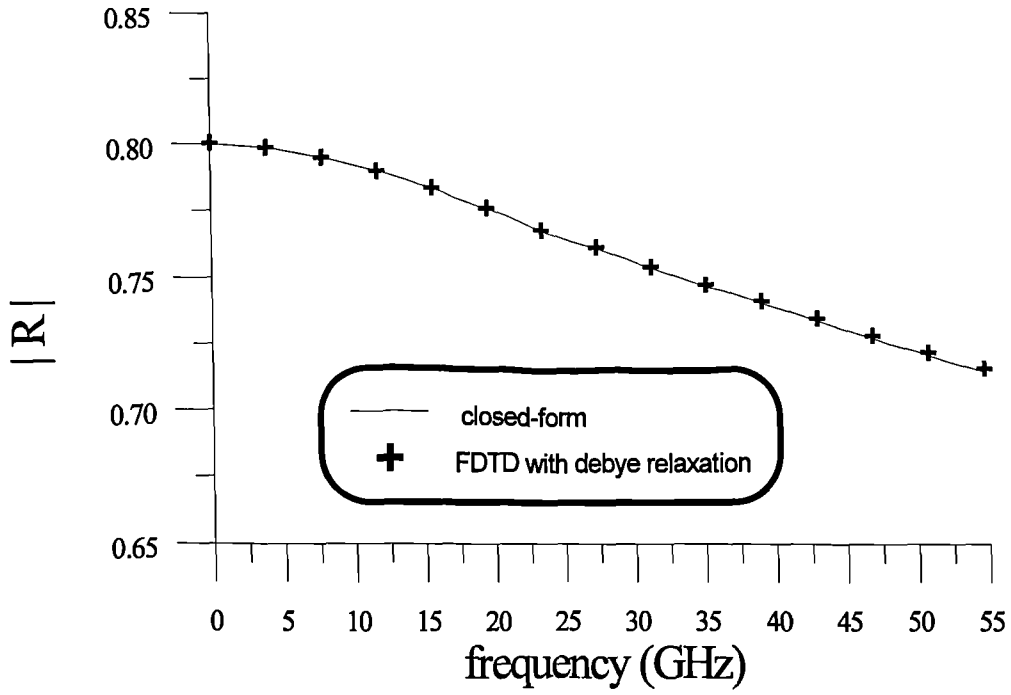

Figure 5.8: Comparison between the amplitude of the reflection coefficient of a normal incident plane wave on a water half-space calculated by the modified FDTD algorithm and analytically.

applications of GPR. Further, although the main reason for such a variation of permittivity is the presence of water, the relaxation times which have been reported in the literature are even orders of magnitude greater than the theoretical relaxation time of water (9.4×10^{-12} seconds). For example, Hoekestra and Delaney (1974) reported relaxation frequencies (τ^{-1}) in the range 1 to 4 GHz. Moreover, values of $\epsilon_{r\infty}$ and ϵ_{rs} are not readily available. Wang (1980) suggests the following empirical formula for $\epsilon_{r\infty}$ and ϵ_{rs} in soil-water mixtures

$$\epsilon_{r\infty} = \epsilon_r(1-p) + (p-w) + 4w \tag{5.25}$$

$$\epsilon_{rs} = 3.14 + 23.83w + 91.58w^2 \tag{5.26}$$

where w is the water content expressed in a volumetric basis and $p \approx 0.5$ is the porosity of the soil. The relative permittivity of rocks varies, but the value $\epsilon_r \approx 5$ is suggested by the same author. However, it should be noted that the above formulae are empirical. Other formulae for wet soils based on a semi-empirical model are given in Dobson et al. (1985). Moreover, Hoekestra and Delaney (1974) found values for $\epsilon_{r\infty}$ and ϵ_{rs} of 7.0 and 14.6 respectively, and 7.0 and 3.0 when they used two Debye relaxation mechanisms to describe the variation of permittivity in a particular type of clay.

In general, because of the wide variation of soil types and soil-water mixtures the simple Debye relaxation model for permittivity is used in this work in a qualitative way to model attenuation and dispersion in GPR. Thus, the parameters of the Debye medium are adjusted according to the requirement for an almost constant real part of permittivity over the frequency range of interest and a linear variation of the imaginary part over the same frequency interval.

In Figure 5.9, the variation of attenuation constant, phase velocity and loss tangent for a Debye medium where $\epsilon_{r\infty} = 2$, $\epsilon_{rs} = 4$ and $\tau = 30 \times 10^{-11}$ (sec) is illustrated for the same values of DC conductivity used in Figure 5.6 ($\sigma_s = 0.001$, 0.01, 0.1 (S/m)). The important difference in comparing Figures 5.9 and 5.6 is the difference in the frequency dependence of the attenuation constant. For the Debye medium, there is an almost linear increase in the attenuation constant with frequency over the frequency range of interest (25-1000 MHz). In increasing the value of DC conductivity, the effect of the Debye relaxation becomes less pronounced. Figure 5.10 presents the same variation of attenuation constant, phase velocity and loss tangent for a Debye medium as in Figure 5.9 but with a smaller relaxation time of $\tau = 30 \times 10^{-12}$ (sec) or, equivalently, with a high relaxation frequency ($f_\tau = \tau^{-1}$ (Hz)). In this medium the overall effect of the Debye relaxation mechanism is less significant, especially for the frequency range of interest (25–1000 MHz).

To examine the effects of the Debye relaxation model on the simulated GPR signals, the same model configuration is used as was presented for the case of frequency independent parameters (**D** in Table 5.1). The response of a perfectly conducting metal cylinder is obtained when the permittivity of the subsurface medium is assumed to be described by the Debye relaxation models discussed above. In Figures 5.11 and 5.12, the simulated responses from the cylinder are presented for the two Debye media of Figures 5.9 and 5.10 respectively, and for the three different values of DC conductivity ($\sigma_s = 0.001$, 0.01, 0.1 (S/m)). The first simulated trace in Figures 5.11 and 5.12 corresponds to the ideal loss-free case described by a frequency independent relative permittivity $\epsilon_r = 4$. Examining the responses in Figures 5.11 and 5.12 is evident that even when the DC conductivity is small dispersion of the GPR signals can occur if the permittivity is described by a Debye relaxation model and the relaxation frequency is not very high compared to the frequency range of the GPR pulse. When the relaxation frequency (τ^{-1}) is much greater than the highest frequency of interest, the influence of the Debye model is much reduced. Moreover, in both cases, when the DC conductivity is high the presence of a Debye relaxation just

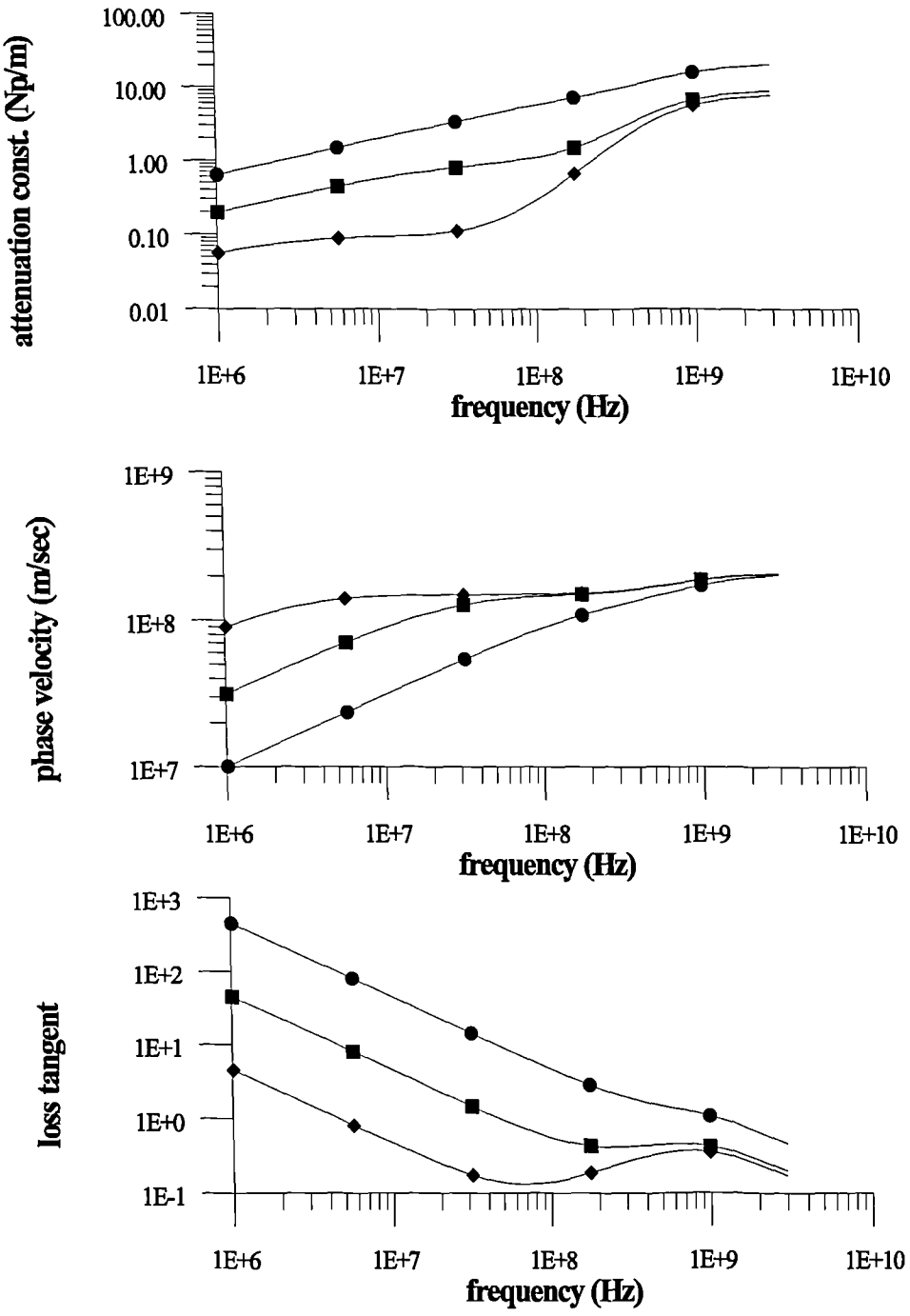

Figure 5.9: Variation of attenuation constant, phase velocity and loss tangent for a medium with frequency dependent relative permittivity (Debye model $\epsilon_{r\infty} = 2$, $\epsilon_{rs} = 4$, $\tau = 30 \times 10^{-11}$ (sec)) and DC conductivity $\sigma_s = 0.001$ (S/m) (diamonds), 0.01 (S/m) (squares), 0.1 (S/m) (circles).

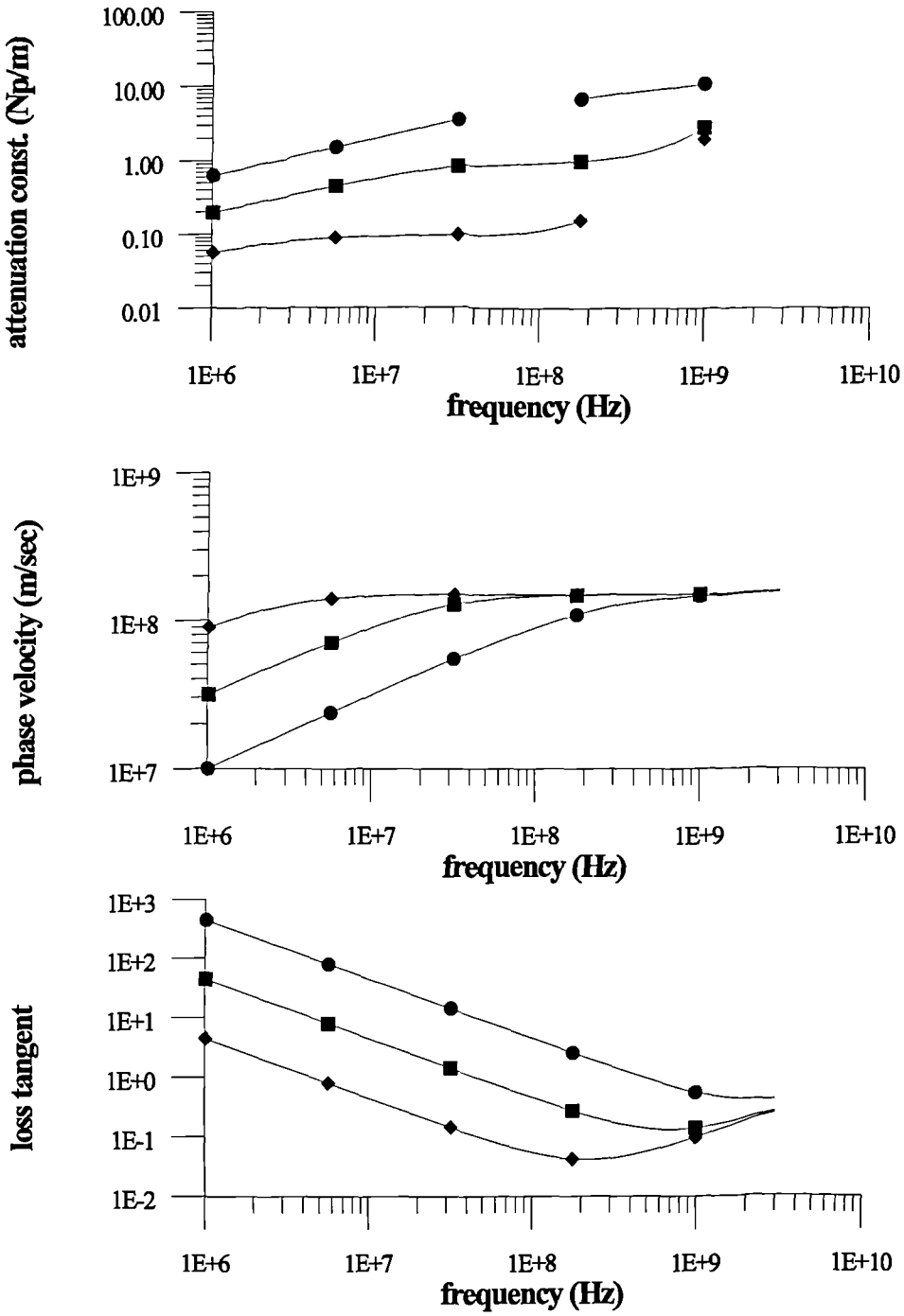

Figure 5.10: Variation of attenuation constant, phase velocity and loss tangent for a medium with frequency dependent relative permittivity (Debye model $\epsilon_{r\infty} = 2$, $\epsilon_{rs} = 4$, $\tau = 30 \times 10^{-12}$ (sec)) and DC conductivity $\sigma_s = 0.001$ (S/m) (diamonds), 0.01 (S/m) (squares), 0.1 (S/m) (circles).

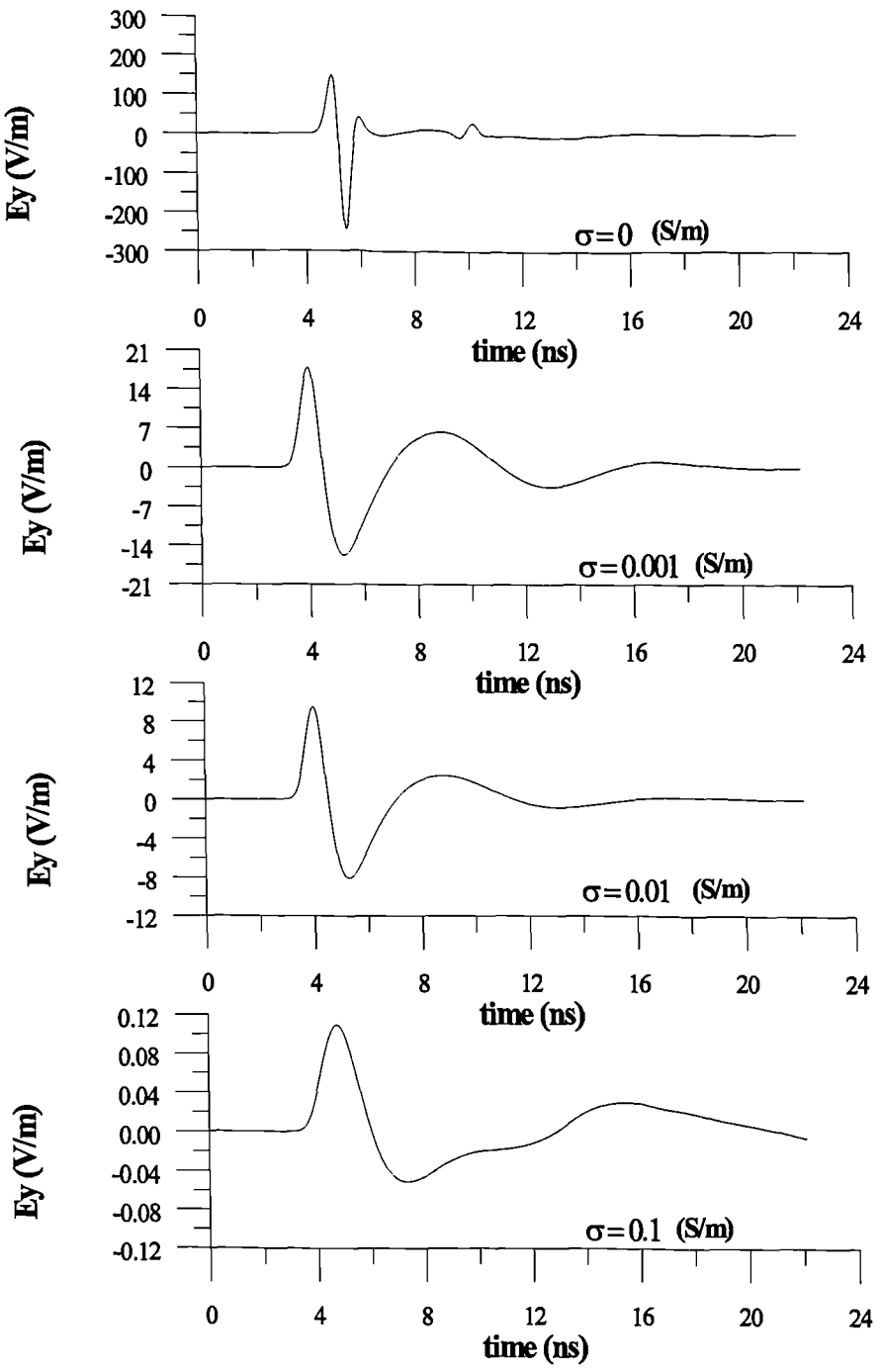

Figure 5.11: Simulated responses (reflected field only) from a perfectly conducting metal cylinder buried at a depth of 0.5 m. The relative permittivity of the host medium is described by the Debye model of Figure 5.9.

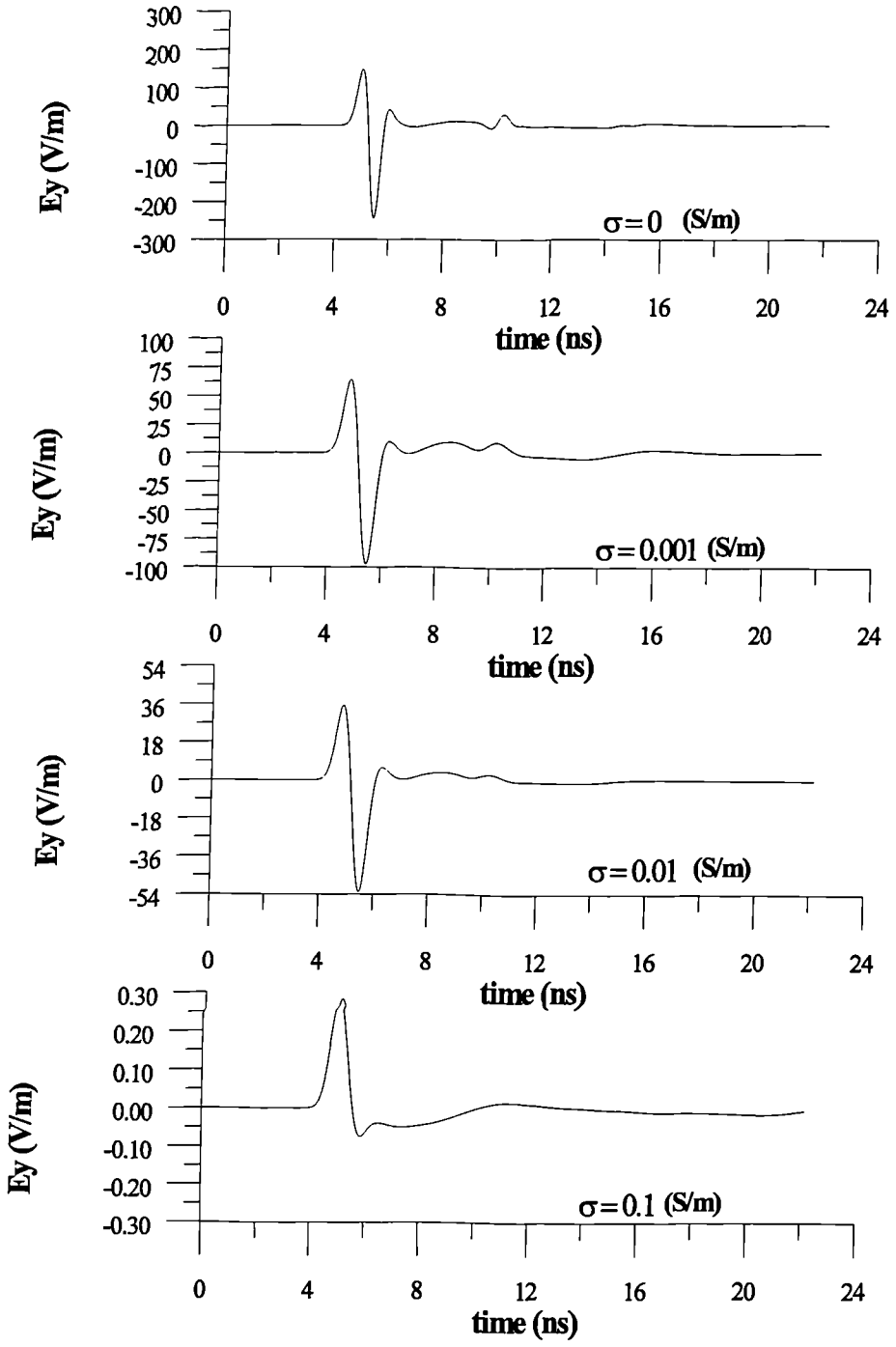

Figure 5.12: Simulated responses (reflected field only) from a perfectly conducting metal cylinder buried at a depth of 0.5 m. The relative permittivity of the host medium is described by the Debye model of Figure 5.10.

accentuates the attenuation and dispersion effects, in a similar fashion to the case of frequency independent constitutive parameters. Therefore, the use, when possible, of other geophysical methods (e.g. resistivity) to obtain information about the variation of DC conductivity in the area of interest can provide important information concerning the applicability of GPR.

5.5 Vertical and lateral resolution using 2D GPR models

Vertical and lateral resolution are measures of how close two targets can be, and yet still be distinguished as individual entities in the GPR data. Vertical resolution is the minimum depth separation between two targets when one is located above the other and lateral resolution is their minimum horizontal separation when they are located at the same depth.

Resolution primarily depends on the bandwidth of the GPR wavelet, but also varies with the constitutive parameters of the subsurface media. Propagation in the subsurface results, as was examined earlier in this Chapter, in shorter wavelengths which improves the general resolution. However, the stronger attenuation of high frequencies has, as a consequence, the effect of broadening the GPR wavelet and hence a reduction of its bandwidth which in turn reduces resolution. Therefore, for example, the resolution in subsurface media with high values of real effective relative permittivity could be theoretically very high but usually in this media attenuation is very strong, therefore limiting the exploration depth.

Resolution can be examined using the 2D TLM and FDTD GPR models (Giannopoulos et al., 1994; Giannopoulos et al., 1995; Millard et al., 1996). For both vertical and lateral resolution the best scenario is when the propagating pulse does not suffer from dispersion which will alter its bandwidth. Giannopoulos et al. (1995) examined the deterioration in vertical resolution, using a 2D TLM model of two vertically aligned targets when their depth separation is reduced. The targets can not be resolved when their separation was less than a quarter of wavelength, defined as the wavelength of the dominant frequency of the GPR wavelet in the subsurface medium.

To illustrate the application of the 2D GPR models in examining vertical resolution the following numerical experiment is used. Two cylindrical voids of the same radius ($r = 5$ centimetres) are located one above the other in a medium of relative permittivity of ($\epsilon_r =$

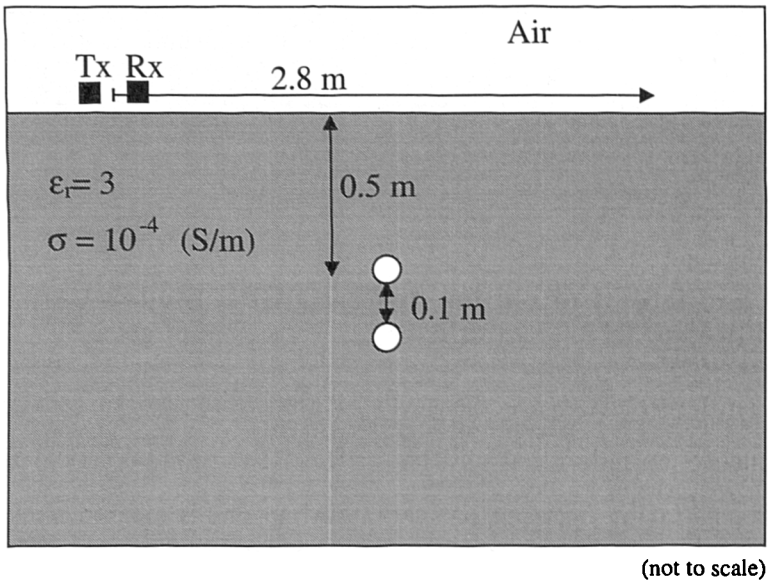

Figure 5.13: Schematic drawing of the 2D TLM model of vertically aligned cylindrical voids.

3) and conductivity ($\sigma = 0.001$) (S/m). Their vertical separation (S) is 10 centimetres (20 centimetres from the centre of the voids). A schematic drawing of the 2D TLM model (E in Table 5.1) used is illustrated in Figure 5.13. Two synthetic GPR scans, comprised of 57 traces, have been calculated using different ricker sources: one with $f_s = 600$ MHz with Tx–Rx separation of 25 centimetres, both located at a height of 5 centimetres above the interface; and the other with $f_s = 300$ MHz with Tx–Rx separation of 50 centimetres, both located at a height of 10 centimetres. Using the good dielectric approximation, the wavelengths in the subsurface medium for these two frequencies are $\lambda_{600} = 0.28$ centimetres and $\lambda_{300} = 0.57$ centimetres respectively. In Figure 5.14 the synthetic GPR scans obtained for the two different excitations are illustrated. When f_s is 600 MHz, the targets are resolved and two distinct hyperbolic responses are recorded, with the one from the deeper void being broader, as is expected, since for this case $\lambda_{600}/4 > S$. However, when f_s is 300 MHz the two targets produce a combined response because $\lambda_{300}/4 < S$.

Horizontal resolution can be examined using a similar model. The constitutive parameters are kept the same and the targets have been replaced by two perfectly conducting metal cylinders of the same radius ($r = 5$ centimetres) buried at the same depth (0.5 metre) with a horizontal separation (S) of 10 centimetres. A schematic drawing of the 2D TLM model (F in Table 5.1) is illustrated in Figure 5.15. Synthetic GPR scans calculated for two different ricker sources with $f_s = 600$ MHz and $f_s = 300$ MHz respectively are illustrated

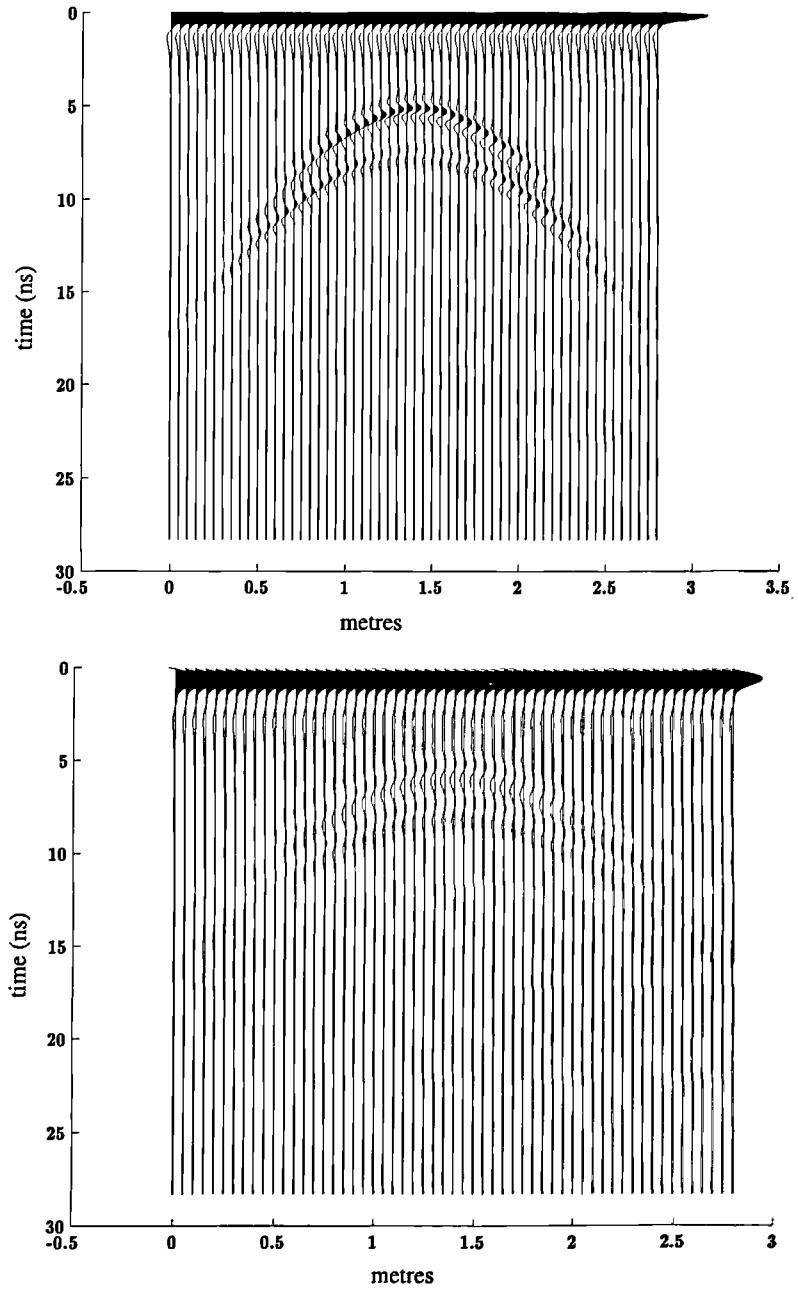

Figure 5.14: Synthetic GPR scans obtained from the 2D TLM model of vertically aligned voids for different source excitations $f_s = 600$ MHz (top) and $f_s = 300$ MHz (bottom).

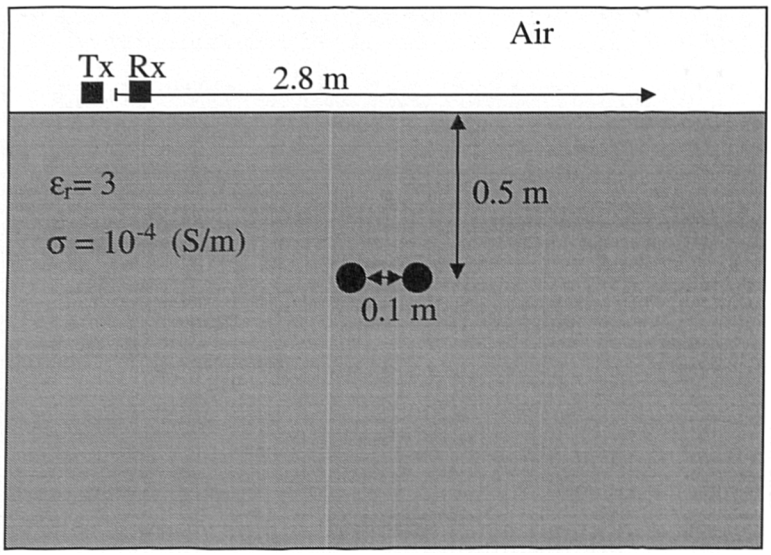

Figure 5.15: Schematic drawing of the 2D FDTD model of horizontally aligned perfectly conducting metal cylinders.

in Figure 5.16. It is clear that the effect of lowering the frequency is to reduce resolution. Moreover, horizontal resolution depends on depth as well. These results are analogous to those obtained in the seismic method and are related to the radius of the Fresnel zone (Yilmaz, 1987, Sheriff, 1991) which increases with depth. The radius (r) of the Fresnel zone is given by the formula (Yilmaz, 1987):

$$r \approx \sqrt{\frac{d\lambda_m}{2}} \tag{5.27}$$

where d is depth (meters) and λ_m is the wavelength of the dominant frequency of the propagating pulse in the medium. Targets separated by a distance less than the radius of the Fresnel zone can not be resolved. In Figure 5.17 the responses of the two perfectly conducting cylinders for burial depths of 0.25 and 1 metre when $f_s = 600$ MHz are presented. The horizontal separation is kept the same as in Figure 5.16 and the parameters of the model are otherwise unchanged. As it is evident from these responses, the horizontal resolution improves when the targets are located at a depth of 0.25 metre and deteriorates when the depth becomes 1 metre in comparison with the 0.5 metre case.

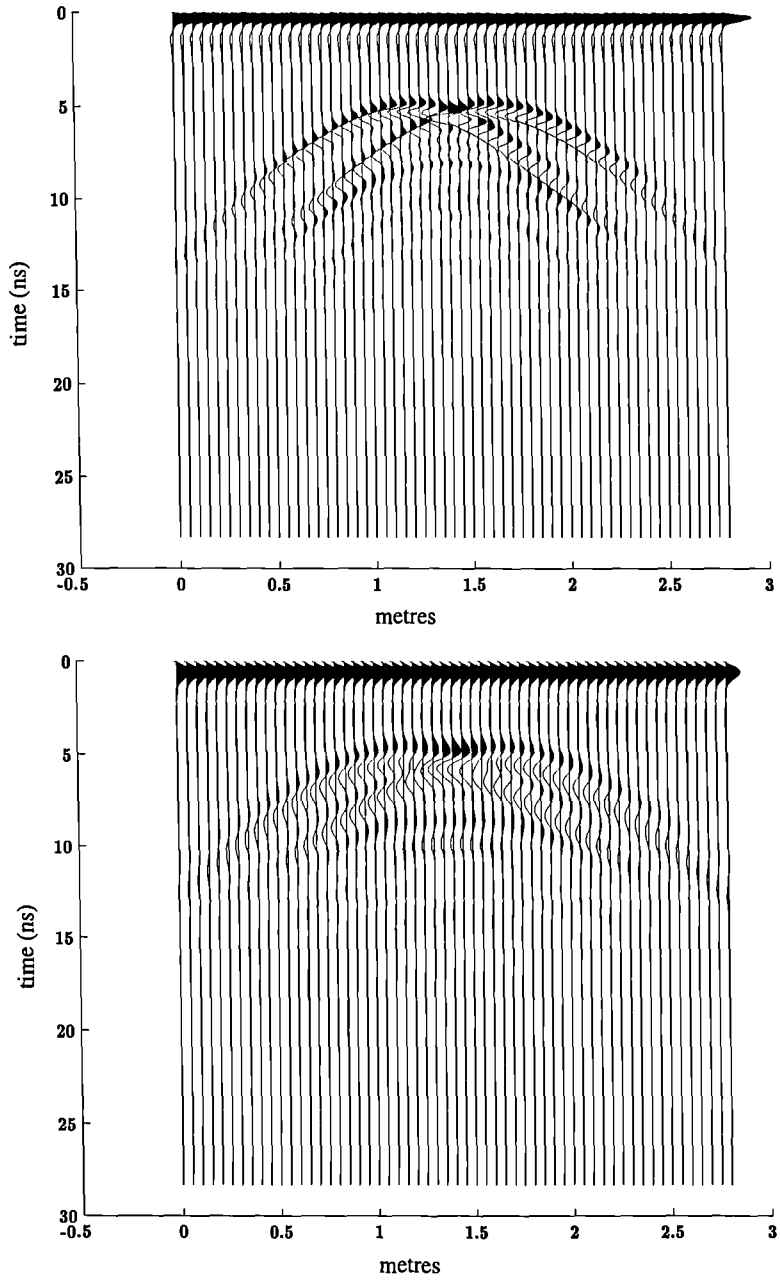

Figure 5.16: Synthetic GPR scans obtained from the 2D FDTD model of horizontally aligned perfectly conducting metal cylinders for different source excitations f_s = 600 MHz (top) and f_s = 300 MHz (bottom).

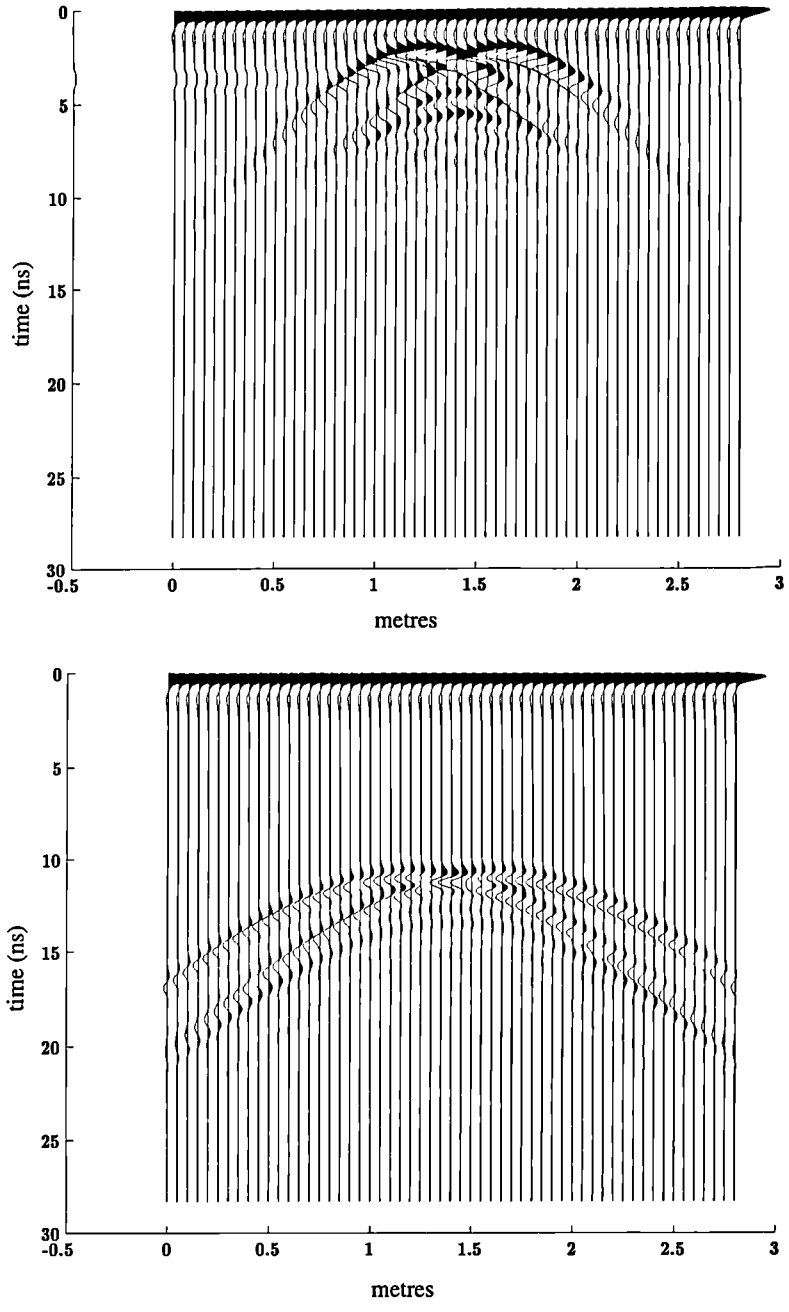

Figure 5.17: Synthetic GPR scans obtained from the 2D FDTD model of horizontally aligned perfectly conducting metal cylinders for different depths d = 0.25 metre (top) and d = 1.0 metre (bottom) and the same excitation f_s = 600 MHz.

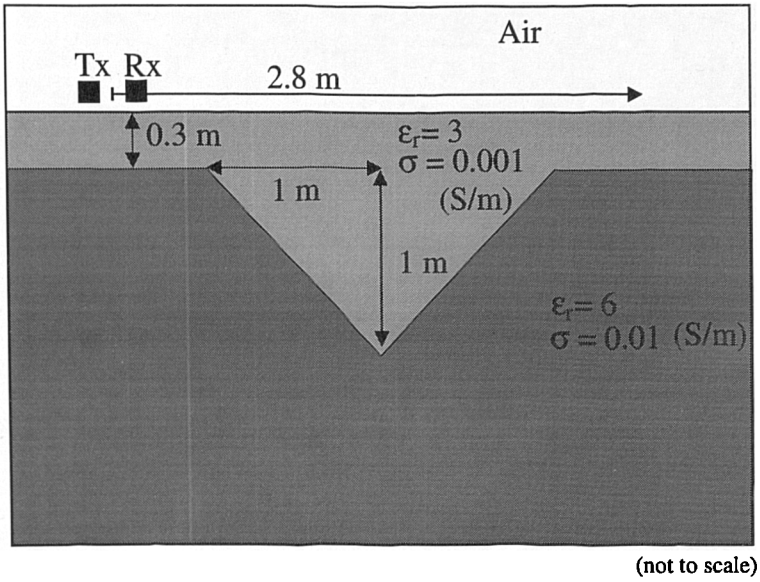

Figure 5.18: Schematic drawing of the 2D FDTD model of V-shaped syncline (ditch).

5.6 2D GPR models of a syncline and a fault

The use of 2D models to obtain synthetic GPR responses from simple targets provides the means to examine the influence of the medium parameters of the GPR signals and to examine the resolving ability of GPR. However, when the underground structure is more complicated the GPR signatures are more important in facilitating interpretation of GPR data. The generality of the modelling approach lends itself as a very important tool since it can provide synthetic GPR responses in these more complicated environments.

In Figure 5.18, a schematic drawing of a 2D FDTD model of a V-shaped syncline (ditch) is presented (**G** in Table 5.1). The synthetic GPR section was obtained using a ricker source with $f_s = 600$ MHz and a Tx–Rx separation of 25 centimetres, with both Tx–Rx being located at a height of 5 centimetres above the air interface. The section (shown in Figure 5.19) is comprised of 57 traces. This response is characteristic of these type of targets and is referred to as a "bow tie".

In Figure 5.20, a schematic drawing of a 2D FDTD model of a normal fault is illustrated (**H** in Table 5.1). The excitation of the model is the same with the syncline model. The synthetic GPR section using a $f_s = 600$ MHz ricker source, with a Tx–Rx separation of 25 centimetres (both located at a height of 5 centimetres above the air interface) is pre-

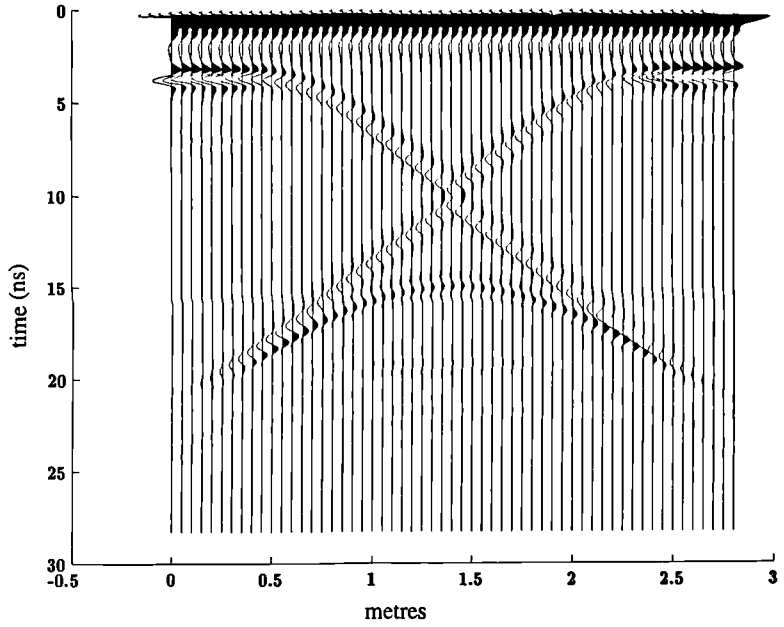

Figure 5.19: Synthetic GPR scan obtained from the 2D FDTD V-shaped syncline model.

sented in Figure 5.21. The important characteristic of this type of target is the diffraction hyperbolas due to the sharp discontinuities in the target's geometry. The two branches of the diffraction hyperbola have opposite polarity (Telford et al., 1990). It should be noted that these type of responses are not obtained when simpler approaches are used for GPR modelling such as ray-tracing (Zeng et al., 1995).

5.7 Comparison of a 2D GPR model and real GPR data

In this section a comparison between real GPR data and a 2D model (Giannopoulos et al., 1995b) is presented. The real data were obtained from a GPR survey contacted in the archaeological site of Fountains Abbey (England) (Szymanski et al., 1992; Coppack et al., 1992) and the section presented in Figure 5.23 (top) is from a GPR scan over a culvert located under the *Cellarium* of the Abbey. The underground tunnel can clearly be seen in the GPR data which were acquired with an ERA Technology GPR system using 500 MHz antennas in a parallel mode configuration. The culvert is almost rectangular in shape and is constructed of the same material (limestone) as the building under which is located. The constitutive parameters for the host material used in the model were set to $\epsilon_r = 5$ and $\sigma = 0.01$ (S/m). Finally, a layer of a material with higher relative permittivity ($\epsilon_r = 10$) and increased conductivity ($\sigma = 0.1$) (S/m) has been used to simulate the wet soil at the

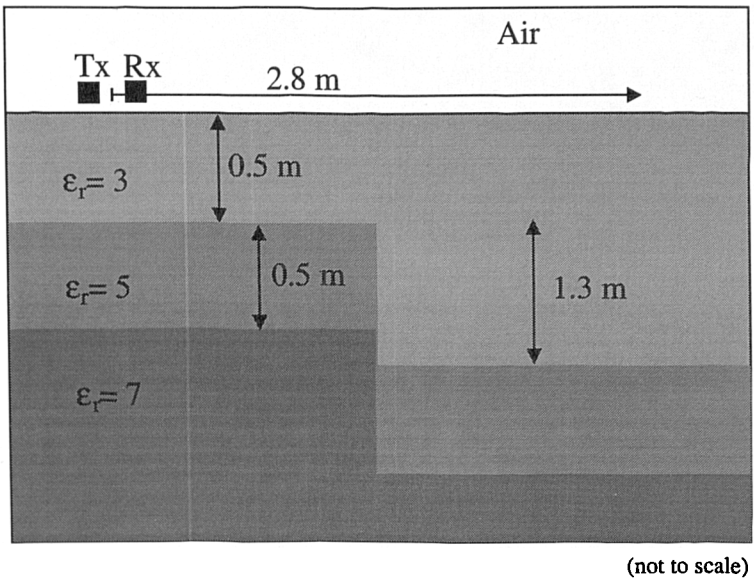

Figure 5.20: Schematic drawing of the 2D FDTD model of a normal fault.

base of the culvert. The excitation used in the model was a ricker source with $f_s = 500$ MHz and an Tx–Rx separation of 0.3 metres (both located very close to the interface —2 centimetres). The synthetic scan is comprised of 65 traces. The measured data (Figure 5.23) were not subjected to any processing apart from a time-zero adjustment as the modelled data. A schematic drawing of the 2D FDTD model (**I** in Table 5.1), used to obtain the modelled response is illustrated in Figure 5.22 and the result of the simulation is presented in Figure 5.23 (bottom). The parameters (size and shape of the target) were only estimates since access inside the culvert was not possible. Comparing the real data and the result of the simulation the signature of the target is adequately predicted by the model, taking into account that the data are not from a clinical clutter-free environment.

5.8 Comparison between 2D TLM and 2D FDTD GPR models

The results obtained using 2D TLM and FDTD models when the constitutive parameters of the subsurface media are considered frequency independent are almost identical. As was discussed in the previous Chapter, although the two methods are based on different modelling philosophies, their dispersion relations are equivalent under the condition that the same time step is used in both 2D TLM and FDTD. The use of efficient absorbing boundary conditions in 2D TLM and their improved performance in comparison to FDTD

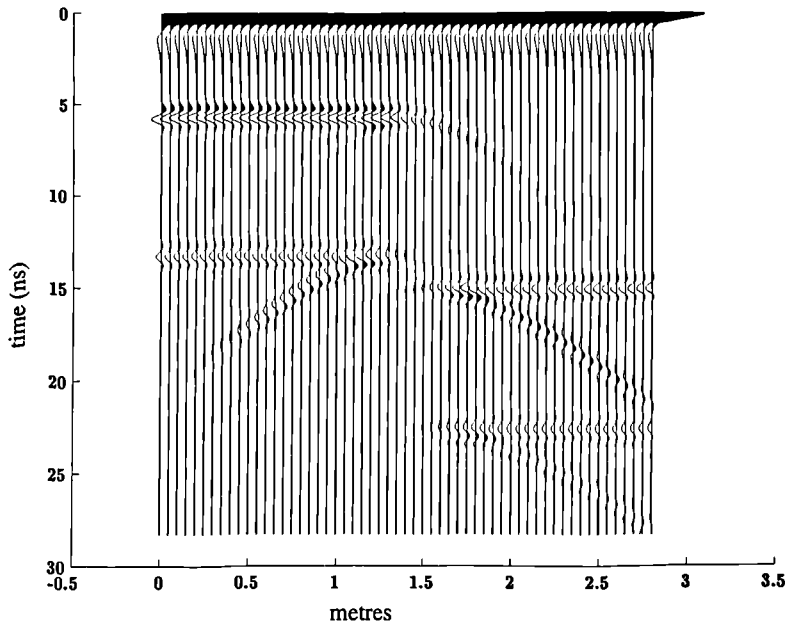

Figure 5.21: Synthetic GPR scan obtained from the 2D FDTD model of a normal fault.

makes TLM more attractive when the size of the computational domain is relatively small. However, the FDTD models are more computationally efficient, since less storage space is needed, and the computation of the required field values using the update equations involves less calculations than the scattering and connect procedures in TLM. The advantages of TLM over FDTD are the finer boundary description and the calculation of all field quantities at the same spatial locations. This, however, is more important in the 3D models (Chapters 6–7) than in the 2D ones. Moreover, the TLM algorithm is always operated with a time-step which corresponds to the stability limit of the FDTD algorithm. Conceptually, this is an advantage of TLM, but no instabilities have been observed here for GPR simulations using the FDTD model with the time step corresponding to its stability limit.

Considering the use of a Debye relaxation model to describe the variation of permittivity with frequency, the FDTD formulation described in this Chapter does not increase the computational load significantly. Although a Debye relaxation can be incorporated into 2D TLM, this will lead to a further increase in its computational requirements. The FDTD model with a Debye relaxation requires less storage space than the ordinary TLM model with frequency independent constitutive parameters and its run-time is found to be less.

In conclusion, the choice between TLM and FDTD for 2D GPR modelling is mostly

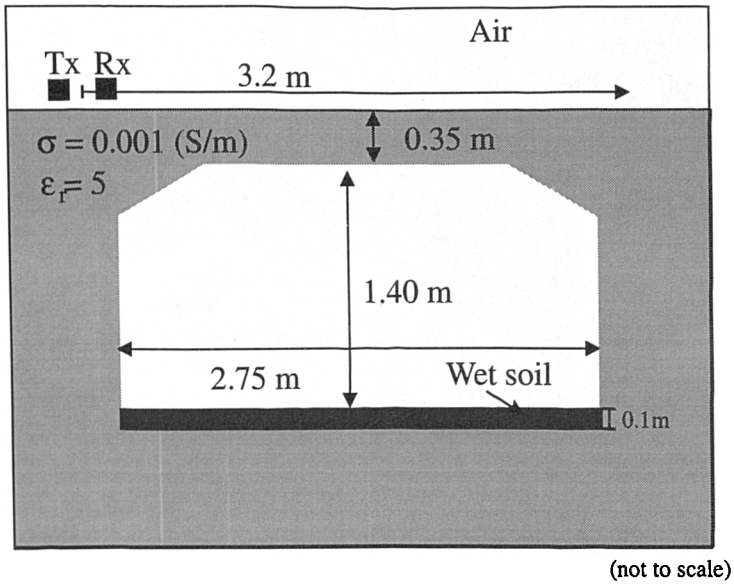

Figure 5.22: Schematic drawing of the 2D FDTD model of the underground culvert.

influenced by one's preference in the modelling philosophy on which the two methods are based. However, when computational resources have to be considered FDTD has a distinct advantage.

5.9 Discussion

In this Chapter results from the application of the 2D TLM and FDTD methods to the GPR forward problem were presented. From the examination of simple modelling scenarios the effects of the media properties on the GPR responses were examined. A Debye relaxation model was introduced in the modelling procedure to provide a more realistic model for the frequency dependence of the constitutive parameters. The effects of attenuation and dispersion in GPR signals and the resolving ability of GPR were examined. Results from more complicated modelling scenarios were presented, illustrating the potential and usefulness of the modelling approach. Finally, a comparison with real GPR data was presented.

As was presented in this Chapter, the time-domain GPR models based on TLM and FDTD are well suited for the study of a number of GPR problems. Apart from the assumptions involved in reducing the 3D GPR problem to a 2D one, there are no other simplifica-

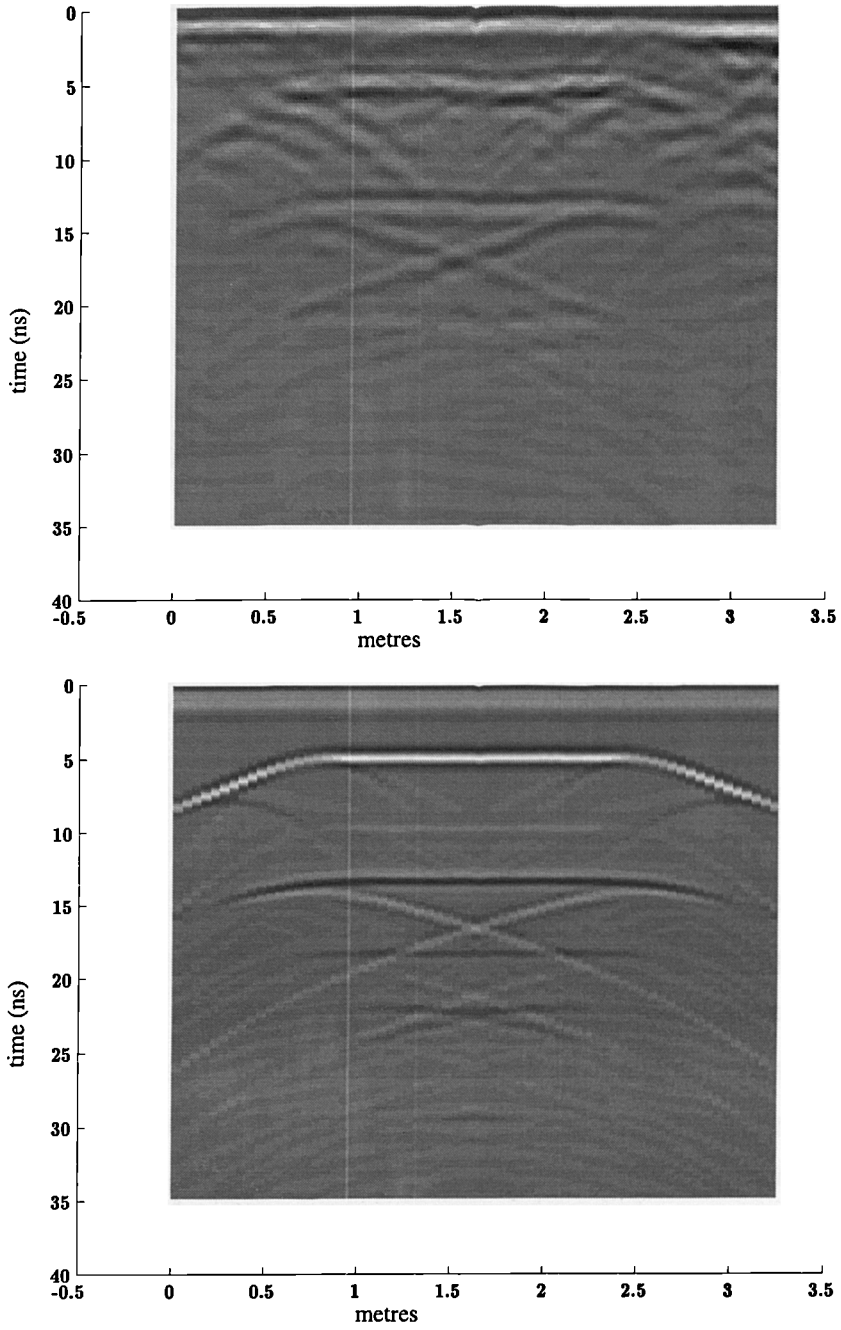

Figure 5.23: Measured GPR data (top) over a culvert located under the Cellarium of Fountains Abbey (England) and the synthetic GPR scan obtained from the 2D FDTD model of the same target.

MODEL	*Type*	*Size (nodes)*	Δl(m)	Δt(ps)	*ABC*
A	TLM	100 × 100	0.01	23.58	Liao 2nd
B	FDTD	500 × 150	0.01	23.58	Liao 3rd
C	TLM	100 × 200	0.01	23.58	Liao 2nd
D	FDTD	100 × 200	0.01	23.58	Higdon 3rd
E	TLM	400 × 140	0.01	23.58	Liao 2nd
F	TLM	400 × 185	0.01	23.58	Liao 2nd
G	FDTD	400 × 185	0.01	23.58	Higdon 3rd
H	FDTD	400 × 250	0.01	23.58	Higdon 3rd
I	FDTD	400 × 220	0.01	23.58	Liao 3rd

Table 5.1: Technical characteristics of 2D GPR models used in this Chapter

tions involved in the modelling procedure. Therefore, all electromagnetic phenomena are taken into account by the models. The applicability of the models is mainly restricted by the available computational resources. In general, single GPR trace simulations can be performed in reasonable time (minutes) on a personal computer. However, simulations of GPR scans are by far more computationally intensive and more powerful mainframe computers have to be used in order to obtain results in reasonable time. The main constraint of the models is the need for small spatial increments in order to control numerical dispersion errors, especially when high values of permittivity are used. This in essence, restricts the applicability of the models in a modest, in terms of resources, computational environment.

6

Three dimensional numerical modelling of GPR — PART I: Methodology

6.1 Introduction

In Chapter 5 results from the application of the 2D approach to the forward GPR problem were presented which demonstrated the usefulness of this type of models in obtaining GPR signatures from targets which could be safely assumed to be "two dimensional". However, the inadequacies of a 2D model are obvious when 3D effects are important, especially from small localized targets. Moreover, information which is obtained by exploiting different transmitting and receiving antenna configurations is not available from a 2D model. The extension to the full 3D case is the only way of obtaining a complete simulation of the GPR response. This, however, results in increasing the complexity of the models and, most importantly, leads to a substantial increase in the required computational resources.

Although the fundamental concepts on which the three dimensional FDTD and TLM models are based do not differ from the respective two dimensional ones, there are important differences in the formulation of the models. In the case of FDTD, these differences

are a consequence of the more complicated structure of the 3D Yee cell and are related to the process of incorporating different media in the model. More subtle differences exist between the formulation of two and three dimensional TLM models. These are the result of different TLM nodes that can be used for 3D modelling.

6.2 3D FDTD method

The application of FDTD to three dimensional electromagnetic problems is completely analogous to the 2D case.[1] The governing equations for the GPR forward problem, when no assumptions about the dimensionality of the sources and targets are introduced, are Maxwell's curl equations. Performing the curl operation and using the constitutive relations — assuming that the constitutive parameters are independent of frequency — results in a system of six coupled first order partial differential equations:

$$\epsilon\frac{\partial E_x}{\partial t} = \frac{\partial H_z}{\partial y} - \frac{\partial H_y}{\partial z} - \sigma E_x \tag{6.1}$$

$$\epsilon\frac{\partial E_y}{\partial t} = \frac{\partial H_x}{\partial z} - \frac{\partial H_z}{\partial x} - \sigma E_y \tag{6.2}$$

$$\epsilon\frac{\partial E_z}{\partial t} = \frac{\partial H_y}{\partial x} - \frac{\partial H_x}{\partial y} - \sigma E_z \tag{6.3}$$

$$\mu_0\frac{\partial H_x}{\partial t} = \frac{\partial E_z}{\partial y} - \frac{\partial E_y}{\partial z} \tag{6.4}$$

$$\mu_0\frac{\partial H_y}{\partial t} = \frac{\partial E_x}{\partial z} - \frac{\partial E_z}{\partial x} \tag{6.5}$$

$$\mu_0\frac{\partial H_z}{\partial t} = \frac{\partial E_y}{\partial x} - \frac{\partial E_x}{\partial y} \tag{6.6}$$

As in the 2D FDTD formulation the same procedures are followed in obtaining the discretized version of the governing equations by applying central differences to their spatial and time derivatives. Moreover, the resulting FDTD update equations are used in an identical iterative procedure to provide the required solution. The placement of electric and magnetic field components in the 3D FDTD lattice is analogous to the 2D case, although a more complicated structure results.

[1] The 2D FDTD algorithm is directly obtainable from the 3D one. However, the approach followed here is to use the simpler 2D case for a discussion of the fundamental concepts of the method which do not depend on the dimensionality of the problem.

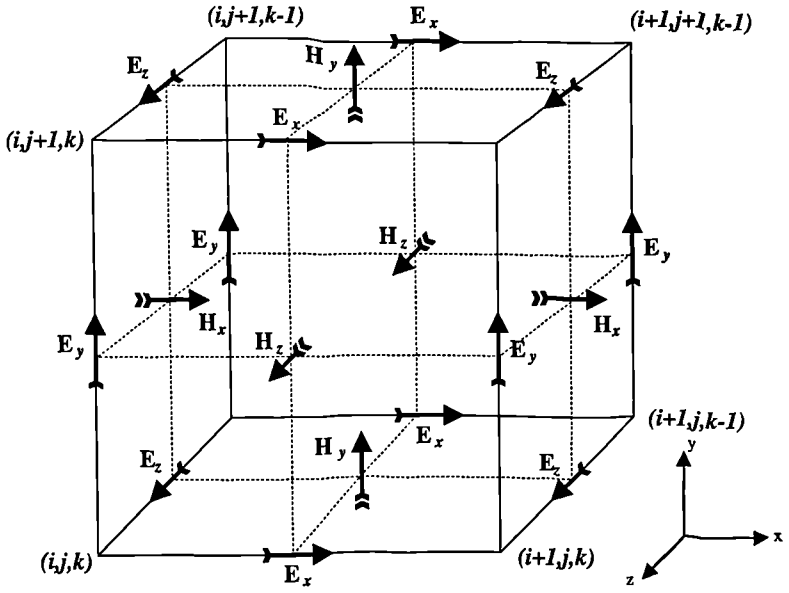

Figure 6.1: The Yee cell.

6.2.1 The 3D Yee cell and the 3D update equations

In a similar fashion to the 2D FDTD model the space and time continua are discretized as:

$$(x, y, z; t) = (i\Delta x, j\Delta y, k\Delta z; n\Delta t) \tag{6.7}$$

In this discretized form the staggered placement of the components of the electromagnetic fields required to implement the central difference approximation to the spatial derivatives of the governing equations results in a structure referred to as the 3D Yee cell (Yee, 1966), illustrated in Figure 6.1. The electric field components are positioned at the edges of the cell and the magnetic field ones are located at the centre of the cell's faces. This definition of the 3D Yee cell is not unique. The positions of the electric and magnetic components can be interchanged without affecting the formulation of the method. In examining the 3D Yee cell which is the building block of the 3D FDTD lattice it is apparent that the placement of the electric and magnetic field components in the FDTD lattice could be interpreted as forming orthogonal interlinked loops of electric and magnetic field components representing a discrete version of the integral forms of Maxwell's equations (Taflove, 1995). These loops (called *Faraday* and *Ampere* contours) lead to a better understanding of the FDTD method and to useful modifications of it for the modelling of problems where an integral representation of Maxwell's equations is more helpful (e.g.

thin wire formulations (Umashankar et al., 1987)).

Placing the components of the magnetic and electric fields as described above in the 3D Yee cell, the governing equations (6.1)-(6.6) can be easily discretized to obtain the 3D FDTD update equations. For example, the 3D FDTD update equations which result from (6.1) and (6.3) are:

$$(6.8)\quad E_x\big|^{n}_{(i+1/2,j,k)} = \left(\frac{1-\frac{\sigma(i+1/2,j,k)\Delta t}{2\epsilon(i+1/2,j,k)}}{1+\frac{\sigma(i+1/2,j,k)\Delta t}{2\epsilon(i+1/2,j,k)}}\right) E_x\big|^{n-1}_{(i+1/2,j,k)} + \left(\frac{\frac{\Delta t}{\epsilon(i+1/2,j,k)}}{1+\frac{\sigma(i+1/2,j,k)\Delta t}{2\epsilon(i+1/2,j,k)}}\right)\left(\frac{H_z\big|^{n-1/2}_{(i+1/2,j+1/2,k)} - H_z\big|^{n-1/2}_{(i+1/2,j-1/2,k)}}{\Delta y} - \frac{H_y\big|^{n-1/2}_{(i+1/2,j,k+1/2)} - H_y\big|^{n-1/2}_{(i+1/2,j,k-1/2)}}{\Delta z}\right)$$

$$(6.9)\quad H_x\big|^{n+1/2}_{i,j+1/2,k+1/2} = H_x\big|^{n-1/2}_{i,j+1/2,k+1/2} + \frac{\Delta t}{\mu_0}\left(\frac{E_y\big|^{n}_{i,j+1/2,k+1} - E_y\big|^{n}_{i,j+1/2,k}}{\Delta z} - \frac{E_z\big|^{n}_{i,j+1,k+1/2} - E_z\big|^{n}_{i,j,k+1/2}}{\Delta y}\right)$$

As is apparent from (6.8) and (6.9), the electric field components are updated at integer multiples of the time step (Δt) and the magnetic ones at a latter time of half time step. A complete list of the 3D FDTD equations is given in Appendix A.

6.2.2 Building an object in FDTD

The FDTD lattice is a construction which represents locations of electromagnetic field components. Therefore, building an object in 3D FDTD involves the assignment of constitutive parameters at appropriate locations of electric and magnetic field components rather than filling Yee cells with material (Kunz and Luebbers, 1993). Because in GPR models it is assumed that the magnetic permeability does not vary, the procedure of building an object is simplified. A cube which has its three dimensions equal to one spatial step is easily constructed by assigning its constitutive parameters to the twelve electric field locations associated with it. At interfaces between different media there is however ambiguity about which value of constitutive parameters should be assigned to the corresponding electric field components located on the interface. This is easier to illustrate by considering the extreme case of an FDTD lattice comprised of two Yee cells

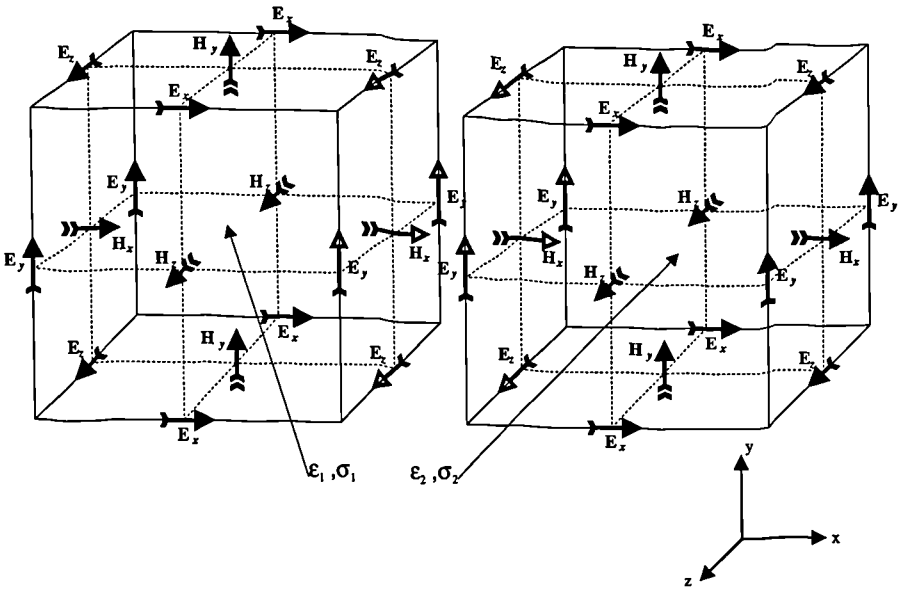

Figure 6.2: Two Yee cells simulating media of different properties. The field components on the interface (y–z plane) shown with white arrow heads should merge into one.

each representing a different dielectric medium (ϵ_1,σ_1) and (ϵ_2,σ_2). These two cells share five electromagnetic field components, shown separated in Figure 6.2. In the FDTD algorithm the set of electrical parameters assigned to the electric field components at the interface depends on the order in which the two blocks of different media are introduced into the lattice — hence there are two possible models. Using such an extreme example, it is evident that the order in which materials are introduced into the FDTD model produce different modelling scenarios. In real situations, objects modelled in FDTD are resolved with many Yee cells, and therefore the difference in the order in which media are introduced in the lattice results in minor discrepancies in the values of the constitutive parameters at the interfaces. A way to remedy this is to use values of constitutive parameters on the boundary between different media which are influenced by both media either side of the interface. This results in the use of *weighted-average* constitutive parameters at an interface. Further, this procedure is used in the generalized Yee method (Taflove, 1995) of which FDTD is a special case. To obtain the weighted-average model, Maxwell's equation in integral form

$$\oint_C \mathbf{H} \cdot d\hat{\mathbf{l}} = \frac{\partial}{\partial t} \iint_S \mathbf{D} \cdot d\hat{\mathbf{s}} + \iint_S \mathbf{J}_c \cdot d\hat{\mathbf{s}} \tag{6.10}$$

is applied around each tangential electric field component at the interface. Using the notation in Figure 6.3 equation (6.10) is discretized as:

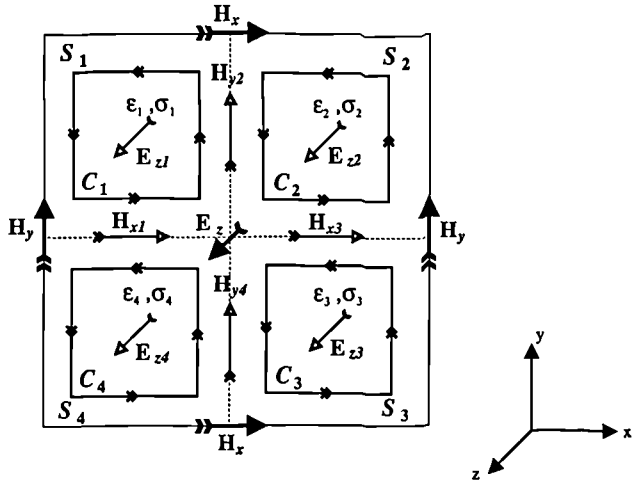

Figure 6.3: The generalized Yee approach to compute values for permittivity and conductivity assigned to the electric field component at an interface. The field components shown with white arrow heads are complementary to aid the calculation and do not exist in the FDTD lattice.

$$\sum_{i=1}^{4}\left(\oint_{C_i} H\cdot d\hat{l}\right)=\sum_{i=1}^{4}\left(\frac{\partial}{\partial t}\iint_{S_i}\epsilon_i E\cdot d\hat{S}+\iint_{S_i}\sigma_i E\cdot d\hat{S}\right) \tag{6.11}$$

Performing the integrations in each of the four small surface patches, with the assumption that the electric flux is constant through each of these patches and invoking the boundary condition that the tangential electric field be continuous on the interface (centre of the patch), the normal FDTD update equation is obtained with the permittivity and conductivity values replaced with:

$$\epsilon_{av}=\frac{\sum_{i=1}^{4}\epsilon_i S_i}{S} \tag{6.12}$$

$$\sigma_{av}=\frac{\sum_{i=1}^{4}\sigma_i S_i}{S} \tag{6.13}$$

As is evident, by using such an approach the same model configuration will result irrespectively of the order in which regions of different constitutive parameters are defined in the FDTD lattice.

6.2.3 Modelling of sources in 3D FDTD for GPR modelling

In general, the incorporation of the actual GPR antenna structure in the FDTD model is possible and no modification of the general 3D FDTD algorithm is required. However, due to the computational costs of such a model, the approach followed here in constructing GPR models was to incorporate of a theoretical source current density term in the governing Maxwell's curl equations. This current density term represents a Hertzian dipole source for the 3D case in the same fashion as the line source used in the 2D model. Modifying the electric field update equations to incorporate the source terms at the location of the GPR transmitting antenna within the model is exactly equivalent to the 2D case. For example, for a x-directed dipole the E_x update equation will be affected at the source's position (i_s,j_s,k_s) and will be:

(6.14)

$$E_x\big|^{n}_{(i_s+1/2,j_s,k_s)} = E_x\big|^{n-1}_{(i_s+1/2,j_s,k_s)} + \left(\frac{\Delta t}{\epsilon_0}\right)\left(\frac{H_z\big|^{n-1/2}_{(i_s+1/2,j_s+1/2,k_s)} - H_z\big|^{n-1/2}_{(i_s+1/2,j_s-1/2,k_s)}}{\Delta y} - \frac{H_y\big|^{n-1/2}_{(i_s+1/2,j_s,k_s+1/2)} - H_y\big|^{n-1/2}_{(i_s+1/2,j_s,k_s-1/2)}}{\Delta z}\right) - \left(\frac{\Delta t}{\epsilon_0}\right) J_s\big|^{n-1/2}_{(i_s+1/2,j_s,k_s)}$$

for other dipole orientations the relevant update equations are modified in the same way. The value of J_s can be related to the infinitesimal current element representing the source as (Buechler et al., 1995)

(6.15)
$$J_s = \frac{I_s \delta l}{\Delta x \Delta y \Delta z}$$

6.2.4 Stability of the FDTD method

By analogy with the 2D case, the time increment with which the FDTD solution is advanced in time can not be assigned arbitrarily. There is an upper bound which is related to the spatial increment used in the model. The stability (CFL) criterion for the 3D FDTD method is (Taflove and Brodwin, 1975; Fang, 1989):

(6.16)
$$\Delta t \leq \frac{1}{c\sqrt{\frac{1}{\Delta x^2} + \frac{1}{\Delta y^2} + \frac{1}{\Delta z^2}}}$$

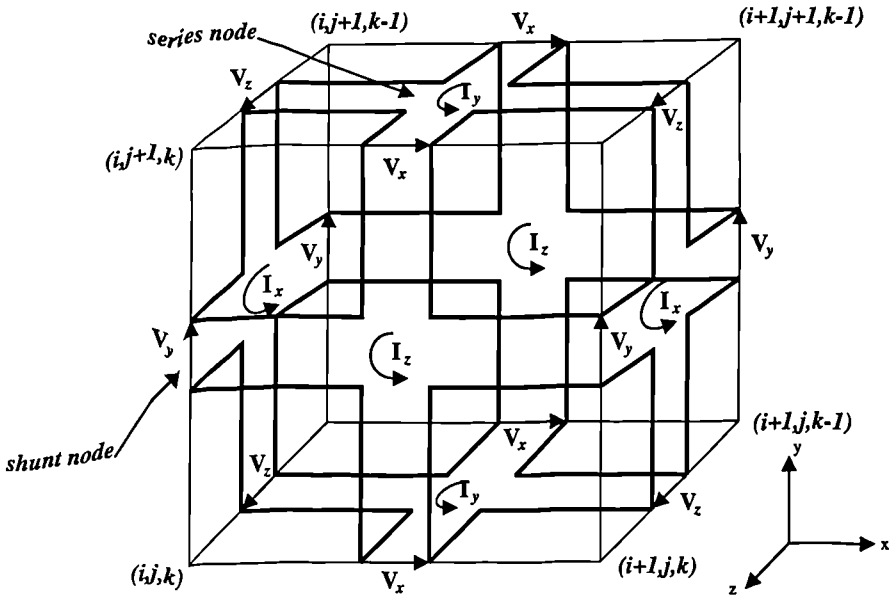

Figure 6.4: The 3D TLM expanded node.

6.3 3D TLM method

The extension of the TLM method to modelling 3D electromagnetic problems is based on the same modelling concepts and procedures as the original 2D models. Therefore, the fundamental concepts of using transmission lines to model the spatial domain, the equivalences of voltage and current with the electric and magnetic fields and the use of circuit parameters to model the constitutive parameters of media are the same for 3D TLM models as for the 2D ones. Most importantly, the **scattering** and **connect** processes are present in the 3D algorithms and the method retains the same relationship with Huygen's models of wave propagation.

Through the course of development of 3D TLM, several different algorithms have been proposed and used. The differences among these algorithms arise from the topology and interconnection of the basic transmission lines which form the various 3D TLM nodes. The first 3D TLM node to appear with the introduction of the TLM method for 3D problems, was the **expanded node** (Akhtarzad and Johns, 1975). This node is a combination of three 2D shunt nodes and three 2D series nodes. Each of the shunt nodes (as discussed in Chapter 4) models TM modes and each of the series nodes models TE modes (Christopoulos, 1995). Combining these 2D nodes in three dimensional space results in the expanded node illustrated in Figure 6.4. In this node electric field components are

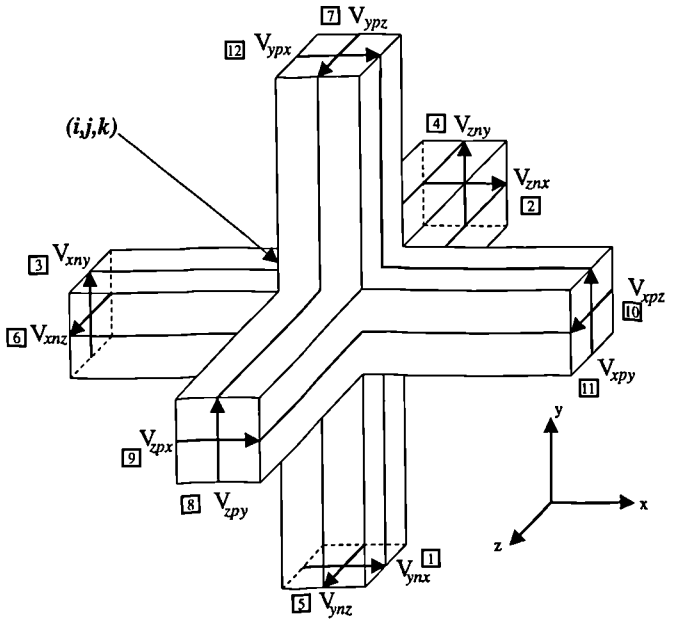

Figure 6.5: The 3D TLM symmetrical condensed node.

modelled by the shunt nodes and magnetic field ones by the series nodes. Comparing the topology of the expanded node with the Yee cell it is apparent that they are very similar. The 3D expanded node TLM model and the 3D FDTD have the same dispersion relation when the time step used in the FDTD algorithm is the same as the time step used in the 3D expanded node TLM (Choi, 1989).

An attempt to remedy the modelling of field components at separate locations resulted in the construction of the **asymmetrical condensed node** (Saguet and Pic, 1982). Although this node models all field components at the same location, the first connection to the node will be either a shunt or a series, hence the characterization of it as asymmetrical. Finally, Johns (1987) introduced the **symmetrical condensed node (SCN)** (see Figure 6.5) which solved the problem of modelling different field components at separate locations without being asymmetrical. However, for the development of the SCN the notion of TLM as a physical realizable network had to be abandoned. The node is not a structure that could be analyzed using an equivalent circuit as, for example, the 2D shunt node. Later developments of the SCN are the **hybrid symmetrical condensed node** (Scaramuza and Lowery, 1990; Berini and Wu, 1994) which has been developed to reduce the computational requirements of the model when modelling inhomogeneous media and TLM networks with variable spatial increment, and recently the **super-condensed symmetrical node** (Trenkic et al., 1994; 1995) which does not need the use of any stubs for

modelling media of different constitutive parameters.

One can immediately identify the advantages of condensed nodes (SCN, HSCN, SSCN) over expanded ones, since all electromagnetic field components are available at a single spatial location in the computational domain and without a time offset and the modelling of different media is simplified both from an algorithmic and conceptual point of view. In addition, early investigations (Choi, 1989), especially for the SCN, have shown that numerical dispersion is less in the symmetrical nodes than in the expanded ones. However, more recent analyses of symmetrical nodes (Nielsen and Hoefer, 1991; Nielsen, 1991; Nielsen and Hoefer, 1993; Krumpholz and Russer, 1994; Trenkic, 1995) have revealed that they can support *spurious modes* which potentially can contaminate the solution (Morente et al., 1994; Krumpholz et al., 1995). Since much evidence exists in the literature for the successful application of TLM using the SCN, its application for the GPR problem was investigated.[2]

6.3.1 The Symmetrical Condensed Node (SNC)

The original formulation of the SCN (Johns, 1987; Christopoulos, 1995) is based on a scattering matrix which in the usual TLM modelling process is used to determine the reflected voltage pulses from the node as a combination of incident ones, and a connection matrix which determines the interchange of voltage pulses between neighboring nodes. Symbolically, the process can be described in the same fashion as in the 2D case

$$ {}^{r}\underline{V}^{n} = \underline{S}\ {}^{i}\underline{V}^{n} \tag{6.17} $$

$$ {}^{i}\underline{V}^{n+1} = \underline{C}\ {}^{r}\underline{V}^{n} \tag{6.18} $$

However, the derivation of the SCN scattering matrix $\underline{S}$ is not based on the use of transmission line theory since equivalent circuits can not be used to describe the SCN. Therefore, the derivation of $\underline{S}$ involves assigning elements of the scattering matrix in a symbolic form using as a guide the interrelations of electromagnetic field components described by Maxwell's equations and their association with voltage pulses on the transmission lines of the SCN (Christopoulos, 1995). Numerical values for the elements of the scattering matrix

[2]Although the HSCN offers significant advantages over the SCN when variable spatial increments are used the difficulties encountered in applying ABCs to 3D TLM led to the use of the more simple regular SCN.

are obtained by invoking principles of energy and charge conservation. This procedure has been used to derive the SCN with stubs (Naylor and Desai, 1989).

It is not known if this "abstract" nature of the SCN has prompted research into alternative derivations. However, it is not apparent in the literature that such works exist for other "realizable" TLM networks. Krumpholz and Russer (1994b) described a derivation of the SCN directly from Maxwell's equations using concepts from the method of moments and LoVetri and Simons (1993) by expressing Maxwell's equations in conservation law form. Both Chen et al. (1991) and Jin and Vahldieck (1994) derived the 3D SCN TLM using finite difference procedures and concepts. However, in Chen et al. (1991) the concept of energy conservation has been used. All the above works involve derivations of the 3D SCN TLM which are more complicated than the original formalism. However, they demonstrated from a theoretical and conceptual point of view the relation of 3D SCN TLM with Maxwell's equations. As Jin and Vahldieck (1994) pointed out, the TLM method:

> "... can be considered as either a physical model of the transmission line network (Huygen's principle) or a mathematical model of the finite difference method (Maxwell's equations), depending on which concept one feels more comfortable with..."

In addition to direct derivations of the method from Maxwell's equations, (Herring, 1993; Trenkic et al., 1993) have introduced a new methodology to determine the scattering procedure of 3D TLM symmetrical condensed nodes without using a scattering matrix but instead via *scattering equations* which relate the reflected voltages from the node to the incident ones. To derive these scattering equations the principles of *conservation of charge* and *magnetic flux* are used, complemented by the requirement for *electric* and *magnetic field continuity* at the centre of the node. However, the principle of energy conservation is not used although the original scattering matrix can be obtained if required. It should be noted that the same scattering equations have been first introduced as empirical relations by Naylor and Ait-Sadi (1992). Their use was suggested as a more efficient and simple way to determine the scattering process in a symmetrical condensed node compared to the algorithm proposed by Tong and Fujino (1991). However, in their derivation Naylor and Ait-Sadi (1992) used non-realizable equivalent circuits for the SCN to aid the calculations (Naylor and Ait-Sadi, 1993).

The procedure of obtaining the scattering equations as introduced by (Herring, 1993) has been improved recently by (Trenkic, 1995). The modifications introduced allow the description of the scattering process of all existing condensed nodes including the new SSCN. The main difference between the two derivations is in the application of the electric and magnetic field continuity principle.

In the following, a short description of the derivation of the scattering equations for a regular ($\Delta x = \Delta y = \Delta z = \Delta l$) SCN node with open circuit and loss stubs is presented which is based on both the works of Herring (1993) and Trenkic (1995). The scattering and connection matrices for this node as well as for the regular SCN without stubs are given in Appendix B. In addition, a recently introduced notation for the ports of SCN (Herring, 1993) is used instead of the traditional numbering scheme (see Figure 6.5). Using this notation, its port of the SCN and the associated pulses are described by three subscripts. The first subscript denotes the direction of the line. The second, the position relevant to the centre of the node (positive or negative) and the third, the polarization of the voltage pulse. For example, V_1 in the original notation is denoted as V_{ynx}.

Consider a TLM SCN (Figure 6.5) representing an elementary volume of space Δl^3. Similar to 2D TLM the electromagnetic field components at the centre of the node are obtained with the following equivalences:

$$E_x \equiv -\frac{V_x}{\Delta l} \quad E_y \equiv -\frac{V_y}{\Delta l} \quad E_z \equiv -\frac{V_z}{\Delta l} \tag{6.19}$$

$$H_x \equiv \frac{I_x}{\Delta l} \quad H_y \equiv \frac{I_y}{\Delta l} \quad H_z \equiv \frac{I_z}{\Delta l} \tag{6.20}$$

where V_x, V_y, V_z are the total node voltages and I_x, I_y, I_z are the total circulating currents at the node. Further, the total capacitance, inductance and conductance in each of the principal directions of the node are associated to the constitutive parameters of the modelled medium

$$C_x = C_y = C_z \equiv \epsilon \Delta l \tag{6.21}$$

$$L_x = L_y = L_z \equiv \mu_0 \Delta l \tag{6.22}$$

$$G_x = G_y = G_z \equiv \sigma \Delta l \tag{6.23}$$

With the constraint that all the main transmission lines of the SCN have the same capacitance and inductance and that the node without stubs should represent the TLM background medium — chosen to be free-space — the distributed capacitance and induc-

tance of the main transmission lines are:

$$2C_d = \epsilon_0 \tag{6.24}$$

$$2L_d = \mu_0 \tag{6.25}$$

and their impedance Z_l is equal to the one of free-space ($Z_l = Z_0$). Thus the velocity of propagation for pulses in the transmission lines is easily deduced to be

$$u_l = 2c \tag{6.26}$$

and hence the time-step with which the TLM solution advances is defined by

$$\Delta t = \frac{\Delta l}{2c} \tag{6.27}$$

With the parameters of the main transmission lines defined, the normalized admittances of the open circuit and loss stubs introduced to model a medium of given ϵ_r and σ can be easily calculated and are

$$\hat{Y}_{sx} = \hat{Y}_{sy} = \hat{Y}_{sz} = \hat{Y}_s = 4(\epsilon_r - 1) \tag{6.28}$$

$$\hat{G}_{sx} = \hat{G}_{sy} = \hat{G}_{sz} = \hat{G}_s = \sigma \Delta l Z_0 \tag{6.29}$$

Since the parameters of the main transmission lines and of the open circuit and loss stubs have been established, the scattering equations are obtained by applying the principles of charge and magnetic flux conservation and by enforcing field continuity relations at the centre of the node.

Electric field continuity

For each electric field component there are two associated transmission lines. For example, considering the E_x component, the lines contributing are the y-directed and z-directed, y-polarized ones. Electric field continuity is expressed as the requirement that the field calculated by the y-directed lines be equal to the field obtained by the z-directed ones. Thus, in terms of the total voltage in each segment of these lines the condition of field continuity is expressed as

$$V_{ynx} + V_{ypx} = V_{znx} + V_{zpx} \tag{6.30}$$

The modification introduced by (Trenkic, 1995) is to require that the flow of charge along the segments of the same line to be continuous at the centre of the node, equating the

sum of charges on the line segments to the charge at the center

$$\frac{C_l}{2}(V_{ynx} + V_{ypx}) = C_l V_x \tag{6.31}$$

$$\frac{C_l}{2}(V_{znx} + V_{zpx}) = C_l V_x \tag{6.32}$$

were V_x is the total node voltage at the centre of the node thus (6.30) becomes

$$V_{ynx} + V_{ypx} = V_{znx} + V_{zpx} = 2V_x \tag{6.33}$$

Using the same procedure for the remaining electric field components and noting that the total voltage on a line is $V = {}^{i}V + {}^{r}V$ the following equations result:

$$V_x = \frac{1}{2}({}^{i}V_{ynx} + {}^{r}V_{ynx} + {}^{i}V_{ypx} + {}^{r}V_{ypx}) \tag{6.34}$$

$$V_x = \frac{1}{2}({}^{i}V_{znx} + {}^{r}V_{znx} + {}^{i}V_{zpx} + {}^{r}V_{zpx}) \tag{6.35}$$

$$V_y = \frac{1}{2}({}^{i}V_{xny} + {}^{r}V_{xny} + {}^{i}V_{xpy} + {}^{r}V_{xpy}) \tag{6.36}$$

$$V_y = \frac{1}{2}({}^{i}V_{zny} + {}^{r}V_{zny} + {}^{i}V_{zpy} + {}^{r}V_{zpy}) \tag{6.37}$$

$$V_z = \frac{1}{2}({}^{i}V_{xnz} + {}^{r}V_{xnz} + {}^{i}V_{xpz} + {}^{r}V_{zpz}) \tag{6.38}$$

$$V_z = \frac{1}{2}({}^{i}V_{ynz} + {}^{r}V_{ynz} + {}^{i}V_{ypz} + {}^{r}V_{ypz}) \tag{6.39}$$

Magnetic field continuity

Similarly to the electric field components, for each magnetic field one there are two associated transmission lines. For example, considering the H_x component the lines contributing to it are the y-directed, z-polarized and the z-directed, y-polarized ones. Magnetic field continuity is expressed by the requirement that the field calculated by the y-directed lines to be equal to the field obtained from the z-directed ones. Hence, the continuity condition is expressed as (Christopoulos, 1995)

$$I_{ynz} - I_{ypz} = I_{zpy} - I_{zny} \tag{6.40}$$

Further to the above condition , the magnetic flux across a line must be continuous. Therefore the sum of total flux linkages on the two segments of a line must be equal to that in the centre of the node (Trenkic, 1995)

$$\frac{L_l}{2}(I_{ynz} - I_{ypz}) = L_l I_x \tag{6.41}$$

$$\frac{L_l}{2}(I_{zpy} - I_{zny}) = L_l I_x \tag{6.42}$$

Hence (6.40) becomes

$$I_{ynz} - I_{ypz} = I_{zpy} - I_{zny} = 2I_x \tag{6.43}$$

Applying the same procedure for the remaining magnetic field components and replacing currents with voltages using

$$I = \frac{{}^{i}V - {}^{r}V}{Z_l} \tag{6.44}$$

the following equations result

$$I_x = \frac{1}{2Z_l}({}^{i}V_{ynz} - {}^{r}V_{ynz} - {}^{i}V_{ypz} + {}^{r}V_{ypz}) \tag{6.45}$$

$$I_x = \frac{1}{2Z_l}({}^{i}V_{zpy} - {}^{r}V_{zpy} - {}^{i}V_{zny} + {}^{r}V_{zny}) \tag{6.46}$$

$$I_y = \frac{1}{2Z_l}({}^{i}V_{zpx} - {}^{r}V_{zpx} - {}^{i}V_{znx} + {}^{r}V_{znx}) \tag{6.47}$$

$$I_y = \frac{1}{2Z_l}({}^{i}V_{xnz} - {}^{r}V_{xnz} - {}^{i}V_{xpz} + {}^{r}V_{xpz}) \tag{6.48}$$

$$I_z = \frac{1}{2Z_l}({}^{i}V_{xpy} - {}^{r}V_{xpy} - {}^{i}V_{xny} + {}^{r}V_{xny}) \tag{6.49}$$

$$I_z = \frac{1}{2Z_l}({}^{i}V_{ynx} - {}^{r}V_{ynx} - {}^{i}V_{ypx} + {}^{r}V_{ypx}) \tag{6.50}$$

Charge conservation

The principle of charge conservation applied to the lines contributing to electric field components requires that the charge associated with the incident voltage pulses to be equal to the charge associated with the reflected voltage pulses. For example, considering the E_x component, charge conservation on the lines contributing to it is expressed as

$${}^{i}Q_x = {}^{r}Q_x \tag{6.51}$$

and since $I = Q\Delta t$, the above is equivalent to Kirchhoff's current law for the lines contributing to the E_x component

$$\sum I = 0 \tag{6.52}$$

which in terms of voltage pulses can be written as

$$\begin{aligned} Y_l({}^{i}V_{ynx} - {}^{r}V_{ynx}) + Y_l({}^{i}V_{ypx} - {}^{r}V_{ypx}) + Y_l({}^{i}V_{znx} - {}^{r}V_{znx}) + Y_l({}^{i}V_{zpx} - {}^{r}V_{zpx}) \\ + Y_s({}^{i}V_{ox} - {}^{r}V_{ox}) - G_s\,{}^{r}V_{gx} = 0 \end{aligned} \tag{6.53}$$

The total voltage V_x at the node can be obtained as the voltage across the total capacitance C_x at the node from the relation

$$V_x = \frac{Q_x}{C_x} \tag{6.54}$$

Further, Q_x can be expressed as the sum of the total charge on the transmission lines and the open circuit stub contributing to V_x (Christopoulos, 1995). Therefore,

$$Q_x = \frac{C_l}{2}V_{ynx} + \frac{C_l}{2}V_{ypx} + \frac{C_l}{2}V_{znx} + \frac{C_l}{2}V_{zpx} + Y_s\frac{\Delta t}{2}V_{ox} \tag{6.55}$$

Since, $C_l = Y_l\Delta t$ and $C_x = 2C_l + Y_s\Delta t/2$ the total voltage V_x is

$$V_x = \frac{{}^iV_{ynx} + {}^rV_{ynx} + {}^iV_{ypx} + {}^rV_{ypx} + {}^iV_{znx} + {}^rV_{znx} + {}^iV_{zpx} + {}^rV_{zpx} + \hat{Y}_s\,{}^iV_{ox} + \hat{Y}_s\,{}^rV_{ox}}{4 + \hat{Y}_s} \tag{6.56}$$

Using (6.53) the reflected voltage pulses in the above equation can be expressed only in terms of incident ones and by noting that $V_{gx} = V_x$ the total voltage V_x for the SCN with open-circuit and loss stubs is

$$V_x = \frac{2}{4 + \hat{Y}_s + \hat{G}_s}({}^iV_{ynx} + {}^iV_{ypx} + {}^iV_{znx} + {}^iV_{zpx} + \hat{Y}_s\,{}^iV_{ox}) \tag{6.57}$$

By repeating the same procedure the total voltages V_y and V_z are obtained as

$$V_y = \frac{2}{4 + \hat{Y}_s + \hat{G}_s}({}^iV_{xny} + {}^iV_{xpy} + {}^iV_{zny} + {}^iV_{zpy} + \hat{Y}_s\,{}^iV_{oy}) \tag{6.58}$$

$$V_z = \frac{2}{4 + \hat{Y}_s + \hat{G}_s}({}^iV_{xnz} + {}^iV_{xpz} + {}^iV_{ynz} + {}^iV_{ypz} + \hat{Y}_s\,{}^iV_{oz}) \tag{6.59}$$

Magnetic flux conservation

Conservation of the magnetic flux applied to the lines contributing to magnetic field components is expressed as the requirement that the magnetic flux linkage of the incident pulses be equal to the one of the reflected pulses. For example, considering H_x, magnetic flux conservation is expressed as

$${}^i\Lambda_x = {}^r\Lambda_x \tag{6.60}$$

and since $\Lambda = V\Delta t$ the above is equivalent to Kirchhoff's voltage law for the lines contributing to the H_x component

$$\sum V = 0 \tag{6.61}$$

which in terms of voltage pulses can be written as

$$({}^iV_{ypz} + {}^rV_{ypz}) - ({}^iV_{zpy} + {}^rV_{zpy}) - ({}^iV_{ynz}) + {}^rV_{ynz}) + ({}^iV_{zny} + {}^rV_{zny}) = 0 \tag{6.62}$$

The total current I_x at the node can be obtained from the total flux linkage as

$$I_x = \frac{\Lambda_x}{L_x} \tag{6.63}$$

Further, Λ_x is the sum of the total flux linkages in the transmission lines contributing to I_x

$$\Lambda_x = \frac{L_l}{2}(I_{ypz} - I_{zpy} - I_{ynz} + I_{zny}) \tag{6.64}$$

Expressing current in terms of voltage pulses using (6.44) and with $L_l = Z_l \Delta t$ and $L_x = 2L_l$ the total current I_x is

$$I_x = \frac{({}^iV_{ypz} - {}^rV_{ypz}) - ({}^iV_{zpy} - {}^rV_{zpy}) - ({}^iV_{ynz} - {}^rV_{ynz}) + ({}^iV_{zny} - {}^rV_{zny})}{4Z_l} \tag{6.65}$$

Using (6.62) the reflected voltage pulses in (6.65) can be expressed in terms of incident ones and I_x can be obtained as

$$I_x = \frac{2}{4Z_l}({}^iV_{ypz} - {}^iV_{zpy} - {}^iV_{ynz} + {}^iV_{zny}) \tag{6.66}$$

Similarly, the other total currents I_y and I_z can be calculated

$$I_y = \frac{2}{4Z_l}({}^iV_{zpx} - {}^iV_{xpz} - {}^iV_{znx} + {}^iV_{xnz}) \tag{6.67}$$

$$I_z = \frac{2}{4Z_l}({}^iV_{xpy} - {}^iV_{ypx} - {}^iV_{xny} + {}^iV_{ynx}) \tag{6.68}$$

The scattering equations

The scattering equations are easily obtained by combinations (addition, subtraction) of one equation from (6.34)—(6.39) with an equation from (6.45)—(6.50). For example, subtracting (6.50) from (6.34)

$${}^rV_{ynx} = V_x - I_z Z_l - {}^iV_{ypx} \tag{6.69}$$

The remaining 11 equations are

$$^{r}V_{ypx} = V_x + I_z Z_l - {}^{i}V_{ynx} \tag{6.70}$$

$$^{r}V_{znx} = V_x + I_y Z_l - {}^{i}V_{zpx} \tag{6.71}$$

$$^{r}V_{zpx} = V_x - I_y Z_l - {}^{i}V_{znx} \tag{6.72}$$

$$^{r}V_{zny} = V_y - I_x Z_l - {}^{i}V_{zpy} \tag{6.73}$$

$$^{r}V_{zpy} = V_y + I_x Z_l - {}^{i}V_{zny} \tag{6.74}$$

$$^{r}V_{xny} = V_y + I_z Z_l - {}^{i}V_{xpy} \tag{6.75}$$

$$^{r}V_{xpy} = V_y - I_z Z_l - {}^{i}V_{xny} \tag{6.76}$$

$$^{r}V_{xnz} = V_z - I_y Z_l - {}^{i}V_{xpz} \tag{6.77}$$

$$^{r}V_{xpz} = V_z + I_y Z_l - {}^{i}V_{xnz} \tag{6.78}$$

$$^{r}V_{ynz} = V_z + I_x Z_l - {}^{i}V_{ypz} \tag{6.79}$$

$$^{r}V_{ypz} = V_z - I_x Z_l - {}^{i}V_{ynz} \tag{6.80}$$

the reflected voltages into the open-circuit stubs are easily obtained from the total voltages V_x, V_y, V_z as

$$^{r}V_{ox} = V_x - {}^{i}V_{ox} \tag{6.81}$$

$$^{r}V_{oy} = V_y - {}^{i}V_{oy} \tag{6.82}$$

$$^{r}V_{oz} = V_z - {}^{i}V_{oz} \tag{6.83}$$

The scattering process is completely described by equations (6.70)–(6.80) and (6.81)–(6.83). This can be easily verified using the scattering matrix of the node (see Appendix A)

6.3.2 Excitation and output of field quantities

The electromagnetic fields are directly obtained at the centre of the SCN using equations (6.57)–(6.59) and (6.66)–(6.68) and the equivalences between total node voltages and currents established by (6.20). The requirement to excite the TLM network using a small Hertzian dipole, which arises for GPR modelling, has not been accounted for in the original derivation of the method. It is possible however to introduce an infinitesimal current element by including its effect when the principle of charge conservation is applied. For example, if an x-directed infinitesimal current element ($I_x \delta l$) is introduced in the SCN,

the charge conservation equation (6.53) is modified as

$$(6.84)\quad Y_l({}^iV_{ynx}-{}^rV_{ynx})+Y_l({}^iV_{ypx}-{}^rV_{ypx})+Y_l({}^iV_{znx}-{}^rV_{znx})+Y_l({}^iV_{zpx}-{}^rV_{zpx})+Y_s({}^iV_{ox}-{}^rV_{ox})-G_s{}^rV_{gx}+I_x=0$$

and the total voltage V_x is then given by

$$(6.85)\quad V_x=\frac{2}{4+\hat{Y}_s+\hat{G}_s}({}^iV_{ynx}+{}^iV_{ypx}+{}^iV_{znx}+{}^iV_{zpx}+\hat{Y}_s{}^iV_{ox})+\frac{I_x}{Y_l(4+\hat{Y}_s+\hat{G}_s)}$$

Therefore, in obtaining the reflected voltage pulses from the SCN where the source is located (6.85) should be used instead of (6.57).

6.4 Numerical dispersion in 3D FDTD and 3D SCN TLM

The process of discretization unavoidably introduces errors in the modelling process. These errors are similar in nature to the ones discussed in Chapter 4 for 2D TLM and FDTD. Although staircasing and coarseness errors both affect the 3D TLM and FDTD in a similar fashion, the velocity error (numerical dispersion) differs significantly. An estimate of the velocity error can be obtained from dispersion relations of FDTD and TLM. As in the 2D case, these relations are obtained by examining the propagation of a monochromatic plane wave in the two models. The dispersion relation of 3D FDTD for a homogeneous and lossless medium is well known and can be easily derived from either the FDTD update equations (Fang, 1989) or from an equivalent finite difference disrcetization of the scalar wave equation (Chew, 1990)

$$(6.86)\quad [\frac{1}{c\Delta t}\sin(\frac{\omega\Delta t}{2})]^2=[\frac{1}{\Delta x}\sin(\frac{\beta_x\Delta x}{2})]^2+[\frac{1}{\Delta y}\sin(\frac{\beta_y\Delta y}{2})]^2+[\frac{1}{\Delta z}\sin(\frac{\beta_z\Delta z}{2})]^2$$

From the above relation it is clear that for propagation along the main diagonal of the FDTD lattice and when $\Delta x=\Delta y=\Delta z$ there is no dispersion at all when the FDTD algorithm is operated with the time step set at the limit of its stability criterion. Moreover, for propagating modes that are resolved well by the FDTD lattice using the small argument approximation for the sine functions in (6.86), the dispersion relation of 3D FDTD reduces to the ideal dispersion relation obtained from Maxwell's equations for a homogeneous loss-free medium:

$$(6.87)\quad \frac{\omega^2}{c^2}=\beta^2=\beta_x^2+\beta_y^2+\beta_z^2$$

The dispersion relation of the 3D SCN TLM is more difficult to obtain. In its general form it is given as a solution to an eigenvalue problem (Nielsen, 1991; Trenkic et al., 1995)

$$\det[\underline{\mathbf{P}}\,\underline{\mathbf{S}} - e^{j\omega\Delta t}\underline{\mathbf{I}}] = 0 \tag{6.88}$$

where $\underline{\mathbf{S}}$ is the scattering matrix and $\underline{\mathbf{P}}$ is the propagation (connection) matrix of the 3D SCN TLM. For a regular SCN the non zero entries of $\underline{\mathbf{P}}$ are (Nielsen, 1991; Morente et al., 1994):

$$P_{3,11} = P_{6,10} = e^{j\beta_x\Delta l} \qquad P_{10,6} = P_{11,3} = e^{-j\beta_x\Delta l} \tag{6.89}$$

$$P_{1,12} = P_{5,7} = e^{j\beta_y\Delta l} \qquad P_{7,5} = P_{12,1} = e^{-j\beta_y\Delta l} \tag{6.90}$$

$$P_{2,9} = P_{4,8} = e^{j\beta_z\Delta l} \qquad P_{8,4} = P_{9,2} = e^{-j\beta_z\Delta l} \tag{6.91}$$

the characteristic polynomial of the determinant in (6.88) relates ω with β_x,β_y and β_z. However, due to the size of the scattering and connection matrices such an expression has only been obtained for the regular SCN for which (with a different arrangement of the rows and columns of the scattering and connection matrices) it is possible to reduce the original eigenvalue problem described by equation (6.88) involving 12×12 matrices to an equivalent one using only 6×6 ones (Trenkic et al., 1995). Therefore, the closed-form expression of (6.88) has been obtained by (Krumpholz and Russer, 1994; Trenkic et al., 1995) only recently, whereas the eigenvalues of $\underline{\mathbf{P}}\,\underline{\mathbf{S}}$ have been studied numerically by (Nielsen and Hoefer, 1991; Nielsen, 1991; Nielsen and Hoefer, 1993). The closed-form expression for the dispersion relation of the regular SCN is (Trenkic et al., 1995):

$$\cos(\omega\Delta t)^2 = \frac{1}{4}\left[\cos(\beta_x\Delta l)\cos(\beta_y\Delta l) + \cos(\beta_y\Delta l)\cos(\beta_z\Delta l) + \cos(\beta_z\Delta l)\cos(\beta_x\Delta l) + 1\right] \tag{6.92}$$

In examining this relation, it is clear that there is no dispersion for propagation along the axis of the SCN. Further, using the small argument approximation to the cosine functions ($\cos(\theta) \approx 1 - \theta^2/2$) it is simple to arrive at (6.87) for a propagating mode in 3D SCN TLM.

A closer examination of (6.92) reveals that there are, however, other possible solutions to the SCN dispersion relation. These solutions do not correspond to the ideal dispersion relation and hence they are called *spurious* (Nielsen, 1991) or *unphysical* (Krumpholz and Russer, 1994) solutions. The existence of such solutions to the SCN dispersion relation can be seen by noting that all the cosine terms in (6.92) appear in products. Therefore,

since $\cos(\pi \pm \theta) = -\cos(\theta)$ it follows that the SCN dispersion relation can be written as:

$$\cos(\pi \pm \omega\Delta t)^2 = \frac{1}{4}\big[\cos(\pi \pm \beta_x\Delta l)\cos(\pi \pm \beta_y\Delta l) + \cos(\pi \pm \beta_y\Delta l)\cos(\pi \pm \beta_z\Delta l) + \cos(\pi \pm \beta_z\Delta l)\cos(\pi \pm \beta_x\Delta l) + 1\big] \tag{6.93}$$

Hence, if a physical solution is $(\omega,\beta_x,\beta_y,\beta_z)$ then the SCN can support spurious solutions of the form:

$$\pi/\Delta t \pm \omega, \pi/\Delta l \pm \beta_x, \pi/\Delta l \pm \beta_y, \pi/\Delta l \pm \beta_z \tag{6.94}$$

Further studies of the SCN dispersion relation reached similar conclusions for the SCN with stubs (Morente et al., 1995; Huber et al., 1995; Berini and Wu, 1995). However, the dispersion relation for this type of node has not been obtained in closed form. From the possible spurious solutions the most troublesome is the one described as $(\omega, \pi/\Delta l \pm \beta_x, \pi/\Delta l \pm \beta_y, \pi/\Delta l \pm \beta_z)$. Spurious solutions involving a high temporal frequency $(\pi/\Delta t \pm \omega)$ can be suppressed by using low frequency excitations in the TLM model (Nielsen and Hoefer, 1993). However, spurious solutions with high wavenumbers and low temporal frequency can not yet be suppressed if excited.

The fact that the SCN can support spurious modes does not necessarily means that any solution obtained by a SCN TLM model is not accurate. A significant amount of comparisons can be found in the literature between solutions obtained by 3D SCN TLM and analytical or experimental results (e.g. (Allen et al., 1987; Duffy et al., 1993; Christopoulos and Herring, 1993)) which suggests that if such spurious modes do exist they are not necessarily contaminating the TLM solutions. However, as will be examined in the following section, instabilities introduced by the application of ABCs in 3D TLM have been attributed to the amplification of spurious modes.

When only propagating physical modes are considered, a comparison can be made between the numerical dispersion in 3D FDTD and 3D SCN TLM. The equivalence of their dispersion relations for 2D models, obviously, does not hold for the 3D ones. Using the, same as in the 2D case, root finding iterative Newton-Raphson procedure (Press et al., 1992), the variations of the numerical phase velocity in 3D FDTD and TLM have been obtained as a function of normalized frequency $(\Delta l/\lambda)$ for three principal directions of propagation denoted as

[1 0 0] for axial propagation $\beta = \beta_x$

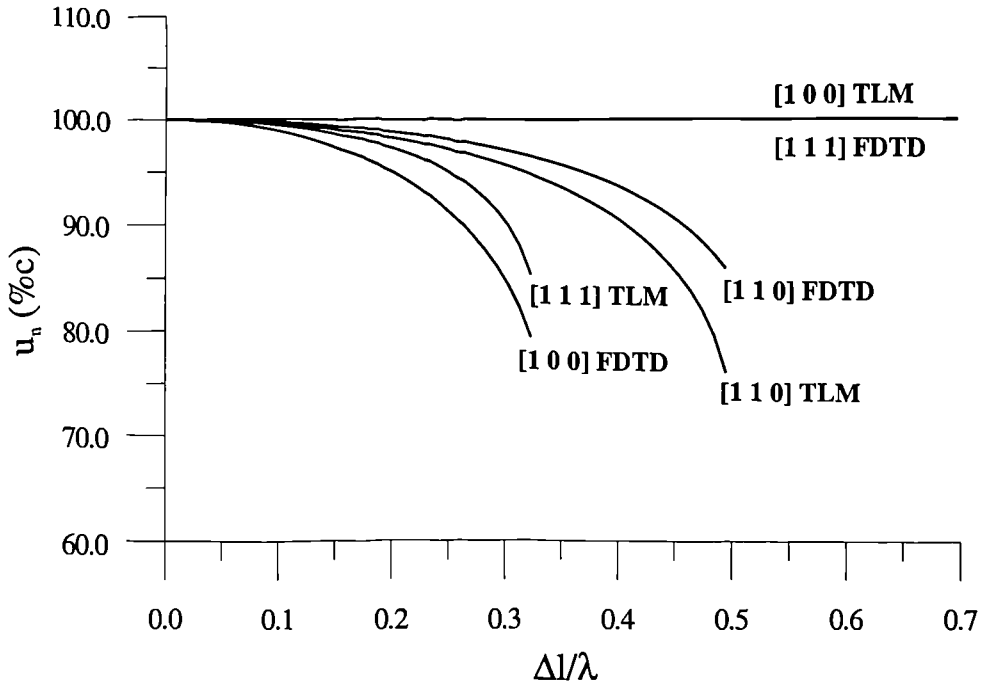

Figure 6.6: Numerical phase velocity as percentage of the free-space velocity for different discretizations ($\frac{\Delta l}{\lambda}$) in 3D TLM and FDTD.

[1 1 0] for diagonal propagation with the wavevector lying on the x–y plane with $\beta = \hat{x}\beta_x + \hat{y}\beta_y$ and $\beta_x = \beta_y$

[1 1 1] for diagonal propagation with $\beta = \hat{x}\beta_x + \hat{y}\beta_y + \hat{z}\beta_z$ and $\beta_x = \beta_y = \beta_z$

From the results presented in Figure 6.6, is evident that for both methods there is a direction of zero numerical dispersion which are not the same. Further, the overall dispersion for propagating modes is less in TLM than in FDTD. Numerical dispersion in FDTD will be further increased if the time step is set to be the same with the time-step of the TLM model, which is less than that allowed by its stability criterion.

6.5 Application of ABCs in 3D FDTD and 3D TLM

The truncation of the computational domain of the 3D GPR models has to be addressed with the application of ABCs. In addition, good ABC performance is very important in a 3D model because the use of "white space" between the truncation boundaries and the source and targets leads to a substantial increase in the required computational resources.

Because of their good performance in the 2D models the ABCs of Higdon and Liao et al.

have been investigated for the 3D models. Their implementation is analogous to the 2D case. The only difference is that since the truncation boundary is a plane in a 3D model they have to be applied to two tangential electric field components and to two voltage pulses at each truncation plane of a 3D FDTD and TLM model respectively.

Application of high order ABCs in the 3D FDTD model resulted in instabilities which were easily controlled by the introduction of loss factors (see Chapter 4). Since the performance of a third order Higdon ABC was found to be almost identical to the one of the third order Liao, the Higdon ABC was employed for the 3D FDTD GPR model because it required less computer storage.[3]

The application of the ABCs in the 3D SCN TLM model resulted in instabilities which unfortunately can not be controlled by the introduction of loss factors without degrading their performance to the point that their application is useless. The fact that even a first order ABC (which usually does not introduce instabilities even for simulations involving thousands of iterations) was found to be unstable clearly indicates that the instabilities of the ABCs are not due only to numerical noise as in the FDTD and 2D TLM models.

In order to ascertain if this problem occurs in general 3D TLM models and not only when symmetrical condensed nodes are used, a 3D TLM algorithm based on the expanded node (Akhtarzad and Johns, 1975) was developed. Both the Higdon's and Liao's ABCs were tested and found to have a similar performance as in the 2D TLM models examined in Chapter 4. Figure 6.7 presents a comparison between 3D FDTD and TLM (expanded node) from a numerical test. This consisted of a small ($30\Delta l \times 30\Delta l \times 30\Delta l$) computational domain excited at its centre by a z-directed Hertzian dipole. A stabilized third order Higdon ABC is used in both models. The z component of the electric field obtained at point [25,254,25] is compared with the closed-form solution (Ziolkowski et al., 1983). The current element used to represent the source had a time variation as

$$I_z \Delta l = \frac{d}{dt} e^{-\zeta(t-\xi\Delta t)^2)} \tag{6.95}$$

where $\zeta = (4/(\xi\Delta t)^2)$ and $\xi = 64.0$. The agreement between the closed-form solution and the response of FDTD and TLM models is very good.

[3]The Higdon ABC uses field components at the current time-step but the Liao ABC uses field components only of past time-steps. The overall number of field components required by both ABCs is the same. However, the components at the current time-step required by the Higdon ABC do not need to be stored in separate arrays.

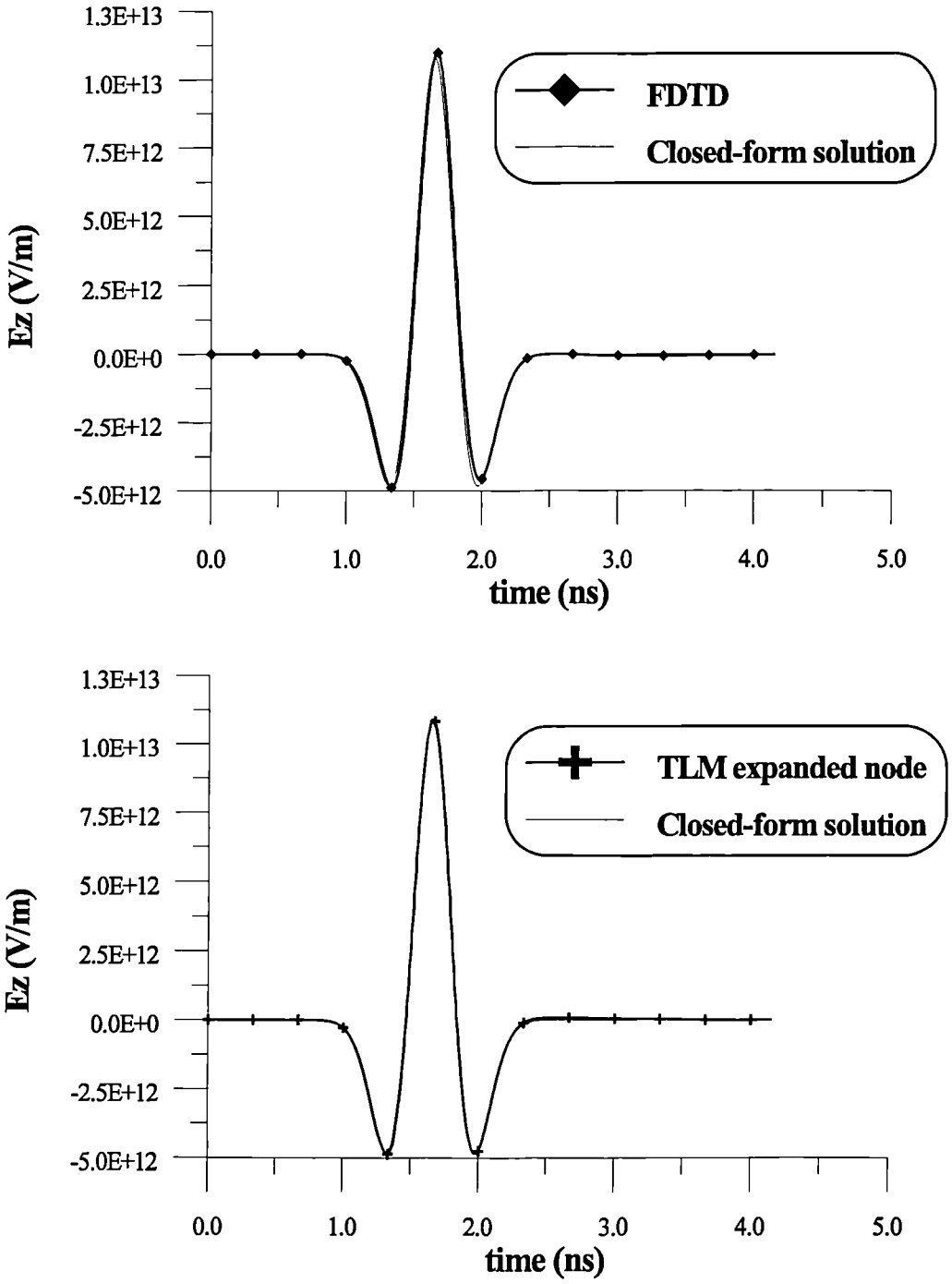

Figure 6.7: Comparison between the closed-form solution and 3D FDTD (top) and 3D expanded node TLM (bottom) of the E_z component radiated from a small z-directed dipole.

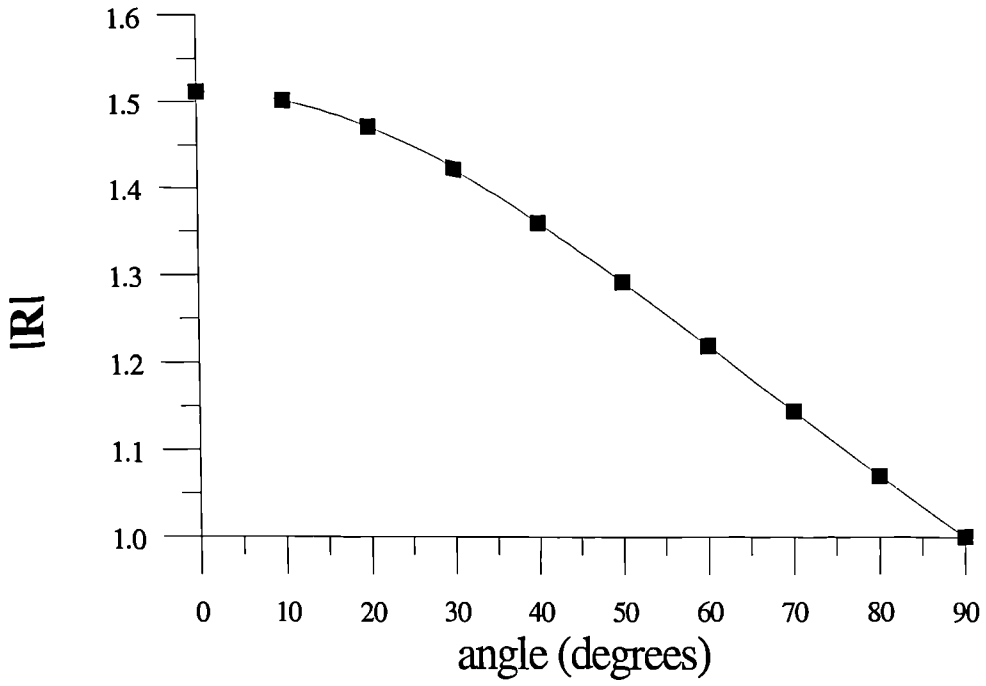

Figure 6.8: Magnitude of theoretical reflection coefficients of the second order Higdon ABC for a possible spurious mode.

In considering that stable ABCs can be implemented in 3D TLM using the expanded node, their unstable behaviour should be related to specific features of symmetrical condensed nodes. Chen et al. (1993) attributed the instabilities to the possible existence of low amplitude spurious modes which, although do not appear to have a significant effect on the solution where a "matched termination" ABC was used, are amplified by a higher order ABC and introduce instabilities. To verify that claim, Chen et al. (1993) calculated the magnitude of the theoretical reflection coefficients of the Higdon's ABC for a possible propagating spurious mode and showed that they are greater than 1. These theoretical reflection coefficients for a second order Higdon ABC are illustrated in Figure 6.8 (Chen et al., 1993). Further, in order to remedy the problem of ABC related instabilities Chen et al. (1993) proposed the use of two ABCs; one for normal modes and one for spurious modes. The ABC for spurious modes was constructed by considering that there is a phase difference of 180 degrees between a normal mode and a spurious one (reverse polarity). Further, a reduction in the temporal sampling rate was introduced from Δt to $2\Delta t$. According to Chen et al. (1993), this reduction was introduced because for an incident pulse at one port of a SCN a reflected pulse appears (due to this incident pulse) after one time-step. The combination of the modified "normal" and "spurious" modes ABC appears to have a magnitude of theoretical reflection coefficients less than 1 for both modes. However,

instabilities were still caused by the modified ABC which were attributed to numerical noise or to the small "white space" between the ABCs and the radiating target (Chen et al. 1993).

Numerical experiments performed in this work with the modified ABC proposed by Chen et al. (1993) did not result in a stable performance. Further, the introduction of loss factors did not increase the stability of the ABC without degrading its performance significantly.

In an earlier investigation of the application of ABCs to the TLM method, Morente et al. (1992) observed that the simple first order "average" ABC as proposed by Higdon (1987) proved to be stable in 3D SCN TLM simulations. Numerical experiments verified the findings of Morente et al. (1992) in terms of stability for this ABC. However, the magnitude of the theoretical reflection coefficients of this ABC for a possible propagating spurious mode are similar to the unmodified general Higdon ABC and therefore the ABC should amplify these type of modes instead of absorbing them. From this contradictory result it is suggested that conclusions can not be drawn about the stability of an ABC based solely on its theoretical reflection coefficients as suggested by Chen et al. (1993).

The formulation of the "average" ABC as reported by Morente et al. (1992) can not be used when the medium adjacent to it is different than free-space. Using the general formula given by Higdon (1987) for this ABC this adjustment is possible. However, the ABC did not exhibit the same stable performance. Moreover, higher orders of this ABC were found to be unstable even for simulations involving only free-space (Morente et al., 1992).

In a more recent investigation concerning the application of ABCs in SCN TLM for modelling planar structures, Eswarappa and Hoefer (1994) suggested that to overcome the problem of ABC instabilities in 3D SCN TLM simulations the mixing parameters in the Higdon ABC have to be reduced from their customary values of 0.5 to 0.25. This was suggested following the remark in Higdon's paper (Higdon, 1987) that the 0.5 value for the mixing parameters correspond to the stability limit of the ABC. Further, the authors remark that the introduction of loss factors to the ABC did not have an effect on its performance. Numerical tests using a small computational domain excited by Hertzian dipoles were carried out and verified partly the claim of Eswarappa and Hoefer (1994). The resultant Higdon ABCs were found to be stable for a greater number of iterations than the original ones. However, instabilities finally occurred which could not be successfully

controlled by the introduction of loss factors in the ABCs.

It is clear from the above discussion that the successful application of ABCs in 3D TLM is still an unsolved problem and the subject of current research. Since a detailed investigation is beyond the scope of this work, an empirical approach was followed and different discretizations of the Higdon ABC were tested. As a result of this investigation a new modification of the Higdon ABC was found to be stable in 3D TLM simulations for both the first and second order. In the following section the modified Higdon ABC will be discussed.

6.6 A stable form of the Higdon ABC for 3D SCN TLM

From the discussion in the previous section it is evident that the discretization of a Higdon's ABC affects its performance and stability when applied to 3D SCN TLM. A stable form for this ABC was found by introducing the following modifications to its original formulation (see Chapter 4):

A. a reduction in the mixing parameters from $a = b = 0.5$ to 0.25

B. an increase in both the spatial and temporal sampling interval or field components from Δl, Δt to $2\Delta l$, $2\Delta t$

The magnitude of the theoretical reflection coefficients of the modified second order ABC for both normal and spurious modes are illustrated in Figure 6.9. Although the reflection coefficients of the modified ABC appear to be greater than the original second order Higdon ABC (see Chapter 4), the ABC still exhibited good performance, as verified by numerical tests.

The stability of this ABC was examined by means of numerical tests using a small 3D SCN TLM network ($30\Delta l \times 30\Delta l \times 30\Delta l$) excited by Hertzian dipoles at its center. Even for very long runs (20000 iterations) no instabilities where observed when the first order of this ABC was used and the introduction of any loss factors was not necessary. Similar tests using the second order of the ABC were found to lead to instabilities which could, however, be suppressed by introducing a small loss factor in the formulation ($e = 0.43/\Delta l$). With the introduction of this loss factor the ABC did not introduce any instabilities for

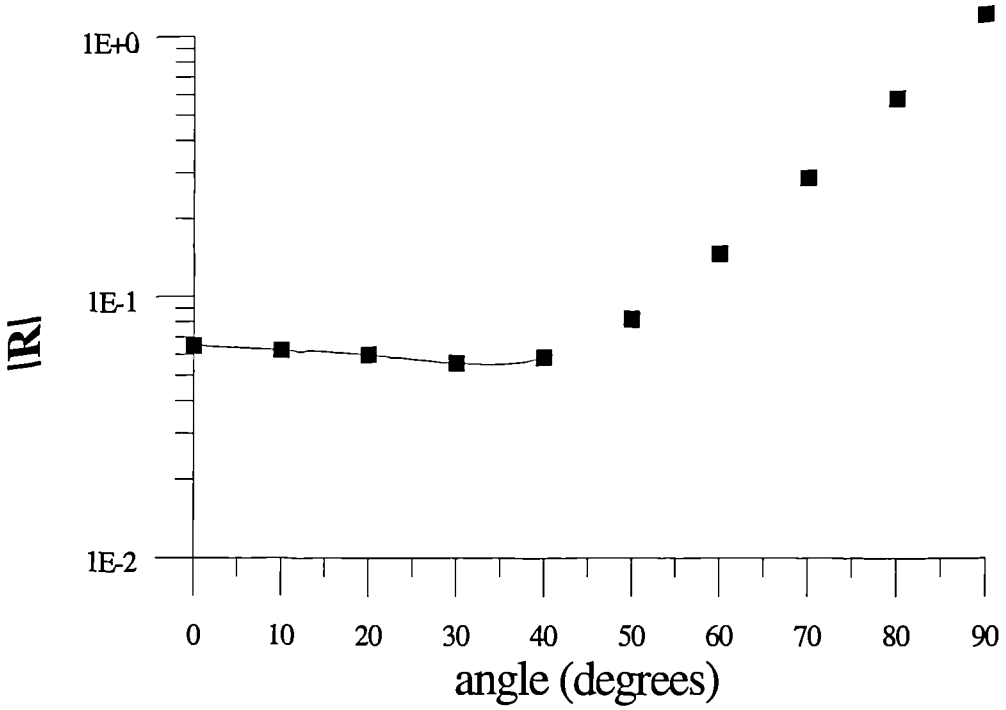

Figure 6.9: Magnitude of theoretical reflection coefficients of the modified ABC for both normal and spurious modes ($\Delta l = 0.1\lambda$).

tests involving thousands of iterations, as in the first order case.

To illustrate the stability of this ABC the first 2500 iterations of the calculated E_z field component of a z-directed Hertzian dipole located at the centre of the small 3D TLM network used for the numerical tests is presented in Figure 6.10, with the output point located at [25,25,25]. The time variation of the source is described by equation (6.95) and, in order to compare the SCN response with the one obtained by 3D FDTD and expanded node TLM, the same parameters were used. The improvement in accuracy can be seen by comparing the same response with the one obtained when the "matched termination" ABC was used. This is illustrated in Figure 6.11 where the TLM responses are compared with the closed-form solution. The comparison clearly indicates the superior performance of the modified ABC.

In order to apply an ABC to a GPR model, the variations in the constitutive parameters of the media adjacent to the ABC have to be taken into account. As demonstrated in Chapter 4, adjusting the velocity of propagation in the ABC formulation to reflect the deviation of permittivity from that of free-space was adequate. Attempting such an adjustment to the modified ABC, however, did not result in the same performance as in the free-space case. Although no instabilities occurred, there were small reflections from the ABC.

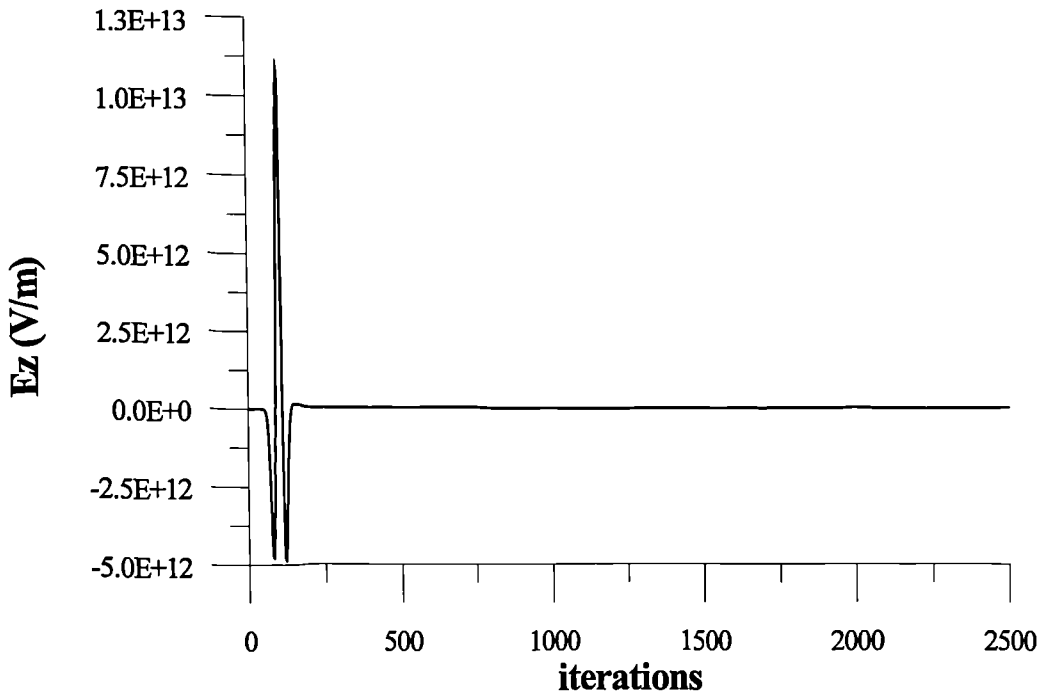

Figure 6.10: First 2500 iterations of the E_z field component radiated from a z-directed dipole calculated by SCN TLM.

For example, results from the same numerical test used to examine the stability of the ABC with a medium with relative permittivity of $\epsilon_r = 3$ clearly indicated the problem. This is illustrated in Figure 6.12, where the SCN TLM response is compared with an identical test using the 3D expanded node TLM model. The reasons for this reduction in performance are not yet clearly established. One possible explanation can be based on the results of recent investigations on the numerical dispersion in 3D SCN TLM. Nielsen and Hoefer (1991) and, more recently Morente et al. (1994), have showed that in a regular SCN without stubs, both the normal and any possible spurious modes propagate with the same velocity in the TLM network. However, when open-circuit stubs are used this is not the case (Huber et al., 1995; Trenkic, 1995). When an open-circuit stub is introduced, it appears that any well-resolved normal modes propagate with a velocity determined by the constitutive parameters of the simulated medium, but any possible spurious modes will still propagate with the velocity of light (free-space).

As the modified ABC does not exhibit a very good performance for media other than free-space, it can not be used without caution in a 3D GPR model based on the SCN. However, its use in other electromagnetic field problems involving targets located in free-space will be of benefit, as is suggested by the improvement in the TLM solution off the Hertzian dipole. This improvement has been further verified by examining TLM solutions

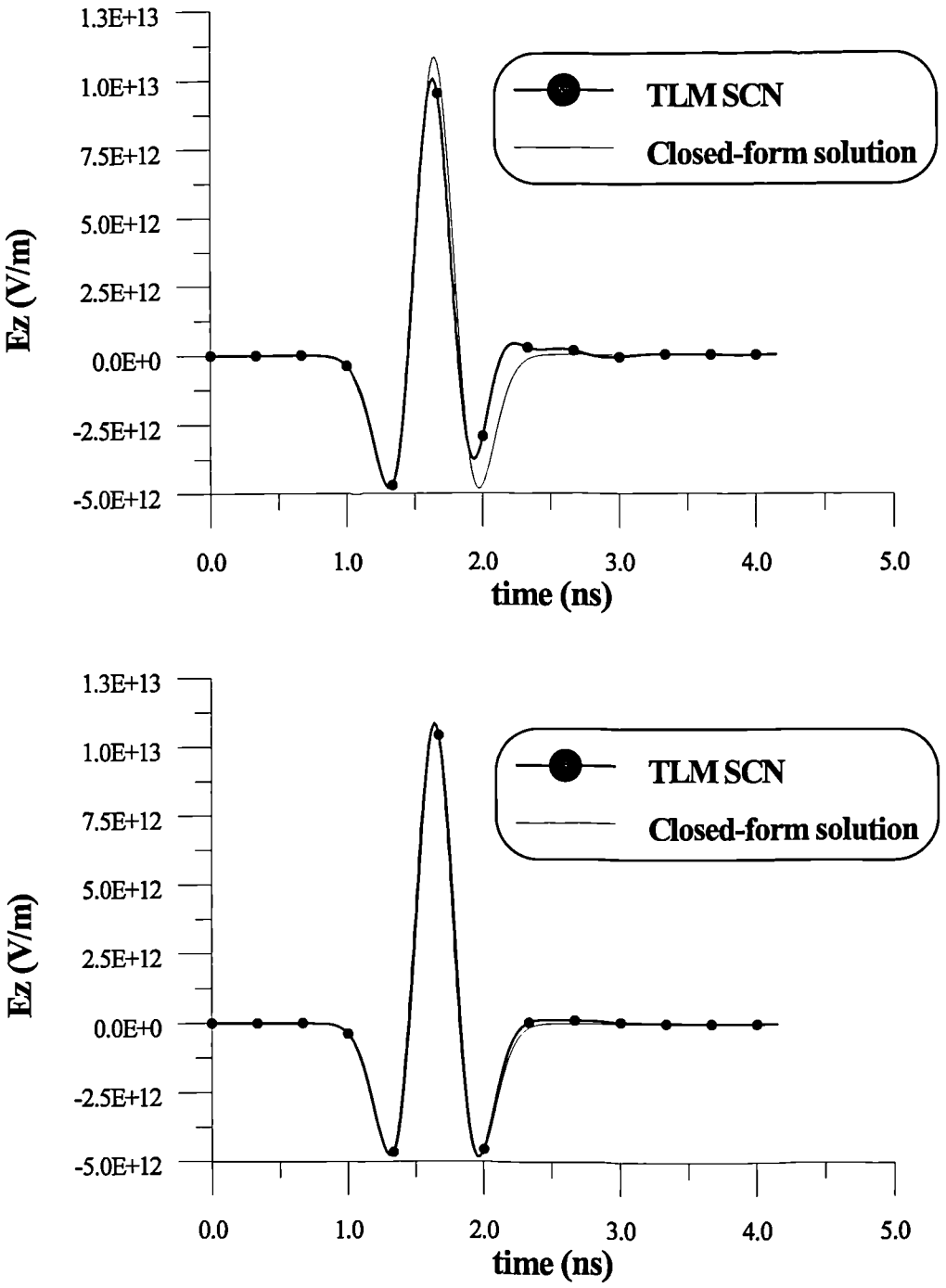

Figure 6.11: Comparison between the closed-form solution and 3D SCN TLM using the "matched termination" ABC (top) and the second order modified Higdon (bottom) of the E_z component radiated from a small z-directed dipole.

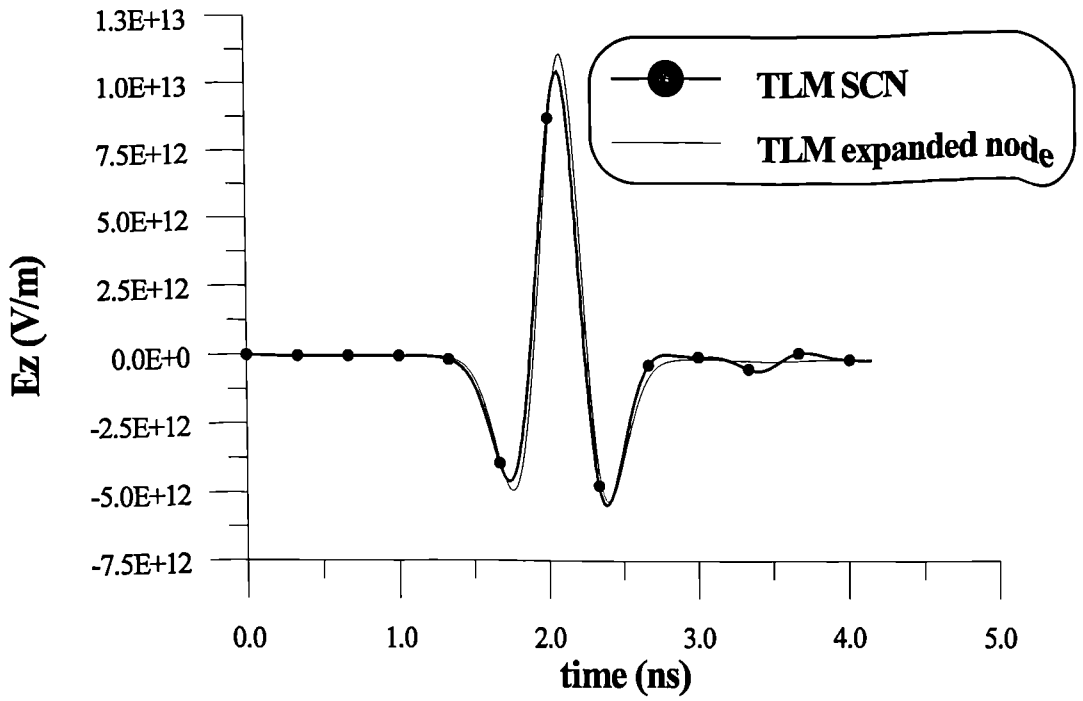

Figure 6.12: Comparison between the responses obtained by 3D expanded node and SCN TLM of the E_z component radiated from a small z-directed dipole located within a homogeneous medium of $\epsilon_r = 3$.

obtained from various targets located in free-space and illuminated by plane waves. For example, in Figure 6.13 the backscatter electric field from a perfectly conducting sphere of radius $r = 10\Delta l$ illuminated by a z-polarized Gaussian pulse plane wave of the form

$$e^{-\zeta(t-\xi\Delta t)^2)} \tag{6.96}$$

($\zeta = (4/(\xi\Delta t)^2)$ and $\xi = 64.0$), is presented and the improvement of the solution over that obtained using the "matched termination" ABC is evident when both are compared to a reference solution obtained using an ($100\Delta l \times 100\Delta l \times 100\Delta l$) TLM network truncated with the second order modified ABC. The wave-vector of the incident field lies in the x–y plane and forms an angle of 45 degrees with the x axis. A schematic drawing of the TLM model is presented in Figure 6.14. Further, the poor performance that the matched termination ABC exhibits can be seen in Figure 6.13 where the reference solution is compared with that obtained from an identical model using the matched termination ABC. Even when a large computational domain is used, there are still observable reflections from the truncation boundaries.

In order to apply the ABC only to outgoing scattered fields, for these type of numerical experiments a new scattered field TLM formulation has been used. In this formulation

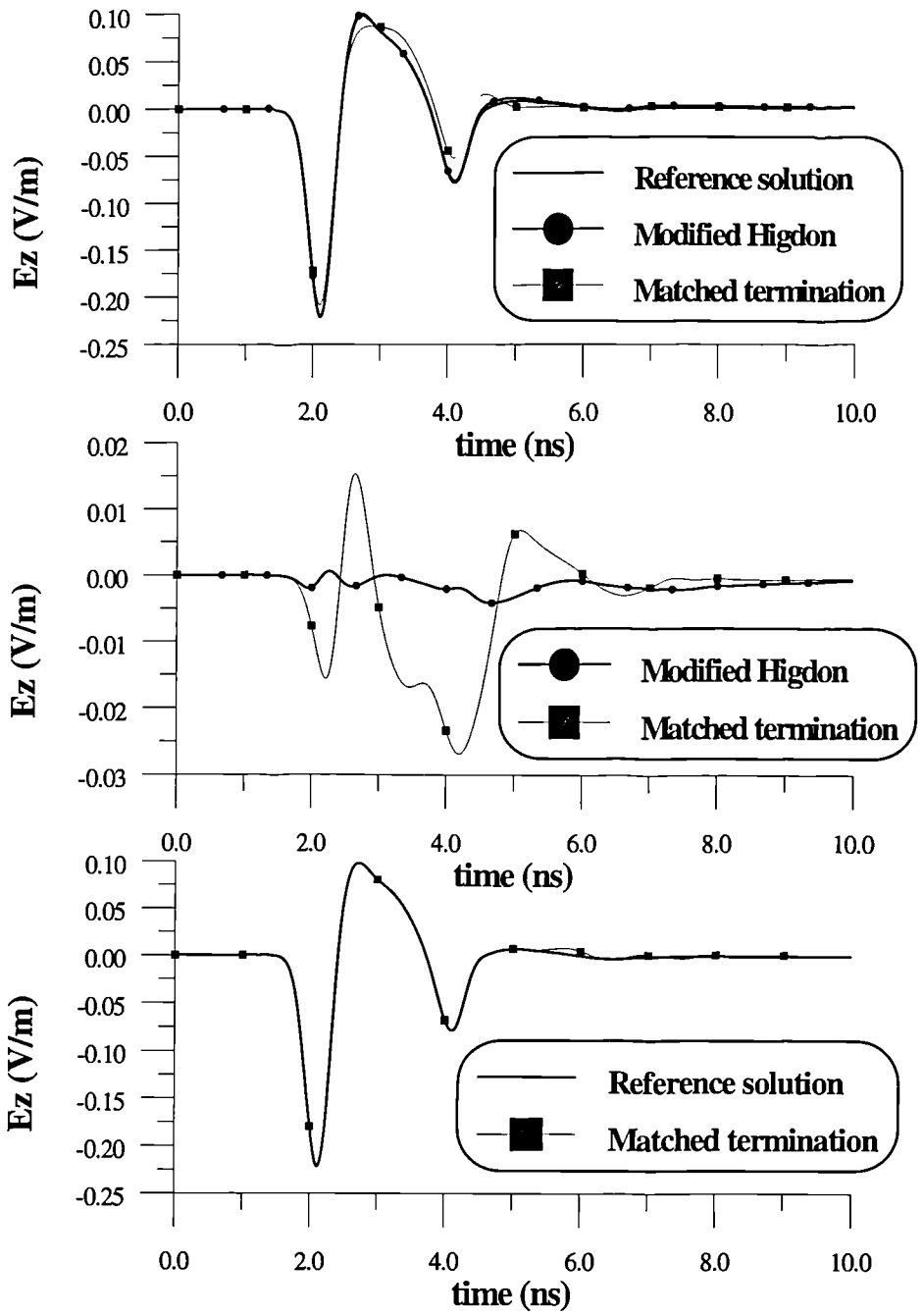

Figure 6.13: Comparison of the back-scattered electric field from a perfectly conducting sphere using different ABCs. [top]: Comparison with the reference solution. [middle]: Difference from the reference solution. [bottom]: Comparison with the reference solution of the back-scattered electric field from the same target using the same size model as the one used to calculate the reference solution but with a "matched termination" ABC.

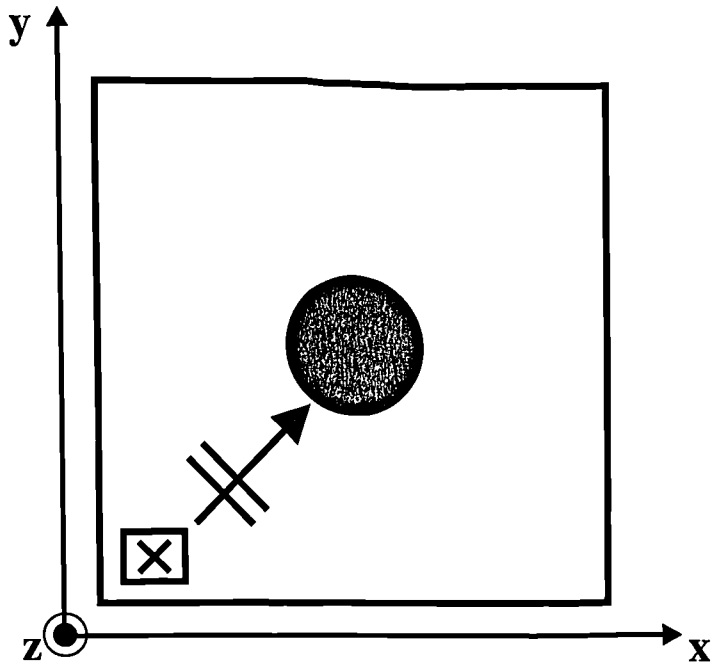

Figure 6.14: Schematic cross section (x–y plane) of the 3D SCN TLM model of the perfectly conducting sphere.

the TLM algorithm is used to simulate only scattered fields, since the incident ones (plane waves) can be specified analytically. This approach, known as the *separate field formalism*, has been used in the FDTD method (Kunz and Luebbers, 1993). However, it appears that such a formulation did not exist for the TLM method. The necessary modifications to the TLM algorithm are described in Appendix B.

6.7 3D FDTD versus 3D SCN TLM

A comparison between 3D SCN TLM and 3D FDTD is appropriate, considering the relevant merits and limitations of the two models. The advantages of the TLM model are the modelling of all six electromagnetic field components at the same point in the computational domain. With the use of stubs to model different dielectric media, the modelling of objects is straightforward, both from algorithmic and conceptual point of view. Another significant advantage of TLM is the finer and easier description of boundaries by placing them between the TLM nodes. There, known conditions affecting the electric and magnetic fields can be introduced (e.g. perfect electric or magnetic conducting surfaces). These conditions are easily incorporated because in TLM electric and magnetic fields are available at the same spatial location. The staggered placement of field components in the

Yee cell introduces a "fuzziness" in the description of such boundaries in FDTD. However, such an advantage is not of great importance in GPR modelling in which one is usually concerned with the modelling of volumetric targets.

The major drawbacks of TLM are the computational requirements of the algorithm. For the SCN without the incorporation of permeability stubs, the total number of variables which should be stored per node are 15, whereas FDTD requires only 6 variables. Moreover, the problem of instabilities when ABCs are incorporated in the TLM algorithm restricts its applicability further since the use of a low order ABC requires that both source and targets are located at a sufficient distance away from the truncation boundary (not less than 20 nodes). The modified Higdon ABC introduced in this Chapter can be used to relax this requirement albeit for models involving targets located in free-space.

The main advantages of the 3D FDTD model are the very good performance of ABCs and the moderate computational requirements (compared to 3D TLM). However, the staggered placement of field components in the Yee cell presents some conceptual difficulties in modelling regions of different constitutive parameters in the computational domain especially if a very fine description of boundaries is required. This will be more apparent when both the permittivity and permeability are varied.

Comparing the propagation characteristics of the two methods TLM exhibits less numerical dispersion than FDTD (Morente et al., 1994). However, such an advantage has to be weighted by the fact that SCN TLM can support unphysical solutions. It has not yet been established if such unphysical solutions contaminate the responses obtained by TLM models and further work is required to establish their significance in TLM analysis.

6.8 Discussion

In this Chapter the methodology on which three dimensional models GPR models are based was presented. From the different TLM formulations which exist that employing the symmetrical condensed node is examined. However, this node supports spurious modes which, although do not appear to contaminate the solution, are suggested to be related to the unstable performance of ABCs in 3D SCN TLM. Because the good performance of ABCs is very important for GPR models, where the increase of "white space" leads to a substantial increase of the required computer resources, a stable formulation

for the Higdon ABC was found by following an empirical approach. The stability and very good performance of this modified ABC was examined by means of numerical experiments and comparisons with FDTD and a 3D TLM model based on the expanded node. However, the good performance of this ABC does not extrapolate to the case when it is located adjacent to media other than free-space. A possible explanation in view of recent analyses of numerical dispersion in a stub loaded SCN, is that any possible small amplitude spurious modes — if excited — will still propagate with the velocity of light in this node instead of the one determined by the properties of the simulated medium (as the physical modes will). Hence, the ABC will be mismatched to these type of modes. The good performance of the modified ABC demonstrated using numerical experiments when the TLM network was excited by a small Hertzian dipole was demonstrated when plane wave scattering from targets located in free-space was considered. This has been studied using a new modification to the TLM algorithm which allows the simulation of scattered electromagnetic fields only, since the known incident field can be specified analytically.

7

Three dimensional numerical modelling of GPR — PART II: Results

7.1 Introduction

In this Chapter, results of 3D GPR modelling using the FDTD and TLM methods are presented. A major advantage of these models is the ability to include in the analysis the effects of the three dimensional nature of targets on GPR scans. Further, they allow the investigation of alternative survey procedures which can possibly enhance the detection of small localized targets which are those mainly sought in shallow-depth applications of GPR. Hence, simulated responses of simple targets such as the perfectly conducting cylinder, circular disk and the rectangular and cylindrical voids are considered here. In a similar fashion to the 2D case, the near-field radiation patterns of the source when located over a half-space are examined first.

For all the simulated responses presented here a ricker wavelet (see Chapter 5) is used to describe the time variation of the current element simulating the GPR transmitting antenna. In addition, GPR scans are presented in a gray-scale image format which is more

advantageous when small amplitude signals are present. Because of the unsatisfactory performance of ABCs in 3D SCN TLM, the FDTD model has been mainly used to obtain synthetic GPR signatures. However, simulated responses obtained by TLM are shown to be in good agreement with the FDTD ones when the effects of the ABCs are kept to a minimum.

7.2 Simulated field patterns of a horizontal dipole over a half-space

The radiation patterns of a dipole antenna located over a half-space is of interest in GPR surveying. Formulas to calculate the radiation patterns of a Hertzian dipole over a half-space have been reported by Smith (1984) and Engheta et al. (1982). These formulas obtained using asymptotic techniques are strictly valid for far-field calculations (Smith, 1984). Calculating numerically these far-field antenna patterns using FDTD or TLM is not a straightforward procedure since the near-field solution from either FDTD or TLM has to be transformed to a far-field one if the use of an unrealistically large computational domain is to be avoided. When the antenna is located within a homogeneous medium a transformation of the near-fields obtained by the numerical simulation to the analogous far-fields is possible and procedures to do so have been reported for FDTD (Taflove, 1995) and TLM (German, 1990). Unfortunately, when the antenna is located close to a half-space such a transformation requires the use of a Greens function which is not available in closed-form (see Chapter 3). However, field patterns obtained using 3D FDTD or TLM when the observation point is not very close to the source should at least exhibit similar characteristics to the far-field ones. In addition, such patterns are of interest since targets are not always located in the far-field region of the GPR antennas.

Most commonly field patterns are obtained in the two principal E- and H-planes (Balanis, 1982). Assuming that the dipole source is oriented in the x direction, these principal planes are illustrated in Figure 7.1. The time domain formulation of the models allows the calculation of a number of field patterns with a single computation. These are obtained by transforming the time domain fields into the frequency domain by means of a fast Fourier transform (FFT) and considering field patterns for different frequency components. Different patterns are obtained since the electrical height of the source from the interface increases with frequency. Further, a similar increase of the electrical distance[1] between the

[1]The electrical distance and height are the distance to the observation point and the height of the

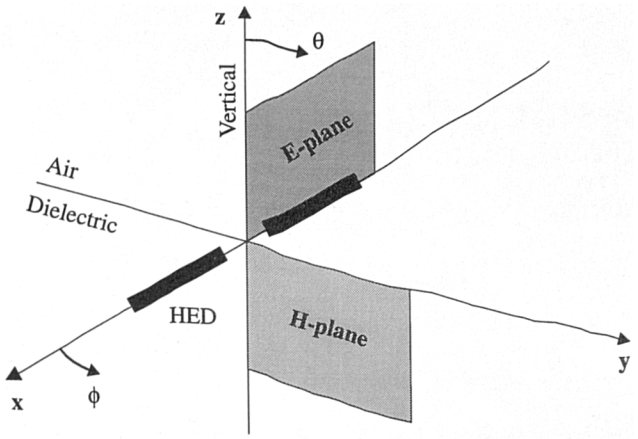

Figure 7.1: Principal H- and E- planes of a horizontal Hertzian dipole located over a half-space.

observation point and the source means that patterns at high frequencies will resemble the theoretical far-field ones. However, numerical dispersion in the model prohibits the use of very high frequency components because then the velocity error becomes significant and distortions in the amplitude and phase of the fields significantly affect the calculations.

Another characteristic of far-field patterns is that they do not depend on the distance between the observation point and the source (which in any case is assumed to be significant). However, this is not true for patterns calculated using a numerical model and are based on observations at a relatively small distance from the source. Because the electrical distance to observation points within the air and the half-space regions in the models differs and is not necessarily long, it was found that it is beneficial to scale the amplitude of the fields by their respective wavelength in both regions. This scaling does not affect the shape of the field patterns but does reduce the effect of the amplitude variation with distance in the two different regions.

antenna normalized with respect to the wavelength.

7.2.1 H-plane patterns

The H-plane patterns of an x-directed dipole have been obtained using an FDTD model comprised of (30,170,170) Yee cells by sampling the $E_\phi = -E_x$ field component every two degrees on a circle of radius $r = 0.6$ metre with its center located at the reference point [15 85 86] on the interface. The source is located 5 centimetres above the interface (5 FDTD cells above the reference point at [15 85 91]), and a ricker wavelet with $f_s = 600$ MHz is used to describe the time variation of the current element. In the model the three principal spatial increments are set to $\Delta l = 0.01$ metre and the time-step to $\Delta t = \Delta l/(2c)$. The H-plane field patterns obtained at a range of frequencies for two different lossless media ($\epsilon_r = 3$ and $\epsilon_r = 6$) are presented in Figures 7.2 and 7.3.

Considering the field patterns for low frequencies, both the observation points and the height of the dipole are small in terms of their wavelength. Therefore, as can be observed in Figure 7.2, the patterns show that the fields are not confined in a small area within the half-space (small directivity) and, in addition, the source radiates preferably within the half-space since the back-lobe (radiation in air) appears to be small. This is in agreement with the observations and the conclusions of Smith, (1984) (see Chapter 2). As the frequency is increased and the electrical height of the source becomes a significant portion of the wavelength, the fields become more directive in the half-space and form a main-lobe with an angular extent, approaching the theoretical far-field one, of $2\theta_c$ where $\theta_c = \sin^{-1}(1/\sqrt{(\epsilon_r)})$ is the critical angle (see Figure 7.3). However, the back-lobe increases. This is consistent with the theoretical far-field patterns (Smith, 1984).

7.2.2 E-plane field patterns

In GPR surveying the H-plane patterns are most important since the scan line lies in that plane. E-plane patterns are easily obtained, however, with the same model configuration employed for the calculation of H-plane ones, using a y-directed dipole instead. The E_θ field component is obtained from the Cartesian components E_y and E_z available in the model on the E-plane as (Kraus, 1991)

$$E_\theta = E_y \frac{z}{\sqrt{y^2 + z^2}} - E_z \frac{y}{\sqrt{y^2 + z^2}} \tag{7.1}$$

where y,z are the coordinates of the observation points on the circle of radius $r = 0.6$ metre with respect to the reference point on the interface. The E-plane patterns calculated by

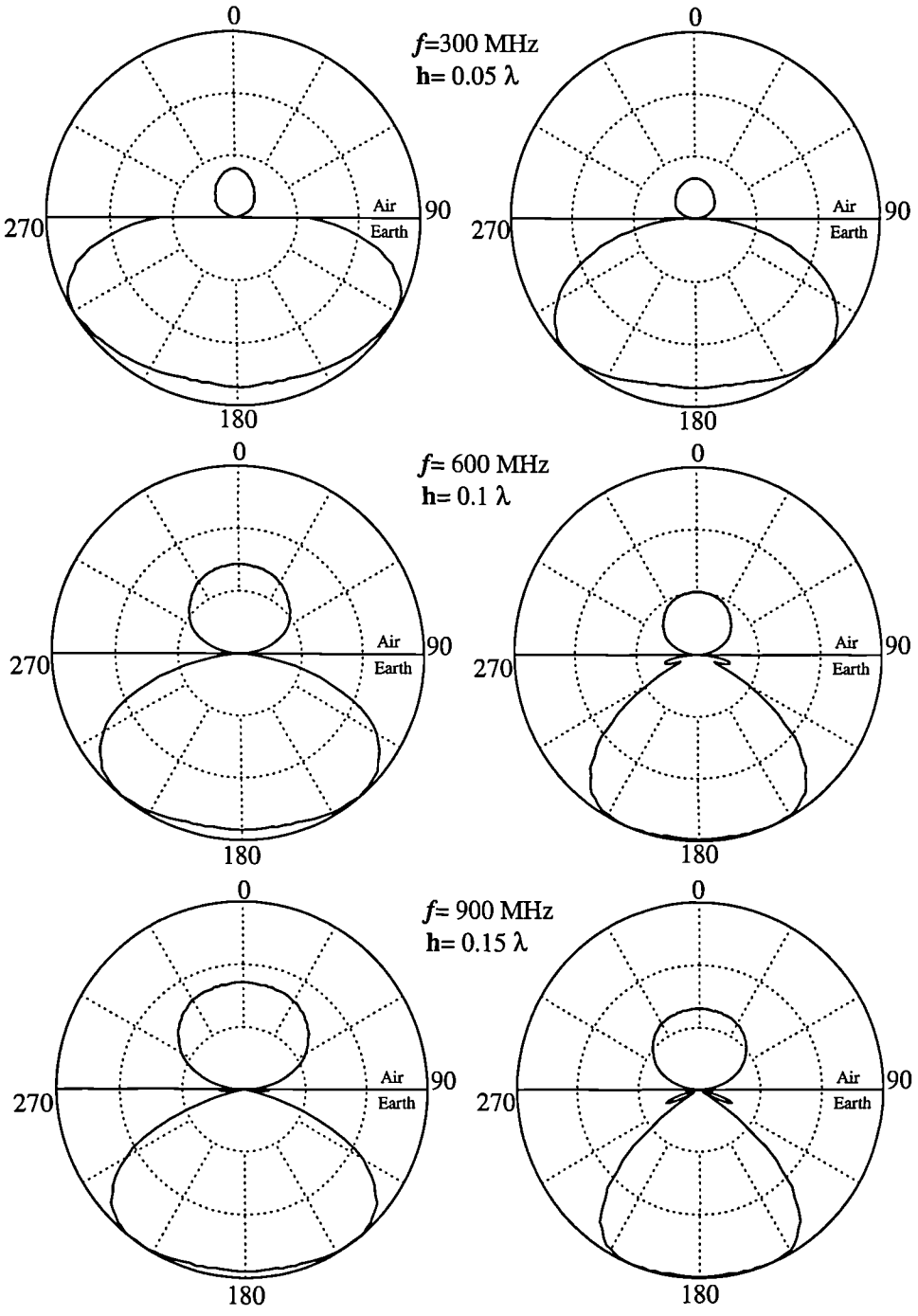

Figure 7.2: H-plane field patterns ($|E_\phi|$) of a horizontal dipole over a lossless half-space for two different values of permittivity $\epsilon_r = 3$ (left) and 6 (right) (Linear scale).

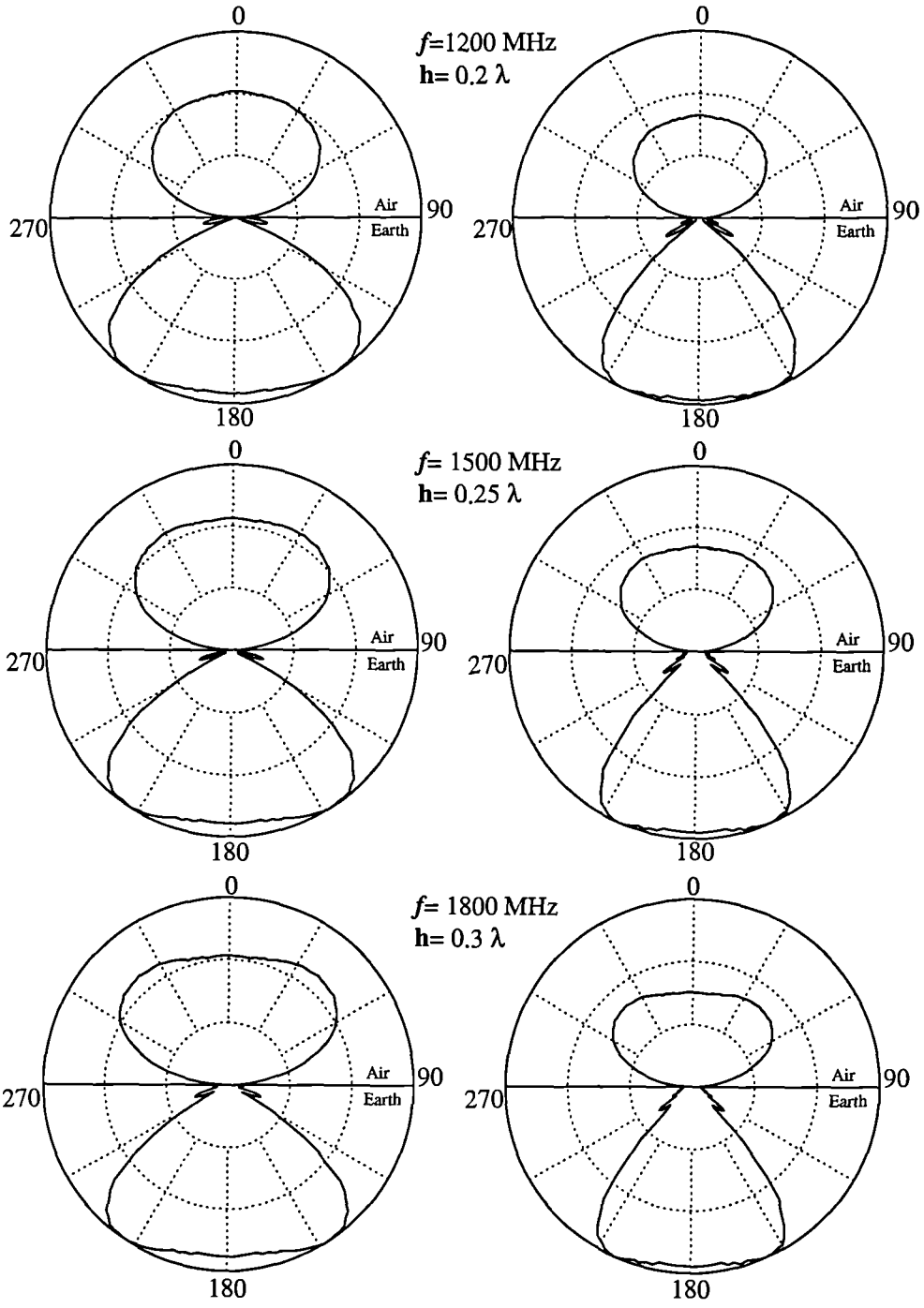

Figure 7.3: H-plane field patterns ($|E_\phi|$) of a horizontal dipole over a lossless half-space for two different values of permittivity $\epsilon_r = 3$ (left) and 6 (right) (Linear scale) .

the FDTD model at different frequencies are presented in Figures 7.4 and 7.5 and they exhibit similar characteristics as the H-plane ones. However, they appear to be more directive, even for low frequencies.

The most significant differences between the calculated H- and E- plane patterns and the theoretical far-field ones (see Chapter 2) are:

A. Sharp details as the nulls in the theoretical E-plane patterns are not present

B. The calculated patterns by FDTD appear to be less directive within the half space especially for lower frequencies.

Both differences can be attributed to the small distance between the observation points and the source and the limited resolution in recording the fields in the FDTD model. Further, for low frequencies the significant contribution of surface waves near the source and interface is not taken into account in the theoretical far-field patterns.

7.3 Comparison of FDTD and SCN TLM simulated GPR responses

Results from FDTD and TLM simulations for the same models are shown to be in good agreement when the differences between the two methods are taken into account and reflections from the truncation boundaries in TLM[2] are kept to a minimum.

The main difference in the formulation of the two methods, which affect the comparisons, is the location of interfaces separating different media in TLM half-way between nodes. Hence, the distance from the source to the air-earth interface in TLM is $\Delta l/2$ less than an equivalent FDTD model. Although such a difference will be of little importance when both the source and receiver are located at sufficient distance from the interface, it affects the direct arrivals recorded when they are located close to it. Therefore, small differences in the early parts of TLM simulated responses with the FDTD ones are expected.

Most important however in using a TLM model — as comparisons with FDTD have shown — is the reflections from the truncation boundaries due to the poor ABC performance. These reflections influence the solution even when a relatively large computational domain

[2]A "matched termination" ABC has been used for all TLM simulations.

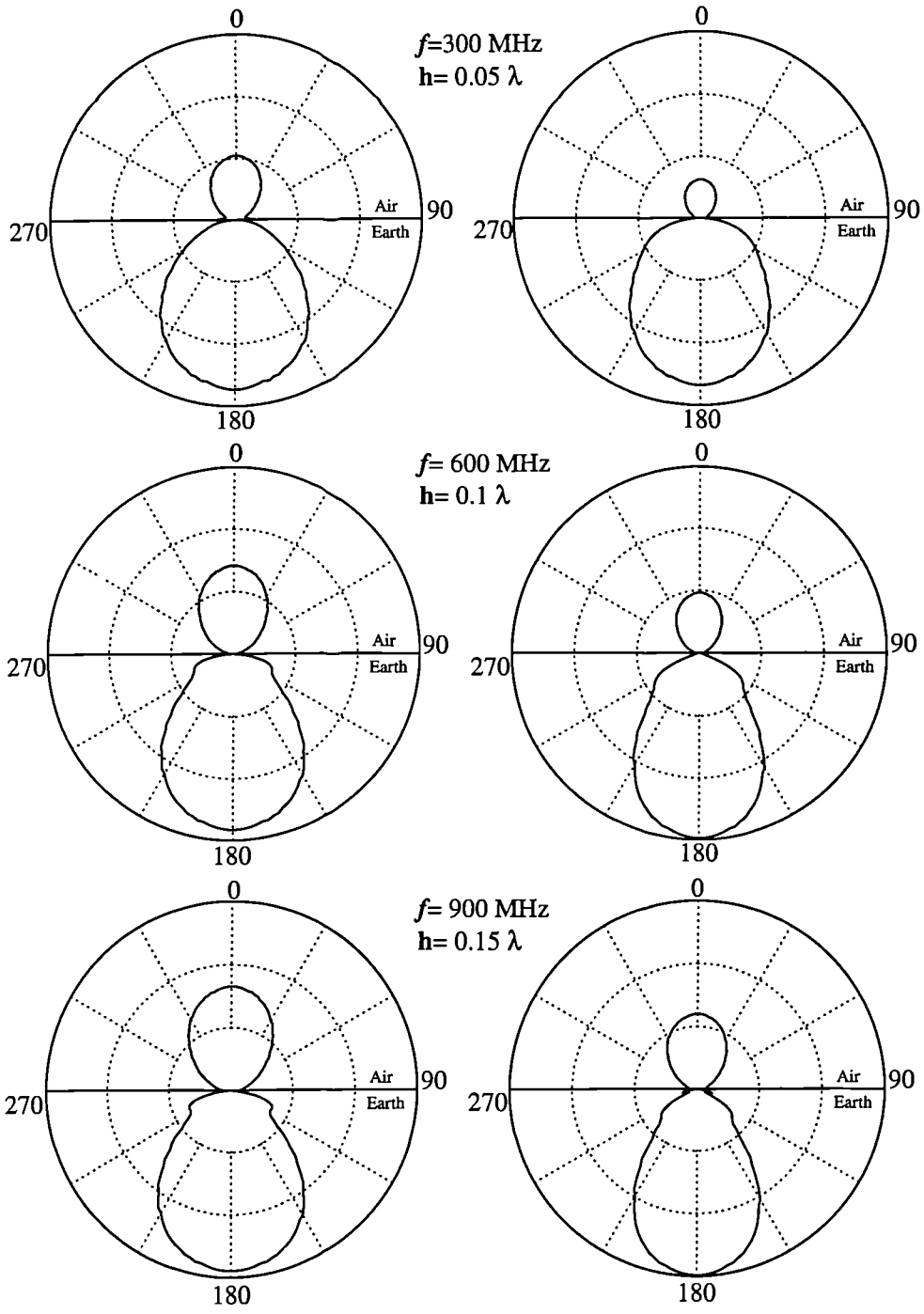

Figure 7.4: E-plane field patterns ($|E_\phi|$) of a horizontal dipole over a lossless half-space for two different values of permittivity $\epsilon_r = 3$ (left) and 6 (right) (Linear scale).

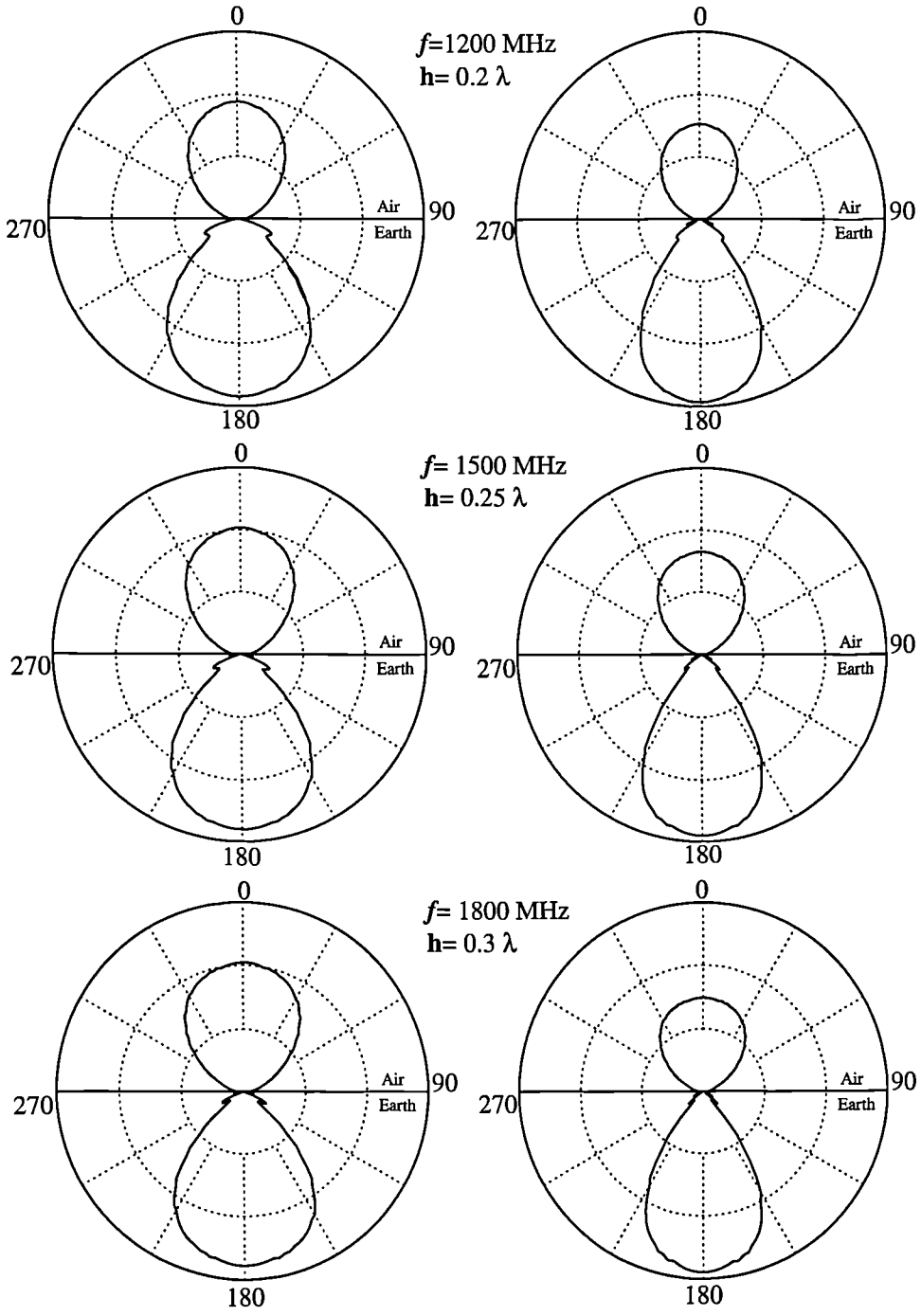

Figure 7.5: E-plane field patterns ($|E_\phi|$) of a horizontal dipole over a lossless half-space for two different values of permittivity $\epsilon_r = 3$ (left) and 6 (right) (Linear scale).

is used. For example, in Figure 7.6 presents H-plane patterns obtained by a TLM model using an identical configuration to the FDTD one discussed above. Although they exhibit similar characteristics to the FDTD ones, they are not as smooth and irregularities appear especially within the half-space. Since numerical dispersion is less in the TLM model than in FDTD and the patterns calculated by the later for the same frequencies do not appear, to be affected, the reason for these irregularities in the TLM patterns is the reflections from the truncation boundaries. This is further demonstrated by considering the H-plane patterns in Figure 7.6 which have been calculated by discarding the late part of the TLM responses and the use instead of zero-padding in the FFT. These patterns appear to be similar to the FDTD and no irregularities are observed.

The reason for the irregularities in the original TLM patterns is that reflected waves from the truncation boundaries constitute the only signal in the model after the main part of the transmitted pulse has left the computational domain. Since there are no losses in the model ($\sigma = 0$) these waves will be further influencing the result, appearing periodically through the observation points.

Similar problems due to the poor performance of ABCs in TLM are encountered when GPR responses from small targets are considered and compared with FDTD simulations. Figure 7.7 presents a comparison between FDTD and TLM simulated responses from a small ($10\Delta l \times 10\Delta l \times 10\Delta l$) rectangular void located at a depth of 15 centimetres ($\Delta l = 1$ centimetre) for different values of relative permittivity of the half-space ($\epsilon_r = 3, 4, 5, 6$) and constant conductivity ($\sigma = 0.01$ (S/m)). Both TLM and FDTD models were comprised of (60,60,60) TLM nodes and Yee cells respectively. The source is a ricker wavelet of $f_s = 600$ MHz and the Tx–Rx separation is 25 centimetres. Further, the midpoint between Tx and Rx is located directly over the centre of the void.

In general, the responses appear very similar, but it is apparent that the TLM ones are affected by reflections from the truncation boundaries. This is clearly demonstrated (see Figure 7.8) by considering only the scattered electric field from the void obtained by subtracting the response of the models without the presence of the target. When a large ($100\Delta l \times 100\Delta l \times 100\Delta l$) but otherwise identical TLM model is used the agreement with the smaller FDTD model is very good.

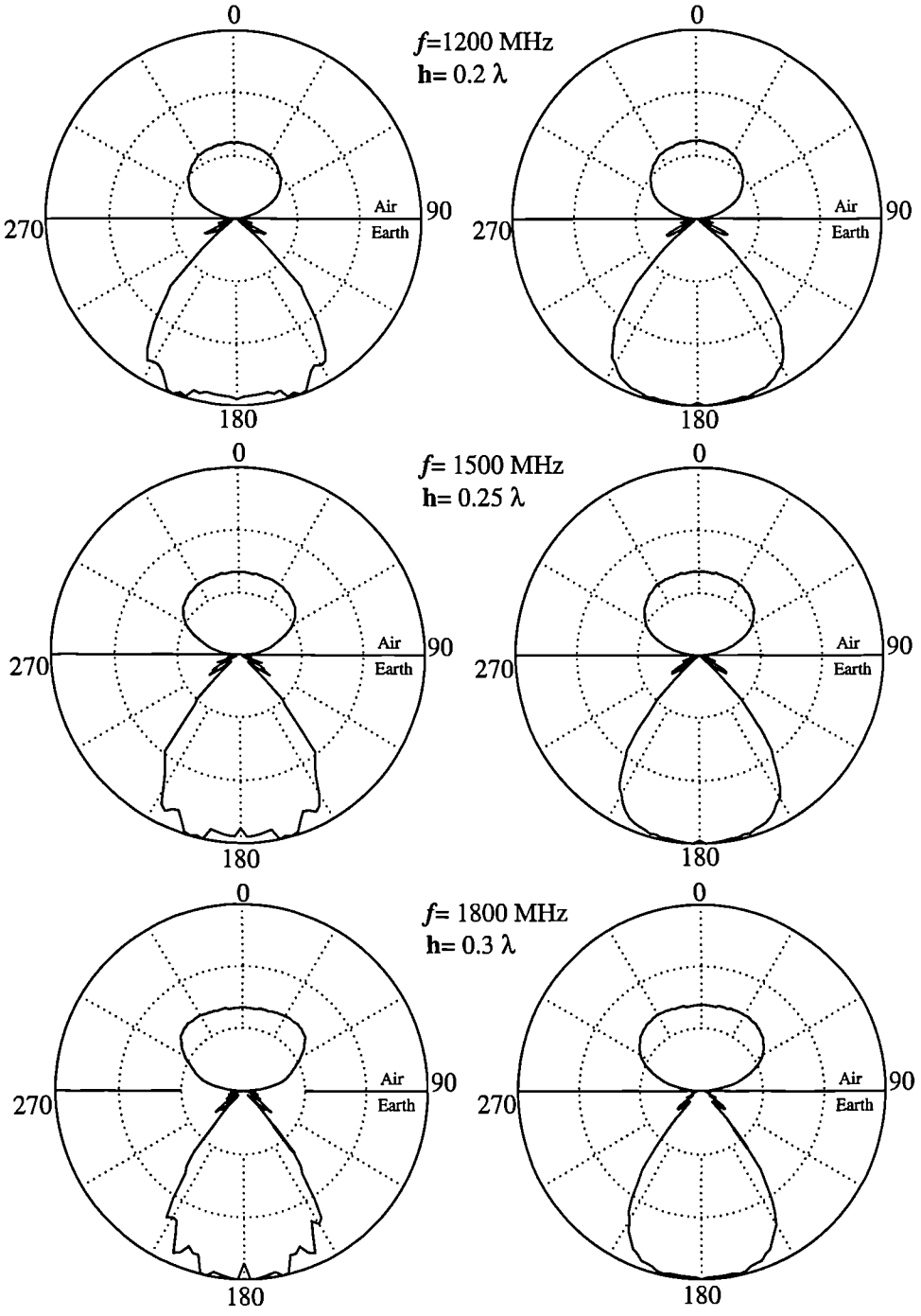

Figure 7.6: H-plane field patterns ($|E_\phi|$) of a horizontal dipole over a lossless half-space ($\epsilon_r = 6$) obtained from a TLM model using the entire TLM response (left) and zero-padding (right) (Linear scale).

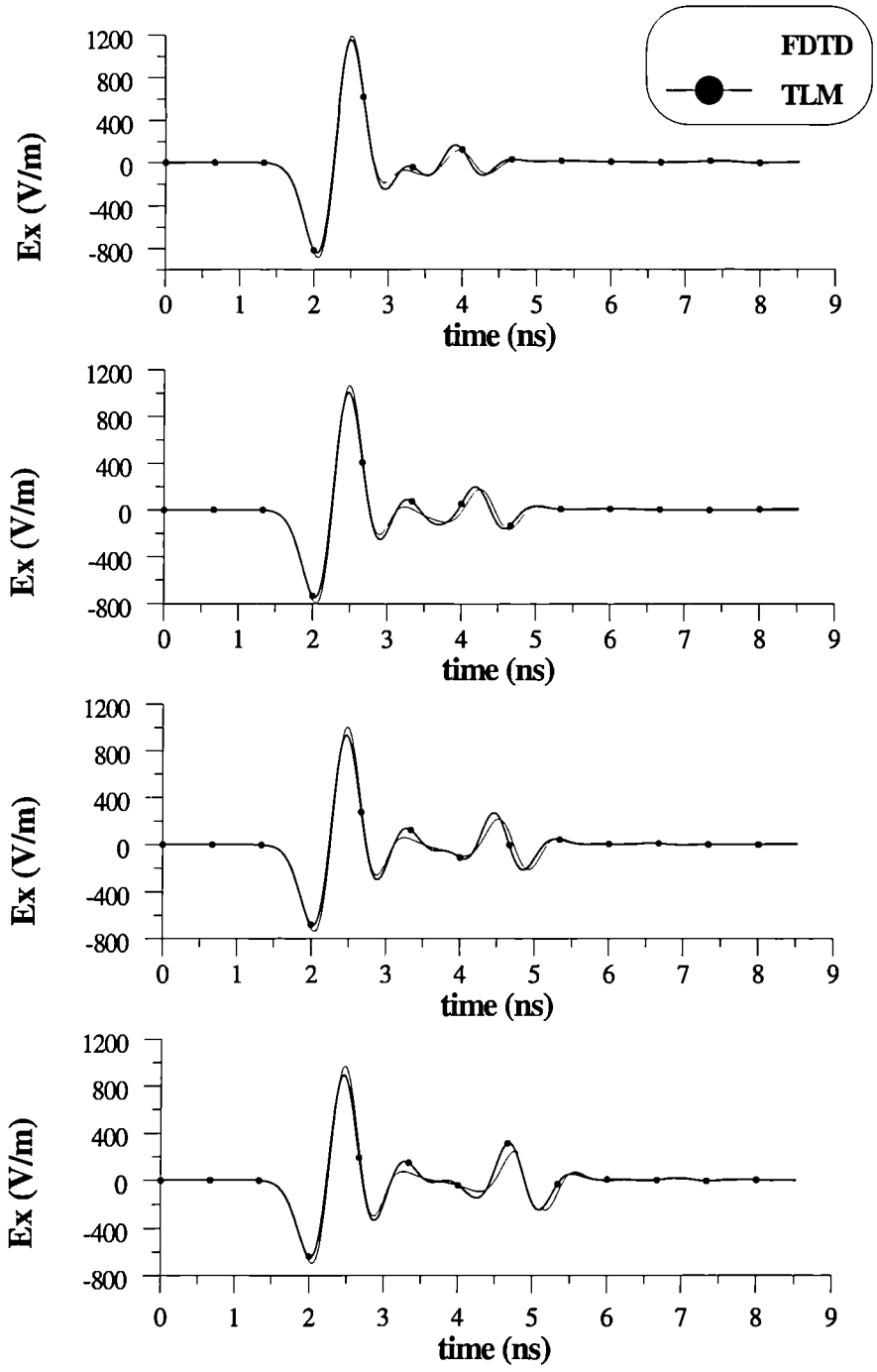

Figure 7.7: Comparison between simulated GPR responses from a small rectangular void located at a depth of 15 centimetres in different media, obtained by FDTD and TLM models.

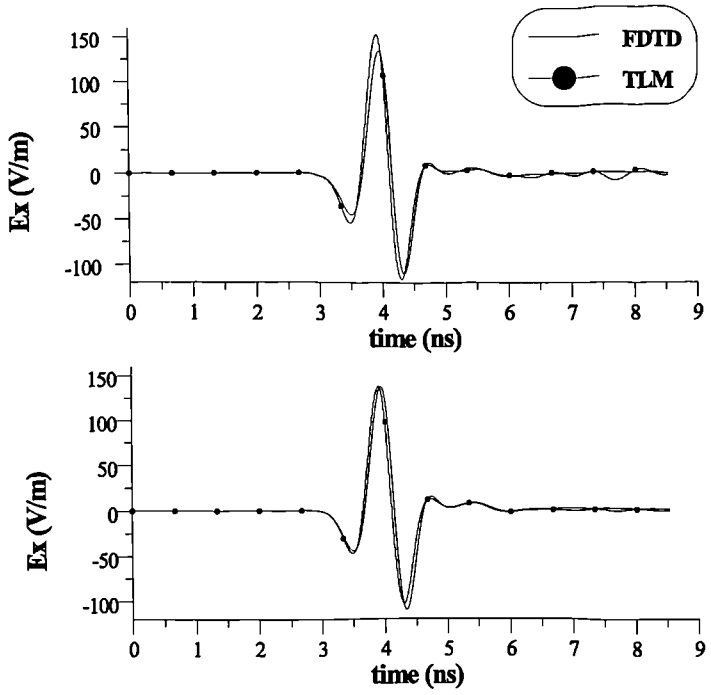

Figure 7.8: Comparison of the scattered electric field from a small rectangular void, located in a half-space of $\epsilon_r = 3$ and $\sigma = 0.01$ (S/m), obtained by FDTD and two different size (60,60,60) nodes (top) and (100,100,100) nodes (bottom) TLM models.

7.4 Modelling GPR signatures of near-surface small targets

The 3D FDTD models are particularly suited for modelling the GPR responses of small targets located close to the air-earth interface. The computational requirements for such models are moderate and they can be obtained in reasonable time without having to resort to a supercomputer.

The signatures of these type of targets for the parallel Tx–Rx configuration are in principal localized hyperbolic responses and, when the scan-line is located directly over the target, are very similar to those obtained by a 2D model. This is evident from the synthetic GPR scans presented in Figure 7.9 obtained over four small targets (perfectly conducting cylinder and box, and rectangular and cylindrical voids). The particulars of the FDTD models used for these simulations are presented in Figures 7.10, 7.11, 7.12, 7.13 where schematic drawings of the models are shown.

The use, however, of a 3D model allows the investigation of off-line effects and different Tx–Rx orientations or even different types of GPR antennas.

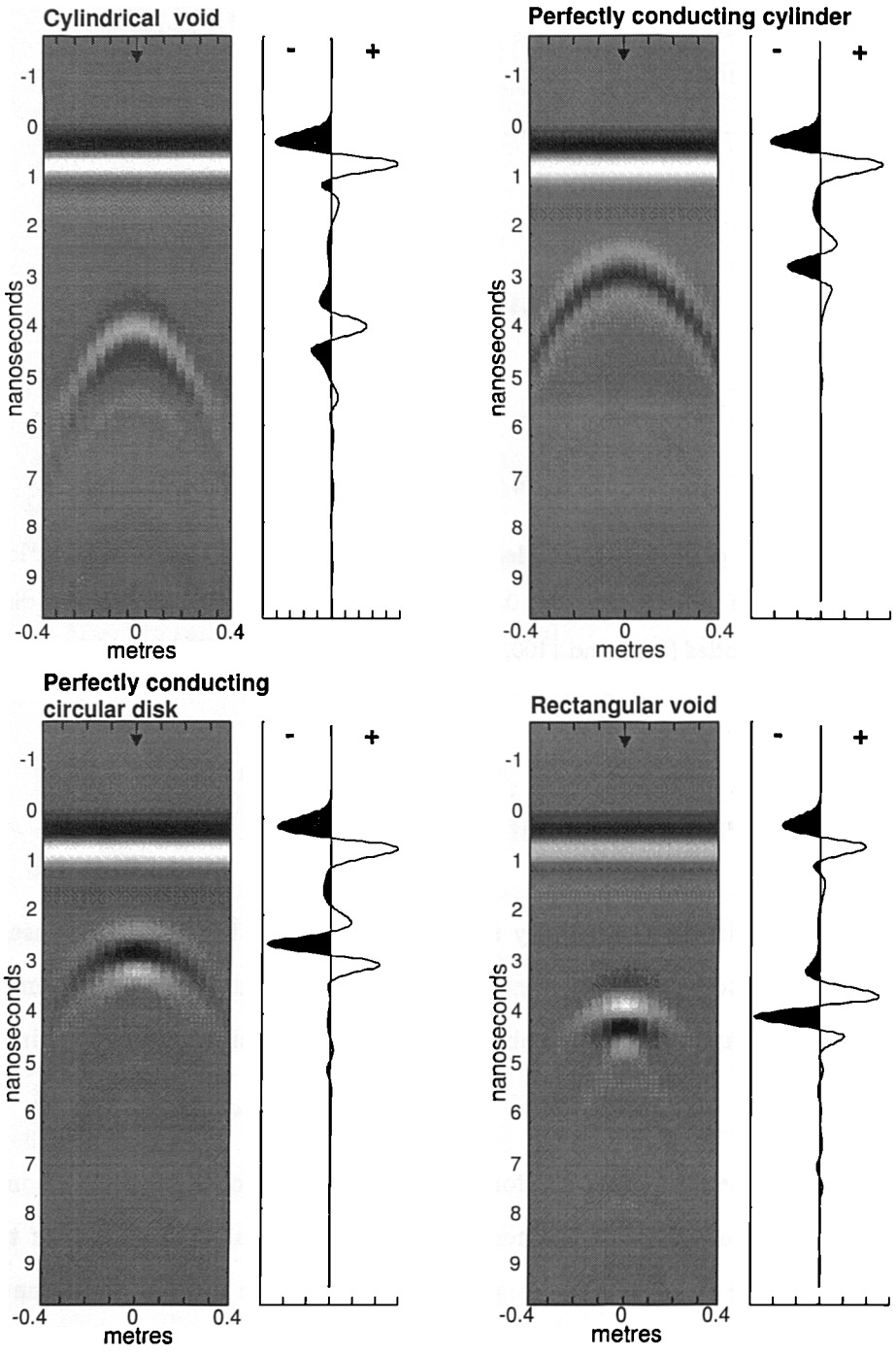

Figure 7.9: Synthetic GPR scans obtained by FDTD over four small targets using a parallel Tx–Rx configuration.

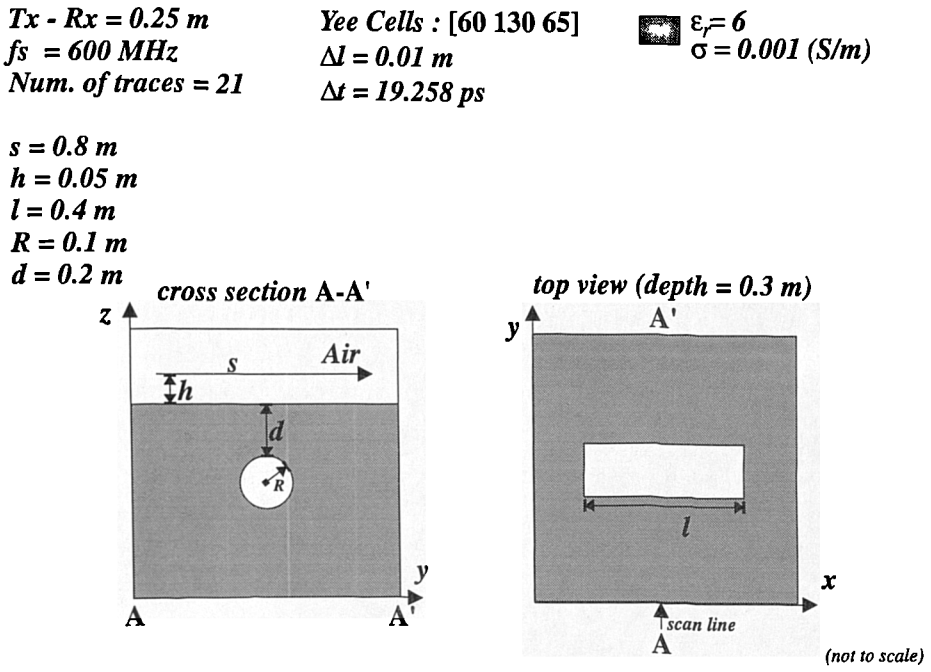

Figure 7.10: Schematic drawing of the FDTD model of a cylindrical void.

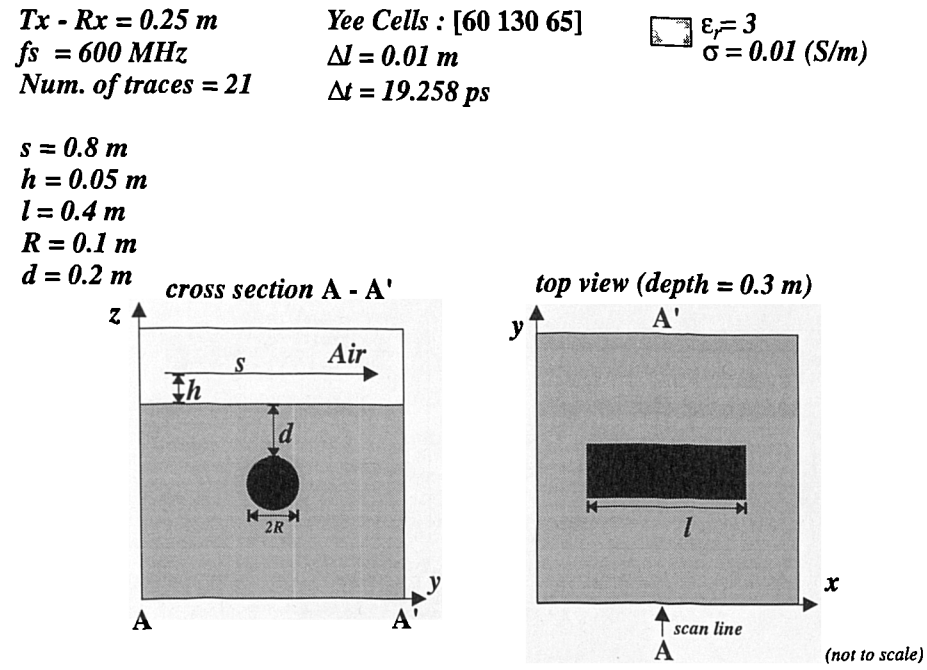

Figure 7.11: Schematic drawing of the FDTD model of a perfectly conducting cylinder.

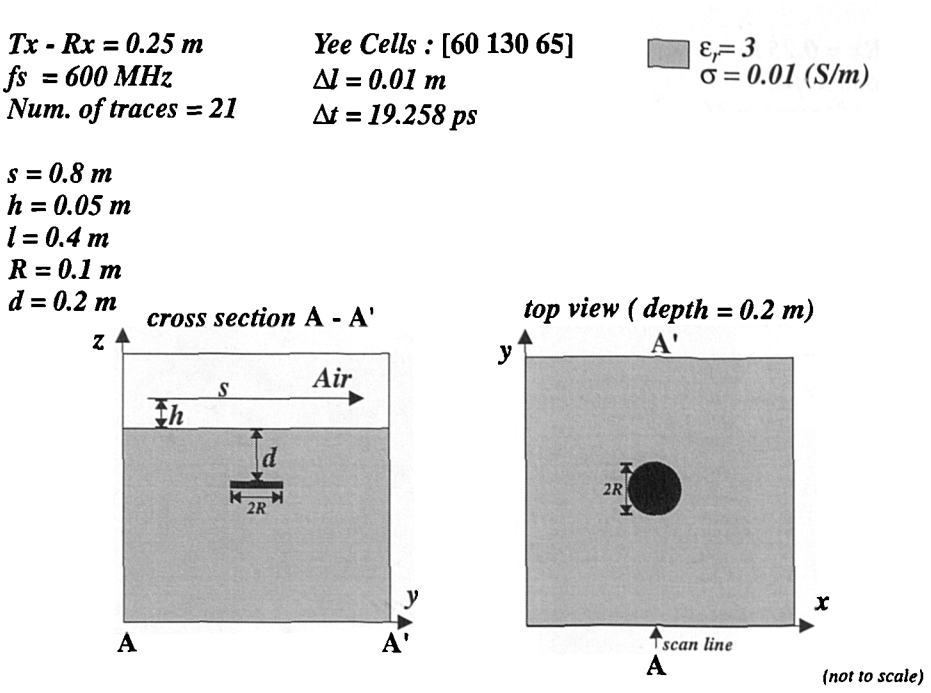

Figure 7.12: Schematic drawing of the FDTD model of a perfectly conducting circular disk.

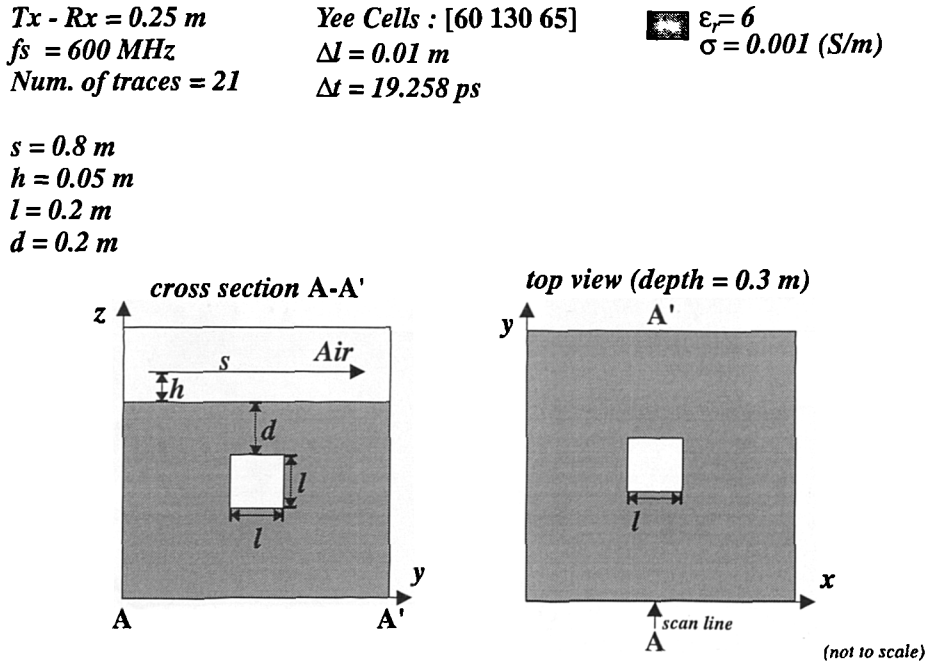

Figure 7.13: Schematic drawing of the FDTD model of a rectangular void.

7.4.1 Off-line effects on GPR signatures

To delineate the position and extent of small near-surface targets a number of parallel GPR scans have to be conducted. The distance between these successive scan lines is a critical factor in the design of a GPR survey and targets can be missed if its not chosen appropriately. Simulated GPR scans at an offset from the centre of a small target can be used to assist in determining the appropriate distance between successive scan lines in order to detect a given target. For example, in Figure 7.14, synthetic GPR scans obtained from an FDTD model of a small perfectly conducting box, with dimensions ($10\Delta l \times 15\Delta l \times 10\Delta l$) located in a homogeneous half-space at a depth of $d = 20\Delta l$, are illustrated when the simulated scan lines are at different offsets from the target's centre. Details of the FDTD model used are presented in Figure 7.15.

It is evident from these results that a minimum distance of 20 centimetre between successive scans will be required if a significant response is to be obtained from the target. In addition, responses from off-line targets play an important role in interpreting GPR data. Most often data are treated as a two dimensional image with reflections being considered to originate only from the plane of the scan-line. Further data processing, such as the application of gain functions which equalizes the amplitude of both small and big events in the GPR record, enhances the possibility of misinterpretation.

The problem of determining responses from off-line targets is not a simple one since it depends on a range of different parameters. For example, when the depth to the target considered in the previous example is increased to $d = 30\Delta l$, the simulated GPR responses are shown in Figure 7.16. Comparing these with the ones obtained from the shallower location of the target (Figure 7.14) it appears that they are very similar with an apparent reduction in amplitude due to the increased influence of the loss mechanisms. However, the conclusion that off-line effects will decrease with depth is not entirely correct. Figure 7.17 presents a comparison of the variation of maximum received signal from the target normalized to the target's response when the scan line is directly over it for the two different depths. It is apparent that the amplitude drops faster with distance for the shallower location. This is a consequence of the source's radiation pattern. The region illuminated by it increases with depth and when amplitude variations in a GPR section are compensated with the application of gain functions, off-line effects from deeper targets will be more pronounced than from shallower ones.

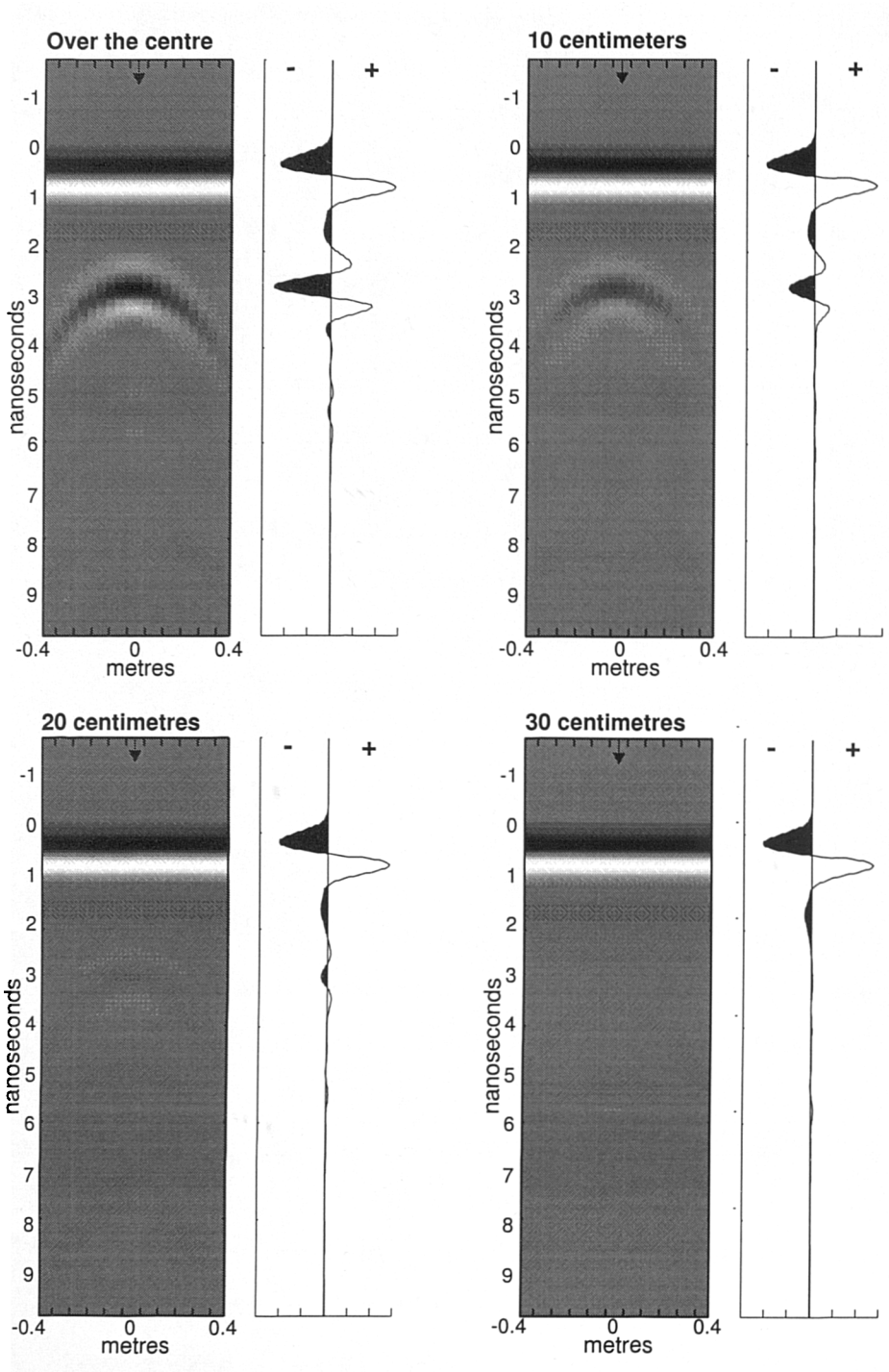

Figure 7.14: Synthetic GPR scans obtained by FDTD over a perfectly conducting box at different offsets from its center. Target's depth is 20 centimetres.

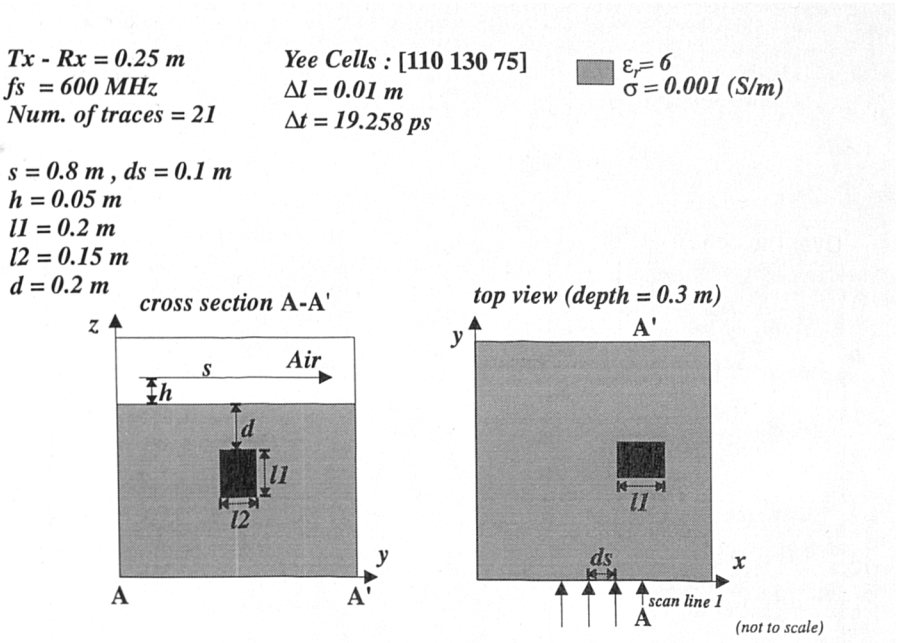

Figure 7.15: Schematic drawing of the FDTD model of a perfectly conducting box.

Other more complicated scenarios can arise where the use of a 3D model will assist interpretation. Consider the model of two perfectly conducting cylinders, as illustrated in Figure 7.18. The synthetic GPR scan shown in Figure 7.19 directly over the centre of one of the targets illustrates the effect of the off-line cylinder in the GPR record. In particular, the semi-hyperbolic responses from the edges of the off-line target are clearly observed. To determine the position of the off-line target and interpret the GPR data additional scans in a direction normal to the axis of the off-line cylinder have to be performed.

7.4.2 Orientation of GPR antennas

The orientation of the GPR receiving antenna relative to the transmitting one has been used in GPR surveying as a means to enhance the returns of a specific class of targets and to minimize the direct arrivals which potentially can mask short range targets. The most common antenna orientation is the parallel mode as used in the GPR models presented earlier. However, using the parallel mode isolation between the transmitting and receiving antenna is difficult to achieve, and the early part of the received signal is affected by the strong direct arrivals from the transmitting antenna (Daniels et al., 1988). The process of subtracting the "average" GPR trace from the data is used to reduce the effect, but it does suppress the returns from targets whose response does not span over only a few waveforms. As an alternative to the parallel mode configuration, the cross configuration has been used,

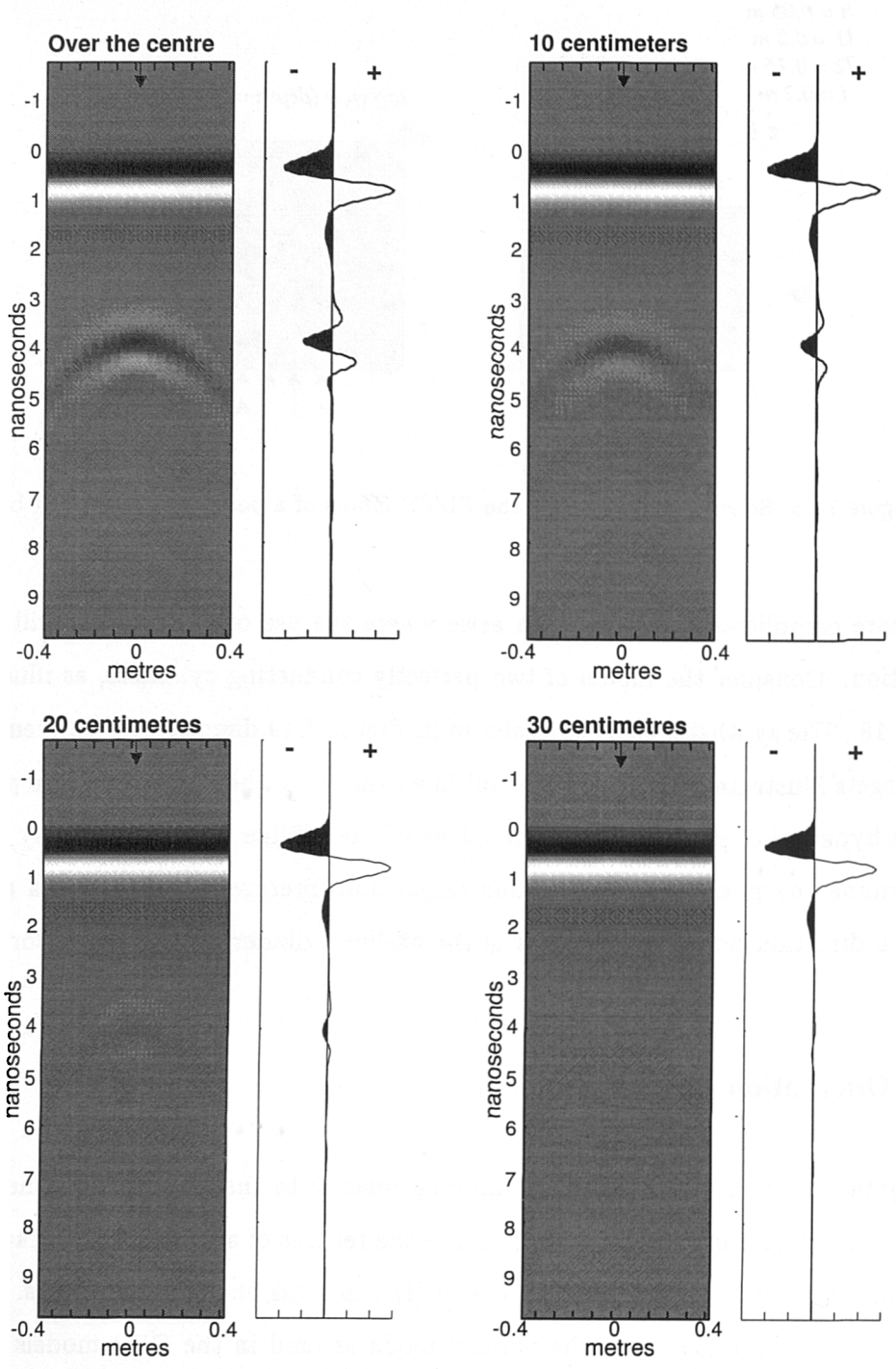

Figure 7.16: Synthetic GPR scans obtained by FDTD over a perfectly conducting box located at different offsets from its center. Target's depth is 30 centimetres.

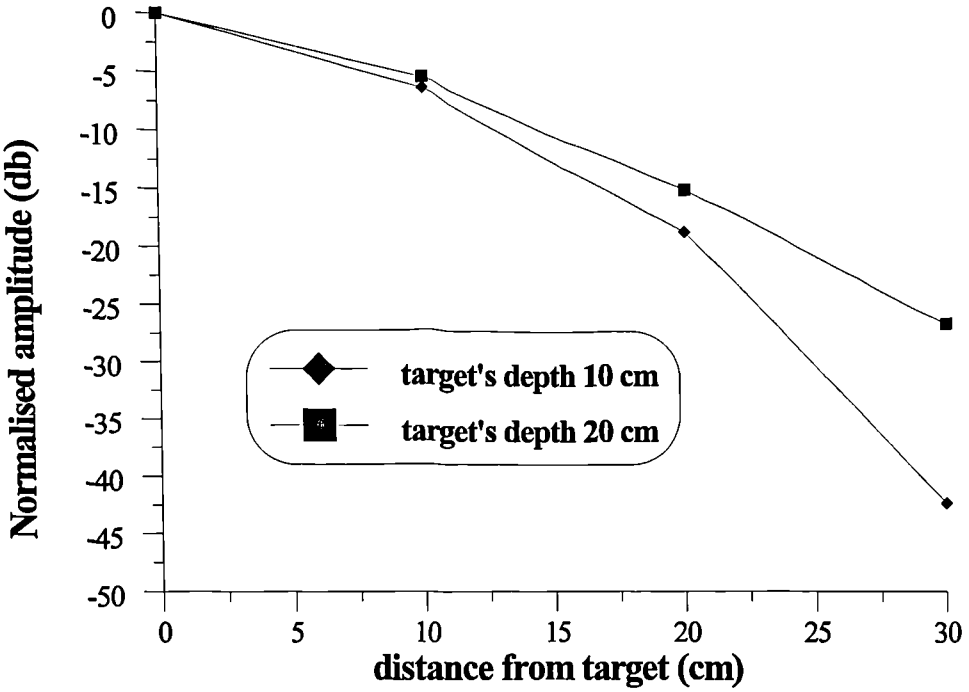

Figure 7.17: Variation with scan line offset of the maximum amplitude received from the rectangular conducting box normalized to the maximum response over the target's centre.

especially for the location of long targets such as pipes, cables, etc. (Chan et al., 1979). Although, theoretically, the isolation between the transmitting and the receiving antennas is much greater than in the parallel configuration because of the polarization mismatch of the two antennas (Mott, 1986) in practice it has been found that this configuration produces less but more irregular clutter which is not as easily suppressed as in the parallel configuration (Daniels et al., 1988). This clutter is caused by uneven ground and/or misalignment of the receiving and transmitting antennas.

An interesting characteristic of the response obtained using a cross configuration of the receiving and transmitting antennas is the sinusoidal variation of the amplitude of the received signal when the antennas are rotated around their electrical centre (Daniels et al., 1988). This effect is illustrated using a 3D SCN TLM model which offers the flexibility of obtaining all the field components at the same spatial location simulating the most commonly used cross configuration of GPR antennas. The source in the TLM model is an x-directed dipole with f_s = 500 MHz located directly over the centre of a perfectly conducting rectangular cylinder located at a depth of $30\Delta l$ in a half-space with $\epsilon_r = 4.0$ and $\sigma = 0.01$ (S/m). The long axis of the cylinder of length ($30\Delta l$) is oriented along the direction of the source (x axis). The orthogonal field component to the direction of the source (E_y) obtained when the long axis of the cylinder and the direction of the

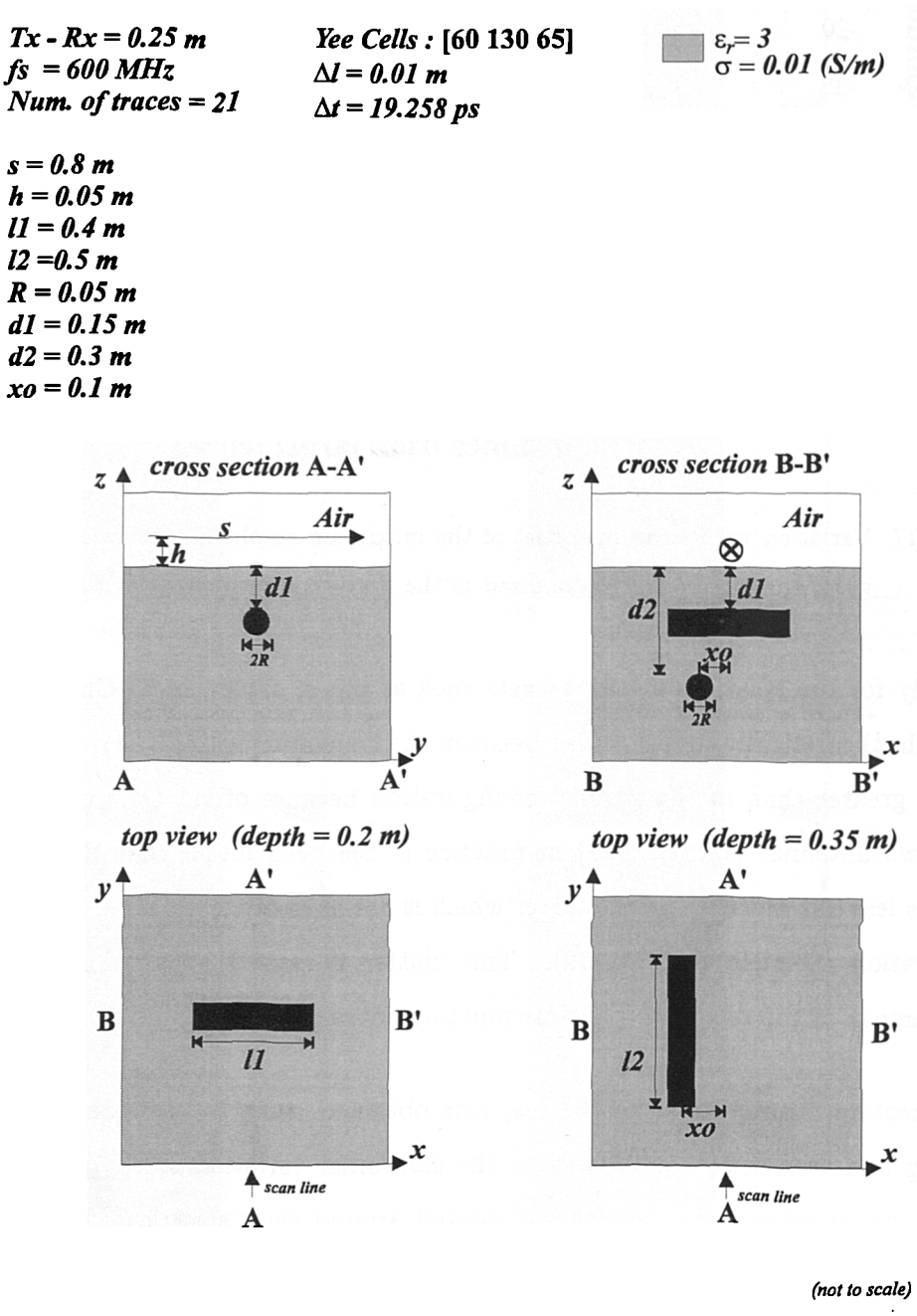

Figure 7.18: Schematic drawing of FDTD model of two perfectly conducting cylinders located at different depths and orientations in respect to the scan line.

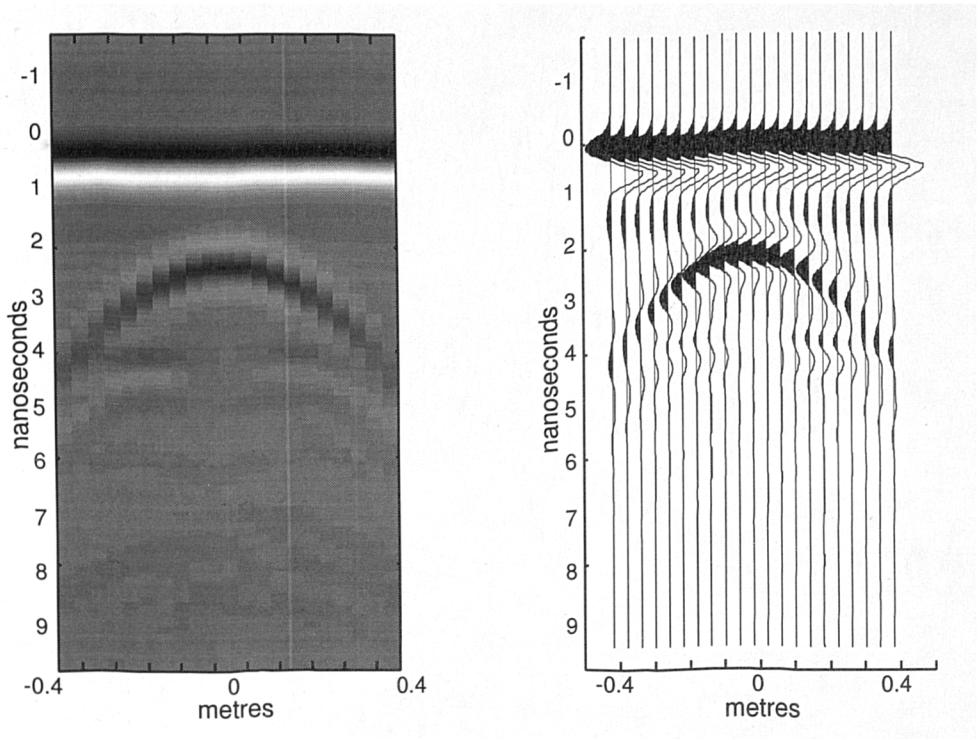

Figure 7.19: Synthetic GPR scan over the model of two perfectly conducting cylinders presented in gray-scale and wiggle-trace formats.

source coincide is zero in the TLM model. By rotating the target in the horizontal plane around the source point and monitoring the maximum amplitude of the received signal its sinusoidal variation is deduced. This is illustrated in Figure 7.20. The maximum response occurs when the angle between the x axis (direction of the source) and the axis of the cylinder is 45 degrees. In Figure 7.20 the response obtained at 45 degrees is compared to the one calculated at a smaller angle.

An alternative orientation of the receiving GPR antenna relative to the transmitting one is the collinear and end-fire configurations. The end-fire configuration has been used in early applications in GPR with very poor results and as noted in (Arcone, 1984). However, the collinear configuration has not been in general exploited in GPR surveying although it has distinct advantages over the most used parallel one (Lee et al., 1995). The advantages of the collinear configuration can be examined when the synthetic GPR scans obtained with the parallel one (Figure 7.9) are compared with the ones obtained over the same targets using a collinear configuration presented in Figure 7.21. The FDTD models used for the simulation of these scans are identical to the parallel configuration ones with the only difference being the arrangement of the receiving and transmitting antennas. In both cases — collinear and parallel — the midpoint between the Rx and Tx is kept the same.

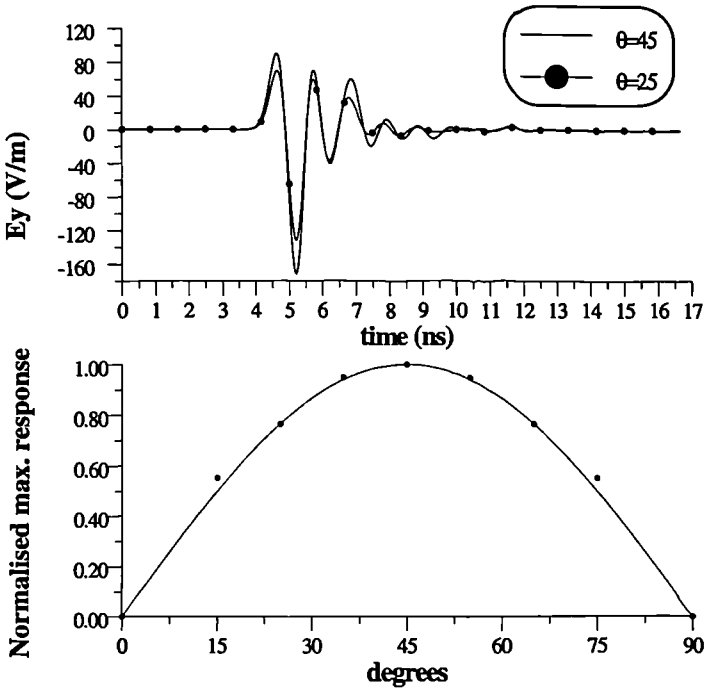

Figure 7.20: Cross configuration simulated GPR responses from a rectangular cylinder obtained by TLM for two different angles of rotation (top). Normalized maximum received signal from the cross configuration as a function of the rotation angle (bottom) (Solid line denotes $\sin(2\theta)$).

The significant advantage of the collinear configuration is that the direct arrivals are of much lower amplitude than the ones in parallel configuration and hence the responses from the targets (although of similar magnitude for both configurations) are enhanced. This is clearly indicated by comparing individual traces obtained when the midpoint of the Tx–Rx pair is located directly over the targets (Figure 7.22).

The reason for the smaller amplitude of direct arrivals in the collinear configuration than in the parallel one can be found in the work of King et al. (1992). Locating the transmitting antenna at the origin of a cylindrical coordinate system, the components of the electric field which dominate the direct arrivals for both the collinear and parallel configuration are depicted in Figure 7.23.

These field components are E_ρ for the collinear configuration and E_ϕ for the parallel one. According to King et al. (1992) in the near-field E_ρ decreases as $1/\rho^3$ and E_ϕ as $1/\rho^2$ (see Figure 5.5.1 in King et al. 1992). Therefore, the rate of decrease of the E_ρ affecting the collinear configuration is faster than the rate of decrease of E_ϕ affecting the parallel one. The E_ρ component decreases less rapidly than E_ϕ for observation points outside the

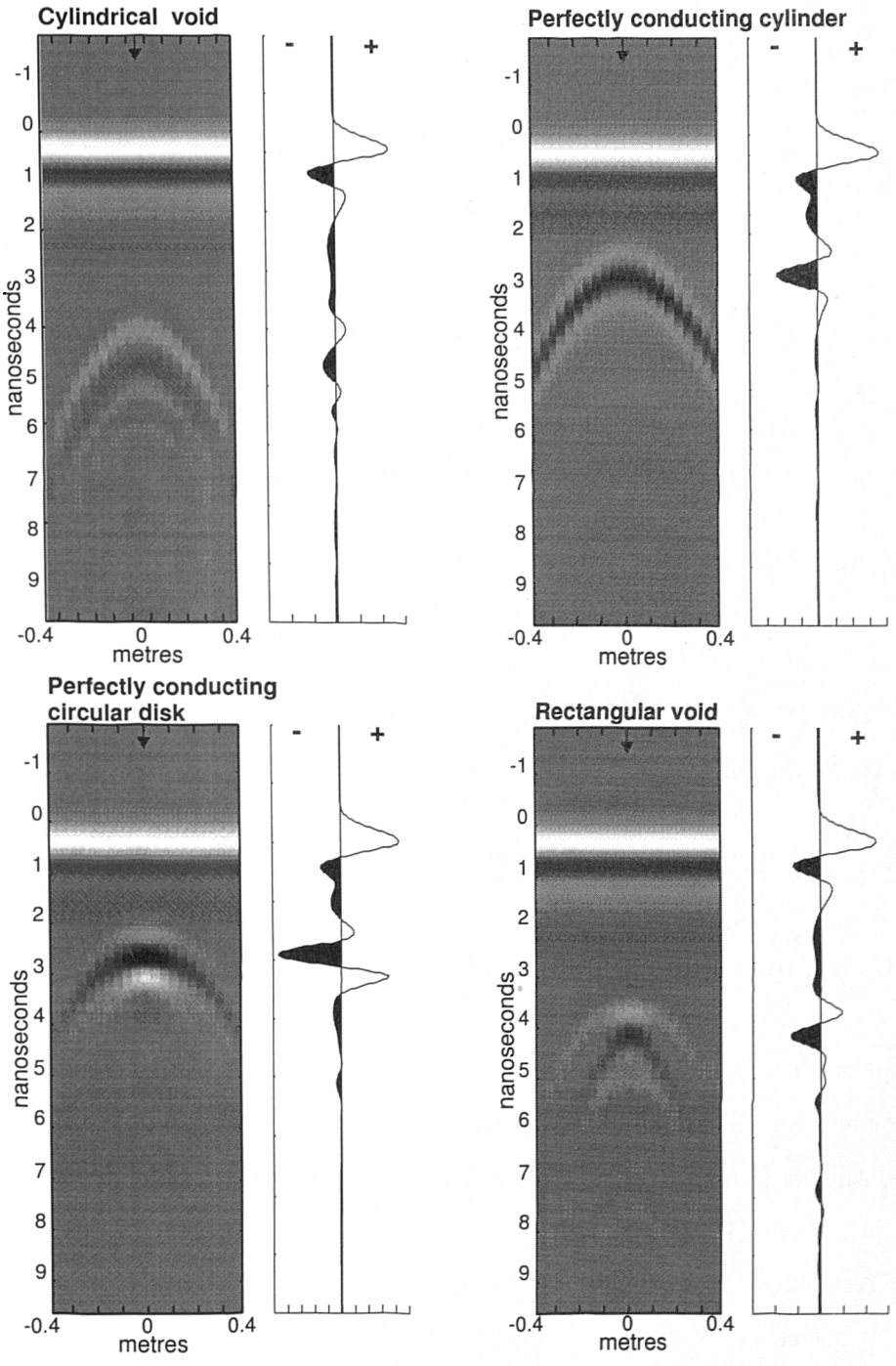

Figure 7.21: Synthetic GPR scans obtained by FDTD over four small targets using a collinear Tx–Rx configuration.

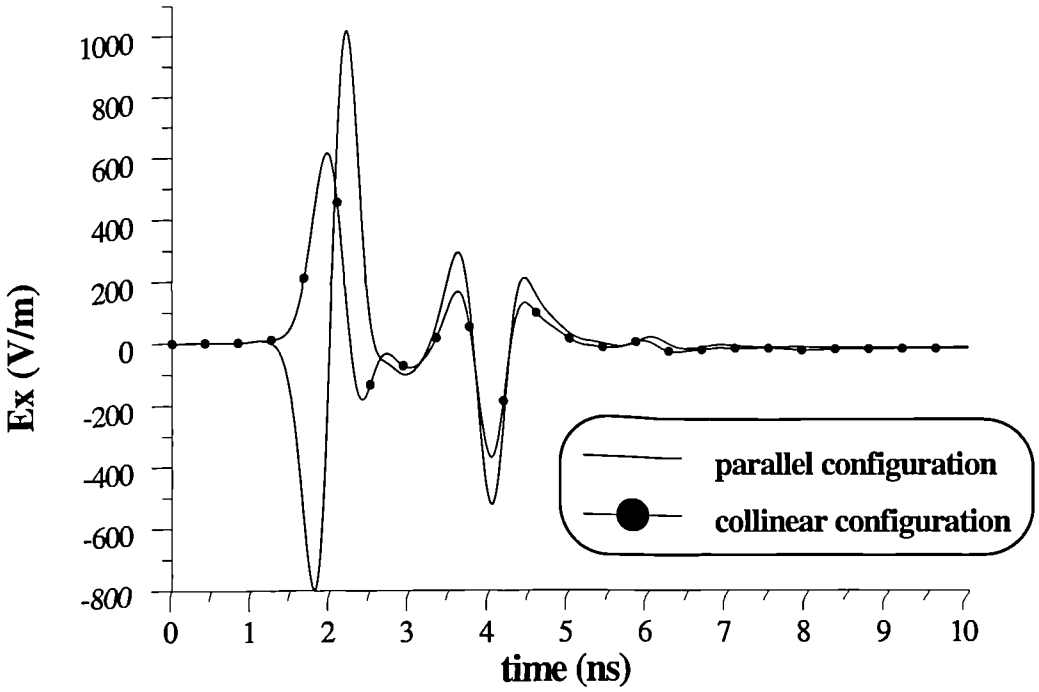

Figure 7.22: Comparison of simulated responses over the centre of a perfectly conducting cylinder using the parallel and collinear configurations.

near-field zone (King et al. 1992). However, this is not of any consequence in using the collinear configuration in GPR since the receiving antenna is located very close to the transmitting one.

7.4.3 Use of magnetic field sensors in GPR

In all applications of GPR the transducers which are used to transmit and receive the electromagnetic signals are all of the electric type and, specifically, dipole antennas. Magnetic field sensors (loop antennas) have not been employed. One possible explanation as reported in Balanis (1982) is that loop antennas are poor transmitters due to their low radiation resistance. However, according to the same author, the use of loop antennas as receivers has certain advantages compared to electric dipoles — especially lower noise levels. Although the actual physical structures of the antennas are not included in the 3D models by monitoring the received magnetic field components an indication is obtained of the GPR signatures received when appropriate magnetic field transducers are used. The modelled GPR signatures obtained by monitoring the magnetic field components instead of the electric ones have additional characteristics that can assist in the detection of GPR targets.

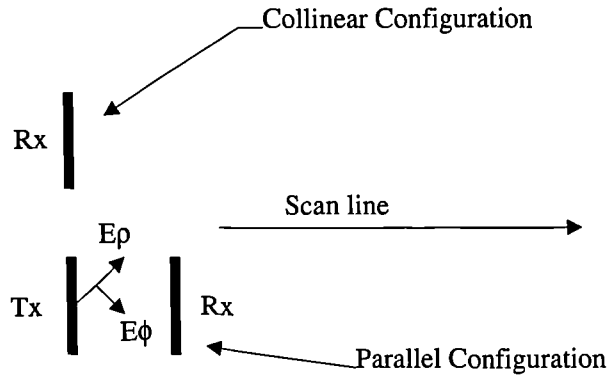

Figure 7.23: Collinear and parallel configurations with respect to scan line direction and principal field components affecting the direct arrivals to the receivers.

This can be observed in Figure 7.24, where the GPR signatures obtained by monitoring the normal to the interface magnetic field component (H_z), for the four targets used to obtain the parallel configuration synthetic GPR scans are presented. In the modelled target signatures of Figure 7.24 there is a null in the received signal and a change in its polarity either side of it. In addition this null does not occur at the apex of the otherwise hyperbolic response (as for example the maximum in the signatures of Figure 7.9). Further, examining the GPR signatures in Figure 7.25, obtained by recording the horizontal component of the magnetic field orthogonal to the transmitting dipole (H_y) although no null is observed, as in the previous case, the maximum of the response is not attained at the apex of the hyperbola.

An explanation of these signatures can be obtained by considering a simplification of the mechanism of basic scattering from the perfectly conducting cylinder. As is illustrated in Figure 7.26, the radiated electric field from the cylinder is polarized in the direction of its long axis, which is the direction of the source in the model. The magnetic field associated with this scattered electric field is φ-polarized. When this magnetic field is recorded at the surface using a finite separation between transmitter and receiver $H_\phi = H_y$ when the receiver is directly over the target and then $H_z = 0$. Hence the null in the synthetic signature obtained when sampling the vertical magnetic component actually denotes the

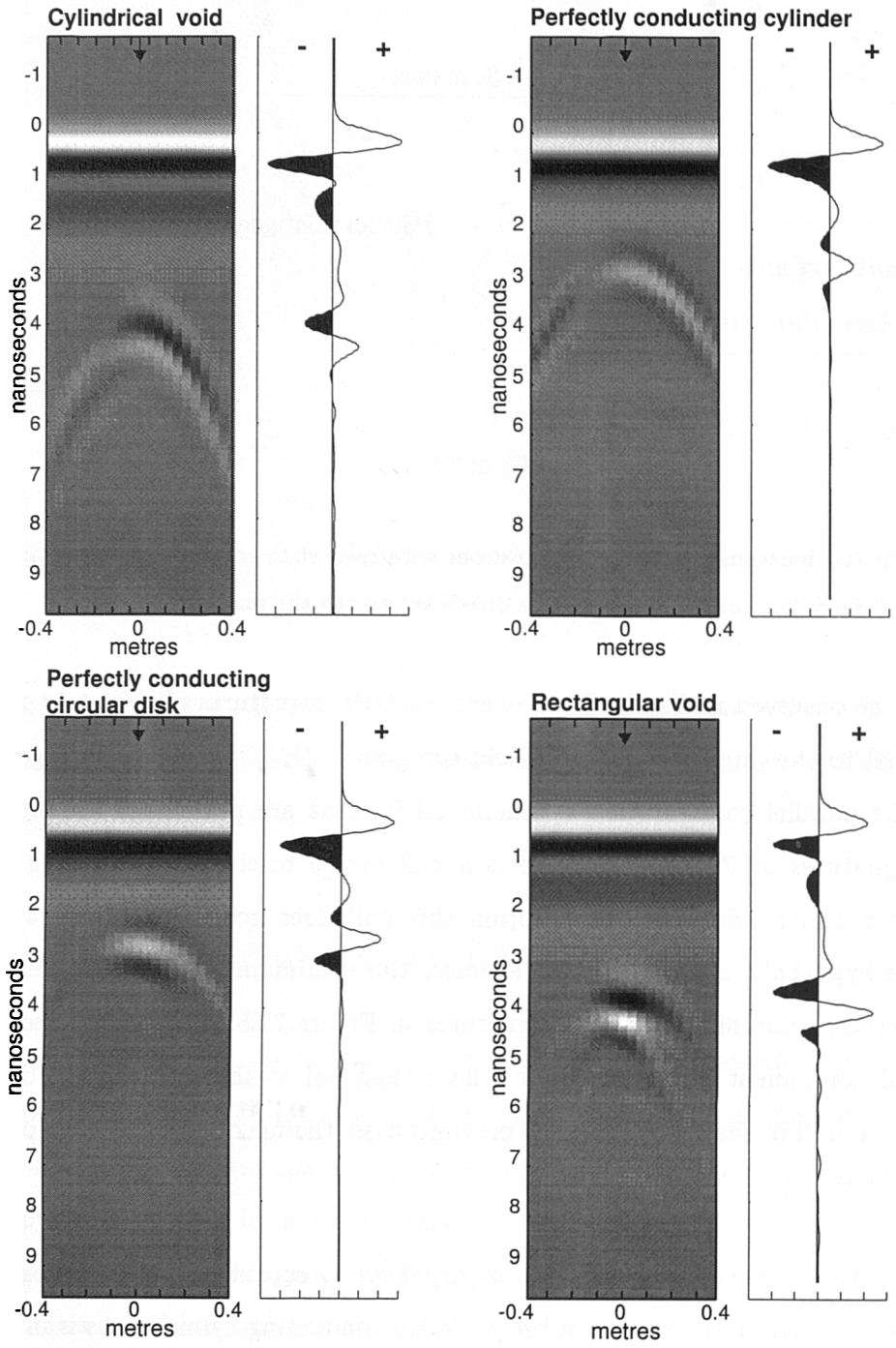

Figure 7.24: Synthetic GPR scans calculated by FDTD over four small targets obtained by monitoring the vertical magnetic field component.

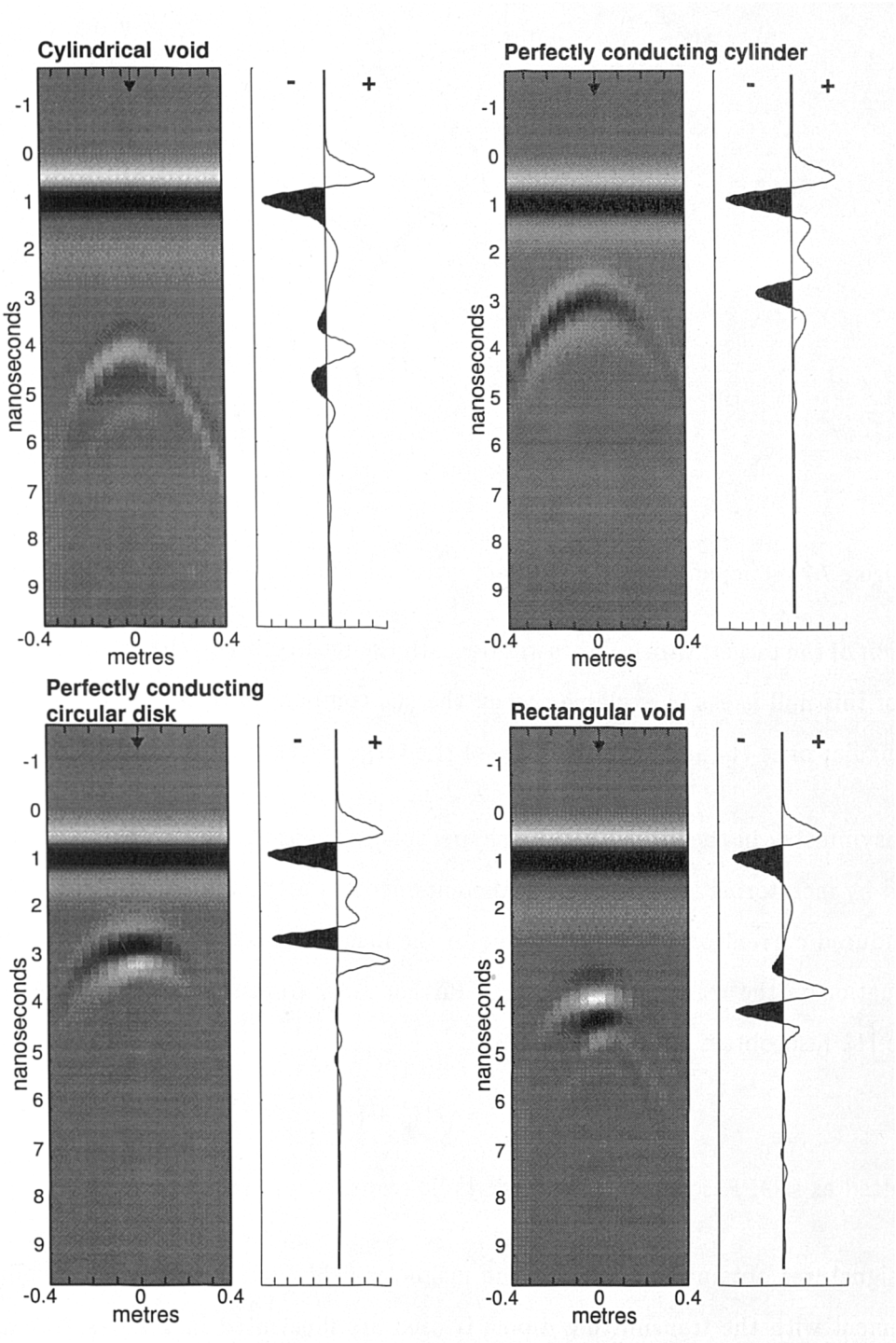

Figure 7.25: Synthetic GPR scans calculated by FDTD over four small targets obtained by monitoring the horizontal magnetic field component.

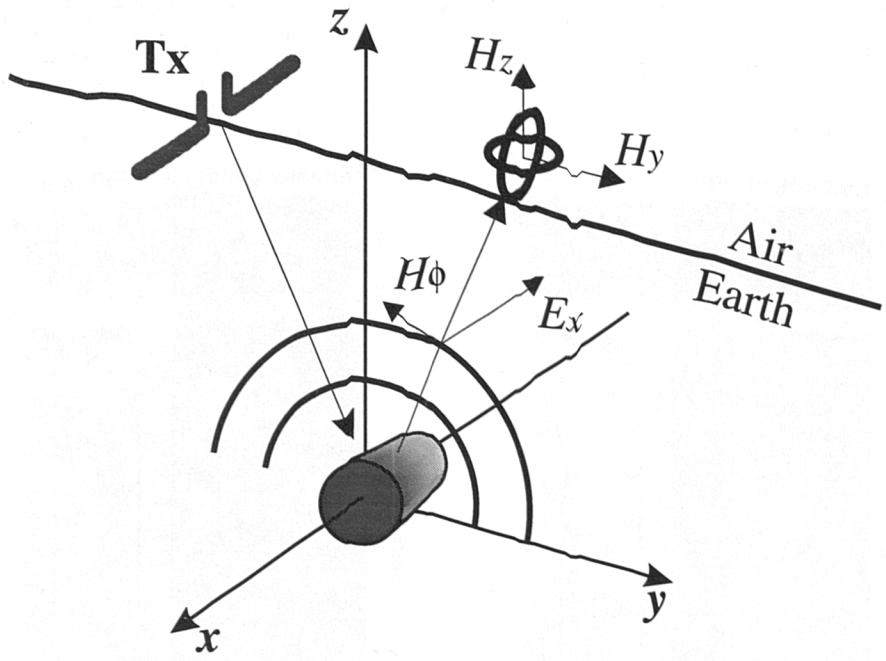

Figure 7.26: Simplified representation of scattering from a perfectly conducting cylinder.

location of the target, which is directly beneath the receiver. The change in polarity either side of this null is easily explained when the H_ϕ component is decomposed into the two rectangular ones H_y and H_z either side of the target's centre.

The asymmetry in the strength of the hyperbolic response in the synthetic signature obtained by monitoring the magnetic field components is easily understood considering that the induced current on the target is due to the incident field, which in turn suffers more attenuation as the transmitter is located further away from the target. If the amplitude of the H_ϕ field obtained by

$$H_\phi = \sqrt{H_y^2 + H_z^2} \tag{7.2}$$

is plotted as a GPR scan a perfect hyperbolic response will result.

The signatures obtained monitoring the magnetic field components when a collinear arrangement with the transmitting dipole is used are illustrated in Figures 7.27 and 7.28.

The responses of the vertical magnetic field component are stronger than when a parallel configuration is used mainly because the direct arrivals are minimum. Further, the null in these signatures is observed at the apex of the hyperbolic response. Another, consequence from using a magnetic field sensor to receive the vertical magnetic field component is

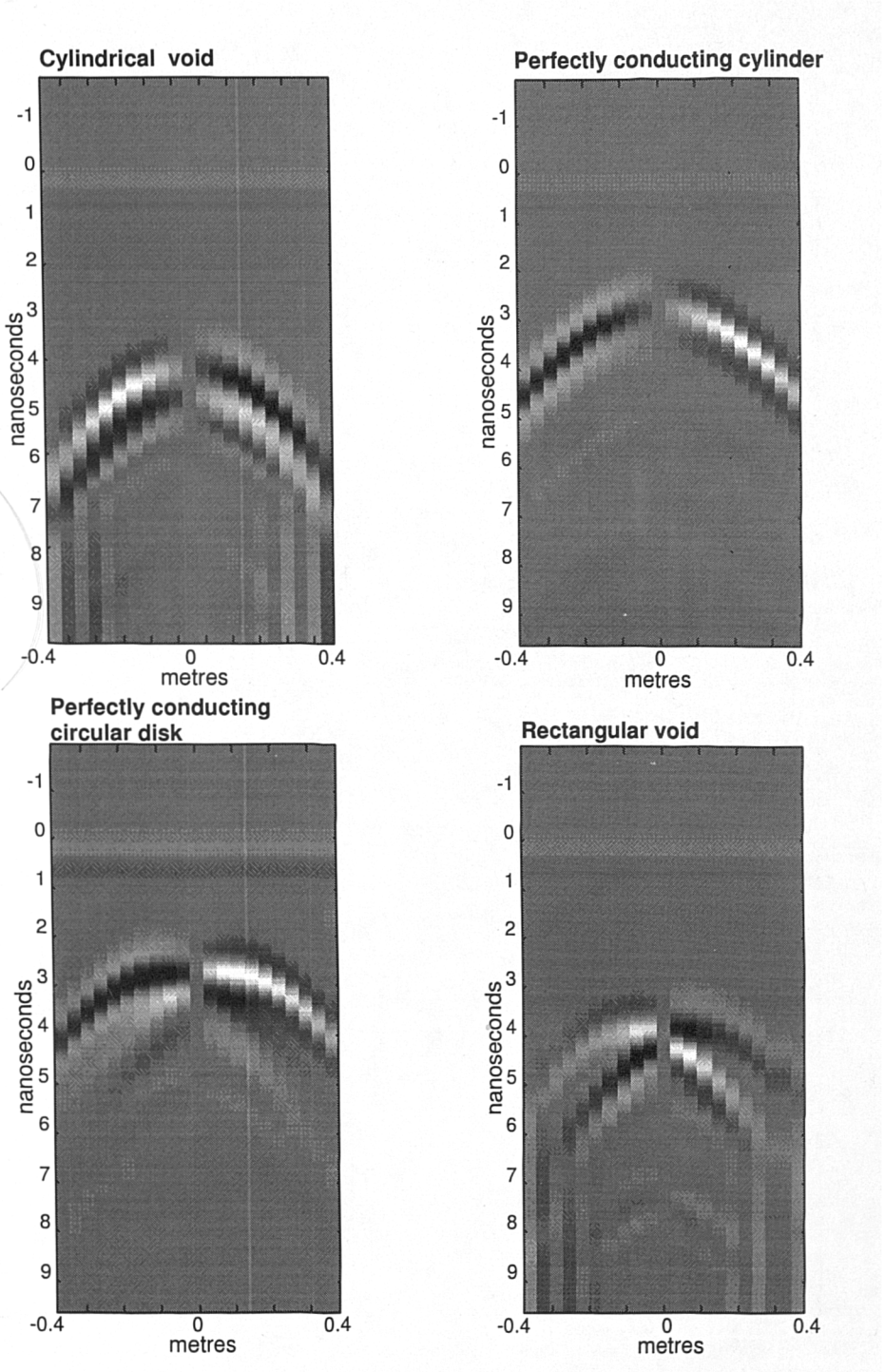

Figure 7.27: Synthetic GPR scans calculated by FDTD over four small targets obtained by monitoring the vertical magnetic field component (collinear configuration).

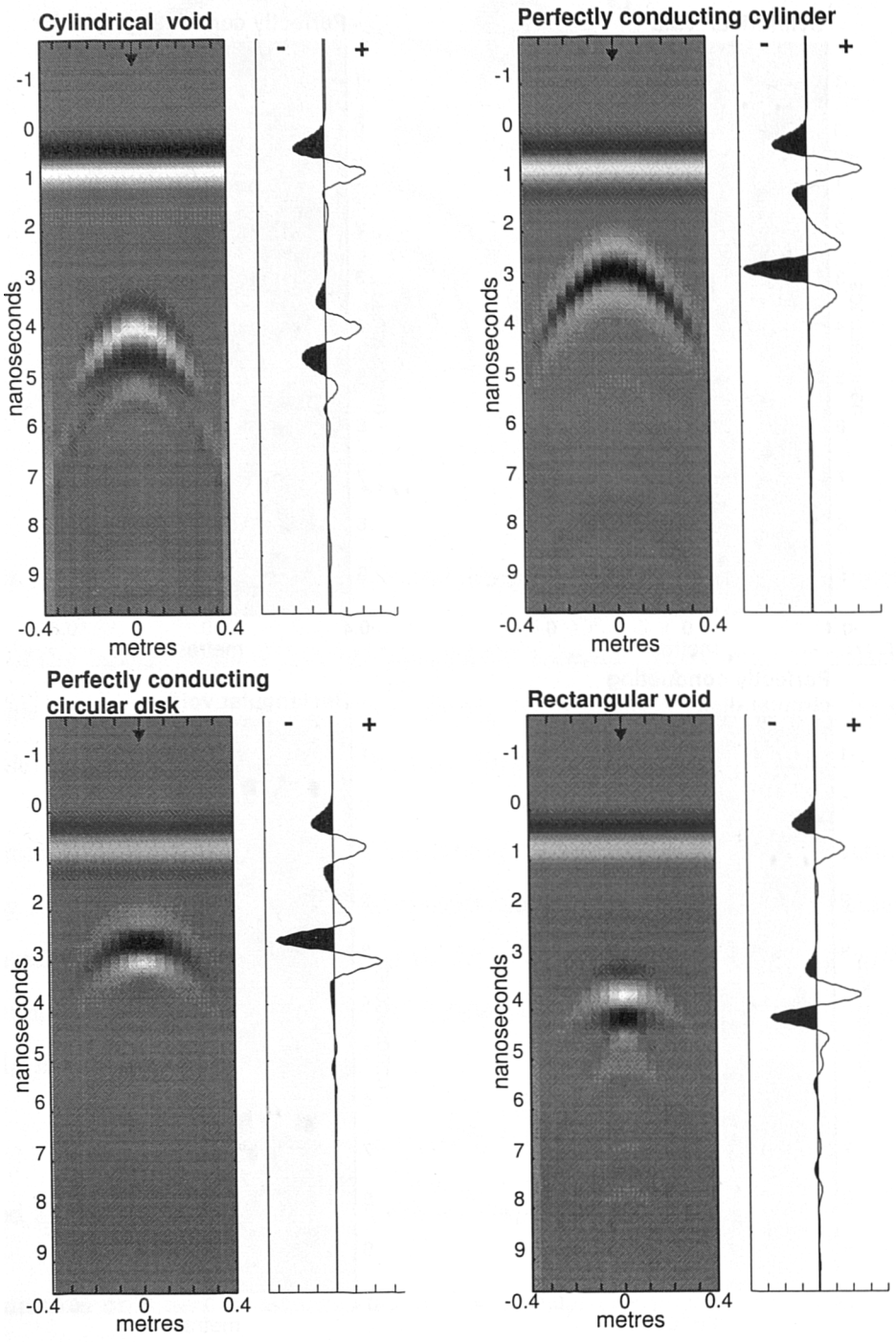

Figure 7.28: Synthetic GPR scans calculated by FDTD over four small targets obtained by monitoring the horizontal magnetic field component (collinear configuration).

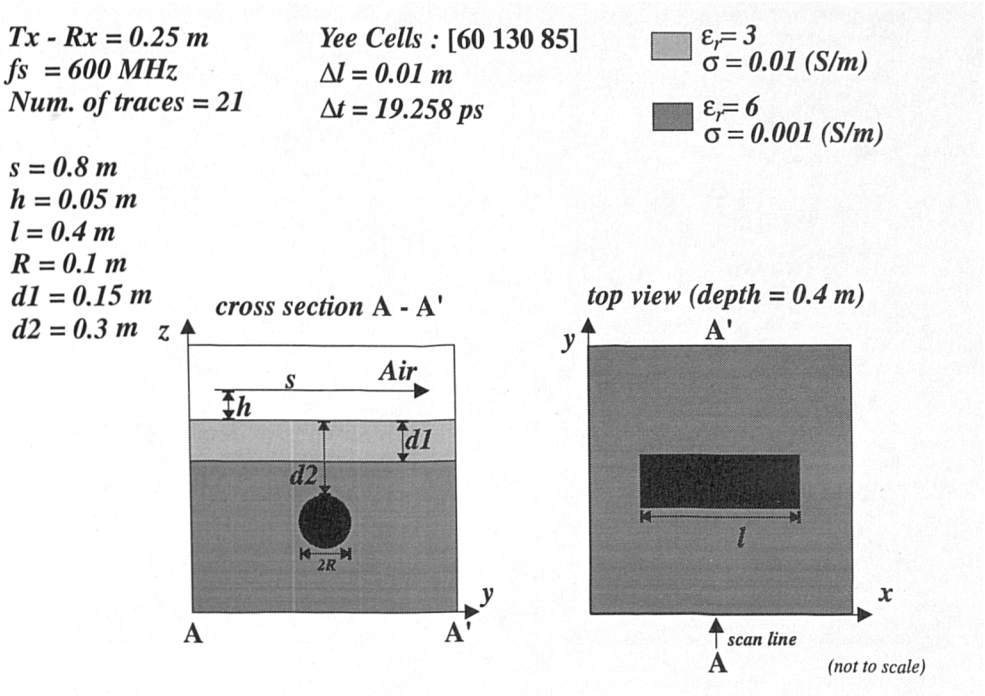

Figure 7.29: Schematic drawing of the FDTD model of a perfectly conducting cylinder located in a two-layer half-space.

that its sensitivity to planar interfaces should be very small especially when a collinear configuration is used. This is demonstrated by considering the synthetic GPR response from a perfectly conducting cylinder using the FDTD model of Figure 7.29. Comparing the signatures from the standard parallel configuration and the collinear one using the vertical magnetic component, illustrated in Figure 7.30, the insensitivity of the later to planar interfaces is apparent. Since, in practice, the detection of a null will be difficult, a magnetic field receiver operating in a differential mode along the scan line will be more appropriate.

7.5 Discussion

In this Chapter results from the application of 3D FDTD and TLM models for the simulation of GPR were presented. Due to the significant computational requirements of the models only small simple targets have been considered. However, these types of targets are of interest in shallow-depth applications of GPR. Field patterns of the sources used in the models were discussed and comparisons between TLM and FDTD models have shown that both models are in good agreement, although care should be exercised to reduce the effects of poor ABC performance in TLM. Off-line effects of targets in GPR records

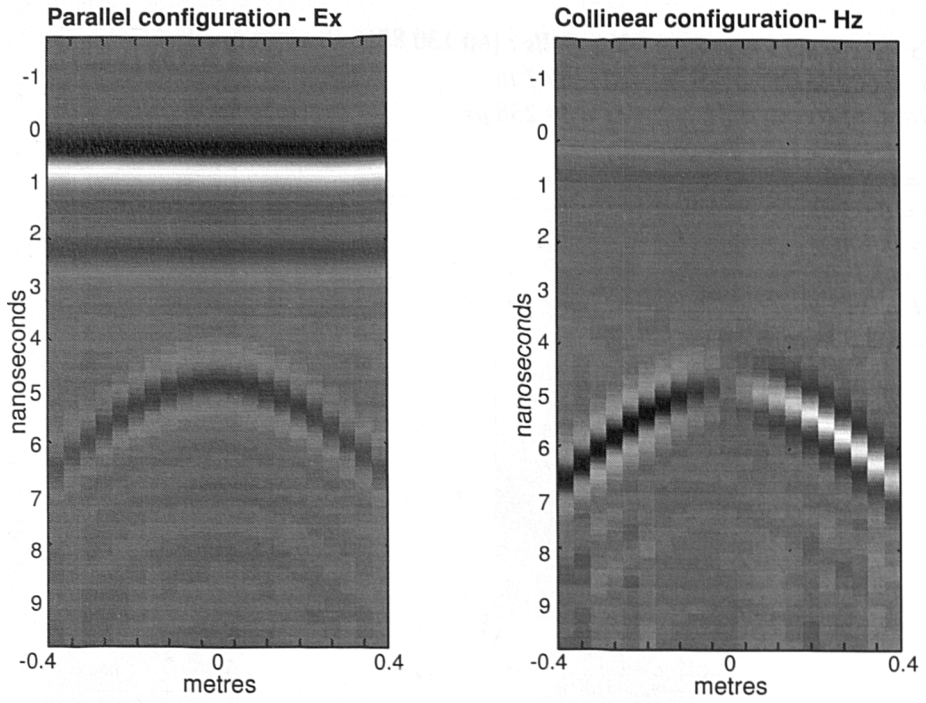

Figure 7.30: Synthetic GPR scans from a perfectly conducting cylinder located in a two-layer half-space using the parallel configuration (left) and the collinear vertical magnetic field (right).

were considered and their relation to the radiation patterns of the transmitting antennas discussed. Alternative GPR survey procedures such as the use of a collinear configuration and the use of magnetic field sensors have been investigated and, from the modelling results, it is suggested that their incorporation in GPR will enhance its detection capabilities. In particular, using magnetic field sensors, reflections from planar targets can be suppressed if desired, which can enhance the detection of a wide range of small targets in GPR. The fact that magnetic field transducers could be of benefit in GPR is not surprising considering their wide range of application in other electromagnetic geophysical methods (Nabighian, 1987).

8

Concluding remarks and lines of research

The aim of this thesis was to investigate the application of the transmission line matrix and the finite-difference time-domain methods to the GPR forward problem. In reporting the findings of this project a discussion at the end of every Chapter has been included as a summary of its main points. Here, a short unified description of each is presented.

The basic principles of GPR have been reviewed and discussed in **Chapter 2** where GPR has been presented both as a radar system and as a geophysical technique. Its differences and similarities with other methods in exploration geophysics and, in particular, the seismic method were discussed and a short account of data acquisition schemes, processing procedures and guidelines for interpretation was provided.

In **Chapter 3** the fundamental laws which govern the forward GPR problem have been discussed on a more formal basis and the factors which mainly influence the GPR signals were examined. The difficulties associated with the rigorous treatment of the problem leads clearly to the requirement of a numerical approach. Examining the pros and cons of different existing formulations for numerical modelling, the suitability of time-domain differential equation models for GPR simulation is demonstrated.

Chapter 4 presented the methodology of the 2D GPR models with particular emphasis

on the application of more efficient absorbing boundary conditions to the TLM method than the existing "matched termination" ABC. In particular, the formulations developed by Higdon and Liao et al. were considered. Different implementation techniques of these ABCs into the TLM algorithm were examined and their performance evaluated and compared, both with the FDTD method and the "matched termination". The problems of instabilities encountered when higher order formulations of the ABCs are used were examined and the necessary procedures to overcome them without sacrificing performance were discussed. Using numerical experiments, comparisons between TLM and FDTD suggest that ABCs have a superior performance in the former. Further, it was shown that an equivalent to FDTD application of an ABC into the TLM algorithm ("Dummy node" approach) is possible and, when a first order Higdon ABC is used, it was found as well to be equivalent to the "matched termination" one in terms of performance.

In **Chapter 5** results from the application of 2D TLM and FDTD to the GPR forward problem were presented. An analysis of the influence that the constitutive parameters of the subsurface have to the GPR signal was presented whether or not these parameters are dependent on the frequency of the electromagnetic fields. From this analysis the effects of the frequency dependence of permittivity described by a Debye model were found to be important only when significant energy is contained in the spectrum of the incident pulse at frequencies close to the relaxation frequencies of the Debye model. Using models of simple cylindrical targets, commonly sought in GPR surveys, both horizontal and vertical resolution were examined and the dependence of the latter to the depth of the targets was demonstrated. Synthetic GPR signatures of geological targets were then discussed which verified the physical reasonableness of the models. Finally, real GPR data obtained over an underground culvert at an archaeological site were compared with the synthetic responses from a model of the same target.

Chapter 6 presented the extension of the methodology of the two dimensional models for three dimensional modelling of GPR. Emphasis was given to the different existing TLM formulations and the advantages of symmetrical condensed nodes were illustrated. However, this node supports spurious modes which, although do not appear to contaminate the solution, are suggested to relate to the unstable performance of ABCs in 3D SCN TLM. Since good ABC performance is very important in three dimensional models, where the increase of "white space" leads to a substantial increase of the required computer resources, an empirical approach was followed and a stable ABC was reported which

is a result of a modification introduced to the Higdon's formulation. The stability and very good performance of this modified ABC was examined by means of numerical experiments and comparisons with FDTD and a 3D TLM model based on the expanded node. However, the good performance of this ABC does not extrapolate to the case when it is located adjacent to media other than free-space. A possible explanation in view of recent analyses of numerical dispersion in a stub loaded SCN is that any possible small amplitude spurious modes will still propagate with the velocity of light in this node instead of that determined by the properties of the simulated medium (as the physical modes will). Hence, the ABC will be mismatched to these type of modes. The good performance of the modified ABC demonstrated when the TLM network was excited by a small Hertzian dipole was also shown when plane wave scattering from targets located in free-space was considered. This has been studied using a new modification to the TLM algorithm which allows the simulation only of scattered electromagnetic fields since the known incident field can specified analytically.

In **Chapter 7** the results of the application of 3D models to GPR were presented. The FDTD model has been used mainly in view of the shortcomings of the ABC performance in the TLM GPR models. However, comparisons of responses obtained by TLM (allowing for sufficient distance to the truncation boundaries) showed good agreement with the FDTD results. The models were used to investigate the signatures of small localized targets and in particular 3D effects on the GPR scans, which have to be considered in interpreting GPR data. Further, by examining different orientations of the transmitting and receiving GPR antennas, the benefits of using a collinear configuration are illustrated. The use of such orientations of the GPR antennas will be more beneficial when targets are located close to the interface and their responses can be obscured by the direct returns from the transmitting antenna when the parallel configuration is used. Examining the synthetic signatures obtained when the magnetic field components are monitored instead of the electric field ones revealed that they can be of benefit in denoting the location of targets. In addition, when the normal to the interface magnetic field component is used, returns from planar interfaces can be suppressed, hence enhancing the response of other targets of interest. This effect, in particular, is more pronounced when a collinear arrangement of the transmitting dipole and a magnetic field sensor is used.

To compare FDTD and TLM models one should make the distinction between two and three dimensional formulations. For the 2D models the methods have been shown to

have identical propagation characteristics. The advantage of using a TLM model is the better performance of ABCs than in the equivalent FDTD one, as has been shown in Chapter 4 which will be important if a small computational domain has to be used. The FDTD model has distinct advantages in terms of the computer resources required by its formulation. However, in view of the constant increase in computing power which is available to the average user, this advantage of the FDTD method may not be as important in the near future. Further, TLM has the ability to model all field components at the same spatial location in the computational domain, and the description of boundaries is more straightforward than FDTD.

In 3D models, when SCN TLM is considered, there are differences in the numerical dispersion exhibited by the two models. Overall this is less in TLM (see Chapter 6) which is an advantage of the method. However, FDTD can be operated using higher time-steps than TLM which are allowed by its stability condition and hence will require fewer iterations than TLM to advance the solution to a set simulated time. The SCN TLM offers a more accurate representation of media into the computational domain and the modelling of all field components in a single location in the network. The staggered placement of field components in FDTD makes the representation of boundaries more difficult and, if variations in magnetic permeability have to be included in the model, the representation of volumetric targets becomes conceptually more obscure.

On the other hand, in FDTD the performance of ABCs is very good irrespective of the parameters of the media adjacent to it. In addition, the savings which result from the use of an FDTD model instead of an SCN TLM one are quite substantial. This is a consequence of the increase in the dimensionality of the models which makes the TLM model rather more demanding in terms of computer resources. As for the 2D models, the constant increase in computing power will eventually make this advantage of FDTD less appealing, but, we are still far from the stage that the average user of a GPR could have access to such increased computing power.

In conclusion, as has been shown in this thesis, both TLM and FDTD can be used successfully for GPR modelling and their use will benefit the process of data interpretation.

8.1 Lines of research

This report is by no means a complete and final investigation of the subject. There is much left to be done. Some suggestions of future work are:

- An investigation into the application of higher order approximations to the partial derivatives of Maxwell's equations which form the basis of the FDTD method. The use of more accurate difference equations will benefit the modelling process by reducing the numerical dispersion thus allowing for coarser discretizations. Hence, larger physical space will be able to be simulated by the GPR models. Although, that is currently possible for homogeneous media the longer finite-difference stencil which will result using a higher order approximation will make the treatment of interfaces more difficult and this has to be addressed.

- Research towards a stable and general ABC for 3D SCN TLM is required and other ABC formulations than the ones discussed here should be considered. Further, the application of the modified ABC, introduced in this work, to general electromagnetic scattering problems should be considered and its performance has to be more carefully examined in relation to these type of problems. In addition, its application in TLM models based on the HSCN and SSCN has to be examined.

  The application of the new "perfectly matched layer" (PML) ABC in the FDTD GPR models has to be studied. Further, the possibility of incorporating this type of ABC into the 3D SCN TLM method should be examined. A problem which will have to be addressed incorporating this ABC into the TLM algorithm is the simulation of an unphysical medium (such a PML absorber) by a "physical" model like TLM.

- The significance of spurious modes in TLM has to be investigated further and in particular their relation with the problem of ABC instabilities.

- The computational efficiency of both TLM and FDTD GPR models can be substantially improved by examining their implementation in parallel computing environments. Such implementations will allow for more realistic simulations since it will be possible to obtain results from large GPR models in reasonable time.

- Experimental verification of the efficiency of alternative arrangements of the GPR transmitting and receiving antennas and of the use of magnetic field sensors is required.

- Further study on the application of the TLM and FDTD GPR models to more specific geophysical and engineering problems is required. Currently, work has begun in examining using the FDTD model the signatures of closely spaced rebars in concrete.

- The investigation of procedures for automated reconstruction of the subsurface targets (data inversion) using as a basis the modelling approaches described here.

A

3D FDTD update equations and SCN TLM scattering and connection matrices

The update equations of 3D FDTD for all six electromagnetic field components are:

$$(A.1)\quad E_x\big|^{n}_{(i+1/2,j,k)} = \left(\frac{1-\frac{\sigma(i+1/2,j,k)\Delta t}{2\epsilon(i+1/2,j,k)}}{1+\frac{\sigma(i+1/2,j,k)\Delta t}{2\epsilon(i+1/2,j,k)}}\right) E_x\big|^{n-1}_{(i+1/2,j,k)} + \left(\frac{\frac{\Delta t}{\epsilon(i+1/2,j,k)}}{1+\frac{\sigma(i+1/2,j,k)\Delta t}{2\epsilon(i+1/2,j,k)}}\right)\left(\frac{H_z\big|^{n-1/2}_{(i+1/2,j+1/2,k)} - H_z\big|^{n-1/2}_{(i+1/2,j-1/2,k)}}{\Delta y} - \frac{H_y\big|^{n-1/2}_{(i+1/2,j,k+1/2)} - H_y\big|^{n-1/2}_{(i+1/2,j,k-1/2)}}{\Delta z}\right)$$

$$(A.2)\quad E_y\big|^{n}_{(i,j+1/2,k)} = \left(\frac{1-\frac{\sigma(i,j+1/2,k)\Delta t}{2\epsilon(i,j+1/2,k)}}{1+\frac{\sigma(i,j+1/2,k)\Delta t}{2\epsilon(i,j+1/2,k)}}\right) E_y\big|^{n-1}_{(i,j+1/2,k)} + \left(\frac{\frac{\Delta t}{\epsilon(i,j+1/2,k)}}{1+\frac{\sigma(i,j+1/2,k)\Delta t}{2\epsilon(i,j+1/2,k)}}\right)\left(\frac{H_x\big|^{n-1/2}_{(i,j+1/2,k+1/2)} - H_x\big|^{n-1/2}_{(i,j+1/2,k-1/2)}}{\Delta z} - \frac{H_z\big|^{n-1/2}_{(i+1/2,j+1/2,k)} - H_z\big|^{n-1/2}_{(i-1/2,j+1/2,k)}}{\Delta x}\right)$$

$$(A.3)\quad E_z\big|^{n}_{(i,j,k+1/2)} = \left(\frac{1-\frac{\sigma(i,j,k+1/2)\Delta t}{2\epsilon(i,j,k+1/2)}}{1+\frac{\sigma(i,j,k+1/2)\Delta t}{2\epsilon(i,j,k+1/2)}}\right) E_z\big|^{n-1}_{(i,j,k+1/2)} + \left(\frac{\frac{\Delta t}{\epsilon(i,j,k+1/2)}}{1+\frac{\sigma(i,j,k+1/2)\Delta t}{2\epsilon(i,j,k+1/2)}}\right)\left(\frac{H_y\big|^{n-1/2}_{(i+1/2,j,k+1/2)} - H_y\big|^{n-1/2}_{(i-1/2,j,k+1/2)}}{\Delta x} - \frac{H_x\big|^{n-1/2}_{(i,j+1/2,k+1/2)} - H_x\big|^{n-1/2}_{(i,j-1/2,k+1/2)}}{\Delta y}\right)$$

$$(A.4)\quad H_x\big|^{n+1/2}_{i,j+1/2,k+1/2} = H_x\big|^{n-1/2}_{i,j+1/2,k+1/2} + \frac{\Delta t}{\mu_0}\left(\frac{E_y\big|^{n}_{i,j+1/2,k+1} - E_y\big|^{n}_{i,j+1/2,k}}{\Delta z} - \frac{E_z\big|^{n}_{i,j+1,k+1/2} - E_z\big|^{n}_{i,j,k+1/2}}{\Delta y}\right)$$

$$(A.5)\quad H_y\big|^{n+1/2}_{i+1/2,j,k+1/2} = H_y\big|^{n-1/2}_{i+1/2,j,k+1/2} + \frac{\Delta t}{\mu_0}\left(\frac{E_z\big|^{n}_{i+1,j,k+1/2} - E_z\big|^{n}_{i,j,k+1/2}}{\Delta x} - \frac{E_x\big|^{n}_{i+1/2,j,k+1} - E_x\big|^{n}_{i+1/2,j,k}}{\Delta z}\right)$$

$$(A.6)\quad H_z\big|^{n+1/2}_{i+1/2,j+1/2,k} = H_x\big|^{n-1/2}_{i+1/2,j+1/2,k} + \frac{\Delta t}{\mu_0}\left(\frac{E_x\big|^{n}_{i+1/2,j+1,k} - E_x\big|^{n}_{i+1/2,j,k}}{\Delta y} - \frac{E_y\big|^{n}_{i+1,j+1/2,k} - E_y\big|^{n}_{i,j+1/2,k}}{\Delta x}\right)$$

The scattering procedure in matrix notation for a regular SCN TLM with open circuit and loss stubs is (Christopoulos, 1995)

(A.7)

$$\begin{bmatrix} {}^{r}V_{ynx} \\ {}^{r}V_{znx} \\ {}^{r}V_{xny} \\ {}^{r}V_{zny} \\ {}^{r}V_{ynz} \\ {}^{r}V_{xnz} \\ {}^{r}V_{ypz} \\ {}^{r}V_{zpy} \\ {}^{r}V_{zpx} \\ {}^{r}V_{xpz} \\ {}^{r}V_{xpy} \\ {}^{r}V_{ypx} \\ {}^{r}V_{ox} \\ {}^{r}V_{oy} \\ {}^{r}V_{oz} \end{bmatrix} = \begin{bmatrix} a & b & d & & & & & & b & & -d & c & g & & \\ b & a & & & & d & & & c & -d & & b & g & & \\ d & & a & b & & & & b & & & c & -d & & g & \\ & & b & a & d & & -d & c & & & b & & & g & \\ & & & d & a & b & c & -d & & b & & & & & g \\ & d & & & b & a & b & & -d & c & & & & & g \\ & & & -d & c & b & a & d & & b & & & & & g \\ & & b & c & -d & & d & a & & & b & & & g & \\ b & c & & & & -d & & & a & d & & b & g & & \\ & -d & & & b & c & b & & d & a & & & & & g \\ -d & & c & b & & & & b & & & a & d & & g & \\ c & b & -d & & & & & & b & & d & a & g & & \\ e & e & & & & & & & e & & & e & h & & \\ & & e & e & & & & e & & & e & & & h & \\ & & & & e & e & e & & & e & & & & & h \end{bmatrix} \cdot \begin{bmatrix} {}^{i}V_{ynx} \\ {}^{i}V_{znx} \\ {}^{i}V_{xny} \\ {}^{i}V_{zny} \\ {}^{i}V_{ynz} \\ {}^{i}V_{xnz} \\ {}^{i}V_{ypz} \\ {}^{i}V_{zpy} \\ {}^{i}V_{zpx} \\ {}^{i}V_{xpz} \\ {}^{i}V_{xpy} \\ {}^{i}V_{ypx} \\ {}^{i}V_{ox} \\ {}^{i}V_{oy} \\ {}^{i}V_{oz} \end{bmatrix}$$

where the elements a, b, c ,d, e, g and h are

$$(A.8)\qquad a = -\frac{\hat{Y}_s + \hat{G}_s}{2(4 + \hat{Y}_s + \hat{G}_s)} \qquad b = \frac{4}{2(4 + \hat{Y}_s + \hat{G}_s)} \qquad c = a$$

$$(A.9)\qquad d = \frac{4}{2(4 + \hat{Y}_s + \hat{G}_s)} \qquad e = b \qquad g = \hat{Y}_s b \qquad h = \frac{\hat{Y}_s - \hat{G}_s - 4}{\hat{Y}_s + \hat{G}_s + 4}$$

The connection procedure is described by

(A.10)

$$\begin{bmatrix} {}^{i}V_{ynx} \\ {}^{i}V_{znx} \\ {}^{i}V_{xny} \\ {}^{i}V_{zny} \\ {}^{i}V_{ynz} \\ {}^{i}V_{xnz} \\ {}^{i}V_{ypz} \\ {}^{i}V_{zpy} \\ {}^{i}V_{zpx} \\ {}^{i}V_{xpz} \\ {}^{i}V_{xpy} \\ {}^{i}V_{ypx} \\ {}^{i}V_{ox} \\ {}^{i}V_{oy} \\ {}^{i}V_{oz} \end{bmatrix} = \begin{bmatrix} & & & & & & & & & & & & & & 1 \\ & & & & & & & & & & & & & 1 & \\ & & & & & & & & & & & & 1 & & \\ & & & & & & & & & & & 1 & & & \\ & & & & & & & & & & 1 & & & & \\ & & & & & & & & & 1 & & & & & \\ & & & & & & & & 1 & & & & & & \\ & & & & & & & 1 & & & & & & & \\ & & & & & & 1 & & & & & & & & \\ & & & & & 1 & & & & & & & & & \\ & & & & 1 & & & & & & & & & & \\ & & & 1 & & & & & & & & & & & \\ & & 1 & & & & & & & & & & & & \\ & 1 & & & & & & & & & & & & & \\ 1 & & & & & & & & & & & & & & \\ & & & & & & & & & & & & 1 & & \\ & & & & & & & & & & & 1 & & & \\ & & & & & & & & & & & & & & 1 \end{bmatrix} \cdot \begin{bmatrix} {}^{r}V_{ynx} \\ {}^{r}V_{znx} \\ {}^{r}V_{xny} \\ {}^{r}V_{zny} \\ {}^{r}V_{ynz} \\ {}^{r}V_{xnz} \\ {}^{r}V_{ypz} \\ {}^{r}V_{zpy} \\ {}^{r}V_{zpx} \\ {}^{r}V_{xpz} \\ {}^{r}V_{xpy} \\ {}^{r}V_{ypx} \\ {}^{r}V_{ox} \\ {}^{r}V_{oy} \\ {}^{r}V_{oz} \end{bmatrix}$$

denoting the location of the SCN where the reflected pulses originate as (i_s, j_s, k_s) the locations of the adjacent SCNs on which these voltage pulses are incident are obtained by an increment of 1 in the direction denoted by the first subscript of the voltage pulse if the second is n and by a decrement of -1 in the same direction if the second subscript is p. The pulses on the open circuit stubs are incident on the same node.

B

Scattered field formulation for the SCN TLM

A scattered field formulation for a regular SCN TLM node can be derived using the same procedures outlined in Chapter 6. Such a formulation is based on expressing the electromagnetic fields as

$$\mathbf{E}^t = \mathbf{E}^i + \mathbf{E}^s \tag{B.1}$$

$$\mathbf{H}^t = \mathbf{H}^i + \mathbf{H}^s \tag{B.2}$$

where the total electromagnetic fields are given as the sum of the incident fields plus the scattered fields which arise on and within the object in response to the incident field. Both incident and scattered fields satisfy Maxwell's equations (assuming linear media) independently (Kunz and Luebbers, 1993). The form of Maxwell's equations that govern only the propagation of scattered fields is obtained by subtracting Maxwell's equations for the incident fields from the ones describing the total fields. Therefore, in free-space the scattered fields satisfy

$$\nabla \times \mathbf{E}^s = -\mu_0 \frac{\partial \mathbf{H}^s}{\partial t} \tag{B.3}$$

$$\nabla \times \mathbf{H}^s = \epsilon_0 \frac{\partial \mathbf{E}^s}{\partial t} \tag{B.4}$$

and in non-magnetic media different than free-space

$$\nabla \times \mathbf{E}^s = -\mu_0 \frac{\partial \mathbf{H}^s}{\partial t} \tag{B.5}$$

$$\nabla \times \mathbf{H}^s = \epsilon \frac{\partial \mathbf{E}^s}{\partial t} + \sigma \mathbf{E}^s + [(\epsilon - \epsilon_0)\frac{\partial \mathbf{E}^i}{\partial t} + \sigma \mathbf{E}^i] \tag{B.6}$$

Examining equations (B.3)–(B.6) and assuming that all voltage pulses in a SCN TLM node are associated only with scattered fields, it is evident that the regular SCN without stubs simulates the propagation of scattered fields in free-space since they satisfy the same equations as the total fields assumed in the derivation of the node. However, in regions with different properties than free space the SCN with stubs simulates the propagation of total fields described by equations (B.5) and (B.6), where the terms in brackets are not present. If it is to be assumed that the SCN models only the propagation of scattered fields, the terms in brackets of equation (B.6) should be taken into account. These terms can be easily identified as representing polarization and conduction currents induced on the object by the incident fields. In TLM notation, these can be simulated by introducing fictitious open circuit and loss stubs on the node. According to equation (B.5), the voltage pulses on these stubs are to be determined from and depend only on the incident fields. The polarization (i_p) and conduction (i_c) currents in TLM notation[1] are

$$i_p = y_s({}^i v_o - {}^r v_o) \tag{B.7}$$

$$i_g = -g_s {}^r v_g \tag{B.8}$$

The admittance of the open circuit and loss stubs are

$$y_s = \frac{2(\epsilon - \epsilon_0)\Delta l}{\Delta t} \tag{B.9}$$

$$g_s = \sigma \Delta l \tag{B.10}$$

The presence of these currents have to be taken into account when the charge conservation principle is applied. Therefore, considering the E_x component charge conservation requires

$$\begin{aligned} Y_l({}^iV_{ynx} - {}^rV_{ynx}) + Y_l({}^iV_{ypx} - {}^rV_{ypx}) + Y_l({}^iV_{znx} - {}^rV_{znx}) + Y_l({}^iV_{zpx} - {}^rV_{zpx}) \\ + Y_s({}^iV_{ox} - {}^rV_{ox}) - G_s {}^rV_{gx} + i_p + i_g = 0 \end{aligned} \tag{B.11}$$

The total node voltage V_x at the SCN (assumed to be associated only with scattered fields) is obtained from the SCN lines contributing to it as described in Chapter 6. However, in order to express it only in terms of incident voltage pulses, equation (B.11) has to be used

[1] Lowercase symbols are use here to denote quantities associated only with incident fields in the SCN

instead of (6.53). Therefore, the total node voltage V_x is given by

(B.12)
$$V_x = \frac{2}{4+\hat{Y}_s+\hat{G}_s}({}^{i}V_{ynx}+{}^{i}V_{ypx}+{}^{i}V_{znx}+{}^{i}V_{zpx}+\hat{Y}_s\,{}^{i}V_{ox}) + \frac{\hat{y}_s({}^{i}\nu_{ox}-{}^{r}\nu_{ox})-\hat{g}_s\,{}^{r}\nu_{gx})}{4+\hat{Y}_s+\hat{G}_s}$$

where y_s and g_s have been normalized with respect to the admittance of the SCN lines. The voltage pulses on the stubs are easily obtained from the known incident fields and no additional storage is required. The pulses associated with i_p can be calculated by considering conditions at the open circuit termination of the stub at time level $n+1/2$. Then

(B.13)
$${}_{n+1/2}\nu_x = {}^{i}_{n+1}\nu_{ox} + {}^{r}_{n}\nu_{ox}$$

and the current on the open circuit termination should be zero hence

(B.14)
$${}^{i}_{n+1}\nu_{ox} = {}^{r}_{n}\nu_{ox}$$

combining the above two equations the voltage pulses on the open stub required in (B.12) at time level n are

(B.15)
$${}^{i}_{n}\nu_{ox} = \frac{{}_{n-1/2}\nu_x}{2}$$

(B.16)
$${}^{r}_{n}\nu_{ox} = \frac{{}_{n+1/2}\nu_x}{2}$$

The voltage pulse associated with i_c is simply

(B.17)
$${}^{r}_{n}\nu_{gx} = {}_{n}\nu_x$$

Finally, the total voltage ν_x is obtained by the established equivalence between voltage and electric field in TLM

(B.18)
$$\nu_x = -\frac{E^i_x}{\Delta l}$$

The other electric field components can be treated in a similar fashion.

Scattering in a short circuit SCN, simulating a perfect conductor, can be determined by considering the appropriate boundary condition which requires the total electric field to be zero. In a scattered field formulation this condition becomes

(B.19)
$$V = -\nu$$

Hence, considering (B.19), the reflected voltage pulses from a short circuit SCN can be estimated. For example, ${}^{r}V_{xny}$ is

(B.20)
$${}^{r}V_{xny} = -\nu_x - {}^{i}V_{xny}$$

This condition can be applied when a perfect conducting boundary is placed between to SCN nodes.

The modifications required in the TLM algorithm to obtain only scattered fields are minimal. The scattering equations are used as in the total field TLM and scattering into the SCN stubs proceeds in the same way. The only difference is the use of (B.12) instead of that derived in Chapter 6. In addition, if total fields are required, they are obtained simply by adding the known incident fields to the scattered fields calculated by TLM.

To verify the accuracy of this formulation, the scattered fields from various dielectric and perfectly conducting objects illuminated by plane waves have been obtained both with this formulation and the formulation based on separating the TLM network in total and scattered field regions as presented by (Simons et al.,1991, Chen et al., 1993, German, 1994). The agreement between the solutions is very good. As an example, Figure B.1 presents the backscatter electric field from a dielectric sphere of radius $r = 10\Delta l$ and $\epsilon_r = 3$, $\sigma = 0.01$ (S/m) and from a perfectly conducting box with dimensions $10\Delta l \times 10\Delta l \times 10\Delta l$ illuminated by a z-polarized Gaussian plane wave of the form

$$e^{-\zeta(t-\xi\Delta t)^2)} \tag{B.21}$$

where $\zeta = (4/(\xi\Delta t)^2)$ and $\xi = 64.0$. The wave-vector of the incident field lies in the $x-y$ plane and forms an angle of 45 degrees with the x axis. In both cases a matched termination ABC is used to truncate the $40\Delta l \times 40\Delta l \times 40\Delta l$ TLM network.

The main advantage of the scattered field formulation over the separation of the TLM network in total and scattered field regions is that the conditions applied at the interface separating the two regions of the later formulation are not exact due to numerical dispersion (Chen et al., 1993). Therefore, when the scattered fields are of a small amplitude, numerical noise can render the solution in the scattered region useless. In a pure scattered formulation such a problem does not exist. In Figure B.2 this is illustrated by considering scattering from a dielectric sphere in an identical configuration to the previous example but with the electrical parameters of the sphere set to $\epsilon_r = 1.001$ and $\sigma = 0$ (S/m). The contamination of the solution by numerical noise when the total field formulation is used is apparent whereas such a problem does not appear in the solution obtained using the scattered field formulation.

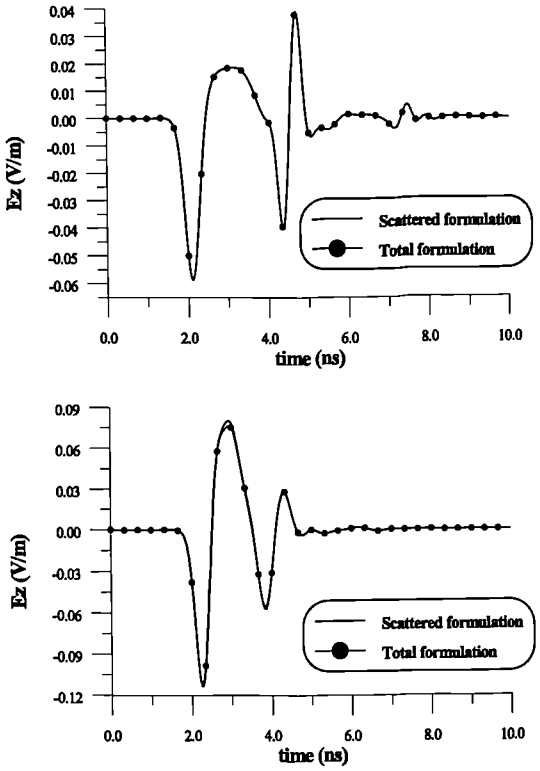

Figure B.1: Backscatter electric field from a dielectric sphere ($\epsilon_{r=}3$, σ = 0.01(S/m)) (top) and from a perfectly conducting box (bottom) obtained with the scattered and total field formulations.

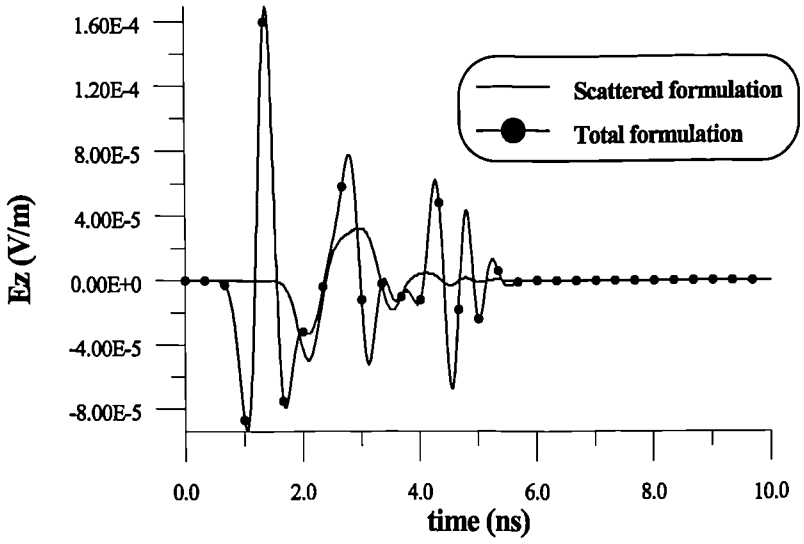

Figure B.2: Backscatter electric field from a dielectric sphere (ϵ_r = 1.001) obtained using the scattered and total field formulations.

List of Symbols and Abbreviations

$\mathbf{E}$	electric field intensity vector (volts/metre)
$\mathbf{H}$	magnetic field intensity vector (amperes/meter)
$\mathbf{D}$	electric flux density vector (coulombs/square metre)
$\mathbf{B}$	magnetic flux density vector (webers/square metre)
$\mathbf{J}_s$	source electric current density vector (amperes/square metre)
$\mathbf{J}_c$	conduction electric current density vector (amperes/square metre)
ϵ	dielectric permittivity (farad/metre)
μ	magnetic permeability (henry/metre)
σ	conductivity (siemens/metre)
c	speed of light (metre/second)
u	wave velocity (metre/second)
u_l	pulse velocity on transmission lines
V	voltage (volts)
I	current (amperes)
C	capacitance (farad)
L	inductance (henry)
C_d	distributed capacitance (farad/metre)
L_d	distributed inductance (henry/metre)
G	conductance (mho)
Z	impedance (ohms)
Y	admittance (mhos)
Z_l	transmission line impedance
Y_l	transmission line admittance

$(i, j, k; n)$	spatial and time indices
$(x, y, z; t)$	space and time coordinates
Δt	time increment
Δl	space increment
$\jmath$	$\sqrt{-1}$
γ	propagation constant
α	attenuation constant (Nepers/metre)
β	phase constant (rad/metre)
ω	angular frequency (rad/second)
θ	angle (degrees)
ABC	Absorbing boundary condition
ADE	Auxiliary differential equation
CSG	Common source gather
CMP	Common mid point
CDP	Common depth point
CFL	Courand-Freidrichs-Lewy (stability condition)
CW	Continuous wave
DC	Direct current
DE	Differential equation
DN	Dummy node
FD	Frequency domain
FDTD	Finite difference time domain
FFT	Fast Fourier transform
FM-CW	Frequency modulated continuous wave
GPR	Ground probing radar
HED	Horizontal electric dipole
HSCN	Hybrid symmetrical condensed node
IE	Integral equation
NV	Node voltage
PML	Perfectly matched layer
PRF	Pulse repetition frequency
PV	Port voltage
RC	Recursive convolution
RCS	Radar cross section

Rx	Receiver
SCN	Symmetrical condensed node
SSCN	Symmetrical super-condensed node
SNR	Signal to noise ratio
TE	Transverse electric mode
TEM	Transverse electromagnetic mode
TD	Time domain
TM	Transverse magnetic mode
TLM	Transmission line matrix
Tx	Transmitter
WARR	Wide angle reflection refraction

References

Akhtarzad S. and Johns P. B., (1975) "Solution of Maxwell's equations in three space dimensions and time by the t.l.m. method of numerical analysis", *IEE Proceedings*, Vol. 122, pp. 1344-1348

Akhtarzad S. and Johns P. B., (1975b) "Generalised elements for t.l.m. method of numerical analysis", *IEE Proceedings*, Vol. 122, pp. 1349-1352

Al-Mukhtar D. A. H., (1980) "A transmission line matrix method with irregularly graded space", *Ph.D thesis*, University of Sheffield, U.K.

Allen R., Mallik A., Johns P., (1987) "Numerical results for the symmetrical condensed TLM node", *IEEE Transactions on Microwave Theory and Techniques*, Vol. 35, pp. 378-382

Ames W. F., (1977) "Numerical Methods for Partial Differential Equations", *Academic Press*

Annan A. P., (1973) "Radio interferometry depth sounding: Part I – Theoretical discussion", *Geophysics*, Vol. 38, pp. 557-590

Annan A. P., (1985) "Radar CDP and WARR soundings: Principles and interpretation", *Technical Note 15*, A-Cubed Inc.

Annan A. P., Davis J. L., Vaughan C. J., (1984) "Radar mapping of buried pipes and cables", *Technical Note 1*, A-Cubed Inc.

Annaert G., (1993) "Evaluation of Sommerfeld integrals using Chebyshev decomposition",

IEEE Transactions on Antennas and Propagation, Vol. 41, pp. 159-164

Arcone S. A., (1981) "Distortion of model subsurface radar pulses in complex dielectrics", *Radio Science*, Vol. 16, pp. 855-864

Arcone S. A., (1984) "Field observations of electromagnetic pulse propagation in dielectric slabs", *Geophysics*, Vol. 49, pp. 1763-1773

Arcone S. A., (1995) "Numerical studies of the radiation patterns of resistively loaded dipoles", *Journal of Applied Geophysics*, Vol. 33, pp. 39-52

Bader B., Krumpholtz M., Russer P., (1994) "Current sources in TLM", *Proceedings of the IEEE Antennas and Propagation International Symposium*, pp. 1110-1115

Balanis C. A., (1982) "Andenna Theory", *John Wiley & Sons*

Balanis C. A., (1989) "Advanced Engineering Electromagnetics", *John Wiley & Sons*

Baños A. Jr., (1966) "Dipole radiation in the presence of a conducting half-space", *Pergamon Press*

Bayliss A. and Turkel E., (1980) "Radiation boundary conditions for wave-like equations", *Communications on Pure and Applied Mathematics*, Vol. 33, pp. 707-725

Benson F. A. and Harrison D., (1975) "Electric-circuit theory", *Edward Arnold Publishers*

Berenger J-P., (1994) "A perfectly matched layer for the absorbtion of electromagnetic waves", *Journal of Computational Physics*, Vol. 114, pp. 185-200

Berini P. and Wu K., (1994) "A pair of hybrid symmetrical condensed TLM nodes", *IEEE Microwave and Guided Wave Letters*, Vol. 4, pp. 244-246

Berini P. and Wu K., (1995) "A comprehensive study of numerical anisotropy and dispersion in 3-D TLM meshes", *IEEE Transactions on Microwave Theory and Techniques*, Vol. 43, pp. 1173-1181

Brewster M. L., Annan A. P., (1994) "Ground-penetrating radar monitoring of a controlled

DNAPL release: 200 MHz radar", *Geophysics*, Vol. 59, pp. 1211-1221

Bruschini C., Gros B., Guerne F., Piece, P-Y., Carmona O., (1996) "Ground penetrating radar and induction coil sensors imaging for antipersonnel mines detection" presented at *6th International conference on ground penetrating radar*

Bubenik D. M., (1977) "A practical method for the numerical evaluation of Sommerfeld integrals", *IEEE Transactions on Antennas and Propagation*, Vol. 25, pp. 904-906

Buechler D. N., Roper D. H., Durney C. H., Christensen D. A., (1995) "Modeling sources in the FDTD formulation and their use in quantifying source and boundary condition errors", *IEEE Transactions on Microwave Theory and Techniques*, Vol. 43, pp. 810-814

Bungey J. H. and Millard S. G., (1995) "Detecting sub-surface features in concrete by impulse radar", *Nondestructive Testing and Evaluation*, Vol. 12, pp. 33-51

Cangellaris A. C. and Wright D. B., (1991) "Analysis of the numerical error caused by the stair-stepped approximation of a conducting boundary in FDTD simulations of electromagnetic phenomena", *IEEE Transactions on Antennas and Propagation*, Vol. 39, pp. 1518-1525

Chan L. C., Moffatt D. L., Peters L. Jr., (1979) "A characterization of subsurface radar targets", *Proceedings of the IEEE*, Vol. 67, pp. 991-1000

Chen Z. and Ney M. M., (1994) "Conversion between the TLM solutions and field solutions", *IEEE Transactions on Microwave Theory and Techniques*, Vol. 42, pp. 529-532

Chen Z., Ney M. M., Hoefer W. J. R.,(1991) "A new finite-difference time-domain formulation and its equivalence with the TLM symmetrical condensed node", *IEEE Transactions on Microwave Theory and Techniques*, Vol. 39, pp. 2160-2169

Chen Z., Ney M. M., Hoefer W. J. R., (1993) "Absorbing and connecting boundary conditions for the TLM method", *IEEE Transactions on Microwave Theory and Techniques*, Vol. 41, pp. 2016-2024

Chew W. C., (1990) "Waves and fields in inhomogeneous media", *Van Nostrand Reinhold*

Choi D. H., (1989) "A comparison of the dispersion characteristics associated with the TLM and FD-TD methods", *International Journal of Numerical Modelling: Electronic Networks, Devices and Fields*, Vol. 2, pp. 203-214

Christopoulos C., (1995) "The transmission-line modelling method", *IEEE Press*

Christopoulos C. and Herring J. L., (1993) "The application of transmission-line modeling (TLM) to electromagnetic compatibility problems", *IEEE Transactions on Electromagnetic Compatibility*, Vol. 35, pp. 185-191

Claerbout J. F., (1992) "Earth Soundings Analysis: Processing versus Inversion", *Blackwell Scientific*

Coppack G., Emerick G., Wilson K., Dittmer J., Szymanski J., Tsourlos P., Giannopoulos A., (1992) "Recent archaeological discoveries at the medieval site of Fountains Abbey", *Medieval Europe*, Vol. 6, pp. 47-52

Daniels D. J., Gunton, D.J., Scott H. F., (1988) "Introduction to subsurface radar", *IEE Proceedings*, Vol. 135, pt. F, pp. 278-320

Davis J. L. and Annan A. P.,(1989) "Ground-penetrating radar for high-resolution mapping of soil and rock stratigraphy", *Geophysical Prospecting*, Vol. 37, pp. 531-551

Davis J. L., Annan A. P., Black G., Leggat C. D., (1985) "Geologic sounding using low frequency radar", *Abstracts of the 55th Annual International SEG Meeting*

De Hoop A. T., (1960) "A modification of Carniard's method for solving seismic pulse problems", *Applied Scientific Research*, Vol. 8, pp. 349-356

De Hoop A. T., (1991) "Reciprocity, discretisation, and the numerical solution of direct and inverse electromagnetic radiation and scattering problems", *Proceedings of the IEEE*, Vol. 79, pp. 1421-1430

Dobson M. C., Ulaby F. T., Hallikainen M. T., El-Rayes M. A., (1985) "Microwave dielectric behavior of wet soil – Part II: Dielectric mixing models", *IEEE Transactions on Geoscience and Remote Sensing*, Vol. 23, pp. 35-46

Duffy A. P., Naylor P., Benson T. M., Christopoulos C., (1993) "Numerical simulation of electromagnetic coupling and comparison with experimental results", *IEEE Transactions on Electromagnetic Compatibility*, Vol. 35, pp. 46-54

Dvorak S. L., (1992) "Application of the Fast Fourier Transform to the computation of the Sommerfeld integral for a vertical electric dipole above a half-space", *IEEE Transactions on Antennas and Propagation*, Vol. 40, pp. 798-805

Elliot R. S., (1966) "Electromagnetics", *McGraw-Hill*

Engheta N., Pappas C. H., Elachi C., (1982) "Radiation patterns of interfacial dipole antennas", *Radio Science*, Vol. 17, pp. 1557-1566.

Engquist B. and Majda A., (1979) "Radiation boundary conditions for acoustic and elastic wave calculations", *Communications on Pure and Applied Mathematics*, Vol. 32, pp. 313-357

Eswarappa C. and Hoefer W. J. R., (1994) "One-way equation absorbing boundary conditions for 3-D TLM analysis of planar and Quasi-planar structures", *IEEE Transactions on Microwave Theory and Techniques*, Vol. 42, pp. 1669-1677

Fang J., (1989) "Time domain finite difference computation for Maxwell's equations", *Ph.D thesis*, University of California at Berkeley, U.S.A.

Fisher E., McMehan G. A., Annan A. P., (1992) "Acquisition and processing of wide-aperture ground-penetrating radar data", *Geophysics*, Vol. 57, pp. 494-504

Frischknecht F. C., (1987) "Electromagnetic physical scale modeling", *Electromagnetic methods in Applied Geophysics, SEG*, eds. Nabighian M. N., Vol. 1, pp. 365-441

Fusco M., (1990) "FDTD Algorithm in Curvilinear Coordinates", *IEEE Transactions on Antennas and Propagation*, Vol. 38, pp. 76-89

Gandhi O. P., Gao B. -Q., Chen J. -Y., (1993) "A frequency-dependent finite-difference time-domain formulation for general dispersive media", *IEEE Transactions on Microwave Theory and Techniques*, Vol. 41, pp. 658-665

German F. J., (1990) "RCS of three-dimensional scatterers using the symmetrical con-

densed TLM method", *Electronics Letters*, Vol. 26, pp. 673-674

German F. J., (1994) "General electromagnetic scattering analysis by TLM method", *Electronics Letters*, Vol. 30, pp. 689-690

Giannopoulos A. and Tealby J. M.,(1995) "Comparison of performance of absorbing boundary conditions in TLM and FDTD", *Electronics Letters*, Vol. 31, pp. 1639-1640

Giannopoulos A., Tealby J. M., Szymanski J. E., (1995b) "Modelling and inversion techniques for radar applied to archaeological investigations", *IEE Colloquium on Radar and microwave techniques for non-destructive evaluation*, 2/1-2/3

Giannopoulos A., Tealby J. M., Tsokas G., (1993) "Ground probing radar – A brief account of its merits and limitations based on case histories in N. Greece", *Proceedings of the 2nd Symposium of the Greek Archaeometry Society*

Giannopoulos A., Tealby J. M., Tsokas G., (1993b) "A 2D forward model of ground probing radar: The transmission line matrix method", *Proccedings of the 2nd Congress of the Greek Geophysical Union*, Vol. II, pp. 172-183

Giannopoulos A., Tealby J. M., Tsokas G., (1994) "Numerical modelling of ground penetrating radar", *Extended Abstracts of the 56th EAEG meeting*, P048

Giannopoulos A., Tealby J. M., Tsokas G., (1995) "Numerical modelling of ground penetrating radar", *Geophysical Prospecting*, (submitted)

Goodman D., (1994) "Ground-penetrating radar simulation in engineering and archaeology", *Geophysics*, Vol. 59, pp. 224-232

Hallikainen M. T., Ulaby F. T., Dobson M. C., El-Rayes M. A., Wu L-K., (1985) "Microwave dielectric behavior of wet soil – Part I: Empirical models and experimental observations", *IEEE Transactions on Geoscience and Remote Sensing*, Vol. 23, pp. 25-33

Harrington R. F., (1993) "Field computation by moment methods", *IEEE Press*

Harmuth H.F., (1981) "Nonsinusoidal wave for radar and radio communication", *Academic Press*

Herring J. L., (1993) "Developments in the transmission-line modelling method for electromagnetic compatibility studies", *Ph.D thesis*, University of Nottingham, U.K.

Higdon R. L., (1986) "Absorbing boundary conditions for difference approximations to the multi-dimensional wave equation", *Mathematics of Computation*, Vol. 47, pp. 437-459

Higdon R. L., (1987) "Numerical absorbing boundary conditions for the wave equation", *Mathematics of Computation*, Vol. 49, pp. 65-90

Hipp J. E., (1974) "Soil electromagnetic parameters as functions of frequency, soil density, and soil moisture", *Proceedings of the IEEE*, Vol. 62, pp. 98-103

Ho G., Kawanaka A., Takagi M., (1994) "Frequency domain migration for subsurface radar considering variations in propagation velocity", *IEICE Transactions on Communications*, Vol. E77-B, pp.1056-1063

Hoefer W. J. R., (1985) "The transmission-line matrix method – Theory and Applications", *IEEE Transactions on Microwave Theory and Techniques*, Vol. 33, pp. 882-893

Hoefer W. J. R., (1991) "Huygens and the computer – A powerful alliance in numerical electromagnetics", *Proceedings of the IEEE*, Vol. 79, pp. 1459-1471

Hoefer W. J. R. and So P. M., (1991) "The electromagnetic wave simulator", *John Wiley & Sons*

Hoekstra P., Delaney A., (1974) "Dielectric properties of soils at UHF and microwave frequencies", *Journal of Geophysical Research*, Vol. 79, pp. 1699-1708

Holland R., Simpson L., Kunz K. S., (1980) "Finite-difference Analysis of EMP Coupling to Lossy Dielectric Structures", *IEEE Transcations on Electromagnetic Compatibility*, Vol. 22, pp. 203-209

Huber C., Krumpholz M., Russer P., (1995) "Dispersion in anisotropic media modeled by three-dimensional TLM", *IEEE Transactions on Microwave Theory and Techniques*, Vol. 43, pp. 1923-1934

Iizuka K., (1984) "Subsurface radars", *Proceedings of the International Symposium on*

Noise and Clutter Rejection in Radars and Imaging Sensors, IEICE, pp. 15-24

Iizuka K., Freundorfer A. P., (1983) "Detection on nonmetallic buried objects by a step frequency radar", *Proceedings of the IEEE*, Vol. 71, pp. 276-279

Iizuka K., Freundorfer A. P., Wu K. H., Mori H., Ogura H., Nguyen V., (1984) "Step-frequency radar" *Journal of Applied Physics*, Vol. 56, pp. 2572-2583

Imai T., Sakayama T., Kanemori T., (1987) "Use of ground-probing radar and resistivity surveys for archaeological investigations", *Geophysics*, Vol. 52, pp. 137-150

Jensen M. A. and Rahmat-Samii Y., (1995) "EM Interaction of Handset Antennas and a Human in Personal Communications", *Proceedings of the IEEE*, Vol. 83, pp. 7-17

Jin H. and Vahldieck R., (1994) "Direct derivations of TLM symmetrical condensed node and hybrid symmetrical condensed node from Maxwell's equations using centered differencing and averaging", *IEEE Transactions on Microwave Theory and Techniques*, Vol. 42, pp. 2554-2561

Johnk C. T. A., (1975) "Engineering electromagnetics. Fields and waves", *John Wiley & Sons*

Johns P. B., (1974) "The solution of inhomogeneous waveguide problems using a transmission-line matrix", *IEEE Transactions on Microwave Theory and Techniques*, Vol. 22, pp. 209-215

Johns P. B., (1974b) "A new mathematical model to describe the physics of propagation", *The Radio and Electronic Engineer*, Vol. 41, pp. 657-666

Johns P. B., (1987) "A symmetrical condensed node for the TLM method", *IEEE Transactions on Microwave Theory and Techniques*, Vol. 35, pp. 370-377

Johns P. B. and Beurle R. L., (1971) "Numerical solution of 2-dimensional scattering problems using a transmission-line matrix", *IEE Proceedings*, Vol. 118, pp. 1203-1208

Johnson W. A. and Dudley D. G., (1983) "Real axis integration of Sommerfeld integrals: Source and observation points in air", *Radio Science*, Vol. 18, pp. 175-186

Junkin G. and Anderson A. P., (1988) "Limitations in microwave holographic imaging over a lossy half space", *IEE Proceedings*, Vol. 135, pt. F, pp. 321-329

Jurgens T. G., Taflove A., Umashankar K., Moore T. G., (1992) "Finite-Differnce Time-Domain Modeling of Curved Surfaces", *IEEE Transactions on Antennas and Propagation*, Vol. 40, pp. 357-366

Kashiwa T. and Fukai I., (1990) "A treatment by FDTD method of dispersive characteristics associated with electronic polarization", *Microwave and Optics Technology Letters*, Vol. 3, pp. 203-205

Kathage A. F., (1992) "A challenge: GPR in advance of horizontal drilling", *Proceedings of the 4th International conference on ground penetrating radar*, pp. 119-124

Katsube T. S., Collett L. S., (1976) "Electromagnetic propagation characteristics of rocks", in *The physics and chemistry of minerals and rocks, John Wiley & Sons* eds. Strens R. G., pp. 279-295

Keller G. V., (1987) "Rock and mineral properties", *Electromagnetic methods in Applied Geophysics, SEG*, eds. Nabighian M. N., Vol. 1, pp. 13-51

Keys R. G., (1985) "Absorbing boundary conditions for acoustic media", *Geophysics*, Vol. 50, pp. 892-902

King R. W. P., Owens M., Wu T. T., (1992) "Lateral electromagnetic waves", *Springer-Verlag*

King R. W. P. and Sandler S. S., (1994) "The electromagnetic field of a vertical electric dipole over the earth or sea", *IEEE Transactions on Antennas and Propagation*, Vol. 42, pp. 382-389

King R. W. P., Smith G. S., Owens M., Wu T. T., (1981) "Antennas in Matter. Fundamentals, Theory and Applications", *The MIT Press*

Kingsley S. and Quegan S., (1992) "Understanding radar systems", *McGraw-Hill*

Kong F-N., Kristiansen J., By T. L., (1992) "A radar investigation of pyramids", *Proceedings of the 4th International conference on ground penetrating radar*, pp. 345-349

Kong J. A., (1986) "Electromagnetic Theory", *John Wiley & Sons*

Kraus J. D., (1991) "Electromagnetics", *McGraw-Hill*

Krumpholz M., Bader B., Russer P., (1995) "On the theory of discrete TLM green's functions in three-dimensional TLM", *IEEE Transactions on Microwave Theory and Techniques*, Vol. 43, pp. 1472-1483

Krumpholz M. and Russer P., (1994) "On the dispersion in TLM and FDTD", *IEEE Transactions on Microwave Theory and Techniques*, Vol. 42, pp. 1275-1279

Krumpholz M. and Russer P., (1994b) "A field theoretical derivation of TLM", *IEEE Transactions on Microwave Theory and Techniques*, Vol. 42, pp. 1660-1668

Kunz K. S. and Luebbers R. J., (1993) "The Finite Difference Time Domain Method for Electromagnetics", *CRC Press*

Lee K. C., Junkin G., Kingsley S. P., "New strategy to locate buried objects in highly lossy ground", *IEE Proceedings*, Vol. 142, pp. 306-312

Liao Z. P., Wong H. L., Baipo Y., Yifan Y., (1984) "A transmitting boundary for transient wave analyses", *Scientia Sinica*, Vol. 27, pp. 1063-1076

Liner C. L. and Liner J. L., (1995) "Ground penetrating radar: A near-face experience from Washington County, Arkansas", *The Leading Edge*, Vol. 14, No. 1, pp. 17-21

Liu C. and Shen L. C., (1991) "Numerical simulation of subsurface radar for detecting buried pipes", *IEEE Transactions on Geoscience and Remote Sensing*, Vol. 29, pp. 795-798

LoVetri J. and Simons N. R. S., (1993) "A class of symmetrical condensed node TLM methods derived directly from Maxwell's equations", *IEEE Transactions on Microwave Theory and Techniques*, Vol. 41, pp. 1419-1428

Luebbers R. J. and Hunsberger F., (1992) "FDTD for Nth-order dispersive media", *IEEE Transactions on Antennas and Propagation*, Vol. 40, pp. 1297-1301

Luebbers R. J., Hunsberger F., Kunz K. S., (1991) "A Frequency-Dependent Finite-

Difference Time-Domain Formulation for Transient Propagation in Plasma", *IEEE Transactions on Antennas and Propagation*, Vol. 39, pp. 29-34

Madsen N. K. and Ziolkowski W., (1988) "Numerical solution of Maxwell's equations in the time domain using irregular nonorthogonal grids", *Wave Motion*, Vol. 10, pp. 583-596

Maijala P., (1992) "Application of some seismic data processing methods to ground penetrating radar", *Proceedings of the 4th International conference on ground penetrating radar*, pp. 103-110

Maloney J. G., (1992) "Analysis and Synthesis of Transient Antennas using the Finite-Difference Time-Domain (FDTD) Method", *Ph.D thesis*, Georgia Institude of Technology, U.S.A.

Maser K. R., (1992) "Non-destructive testing of bridge, highway and airport pavements", *Proceedings of the 4th International conference on ground penetrating radar*, pp. 267-276

Mei K. K. and Fang J., (1992) "Superabsorbtion – A method to improve absorbing boundary conditions", *IEEE Transactions on Antennas and Propagation*, Vol. 40, pp. 1001-1010

Menezes (de) L. R. A. X. and Hoefer W. J. R., (1994) "Modelling frequency dependent dielectrics in TLM", *Proceedings of the IEEE Antennas and Propagation International Symposium*, pp. 1140-1143

Michiguchi Y., Hiramoto K., Nishi M., Ootaka T., Okada M., (1988) "Advanced subsurface radar system for imaging buried pipes", *IEEE Transactions on Geoscience and Remote Sensing*, Vol. 26, pp. 733-740

Millard S. G., Shaw M. R., Giannopoulos A., Soutsos M. N., (1996) "Modelling of subsurface pulsed radar for non-destructive testing of structures", *Journal of Materials in Civil Engineering*, (submitted)

Miller E. K., (1988) "A selective survey of computational electromagnetics", *IEEE Transactions on Antennas and Propagation*, Vol. 36, pp. 1281-1305

Moffat D. L. and Puskar R. J., (1976) "A subsurface electromagnetic pulse radar", *Geophysics*, Vol. 41, pp. 506-518

Moghaddam M. and Chew W. C., (1991) "Stabilizing Liao's absorbing boundary conditions using single-precision arithmetic", *Proceedings of the IEEE Antennas and Propagation International Symposium*, pp. 430-433

Moghaddam M., Yannakakis E. J., Chew W. C., (1991) "Modeling of the subsurface interface radar", *Journal of Electromagnetic Waves and Applications*, Vol. 5, pp. 17-39

Moore T. G., Blaschak J. G., Taflove A., Kriegsman G. A., (1988) "Theory and application of radiation boundary operators", *IEEE Transactions on Antennas and Propagation*, Vol. 36, pp. 1797-1812

Morente J. A., Gimenez G., Porti J. A., Khalladi M., (1994) "Group and phase velocities in the TLM-symmetrical-condensed node mesh", *IEEE Transactions on Microwave Theory and Techniques*, Vol. 42, pp. 514-517

Morente J. A., Gimenez G., Porti J. A., Khalladi M., (1995) "Dispersion analysis for a TLM mesh of symmetrical condensed nodes with stubs", *IEEE Transactions on Microwave Theory and Techniques*, Vol. 43, pp. 452-456

Morente J. A., Porti J. A., Khalladi M., (1992) "Absorbing boundary conditions for the TLM method", *IEEE Transactions on Microwave Theory and Techniques*, Vol. 40, pp. 2095-2099

Morita N., Kumagai N., Mautz J., (1990) "Integral equation methods for electromagnetics", *Artech House*

Motoyuki S., (1992) "Polarimetric borehole radar", *Extended Abstracts of the 54th EAEG meeting*, pp. 438-439

Motoyuki S., Ohkubo T., Niitsuma H., (1995) "Cross-polarization borehole radar measurements with a slot antenna", *Journal of Applied Geophysics*, Vol. 33, pp. 53-61

Mott H., (1986) "Polarization in antennas and radar", *John Wiley & Sons*

Mur G., (1981) "Absorbing boundary conditions for the finite-difference approximation of the time-domain electromagnetic-field equations", *IEEE Transactions on Electromagnetic Compatibility*, Vol. 23, pp. 377-382

Nabighian M. N., (1987) "Electromagnetic methods in applied geophysics", *Society of Exploration Geophysicists*, Vol. 1

Naylor P. and Ait-Sadi R., (1992) "Simple method for determining 3-D TLM nodal scattering in nonscalar problems", *Electronics Letters*, Vol. 28, pp. 2353-2354

Naylor P. and Ait-Sadi R., (1993) REPLY to COMMENT on "Simple method for determining 3-D TLM nodal scattering in nonscalar problems" by J. A. Morente and J. A. Porti, *Electronics Letters*, Vol. 29, pp. 1056-1057

Naylor P. and Desai R. A., (1990) "New three dimensional symmetrical condensed lossy node for solution of electromagnetic wave problems by TLM", *Electronics Letters*, Vol. 26, pp. 492-494

Nielsen J. S., (1991) "Spurious modes of the TLM-condensed node formulation", *IEEE Microwave and guided wave letters*, Vol. 1, pp. 201-203

Nielsen J. S. and Hoefer W. J. R., (1991) "A complete dispersion analysis of the condensed node TLM mesh", *IEEE Transactions on Magnetics*, Vol. 27, pp. 3982-3985

Nielsen J. S. and Hoefer W. J. R., (1993) "Generalized dispersion analysis and spurious modes of 2-D and 3-D TLM formulations", *IEEE Transactions on Microwave Theory and Techniques*, Vol. 11, pp. 1375-1384

Nikoskinen K. I., (1993) "Time-domain study of half-space transmission problem with vertical and horizontal dipoles", *IEEE Transactions on Antennas and Propagation*, Vol. 41, pp. 1399-1407

Nikoskinen K. I., (1990) "Time-domain analysis of horizontal dipoles in front of planar dielectric interface", *IEEE Transactions on Antennas and Propagation*, Vol. 38, pp. 1951-1957

Olhoeft G. R., (1976) "Electrical properties of rocks", in *The physics and chemistry of*

minerals and rocks, John Wiley & Sons eds. Strens R. G., pp. 261-278

Olivier J. C., (1992) "On the synthesis of exact free space absorbing boundary conditions for the finite-difference time-domain method", *IEEE Transactions on Antennas and Propagation*, Vol. 40, pp. 456-460

Olver A. D., Cuthbert L. G., Nikolaides M., Carr A. G., (1982) "Portable FMCW radar for locating buried pipes", *RADAR – 82*, IEE Conference publ., No. 26, pp. 413-418

Omick S. R., (1993) "A new finite-difference time-domain algorithm for the accurate modeling of wide-band electromagnetic phenomena", *IEEE Transactions on Electromagnetic Compatibility*, Vol. 35, pp. 215-222

Oristaglio M. L. and Hohmann G. W., (1984) "Diffusion of electromagnetic fields in a two-dimensional earth: A finite-difference approach", *Geophysics*, Vol. 49, pp. 870-894

Overmeeren (van) R. A., (1996) "Georadar in hydrogeology", *First Break*, Vol. 12, No. 8, pp. 401-408

Parry N. S. and Davis J. L., (1992) "GPR systems for roads and bridges", *Proceedings of the 4th International conference on ground penetrating radar*, pp. 247-257

Patterson A., Tealby J. M., Allinson N. M., (1995) "GPR imaging with focused migration", *Extended Abstracts of the 57th EAGE meeting*, P053

Peters L. Jr., Young J. D., (1986) "Applications of Subsurface radar", in *Time-domain measurments in electromagnetics, Van Nostrand Reinhold* eds. Miller E. K., pp. 296-351

Peters L. Jr., Daniels J. J., Young J. D., (1994) "Ground penetrating radar as a subsurface environmental sensing tool", *Proceedings of the IEEE*, Vol. 82, pp. 1802-1822

Pilon J. A. and Grieve R. A. F., (1991) "The Subsurface character of meteor crater, Arizona, as determined by ground-probing radar", *Journal of Geophysical Research*, Vol. 96, pp. 15563-15576

Potter D., (1973) "Computational Physics", *John Wiley & Sons*

Press W. H., Teukolsky S. A., Vetterling W. T., Flannery B. P., (1992) "Numerical Recipes in C", *Cambridge University Press*

Rahmat-Samii Y., Mittra R., Parhami P., (1981) "Evaluation of Sommerfeld integrals for lossy half-space problems", *Electromagnetics*, Vol. 1, pp. 1-28

Ramo S., Whinnery J. R., Duzer (van) T., (1994) "Fields and waves in communication electronics", *John Wiley & Sons*

Robinson E. A. and Treitel S., (1980) "Geophysical signal analysis", *Prentice-Hall*

Rosenberg (von) D. U., (1969) "Methods for the Numerical Solution of Partial differential Equations", *Elsevier Publishing Company*

Saguet P. and Pic E., (1982) "Utilisation d'un nouveau type de noeud dans la methode TLM en 3 dimensions", *Electronics Letters*, Vol. 18, pp. 478-480

Scaramuzza R. and Lowery A. J., (1990) "Hybrid summetrical condensed node for the TLM method", *Electronics Letters*, Vol. 26, pp. 1947-1949

Scott H. F., (1989) "Buried plant mapping by ground probing radar", *Proceedings of the 2nd National conference of the National Joint Utilities Group, U.K.*, E665

Sezginer A. and Chew W. C., (1984) "Closed form expression of the Green's function for the time-domain wave equation for a lossy two-dimensional medium", *IEEE Transactions on Antennas and Propagation*, Vol. 32, pp. 527-528

Sheriff R. E., (1991) "Encyclopedic Dictionary of Exploration Geophysics", *Society of Exploration Geophysicists*

Shlager K. L. and Schneider J. B., (1995) "A selective survey of the finite-difference time-domain literature", *IEEE Antennas and Propagation Magazine*, Vol. 37, No. 4, pp. 39-56

Siegel M., King R. W. P., (1970) "Electromagnetic fields in a dissipative half-space: A numerical approach", *Journal of Applied Physics*, Vol. 41, pp. 2415-2423

Simons N. R. S. and Bridges E., (1990) "Method for modelling free space boundaries in

TLM simulations", *Electronics Letters*, Vol. 26, pp. 453-455

Simons N. R. S. and Bridges E., (1991) "Equivalence of propagation characteristics for the transmission-line matrix and the finite-difference time-domain methods in two dimensions", *IEEE Transactions on Microwave Theory and Techniques*, Vol. 39, pp. 354-356

Simons N. R. S., Sebak A. A., Bridges E., Antar Y. M. M., (1991) "Transmission-line matrix (TLM) method for scattering problems", *Computer Physics Communications*, Vol. 68, pp. 197-212

Skolnic M. I., (1981) "Introduction to radar systems", *McGraw-Hill*

Smith G. D., (1978) "Numerical solution of partial differential equations", *Clarendon Press*

Smith G. S., (1984) "Directive properties of antennas for transmission into a material half-space", *IEEE Transaction on Antennas and Propagation*, Vol. 32, pp. 232-246

Smith G. S. and Scott W. R. Jr., (1989) "A scale model for studying ground penetrating radars", *IEEE Transactions on Geoscience and Remote Sensing*, Vol. 27, pp. 358-363

Sommerfeld A., (1909) "Propagation of waves in wireless telegraphy", *Annalen de Physik* (Leipzig), Vol. 28, pp. 665-737

Steich D. and Luebbers R., (1994) "Higher order FDTD absorbing boundaries", *Proceedings of the 10th Annual Review of Progress in Applied Computational Electromagnetics*,

Stewart R. D. and Underberger R. R., (1976) "Seeing through rock salt with radar", *Geophysics*, Vol. 41, pp. 123-132

Stolt R. H., (1978) "Migration by Fourier transform", *Geophysics*, Vol. 43, pp. 23-48

Stratton J. A., (1941) "Electromagnetic Theory", *McGraw-Hill*

Sullivan D. M., (1992) "A Frequency-Dependent FDTD Method for Biological Applications", *IEEE Transactions on Microwave Theory and Techniques*, Vol. 40, pp. 532-539

Szymanski J., Campbell T., Dittmer J., Giannopoulos A., Tsourlos P., (1992) "Non-destructive site diagnosis at medieval abbey sites in the U.K.", *Medieval Europe*, Vol. 6, pp. 201-206

Taflove A., (1980) "Application of the finite-difference time-domain method to sinusoidal steady-state electromagnetic-penetration problems", *IEEE Transactions on Electromagnetic Compatibility*, Vol. 22, pp. 191-202

Taflove A., (1995) "Computational Electrodynamics: The Finite-Difference Time-Domain Method", *Artech House*

Taflove A. and Brodwin M. E., (1975) "Numerical solution of steady-state electromagnetic scattering problems using the time-dependent Maxwell's equations", *IEEE Microwave Theory and Techniques*, Vol. 23, pp. 623-630

Taflove A. and Umashankar K. R., (1989) "Review of FD-TD Numerical Modeling of Electromagnetic Wave Scattering and Radar Cross Section", *Proceedings of the IEEE*, Vol. 77, pp. 682-699

Taflove a., Umashankar K. R., Beker B., Harfoush F. A., Yee K. S., (1988) "Detailed FD-DT analysis of electromagnetic fields penetrating narrow slots and lapped joints in thick conducting screens", *IEEE Transactions on Antennas and Propagation*, Vol. 36, pp. 247-257

Tealby J. M., Oxley J., Campbell T., Giannopoulos A., Dittmer J., (1993) "Analysis of ground probing radar data, including polarization effects, when used in condition assesment of ancient monuments", in *Geophysical Exploration of Archaeological Sites, SERIES: Theory and Practice of Applied Geophysics, Vieweg Verlag*, A. Vogel and G. Tsokas eds., Vol. 7, pp. 235-247

Telford W. M., Geldart L. P., Sheriff R. E., (1990) "Applied Geophysics", *Cambridge University Press*

Tong C. E. and Fujino Y., (1991) "An efficient algorithm for transmission line matrix analysis of electromagnetic problems using the symmetrical condensed node", *IEEE Transactions on Microwave Theory and Techniques*, Vol. 39, pp. 1420-1424

Trenkic V., (1995) "The development and characterization of advanced nodes for the TLM method", *Ph.D thesis*, University of Nottingham, U.K.

Trenkic V., Benson T. M., Christopoulos C., (1995) "Dispersion analysis of a TLM mesh using a new scattering matrix formulation", *IEEE Microwave and Guided Wave Letters*, Vol. 5, pp. 79-80

Trenkic V., Christopoulos C., Benson T. M., (1993) "Simple and elegant formulation of scattering in TLM nodes", *Electronics Letters*, Vol. 29, pp. 1651-1652

Trenkic V., Christopoulos C., Benson T. M., (1994) "New symmetrical super-condensed node for the TLM method", *Electronics Letters*, Vol. 30, pp. 329-330

Trenkic V., Christopoulos C., Benson T. M., (1995) "Theory of the symmetrical super-condensed node for the TLM method", *IEEE Transactions on Microwave Theory and Techniques*, Vol. 43, pp. 1342-1348

Tsokas G., Giannopoulos A., Tsourlos P., Vargemezis G., Tealby J. M., Sarris A., Papazachos C., Savopoulou Th., (1994) "A large scale geophysical survey in the archaeological site of Europos (Northern Greece)", *Journal of Applied Geophysics*, Vol. 32, pp. 85-98

Tsuchihashi H., Satoh K., Matsuura T., Noguchi H., Uekubo Y., Usami T., (1989) "A radar system for underground pipe detection", *Proceedings of the International Symposium on Noise and Clutter Rejection in Radars and Imaging Sensors, IEICE*, pp. 651-655

Turner G., (1994) "Subsurface radar propagation deconvolution", *Geophysics*, Vol. 59, pp. 215-223

Umashankar K. R., Taflove A., Beker B., (1987) "Calculation and experimental validation of induced currents on coupled wires in an arbitrary shaped cavity", *IEEE Transactions on antennas and Propagation*, Vol. 35, pp. 1248-1257

Vainikainen P., Tiuri M., Kontra V., Nyfors E., (1992) "Portable short range subsurface radar", *Proceedings of the 4th International conference on ground penetrating radar*, pp. 29-33

Vaughan C. J., (1986) "Ground-penetrating radar used in archaeological investigations",

Geophysics, Vol. 51, pp. 595-604

Wagner R. L. and Chew W. C., (1995) "An analysis of Liao's absorbing boundary condition", *Journal of Electromagnetic Waves and Applications*, Vol. 9, pp. 993-1009

Wait J. R., (1961) "The electromagnetic fields of a horizontal dipole in the presence of a conducting half-space", *Canadian Journal of Physics*, Vol. 39, pp. 1017-1027

Wait J. R., (1986) "Introduction to Antennas & propagation", *Peter Peregrinus, Ltd.*

Wang J. R., (1980) "The dielectric properties of soil-water mixtures at microwave frequencies", *Radio Science*, Vol. 15, pp. 977-985

Ward S. H. and Hohmann G. W., (1987) "Electromagnetic theory for geophysical applications", *Electromagnetic methods in Applied Geophysics, SEG*, eds. Nabighian M. N., Vol. 1, pp. 131-311

Wensink W. A., (1993) "Dielectric properties of wet soils in the frequency range 1-3000 MHz", *Geophysical Prospecting* Vol. 41, pp. 671-696

Wobschall D., (1977) "A theory of the complex dielectric permittivity of soil containing water: The semidisperse model", *IEEE Transactions on Geoscience and Remote Sensing*, Vol. 15, pp. 49-58

Yee K. S., (1966),"Numerical Solution of Initial Boundary Value Problems Involving Maxwell's Equations in Isotropic Media", *IEEE Transactions on Antennas and Propagation*, Vol. 14, pp. 302-307

Yilmaz O., (1987) "Seismic data processing", *Society of Exploration Geophysicists*

Yokoyama A., (1994) "Electromagnetic fields of dipoles effected by a semi-infinite media", *IEICE Transactions on Communications*, Vol. E77-B, pp. 56-63

Young J. L., (1995) "Propagation in linear dispersive media: Finite difference time-domain methodologies", *IEEE Transactions on Antennas and Propagation*, Vol. 43, pp. 422-426

Young R. A., Deng Z., Sun J. (1995), "Interactive processing of GPR data", *The Leading*

Edge, Vol. 14, No. 4, pp. 275-280

Zeng X., McMechan A., Cai J., Chen H. -W., (1995) "Comparison of ray and Fourier methods for modeling monostatic ground-penetrating radar profiles", *Geophysics*, Vol. 60, pp. 1727-1734

Ziolkowski R. W., Madsen N. K., Carpenter C., (1983) "Three-dimensional computer modeling of electromagnetic fields: A global lookback lattice truncation scheme", *Journal of Computational Physics*, Vol. 50, pp. 360-408